Western Graduate&PostdoctoralStudies

Western University
Scholarship@Western

Electronic Thesis and Dissertation Repository

2-15-2013 12:00 AM

A Multispectral Assessment of Complex Impact Craters on the Lunar Farside

Bhairavi Shankar
The University of Western Ontario

Supervisor
Dr. Gordon R. Osinski
The University of Western Ontario

Graduate Program in Planetary Science
A thesis submitted in partial fulfillment of the requirements for the degree in Doctor of Philosophy
© Bhairavi Shankar 2013

Follow this and additional works at: https://ir.lib.uwo.ca/etd

Part of the Geology Commons, Geomorphology Commons, Physical Processes Commons, and the The Sun and the Solar System Commons

Recommended Citation

Shankar, Bhairavi, "A Multispectral Assessment of Complex Impact Craters on the Lunar Farside" (2013). *Electronic Thesis and Dissertation Repository*. 1137.
https://ir.lib.uwo.ca/etd/1137

This Dissertation/Thesis is brought to you for free and open access by Scholarship@Western. It has been accepted for inclusion in Electronic Thesis and Dissertation Repository by an authorized administrator of Scholarship@Western. For more information, please contact wlswadmin@uwo.ca.

A MULTISPECTRAL ASSESSMENT OF COMPLEX IMPACT CRATERS ON THE LUNAR FARSIDE

(Spine title: Multispectral Analyses of Lunar Impact Craters)

(Thesis format: Integrated Article)

by

Bhairavi Shankar

Graduate Program in Geology: Planetary Science

A thesis submitted in partial fulfillment
of the requirements for the degree of
Doctor of Philosophy

The School of Graduate and Postdoctoral Studies
The University of Western Ontario
London, Ontario, Canada

© Bhairavi Shankar 2013

Abstract

Hypervelocity collisions of asteroids onto planetary bodies have catastrophic effects on the target rocks through the process of shock metamorphism. The resulting features, *impact craters*, are circular depressions with a sharp rim surrounded by an ejecta blanket of variably shocked rocks. With increasing impact energy, the inner crater cavity can preserve complex morphologies including terraced walls, central uplifts, and melted rocks. The lack of erosion due to the absence of water or an atmosphere makes the Moon the perfect target to study impact crater processes, in particular the distribution of highly shocked materials within impact craters of different sizes. This study focuses on the characterization and distribution of highly shocked impact melt deposits using multispectral satellite datasets around three complex craters on the farside of the Moon. The study sites have varying morphologies of central uplifts on the crater floor: 1) the 81 km Olcott crater has a cluster of peak hills; 2) Kovalevskaya crater is a 113 km diameter complex crater with a central peak; and 3) Schrödinger basin has a central peak ring. Models propose that the collapse of crater walls and central uplifts during the final stages of crater formation determine where much of the melt rich rocks are eventually emplaced. The results of this study indicate that for increasing crater sizes, the volume of melt-rich rocks generated also increases – at rates greater than model estimates. Impact melt deposits are emplaced beyond the crater rims at each of the sites and preserve a range of morphologies, including melt veneers, melt sheet, and ponded deposits. The regional and local topography, together with crater modification processes greatly affect where the impact melts are finally emplaced. The compositional analyses of the farside crust, using multispectral reflectance spectroscopy in the UV-VIS-NIR range, indicates that there is increasing evidence of highly mafic compositions (i.e., rocks rich in high-Ca pyroxene, olivine, spinel) intercalated within the original crustal highlands (rocks rich in plagioclase feldspar, and low-Ca pyroxenes) on the lunar farside, proving that the lunar farside is a far more geologically complicated terrain than originally assumed.

Keywords

Impact Cratering, Moon, Multispectral, Remote Sensing, Mineralogy, Data Fusion, Surface Processes

Co-Authorship Statement

Chapter 1 was a compilation of the existing literature relevant to the topic of this study. Dr. G. R. Osinski and Dr. I. Antonenko contributed to the editing of the chapter.

Chapter 2 of this thesis has been accepted as a scientific publication in the January 2013 edition of the Canadian Journal of Earth Science. This article is published in the special issue of Canadian contributions to Planetary Geoscience. The title of the article is "A Multispectral geological study of the Schrödinger impact basin", and co-authors of the paper are Dr. G. R. Osinski and Dr. I. Antonenko (Centre for Planetary Science and Exploration – Western University, London, ON), and Dr. C. D. Neish (Applied Physics Laboratory – The Johns Hopkins University, Laurel, MD). The processing and analysis of the data was done by B. Shankar. The co-authors contributed to the writing and editing of the manuscript. Dr. I. Antonenko provided the automated script for the identification of basalt-rich spectra (Fig. 2.7) and the 3-D LRO-LOLA topography data (Fig. 2.14). Dr. C.D. Neish provided the Mini-RF radar data (Figs. 2.10, 2.11) in Chapter 2 and Appendix A (Fig. A3). Dr. Scott Mest (Planetary Science Institute) and an anonymous reviewer provided reviewer comments during the journal submission process.

Data processing and analysis for Olcott crater (Chapter 3) was done by B. Shankar. Dr. G. R. Osinski, Dr. I. Antonenko, Dr. L. L. Tornabene (Centre for Planetary Science and Exploration – Western University, London, ON), and Dr. B.R. Hawke (Hawai'i Institute of Geophysics and Planetology – University of Hawai'i at Manoa) contributed to the writing and editing of the chapter.

Processing and analysis of data for Kovalevskaya crater (Chapter 4) was done by B. Shankar. Valuable discussion on the techniques for melt calculation was provided by Dr. G. R. Osinski, I. Antonenko, and Dr. L. L. Tornabene (Centre for Planetary Science and Exploration – Western University, London, ON). Dr. G. R. Osinski and Dr. I. Antonenko (Centre for Planetary Science and Exploration – Western University, London, ON) also contributed to the writing and editing of the chapter.

Chapter 5 was a summary on the contributions of the study. Dr. G. R. Osinski and Dr. I. Antonenko (Centre for Planetary Science and Exploration – Western University, London, ON) contributed to the writing and editing of the chapter.

The examining committee provided valuable feedback and comments on various topics discussed in the text that were later implemented in the thesis manuscript.

Acknowledgments

It has been an interesting journey getting to this point of my academic career. If you had asked me 10 years ago if I'd do a Ph.D., I would have given an appalling stare given how well (not) my undergraduate study was going that sophomore year. But I am glad I stuck around. The one good thing that came from doing my undergraduate in a small program of Planetary Science was the opportunity to take a geology course in my third year. As soon as I took that mineralogy class, I knew I was hooked. I finally found a way to combine my love of Astronomy, and my fascination with volcanism and plate tectonics. The concept of studying and graduating with a degree in such a topic was becoming real. I really value the opportunity, as an undergrad, to attend the 2005 Planetary Science Workshop in Whistler, BC. It was the first opportunity for me to learn the 101 of Planetary Science, meet other members in the field (academia, and grad students), and learn about the varied types of research that was happening in Canada. The opportunity was truly enriching, particularly conversations with other students (both undergraduate and graduate) who encouraged me to continue, and more importantly not to give up the thought of doing scientific research just because my marks were not at the top. I would like to acknowledge Dr. Ralph Chou and Leslie Harvey (from the Toronto chapter of the R.A.S.C.), Mrs. Barbara Stewart (from my high school in Mississauga, ON), and Drs. James Mungall, Grant Henderson, and James Brennan for many insightful conversations and guidance during those formative years. Special acknowledgment also goes to my Master's degree advisor Dr. Vicki Hansen (University of Minnesota – Duluth), whose role as a mentor was truly valued. Her support throughout the degree program, introducing me to the endless excitement and possibilities of understanding another planet, has made the first part of my graduate experience enriching. The scientific results from the Master's study, and the general sense of accomplishment in contributing to science encouraged me to continue further, and embark on a doctoral study.

The past four and a half years have honestly gone in a flash and as I reflect back on my Ph.D. experience, I have many positive experiences to take away with me. Firstly, "*thanks for the opportunity"* is too small a phrase to express my gratitude to my Ph.D. advisor, Dr. Gordon Osinski. As a thesis advisor, he has been very approachable, and has provided valuable

insights in helping me define the scope of this doctoral study. He has been a great mentor, providing the resources and opportunities to conduct effective research. Under his direction I was able to participate with the rest of our research team on analogue missions, hone many of my technical research skills, and really self-discover aspects of scientific research I see myself conducting in the future. He has also been highly supportive in letting me work from home to accommodate my family commitments this past year, which is greatly appreciated.

The other person who has provided immense guidance is Dr. Irene Antonenko, who was on my supervisory committee. I cannot properly express my gratitude in writing of how much her mentoring has been of value. The conversations have been endless, and more often than not she has picked on my writing styles. But it has, in my mind, made me a better scientific researcher. Others who have provided advice and constructive reviews on Chapters 1 – 4 include Dr. B. Ray Hawke, Dr. Catherine Neish, Dr. Louisa Preston, and Dr. Livio Tornabene, and they are thanked.

Many have assisted in the large data processing work in support of this thesis, particularly navigating through the vast LRO Camera database in searching for photo images. They include Chris Shaver, Christine Preston, and Jacky Clayton. Financial support has come mainly from the Industrial Research Chair award for Dr. Osinski, sponsored by the Canadian Space Agency, MacDonald Dettwiler and Associates (MDA), and NSERC. The Career Development Award from the Lunar and Planetary Institute has provided some travel support towards conference presentations. The Centre for Planetary Science and Exploration at Western University, and the annual Lunar and Planetary Science Conference in Houston, Texas have been valuable hubs for gaining scientific knowledge, and engaging in research discussions with researchers from varied scientific backgrounds in Planetary Science.

I would like to acknowledge all the encouragement and support from extended family, friends, and well-wishers on both continents. Special mention goes to my grand-uncle and aunt in Denmark, my aunts in India, cousins, the Kaushika gothram and VSN groups, Sarika, Tabinda, and Abhilasha. Big thanks also to the London crew particularly Annemarie, Cass, Marc, Marianne, Alaura, Haley, Mel, Laura T., Anna C., Ryan, Raymond, Mahdia, Nicky, Alyssa, and Jen for multiple conversations on life, food, and of course science in the office and labs.

Finally, I would like to express my deep felt gratitude to my parents who have been a tremendous source of support through the entire process. They have encouraged me, right from childhood, to study and pursue whatever I was interested in, and reminded me to appreciate the greater role of knowledge (spiritual and scientific) in one's life. This thesis is dedicated in memory of my mother – who loved every aspect of all the research topics I have worked on to date. She also instilled in me the core values of perseverance and duty towards completing every task, big or small.

Table of Contents

Abstract ii

Co-Authorship Statement iii

Acknowledgments v

Table of Contents viii

List of Tables xii

List of Figures xiii

List of Appendices xxvi

Chapter 1 1

1 Introduction 1

1.1 Impact Cratering – A Geological Process 4

1.1.1 Contact and Compression 4

1.1.2 Excavation 5

1.1.3 Crater Modification 8

1.2 Impact Crater Morphologies 8

1.3 Crater Impactites 9

1.3.1 Crater Ejecta 10

1.3.2 Impact Melt Deposits 11

1.4 Use of Remote Sensing Datasets in Geological Interpretations 12

1.4.1 Role of Spectroscopy 12

1.5 The Moon 14

1.5.1 The Lunar Stratigraphy 14

1.5.1.1 Highland Crust 14

1.5.1.2 Lunar Maria 14

1.5.2 Impact Craters on the Moon 16
1.5.3 Lunar Missions 19
1.5.4 Spectral characteristics of Lunar materials 19
1.6 Thesis Outline 22
1.7 References 25
Chapter 2 34
2 A multispectral geological study of the Schrödinger impact basin 34
2.1 Geological setting of the Schrödinger impact basin 35
2.2 Methods 39
2.2.1 Multispectral Study 39
2.2.2 Mapping exterior melt deposits 44
2.3 Results 45
2.3.1 Regional context 45
2.3.2 Basin interior pyroclastic deposits, tectonic ridge, and mare patches 61
2.3.3 Basin interior melt deposits 61
2.3.4 Peak ring 62
2.3.5 Terraces and basin wall 62
2.3.6 Exterior ejecta and impact melt deposits 62
2.3.7 Post-Schrödinger impact features and secondary craters 64
2.4 Discussion 65
2.4.1 Regional context 65
2.4.2 Inner basin materials 67
2.4.3 Mare patches and pyroclastic deposits 67
2.4.4 Peak ring 68
2.4.5 Post-Schrödinger crater units 68

2.4.6 Spectral unmixing model results 69

2.4.7 Impact melt and ejecta deposits 69

2.5 Summary and future work 71

2.6 References 72

Chapter 3 79

3 Multispectral Analyses of Olcott Crater Using Current Lunar Datasets 79

3.1 Methods 81

3.1.1 Multispectral Data Analyses 83

3.2 Results 86

3.3 Discussion 96

3.3.1 Effects of pre-existing topography on crater formation 96

3.3.2 Nature of the central uplift at Olcott crater 97

3.3.3 Recognition of impact melt deposits 101

3.3.4 Olcott as a window into the subsurface 106

3.4 Summary 108

3.5 References 109

Chapter 4 115

4 Identification and Distribution of Impact Melt Deposits surrounding Complex Impact Craters on the Lunar Farside: A comparison between different crater sizes 115

4.1 Study Sites 120

4.2 Methods 121

4.2.1 Identification of impact melt deposits 121

4.2.2 Calculating melt volumes 128

4.3 Results 136

4.3.1 Impact Melt Deposits within Olcott Crater 140

4.3.2 Impact Melt Deposits associated with Schrödinger Basin 146

4.3.3 Estimates on the volume of melt present around complex craters..... 147

4.4 Discussion..... 149

4.4.1 The identification of exterior melt deposits..... 149

4.4.2 Melt Volumes..... 151

4.5 Summary..... 154

4.6 References:..... 155

Chapter 5 161

5 Discussion on the spectral and spatial characteristics of impact melt deposits surrounding lunar complex craters..... 161

5.1 The distribution of impact melt deposits beyond the crater rim..... 163

5.2 The role of multispectral datasets in identifying impact melt deposits 164

5.2.1 Challenges in using the multispectral datasets..... 165

5.3 Central Uplifts of Complex Craters - Assessing the depths of excavation and melting 166

5.3.1 The central uplift at Olcott crater..... 149

5.3.2 The central uplift at Kovalevskaya crater..... 151

5.3.3 The central uplift at Schrödinger crater..... 151

5.4 Implications..... 169

5.5 Future Work..... 171

5.6 References..... 173

Appendices..... 177

Curriculum Vitae 190

List of Tables

Chapter 1

Table 1.1: Spectral and spatial resolution details of various instruments sent on recent lunar missions with global coverage……..... 20

Chapter 4

Table 4.1: Numerical Calculations of the Transient Cavity and observed melt volumes for the study sites……...131

Table 4.2: Parameter values used for transient cavity and impact melt calculations....……...133

Appendix C

Table C.1: M^3 Product Information for Olcott Crater…….....185

Table C.2: M^3 Product Information for Kovalevskaya Crater…….....186

Table C.3: M^3 Product Information for Schrödinger Basin…….....186

List of Figures

Chapter 1

Figure 1.1: Typical shock pressures (log scale) experienced during an impact event. With increasing shock pressures, the deformations on original rock are more permanent (from Stöffler, 1971).……...…2

Figure 1.2: Global mosaics of the lunar surface captured by the Lunar Reconnaissance Orbiter Wide Angle Camera (LROC –WAC). A) The lunar nearside hemisphere is comprised of round impact craters, light highland crustal rocks and darker volcanic mare deposits. B) The lunar farside has many impact craters; however, there is a lack of much volcanism filling large craters (Hörz et al., 1991). The outline of the South Pole- Aitken basin is marked by the black dashed line. [Image source: NASA/GSFC/ASU].……...……3

Figure 1.3: Three stages of impact crater formation showing the progression of shock waves and emplacement of shocked materials such as crater ejecta and melt sheets (from Melosh, 1989).……..……...…....6

Figure 1.4: Cross sectional view of the excavation flow lines within a target surface (left), and the resulting scale of deformation within the rocks (right). Modified from Melosh, 1989.…….…….……....7

Figure 1.5: The absorption responses of elements for various parts of the electromagnetic spectrum. The cause of response is dependent on the crystal structure, or presence of any crystal defects. For example, within the ultraviolet, visible, and infrared range, the cause of absorption is due to the electronic and vibrational effects on molecules…….……..…..13

Figure 1.6: Cross sectional view of the lunar crust. The top 25 km is comprised of impactite materials emplaced from the formation of large impact basins (modified from Hiesinger et al., 2006 and references therein).……..……..15

Figure 1.7: Impact craters on the Moon show a diverse range of morphologies. A) Typical simple crater (1 km diameter) displays a sharp rim, sloped walls, and inner depression. B)

Theophilus crater, a 100 km complex crater, displays terraced walls, a smooth floor, and a central uplifted peak. C) Schrödinger basin is a 312 km complex crater with an interior peak ring (Chapter 2). D) Orientale basin is a ~930 km complex crater with multiple peak rings and mare deposits within the interior. [Image source: NASA/GSFC/ASU]……..……18

Figure 1.8: Laboratory derived spectral profiles of lunar materials [Source: RELAB Spectral Library]……..**.....**21

Chapter 2

Figure 2.1: A) The location of Schrödinger (dashed circle) shown within the topographic extent of the South Pole - Aitken basin (topography using LOLA data). B) Regional view of the Schrödinger impact basin centered at 75^{o}S/130^{o}E (Clementine 750 nm band). C) A close up of Schrödinger shows a well preserved impact crater with a basin wall, terraces, peak ring, interior mare patches, and a pyroclastic deposit within the basin floor…….……36

Figure 2.2: Original geologic map of Schrödinger impact basin. Adapted from Shoemaker et al. (1994)……37

Figure 2.3: A) Clementine-derived false colour ratio composite map of the study area. The area appears to be a largely matured surface with the exception of post – Schrödinger impact craters within and around the basin. The pyroclastic deposits and mare patches are relatively mafic rich compared to the rest of the study area. B) FeO weight % map of the study area. Values were derived using algorithms defined by Lucey et al., 2000. Both the mare patches and pyroclastic deposits have higher than average FeO content. Shadowed areas also show high FeO content, but this is a known artefact……..41

Figure 2.4: A) Context view of Chandrayaan-1 M^{3} data used in this study (M^{3} strip M3G20090529T013507). The blue box and roman numerals indicate context of 4C. B) Product footprint showing coverage of 4A, with a Clementine 750nm basemap. C) i – v: Context views of sampled geologic units for Fig. 9. i) red box = Exterior melt deposits; ii) orange box = terrace surfaces; iii) yellow boxes = basin interior melts, pink dashed line = peak ring surface, blue arrow = mare patch; iv) blue box = pyroclastic deposit, pink lines =

peak ring surface; v) yellow box = basin interior melts, orange box= terrace surfaces, green box= crater ejecta.....43

Figure 2.5: Locations of sample spectra obtained for all mapped geologic units mapped in Fig. 2.2, as well as the crater ejecta extending to the limits of this image. The sample number is low due to the lack of fresh craters resolvable within the instrument parameters. The distribution of basalt and anorthosite materials is heterogeneous……..……47

Figure 2.6: Sample spectra of mapped units in and around Schrödinger using Clementine data. A) Normalized sample spectra from the mare, pyroclastic deposits and tectonic ridge within the basin floor of Schrödinger. B) and C) Normalized sample spectra from the melt deposit units and exterior ejecta respectively…….……48

Figure 2.7: Mafic rich spectral distribution using algorithm defined by Antonenko and Osinski, 2011. The distribution shows mafic spectral content for the pyroclastic deposits on the basin floor, sporadic distribution along the peak ring, within post Schrödinger impact craters, and along the eastern half of the study area.....49

Figure 2.8: Spectral un-mixing fraction maps. A) Anorthosite distribution: most materials within and around Schrödinger are rich in anorthosite, however, topography is preserved so this endmember includes some component that is not associated with composition. B) Basalt distribution: Crater ejecta (north of basin rim), an external impact crater ray, and tectonic ridge are basalt rich. C) Dark fraction: shadow areas are well highlighted. However, both the mare patches and pyroclastic deposits are picked up as well indicating more spectral endmembers are required to accurately characterize the compositions of these units. D) Root mean square (RMS) error map of spectral un-mixing results……..……...…….50

Figure 2.9A: Chandrayaan-1 M^3 derived sample spectra of basin floor pyroclastic and mare units indicate the presence of mafic minerals, as expected…..……..…….……....52

Figure 2.9B: Chandrayaan-1 M^3 derived sample spectra of the basin interior impact melt unit indicate the presence of low-Ca pyroxene and some plagioclase feldspar. ……..……53

Figure 2.9C: Chandrayaan-1 M^3 derived sample spectra of the peak ring indicate the presence of mostly low-Ca pyroxene, with potentially some plagioclase feldspar. ……..……..…..…54

Figure 2.9D: Chandrayaan-1 M^3 derived sample spectra of the terraced surfaces indicate materials are mostly low-Ca pyroxene. ……..……55

Figure 2.9E: Chandrayaan-1 M^3 derived sample spectra of the ejecta unit suggests a mixture of various materials including plagioclase feldspar and both low and high-Ca pyroxene.…56

Figure 2.9F: Chandrayaan-1 M^3 derived sample spectra of the exterior melt deposits indicates a strong signature of low-Ca pyroxene. …….…… ……57

Figure 2.10: Mini-RF results of study area. (A) Total radar backscatter mosaic of Schrödinger crater in S–Band, from the mini–RF instrument aboard the Lunar Reconnaissance Orbiter. Red box outlines location of Fig. 11. (B) CPR mosaic of Schrödinger crater overlaid on a total radar backscatter mosaic. Here, the CPR has been scaled from 0 (purple) to 1.2 (red). [Image credit: ISRO/NASA/JHUAPL/LPI]……....58

Figure 2.11: Mini-RF results of study area. A) Inset view of Fig. 2.10 showing radar properties of three sites, (1) radar bright mare patches, (2) radar bright crater ray, and (3) radar dark pyroclastic deposits. B) Clementine 750 nm band view of same area as in A)..…59

Figure 2.12: Compiled geologic map of the Schrödinger basin (building on work from Shoemaker et al. (1994), and Mest and vanArsdall (2008)) including the locations of exterior melt deposits. ……....60

Figure 2.13: A) LROC images of inner basin melts and peak ring material that are similar in texture to the exterior deposits (product M141473253RC). B – D) LROC images of ejecta and melt deposit regions beyond Schrödinger crater rim (products M105860485LC; M141418958RC; M141473253RC)..……..……63

Figure 2.14: Digital Elevation Model of Schrödinger and surrounding region (with 7x vertical exaggeration, source: LOLA). Elevation decreases moving eastward and along the northern edges of the area. ……..……..……..66

Chapter 3

Figure 3.1: Morphological variations of lunar impact melt deposits. A) LRO WAC global mosaic context view of Tycho crater (85 km). Red and yellow boxes indicate locations of 3.1B and 3.1C respectively. B) Kaguya Terrain Camera image of impact melts along the crater floor within Tycho crater. Image credit: JAXA/SELENE. C) Mini-RF Image of Tycho crater shows the variations in texture roughness of impact melts. Image credit: Neish et al. (2011). D) LRO NAC image of the crater floor impact melt deposits within Moore F crater. [Image credit: NASA/GSFC/Arizona State University] . ……..……..……..…..80

Figure 3.2: Context view of Olcott crater at various observable scales. Major mare areas are labeled for context. Image sources: NASA/GSFC/Arizona State University. A) Global context view of study region using the LRO WAC monochrome mosaic, centred at 120^{o}. Red box shows area coverage for 3.2B. B) Regional context view, using LRO WAC global mosaic, of the Lomonosov-Fleming Basin area. The main rim location of the degraded basin is outlined in black (modified from Hawke et al., 2003). LRO WAC global mosaic of Olcott crater, displaying the crater morphology. [Image credit: NASA/GSFC/Arizona State University]…….…...……..82

Figure 3.3: Composite maps of the study area created using various multispectral datasets overlaid on LROC WAC mosaics. The legends in Figs. 3.3A–C refer to the composite map parameters. A) Clementine false colour ratio over LROC WAC mosaic. Black boxes outline locations of high mafic content found in addition to the strong features in the southern section. B) Clementine iron content derived from Clementine data over LROC WAC mosaic. C) M^3 derived RGB spectral parameter map of the study area. The colour illustrates the occurrence of integrated band depths at 1, 2, and 1.3 µm respectively in various strengths. D) M^3 (1508nm) mosaic of Olcott crater highlighting locations where spectral profiles (green dots) were sampled. Red box refers to the context location of Fig. 3.8. [Image credit: ISRO/NASA/GSFC/Arizona State University]……...……...…….84

Figure 3.4: Geological sketch map of Olcott crater. [Image credit for basemap: NASA/GSFC/Arizona State University]……... …….87

Figure 3.5: Chandrayaan-1 Moon Mineralogy Mapper (M^3) derived spectral profiles of morphological units identified for Olcott crater. A) Spectral profiles of the crater ejecta indicate the presence of plagioclase feldspar, and low-Ca pyroxene within the northern ejecta deposits; and high-Ca pyroxene within the southern ejecta deposits. B) Spectral profiles of the rim and terraces of Olcott indicate the presence of plagioclase feldspar, low-Ca, and a strong signature of high-Ca pyroxene along the southern area of the crater……89

Figure 3.5 (cont'd): Chandrayaan-1 Moon Mineralogy Mapper (M^3) derived spectral profiles of morphological units identified for Olcott crater. C) Spectral profiles of the melt deposits within and beyond the crater floor indicate the presence of high-Ca pyroxene. Weak absorption features indicating plagioclase feldspar are detected within the crater floor deposits. D) Spectral profiles of the central uplifts within the crater indicate the presence of high-Ca pyroxene and plagioclase feldspar. This indicates a varied morphology within the central uplifts……..…90

Figure 3.6A: Chandrayaan-1 Moon Mineralogy Mapper (M^3) derived spectral profiles of morphological units identified for Olcott crater. A) Spectral profiles of the crater ejecta indicate the presence of plagioclase feldspar, and low-Ca pyroxene within the northern ejecta deposits; and high-Ca pyroxene within the southern ejecta deposits. B) Spectral profiles of the rim and terraces of Olcott indicate the presence of plagioclase feldspar, low-Ca, and a strong signature of high-Ca pyroxene along the southern area of the crater…….……...92

Figure 3.6B: Topography detail of Olcott crater along the W-E direction. (Top) LRO LOLA shaded relief map with context view of the profiled area. (Bottom) The central uplifts on the crater floor range in height from ~200 m to 1 km (black arrows). [Image credit: MIT/NASA]……..…….93

Figure 3.7: A) Context view of Olcott crater highlighting areas where occurrences of impact melts are mapped (red polygons). Marked boxes are context views for close-ups of melt deposits in Fig. 3.7B–G. The image widths for 3.7B–G are 2.5 km. B) Impact melt deposits atop central uplifts are long and narrow, and appear superposed and embayed. LRO Camera NAC image M108460950LC. C) Impact melt deposits on the crater floor are smooth and have low albedo when compared to the central uplift materials which appear rugged. LRO

Camera NAC image M103739096RC. D)–G) Impact melts along the crater walls and terrace zones appear as thin veneers. LRO Camera NAC images M103739096RC; M159189508LC; M115543039RC; M161544383RC. [Image credit: NASA/GSFC/Arizona State University]……..95

Figure 3.8: 3-D views of the central peak hills within Olcott crater. The black dashed rectangle refers to the location of the central peak hill discussed in the text, and featured in Fig. 3.8C. The lettered legend refers to the location of spectral profiles in Fig. 3.8D. A) This is a LRO-WAC context view of central uplift area discussed in 3.8C, D (10x vertical exaggeration). Image width is ~55 km. White arrow refers to location of spectral sampling in Fig. 3.8C. B) M^3 derived IBD parameter map of the area in Fig. 3.8A (10x vertical exaggeration). Image width is ~55 km. [Image credit: ISRO/NASA/GSFC/Arizona State University]……..98

Figure 3.8 (cont'd): Image and spectral characterizations of a central peak hill at Olcott crater. C) LRO NAC (product # M108460950RC) of the central peak hill discussed in text and highlighted in Fig. 3.8A, B. The surface texture is similar to that characterized in Figure 3.7B. Image width is 2.5 km across. The letters refer to sample spectral profiles in Fig. 3.8D. D) Sample spectral profiles of spots identified in Fig. 3.8C. There are variable absorption strengths near 1 µm, 1.3 µm and 2 µm suggesting the presence of high-Ca pyroxene, Mg-spinel and plagioclase feldspar at this central peak hill. [Image credit: NASA/GSFC/Arizona State University]…….……99

Figure 3.9: 3-D views of Olcott crater looking towards the southeast direction. A) 3-D view of the M^3 IBD spectral parameter map draped over LRO-LOLA altimetry data (512ppd resolution and15x vertical exaggeration). Numbered annotations refer to sites with colour anomalies as discussed in the text. B) 3-D image view of the same area as Fig. 3.9A. LRO-WAC global mosaic draped over LRO-LOLA altimetry data (512ppd resolution, 15x vertical exaggeration). [Image credit: NASA/GSFC/Arizona State University]…..……...……103

Figure 3.9 (cont'd): C) Sampled spectral profiles of the three sites (i-iii). The profiles indicate a pyroxene-rich terrain, with absorption features near 1 and 2 µm. There is minimal presence of plagioclase feldspar indicated (lack of absorption feature near 1.3 µm)...……...104

Figure 3.9 (cont'd): Closeups of the spectral anomalies. D) M^3 IBD parameter map overlaid on LRO NAC views of the three sites discussed in Fig. 3.9A–C. Black dashed lines highlight the colour anomalies identified. The ratio of spectral parameters varies significantly compared to the immediate surrounding areas, resulting in the different colours in the IBD map of these three sites. The morphologies vary between all three locations, with smooth low albedo impact melt deposits (site i), crater wall material with variable textures (site ii), and a freshly excavated crater with exposed ejecta deposits (site iii). LRO NAC images: M159189508LC and M115543039RC for site i, M161544383RC for site ii, and M115536257LC for site iii. [Image credit: ISRO/NASA/GSFC/Arizona State University]…….105

Figure 3.10: Illustration of the proposed pre-impact stratigraphy in the Olcott crater region. The impact event occurred within a heterogeneous target, potentially tapping into buried mafic rich materials, likely from the Lomonosov-Fleming basin……107

Chapter 4

Figure 4.1: Cross sectional sketches of the impact cratering process and the emplacement of melt deposits within complex impact craters. A) Zones within an expanding transient cavity. B - D) The location of impact melt within sections of the transient cavity during the evolving stages of crater formation. E) The final crater morphology of a complex crater, with the location of impact melts within both the inner crater fill and beyond the crater rim as ponded deposits. Modified from Melosh, 1989 and Osinski et al., 2011……116

Figure 4.2: Examples of pristine impact melt deposits within complex lunar impact craters taken by the Narrow Angle Camera (NAC) aboard the Lunar Reconnaissance Orbiter (LRO). All images acquired by NASA/GSFC/Arizona State University. A) Smooth impact melt deposit along the rim of the 22 km Giordano Bruno (LRO - NAC image M113282954RE; image width is ~1 km). B) Impact melt flow features at the 30 km Necho crater (LRO – NAC

mosaic of M134374642L and R images; image width is 5 km). C) Thin, smooth veneer of impact melt draped over an ejecta block in the 85 km Tycho crater (LRO – NAC image M142334392R; image width is ~400 m). D) Fractures within a melt pond on the 71 km Jackson crater (LRO – NAC image M118560367L; image width is ~ 700 m). [Image credit: NASA/GSFC/Arizona State University]. ……..…….….118

Figure 4.3: (Top) Lunar Reconnaissance Orbiter Wide Angle Camera greyscale mosaics of the three crater sites selected for this study – (A) Olcott crater, (B) Kovalevskaya crater, and (C) Schrödinger basin. (Bottom) Topographic profiles of the complex craters, data acquired from the Lunar Orbiter Laser Altimeter instrument. Topography values are relative to a lunar radius of 1737.4 km. [Image credit: MIT/NASA/GSFC/Arizona State University]……123

Figure 4.4: Composite maps of the study sites derived from Clementine UV-VIS data overlaid on LROC WAC mosaics. A) - C) Colour ratio composite maps highlight the distribution of mature (red) and fresh (blue) surfaces, and the presence of mafic content (green). D) - F) FeO weight % maps of each site. Iron rich regions of Olcott and Kovalevskaya craters spatially match the mafic rich areas of the colour ratio composite maps. The range of iron content within Schrödinger is likely skewed due to the high phase angles likely present at the latitude range of the basin. [Image credit: ISRO/NASA/GSFC/Arizona State University] ……...125

Figure 4.5: Integrated Band Depth (IBD) composite parameter maps derived from Chandrayaan-1 M^3 data for each of the study sites overlie LRO Wide Angle Camera (WAC) global mosaics to accentuate the distribution of absorption band features over impact related morphological features. [Image credit: ISRO/NASA/GSFC/Arizona State University]….……..……..126

Figure 4.6: Circular polarization ratio (CPR) mosaics overlaid on total radar backscatter mosaics to generate colourized radar mosaics for the study sites (from the Mini-RF instrument aboard LRO). The colour bar refers to the unitless range in circular polarization ratio. Smooth surfaces have low CPR and total backscatter, appearing purple in the colour mosaics. Rough surfaces have high CPR and total backscatter levels, and appear red in the colour mosaics. [Image credit: ISRO/NASA/JHUAPL/LPI]……..……..129

Figure 4.7: Estimates on the depth of excavation and depth of melting for materials within a transient cavity with increasing diameter size. For reference, the locations of the three study sites are plotted on the figure. Modified from Cintala and Grieve (1998)……134

Figure 4.8: Percentage of total melt volume retained within a transient cavity or ejected from the transient cavity. For reference, the locations of the three study sites are plotted on the figure. Modified from Cintala and Grieve (1998)…….……135

Figure 4.9: Geological sketch maps of Olcott crater, Kovalevskaya crater, and Schrödinger basin focusing on the distribution of impact melt deposits recognized beyond the crater floor. The basemap is a global mosaic derived from the Lunar Reconnaissance Orbiter Wide Angle Camera. The distribution maps for Olcott crater and Schrödinger basin are modified from versions included in Chapters 2 and 3. [Image credit for basemaps: NASA/GSFC/Arizona State University]……..…….…….138

Figure 4.10: Chandrayaan-1 M^3 derived spectral profiles of sampled geological units for Olcott crater, Kovalevskaya crater, and Schrödinger basin. There is a strong presence of low-Ca pyroxenes in all craters, but some areas indicate the presence of plagioclase feldspar and high-Ca pyroxene rich materials**.**…….…..139

Figure 4.11: Impact melt deposits of Olcott crater. A) LRO WAC mosaic context view of melt deposits highlighted in 4.11B–F. B) Smooth, low albedo impact melt deposit near the crater rim. NAC M130870650LC. C) Crater rim area and context view for Fig. 4.11D. NAC M182767638LC. D) 3-D view of thin impact melt veneers drape over the crater ejecta just beyond the rim, 100x vertical exaggeration. E) Smooth low albedo melt fill areas between the central uplifts on the crater floor. Image width is 2.5km. NAC M108460950RC. F) Smooth, low albedo melt is draped over much of the peak surface, with some exposures of bright, presumably blocky, peak material. [Image credit: NASA/GSFC/Arizona State University]……141

Figure 4.12: Comparison between the radar and visible observations of impact melt deposits around Olcott crater. A) LRO WAC global context view of the crater area. Black box outlines the context location of Fig. 4.12 B–D. Orange box provides a context location of the

bright wall slope for reference in Fig. 4.12B–D. B) Mapped melt deposits (red polygons) overlaid on LRO WAC image mosaic. Image modified from Fig. 4.9A. C) Circular polarization radar map of the area within 4.12B. Much of the melt deposits (where data is available) have low CPR. D) Total radar backscatter map of the area within 4.12B. Much of the area including the melt deposits is radar dark, with the exception of some of the central uplifts on the crater floor. [Image credit: ISRO/NASA/JHUAPL/LPI]…….142

Figure 4.13: Impact melt deposits of Kovalevskaya crater. A) LRO WAC mosaic context view of melt deposits highlighted in Fig. 4.12 B–F. B) Thin melt veneers drape wall slopes and terrace surfaces. LRO NAC M136029701LC. C) A pooled melt deposit (within white dash polygon) is observed along the crater wall, close to the crater floor. NAC mosaic M136029701LC; RC. D) Sinuous feature on the crater floor, either indicative of melt flow or a scarp: LRO NAC M103001717LC. E) Smooth melt deposits on terrace floor. LRO WAC global mosaic basemap; LRO NAC M178488703LC. F) Melt veneers draped along the crater rim edge. LRO NAC M178488703LC. [Image credit: NASA/GSFC/Arizona State University]…….……143

Figure 4.14: Comparison between the radar and visible observations of impact melt deposits around Kovalevskaya crater. A) LRO WAC global context view of the crater area. Black box outlines the context location of Fig. 4.14B–D. Orange box provides a context location of the simple crater for reference in Fig. 4.13 B–D. B) Mapped melt deposits (red polygons) overlaid on LRO WAC image mosaic. Image modified from Fig. 4.9B. C) Circular polarization radar map of the area within Fig. 4.14B. Much of the melt deposits (where data is available) have low CPR. D) Total radar backscatter map of the area within Fig. 4.14B. Much of the area including the melt deposits is radar dark, with the exception of materials on the crater floor. [Image credit: ISRO/NASA/JHUAPL/LPI]..…….……..145

Figure 4.15: Impact melt deposits of Schrödinger basin. A) LRO WAC mosaic context view of melt deposits highlighted in 13 B–F. B) Melt ponds (within white polygons) beyond the basin rim appear smooth and fill pre-existing crater depressions, NAC M115422614LC. C) Impact melt deposits draped over the central uplifts and along the basin floor, NAC M115422614LC. D) Smooth deposit nestled in a topographic low within the central uplift. E) Melt deposits along wall terraces on the western rim, LRO WAC basemap, NAC

M172182757RC. F) Comparison of the appearance of impact melts between the global WAC and high resolution NAC data. With optimal phase angles, the presence of melt deposits can be identified at latitudes of Schrödinger basin. [Image credit: NASA/GSFC/Arizona State University]……...……..148

Chapter 5

Figure 5.1: Comparison of the M^3 IBD parameter maps of the central uplift area for Olcott (top) and Kovalevskaya (bottom) craters. (Left) LRO WAC global mosaics of the craters with context views (white boxes) for the IBD parameter maps. (Right) M^3 IBD parameter maps highlighting the known (black dash box) and potential locations (white arrows) of absorption features indicative possibly of Mg-spinel. [Image credit: ISRO/NASA/GSFC/Arizona State University] ……170

Appendix A

Figure A.1: Grayscale Mini-RF radar maps of Olcott crater. [Image credit: ISRO/NASA/ JHUAPL/LPI]……..……...……177

Figure A.2: Grayscale Mini-RF radar maps of Kovalevskaya crater. [Image credit: ISRO/NASA/ JHUAPL/LPI]……...…….…….178

Figure A.3: Grayscale Mini-RF radar maps of Schrödinger basin. [Image credit: ISRO/NASA/ JHUAPL/LPI]……..…….…….179

Appendix B

Figure B.1: Cross section of a complex crater showing the apparent and true depth- diameter relation (modified from Croft, 1980)…….…...180

Figure B.2: Cross section view of a pooled deposit along terraces or beyond the crater rim. The depth of the melt deposit is the same as melt thickness. Where available multiple topographic profiles are taken to acquire a potential range in melt thickness to better constrain the melt volume…….182

Figure B.3: An example of calculating the thickness of a melt veneer at Olcott crater. The measure height of shadow near a rim scarp provides a minimum estimate on the melt thickness of the deposit. [Image credit: NASA/GSFC/Arizona State University]……..183

List of Appendices

Appendix A: Mini-RF grayscale Circular Polarization Ratio (CPR) and total backscatter mosaic maps for the study sites…….……177

Appendix B: Techniques for Calculating the Thickness of Observed Impact Melt Deposits within Lunar Complex Craters…….…….……180

B.1 Thickness of the impact melt sheet on the crater floor…..……..…180

B.2 Thickness of impact melt deposits along terrace surfaces, melt ponds, and melt veneers……..……....….180

Appendix C: Moon Mineralogy Mapper (M^3) Data Product List and Processing Summary……180

C.1 Deriving individual reflectance absorption spectral profiles each of the study sites……...……...180

C.2 Generating Integrated Band Depth (IBD) Composite Maps...…….…...180

C.3 References...……...……...180

Chapter 1

1 Introduction

Impact craters are very common geological features through the Solar System, occurring on the rocky surfaces of satellites, planets, and asteroids. Projectiles (asteroids or comets) collide with a target body at cosmic velocities. Together with the cosmic velocities and the subsequent effects of planetary gravity, the surface experiences variable shock pressures (Fig. 1.1), many orders of magnitude greater than pressures terrestrial rocks experience during regular, endogenous metamorphism (Stöffler, 1971). This results in permanent deformations with the target rock that range from brittle deformations to melting and vapourization. Impact craters are often thought of as "natural drills", enabling scientists to determine the planetary subsurface due to the excavation of materials during the cratering event.

The high levels of erosion (from both water and wind), volcanic activity, and plate tectonics throughout Earth's history make it challenging to locate and sample materials from well-preserved impact craters. The Moon is, therefore, one of the best places to study impact craters. The lack of an atmosphere or water results in the surface recording an impact history on the lunar surface. As a result, the lunar surface is covered with impact craters, round features with morphological depressions that range from a few metres to a few thousand km's in diameter. The lunar nearside, the hemisphere permanently facing the Earth, is comprised of bright crustal materials (typically called *the highlands*), impact craters, and dark volcanic areas (lunar maria) filling large impact basins (Fig. 1.2A). The lunar farside, the hemisphere facing away from Earth, consists of highland rocks (Fig. 1.2B) and is interestingly void of widespread volcanic activity (Hiesinger and Head, 2006). The farside has an older surface with high impact crater densities and fewer large impact craters that are filled with volcanism (Hörz et al., 1991). The largest known impact crater in the solar system is on the lunar farside, the ~2000 km diameter South Pole -Aitken basin (Fig. 1.2B; Stuart-Alexander, 1978; Head et al., 1993). Studying impact craters on the lunar farside allows a better understanding of the effect of cratering on crustal materials, including the depth and degree from which materials on the lunar surface are excavated.

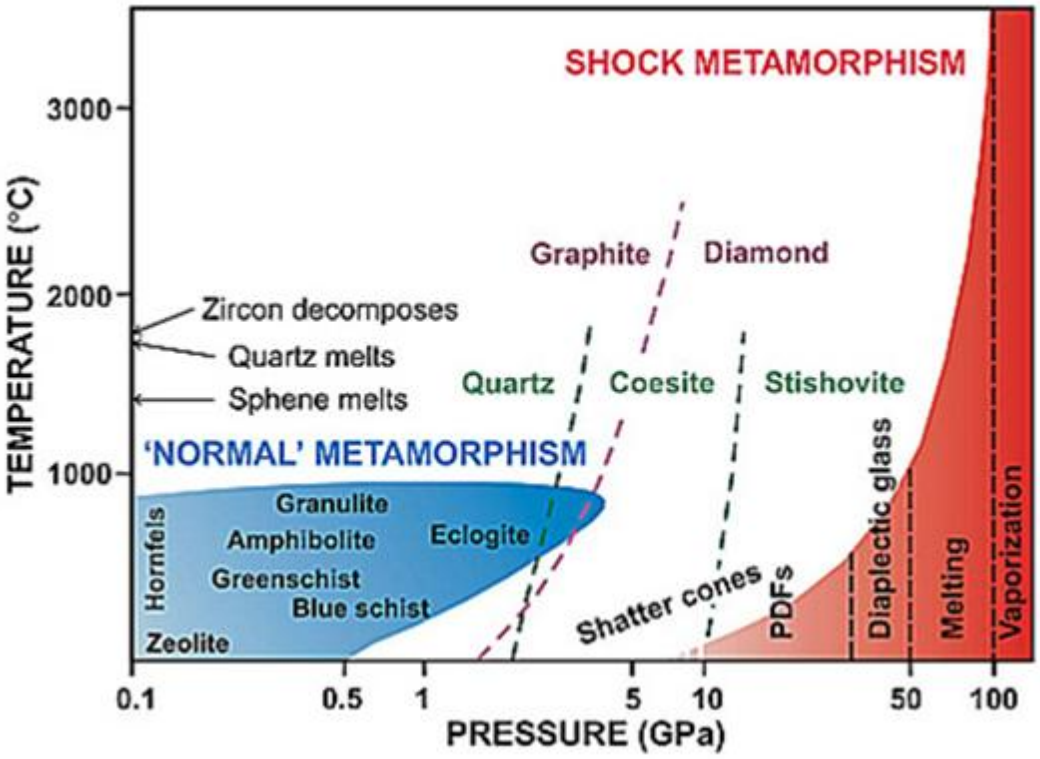

Figure 1.1: Typical shock pressures (log scale) experienced during an impact event. With increasing shock pressures, the deformations on original rock are more permanent (from Stöffler, 1971).

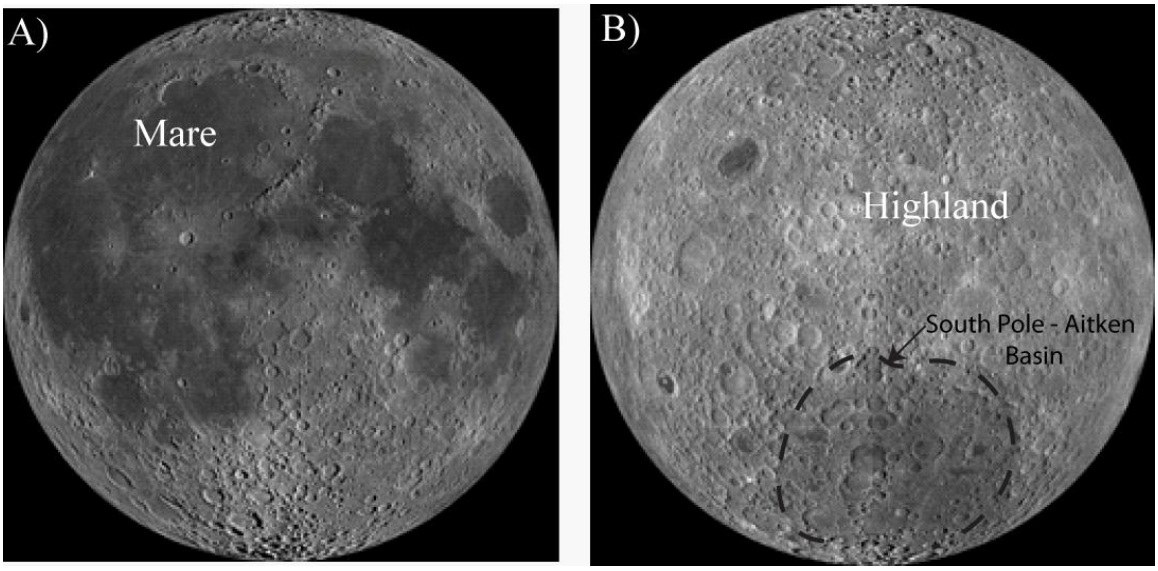

Figure 1.2: Global mosaics of the lunar surface captured by the Lunar Reconnaissance Orbiter Wide Angle Camera (LROC –WAC). A) The lunar nearside hemisphere is comprised of round impact craters, light highland crustal rocks and darker volcanic mare deposits. B) The lunar farside has many impact craters; however, there is a lack of much volcanism filling large craters (Hörz et al., 1991). The outline of the South Pole-Aitken basin is marked by the black dashed line. [Image source: NASA/GSFC/ASU]

Remotely derived datasets are often used in planetary studies to determine the morphological characteristics of impact craters including the shape, size, and extent of impact materials. The use of multispectral data has additionally benefited scientists in characterizing the mineralogical compositions of planetary surfaces. The use of spectroscopy on laboratory samples has further allowed scientists to determine the effects of impact derived shock pressures on mineral structures (Adams et al., 1979; Bruckenthal and Pieters, 1984; Smrekar and Pieters, 1985; Pieters, 1996; Johnson and Hörz, 2003).

In this study, various remote sensing datasets have been used in characterizing the distribution of impact materials around three complex impact craters on the lunar farside. The following sections in this chapter provide introductory details on the formation of impact craters, the preservation of impact craters on the Moon, a brief overview of the lunar geology, and the role remote sensing instruments have played in our understanding of the lunar surface.

1.1 Impact Cratering – A Geological Process

Impact craters form from catastrophic events that alter planetary surfaces and redistribute materials on the surface. Three main stages (Fig. 1.3) lead to the formation of an impact crater on a surface (Gault et al., 1968; Melosh, 1989), permanently deforming the surrounding area: (i) contact and compression of the projectile into the target; (ii) excavation and formation of a transient cavity; and lastly (iii) crater modification. The entire process of crater formation is instantaneous in a geological context, and the transition between each stage is a continuum. The following sections describe each of the impact cratering stages in more detail.

1.1.1 Contact and Compression

During the contact and compression stage, the projectile penetrates into the target, from model estimates as much as one to two times the diameter of the projectile (Kieffer and Simonds, 1980; O'Keefe and Ahrens, 1982). High pressure waves (shock waves) are formed, propagating through the projectile and into the target (Fig. 1.3A). The waves pass through the projectile, reach its rear surface, and are reflected back through the projectile as rarefaction waves thereby vapourizing the projectile (Ahrens and O'Keefe, 1972; Melosh, 1989). The

area of target surface immediately surrounding the projectile (depth equivalent to roughly two projectile diameters) is vapourized or melted (Ahrens and O'Keefe, 1972; Grieve et al., 1977). With greater distances from the projectile, the target materials are fractured and displaced due to the passage of shock waves (the displaced rocks are called "*impact breccias*"; Stöffler, 1971). More details about the types of deformations within target rocks are listed in section 1.1.2. The duration of the contact and compression stage depends on the time taken for the shock wave to pass through the projectile (Melosh, 1989). The time taken for the projectile to vapourize generally depends on the size, composition, and velocity of the projectile, but typically it lasts for a fraction of the entire crater forming process (Melosh, 1989). The maximum impact shock pressures and temperatures experienced by the target surface occur during the contact and compression stage (Melosh and Ivanov, 1999).

1.1.2 Excavation

The contact and compression stage is followed by the excavation stage, where the shock waves and reflected rarefaction waves propagate away from the point of impact radially along various paths along excavation flow lines through the target (Fig. 1.3B; Grieve and Cintala, 1981; Melosh, 1989). The shock wave propagates at supersonic speed away from the impact point, compressing the rocks and setting them in motion, moving down and outward (Fig. 1.4). The rarefaction waves have a similar effect on the rocks, however, they move in the opposite direction to the shock waves. At increasing depths beneath the point of impact, target rocks are driven by both shock and rarefaction waves, downward and outward. The movement of rocks in both directions results in the excavation of target rock, and the formation of a so-called transient cavity (Dence, 1968; Grieve and Cintala, 1981). The depth of a transient cavity is ~1/3rd the cavity diameter (Dence, 1973; Grieve et al., 1989). Depending on the location within the transient cavity, materials move along excavation flow lines (Fig. 1.4) and get displaced within two zones of the transient cavity – the excavated and displaced zones (Fig. 1.3C). Materials within the "excavated zone" lie close to the surface and are eventually emplaced beyond the crater rim, forming crater ejecta (Oberbeck, 1975). This results in the redistribution of shocked materials and the emplacement of crater ejecta. A second zone, the "displaced zone" lies deeper within the transient cavity (Fig. 1.3C), and is

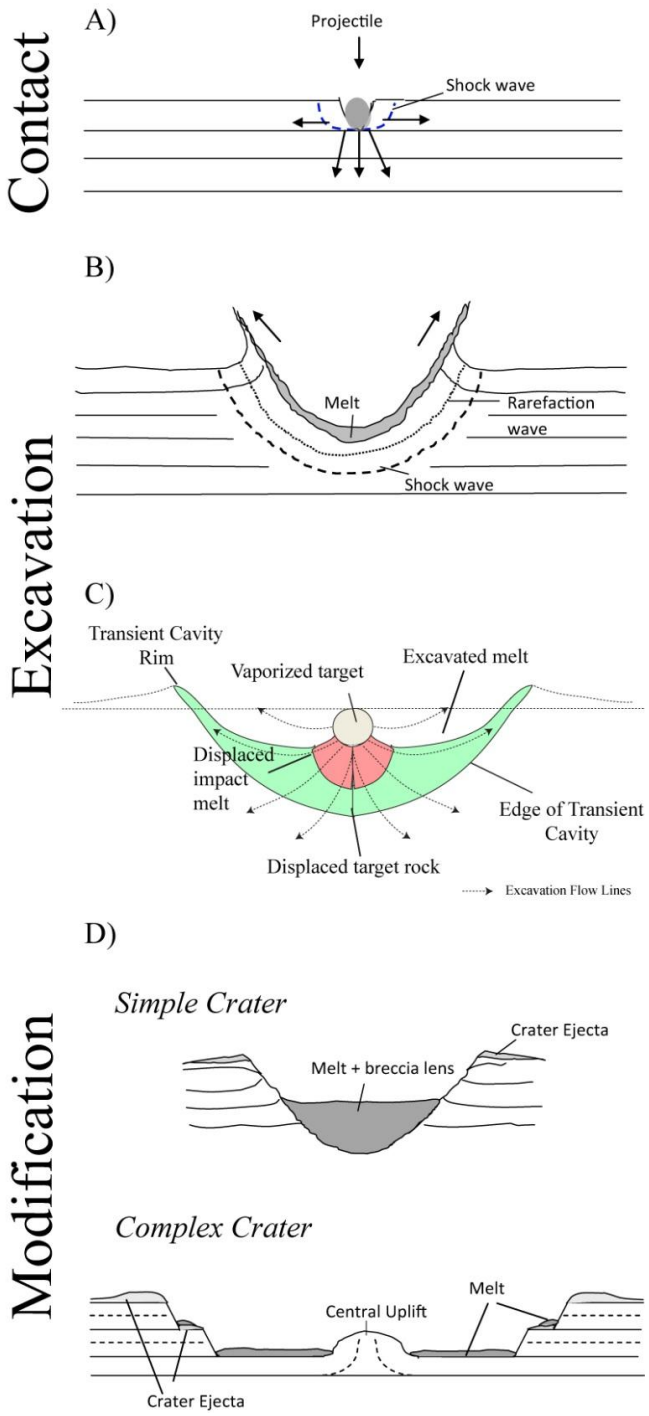

Figure 1.3: Three stages of impact crater formation showing the progression of shock waves and emplacement of shocked materials such as crater ejecta and melt sheets (from Melosh, 1989).

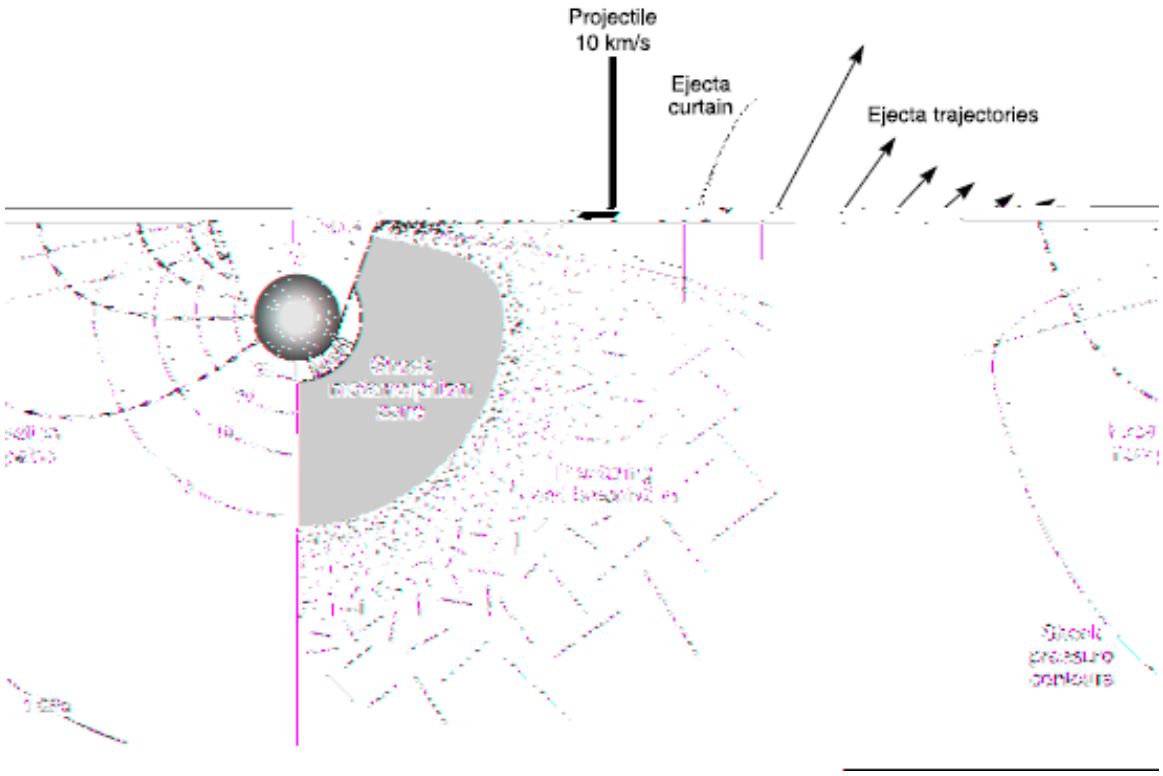

Figure 1.4: Cross sectional view of the excavation flow lines within a target surface (left), and the resulting scale of deformation within the rocks (right). Modified from Melosh, 1989.

comprised of materials that remain within the crater interior. The excavation flow lines transect different depths and shock pressures within the target (Fig. 1.4), and as a result materials excavated along these lines have variable degrees of shock. The displaced zone is filled with melt-rich and fractured rocks. The passage of shock waves through the target results in various degrees of deformation within the target rock. At low shock levels (< 5 GPa), deformation is evident in the form of shatter cones and planar deformation features (PDFs). At moderate shock pressures (10 – 50 GPa) and temperatures, shocked materials preserve distinct features including an amorphous phase of minerals known as *diaplectic glass* (French, 1998 and references therein; Pieters et al., 1996). At the highest pressures (> 50 GPa), the release of heat from the transfer of energy from the shock and rarefaction waves into the target melt and vapourize the original materials. With larger impact events, gravitational effects of the planet result in less of shocked target materials being ejected from the transient cavity. This results in a diverse range of shocked rocks being preserved within the cavity interior. More impact melt rocks are present within larger impact structures (Melosh, 1989). The transient cavity stops expanding once the shock and rarefaction waves are no longer able to excavate and displace the target rocks (Melosh, 1989).

1.1.3 Crater Modification

The final part of crater formation is the modification stage. The gravitational effects and target lithologies of the impacted planetary body affect the final impact crater shape, starting with the collapse of the crater wall. Depending on the size of the transient cavity, and the properties of the target rock, the resulting impact crater feature can have variable morphologies (Fig. 1.3D) – starting with a simple bowl shape cavity (*simple crater*) and transitioning to a cavity with an interior uplift and terraced walls (*complex crater*) (Melosh, 1989). More about the morphologies of impact craters are discussed in the following section.

1.2 Impact Crater Morphologies

Impact craters can be classified into two main groups: simple or complex (Fig. 1.3D). Simple craters are roughly the same size as the transient cavity, characterized by a bowl-shaped depression filled with impact melt deposits overlaid on brecciated rocks, and smooth walls lacking terraces (Pike, 1980; Hörz et al., 1991). Beyond a given crater diameter, the transient

cavity is unstable and gravity of the target body modifies the transient cavity, and the simple bowl shape crater is now a more complex structure – with a rim, wall terraces and central uplifts on the crater floor (Pike, 1980; Melosh, 1989). The simple to complex transition size is different for various planetary surfaces but is predominantly governed by gravity (Pike, 1980; Melosh, 1989). The ratio between the depth of the crater and the final crater diameter for a simple crater is around 1:5 (Pike, 1977). The depth to diameter ratio for a complex crater is lower than the ratio of a simple crater, but can range between 1/10 to 1/20 depending on the planetary body and size of the complex impact structure (Melosh, 1989).

A fresh simple impact crater consists of a sharp rim (structurally uplifted rock) and a radial distribution of impact ejecta deposits surrounding the rim (more details about impact ejecta deposits can be found in section 1.3.1). The floor of a simple crater consists of a mixture of highly shocked impact melts and broken rock fragments (breccia lens) (Shoemaker, 1960).

A fresh complex crater consists of an uplifted rim, gradually slumping terraces along the inner crater wall, and an uplifted structure on the crater floor. Melt deposits typically line the crater floor and overlie on brecciated crater floor rocks (Pike, 1980). The uplifted structures are either peaks or peak rings, representing rocks excavated from great depths beneath the centre of the transient cavity that rise during the modification stage. The uplift depth is typically 1/10 the final crater diameter (Melosh and Ivanov, 1999). Impact melt and ejecta deposits are also emplaced along terrace walls during the collapse and modification stages (Osinski et al., 2011).

1.3 Crater Impactites

Circular depressions on a planetary surface can be interpreted as a formation resulting from either exogenic (impact cratering) or endogenic (volcanism) processes. Often the identification of characteristic morphologies is required to determine the mode of formation. In the case of an exogenic origin; this includes identifying rocks that have been affected by the passage of shock waves, causing deformation. Rocks modified by impact events, including crater ejecta and impact melt deposits, are known as *impactites* (Stöffler and Grieve, 2007), and is discussed in detail below.

1.3.1 Crater Ejecta

All fresh impact craters are surrounded by a continuous radial deposit of debris known as the "ejecta blanket". This ejecta blanket is comprised of materials ejected from the excavated portion of the transient cavity and emplaced over the crater rim. Ejecta deposits are thickest at the crater rim and thin out with increasing distance from the crater rim (Oberbeck, 1975). Continuous ejecta deposits account for nearly half of the ejecta volume, and typically extend out one crater radius beyond the crater rim (Melosh, 1989). "*Proximal*" ejecta are continuous ejecta deposits that extend less than 5 crater radii from the rim (Melosh, 1989). "*Distal*" ejecta are deposits that extend farther out (>5 crater radii) from the rim and tend to be patchy in extent (Melosh, 1989).

The continuous ejecta blanket around a crater is typically emplaced by a process called *ballistic sedimentation* (Oberbeck, 1975). On the Moon, ejected materials escape beyond the crater rim with some initial velocity and follow a nearly parabolic trajectory. The materials fall back to the surface striking with the same velocity possessed upon ejection. This type of ejecta is called "*ballistic*" ejecta (Oberbeck, 1975). Excavated materials that are close to the point of impact within the transient cavity are ejected first with the highest velocities. Therefore, these materials are propelled the farthest outward and strike the ground with high velocity. Excavated materials that originate far from the point of impact, closer to the walls of the transient cavity, are ejected out with lower velocities being emplaced close to the crater rim. Once emplaced, the ballistic ejecta material still has momentum to travel further laterally until frictional forces terminate the process (Oberbeck, 1975). Around complex craters, this lateral movement results in the incorporation of pre-existing ground material into ballistic ejecta, and is known as "*secondary*" ejecta (Oberbeck, 1975). Because materials in the transient cavity travel along excavation flow lines, they experience a range in pressures and temperatures (Fig. 1.4). Therefore, ejecta at any given location are a mixture of materials shocked to different levels. Proximal ejecta are made of rocks affected by various degrees of shock metamorphism – and include the mixing of breccias and impact melt rocks (Melosh, 1989; French, 1998). Distal ejecta tend to be comprised of materials that experienced higher degrees of shock pressures, materials that have condensed from vapour or glassy spherules

solidified from melt (Melosh, 1989; French, 1998). Ejecta deposits around large craters may also incorporate large amounts of pre-existing ground material (Oberbeck, 1975).

In addition to the ballistic ejecta and secondary ejecta, numerous observations have been made on another type of ejecta on terrestrial planets – a layer that has a sharp contact with the ballistic ejecta. Typically, these layers are impact melt-rich deposits, and can be found on crater terraces and beyond the crater rim as patchy deposits with varying morphologies. The morphologies of identified impact melt deposits on the Moon range from thin veneers to flows, lobes, and pooled ponds (Howard and Wilshire, 1975; Hawke and Head, 1977; Bray et al., 2010; Osinski et al., 2011). This layer is proposed to be emplaced at a later temporal point of the crater modification process, part of a multi-stage ejecta emplacement process (Osinski et al., 2011 and references therein). A melt rich layer within the displaced zone of the transient cavity may have been ejected out during the crater modification stage due to the effects of gravitational collapse of the crater walls and central uplift. Factors including the size of impactor, the angle of impact, original volume of melt produced within the transient cavity, and local topography can affect the locations of impact melt deposits overlying continuous ejecta.

1.3.2 Impact Melt Deposits

Impact melts are generated by the passage of shock waves and rarefaction waves through the target body, particularly at shock pressures of 50 GPa – 100 GPa (Fig. 1), resulting in the melting of target rocks. These melt deposits form a considerable part of an impact crater. Melt deposits can range from small glassy fragments to large kilometre-thick coherent sheets. The amount of impact melt produced during an impact event depends largely of the planetary gravity, size of impact, and rock porosities of the target (Cintala and Grieve, 1998; Osinski et al., 2011). As the magnitude of the crater event increases, the volume of melt generated also grows (Cintala and Grieve, 1998). The final modification phase of crater formation determines where impact melts are largely concentrated. In simple craters, much of the melt remains within the crater interior, overlying brecciated target rocks (Grieve and Cintala, 1981). The melt deposits within complex craters form most of the crater fill deposits, however melt deposits can also be found on terrace walls and overlying impact crater ejecta beyond the rim (Hawke and Head, 1977). Gravitational effects of the planetary body result in

the collapse of the crater walls and central uplifts, providing further momentum for the melts to emplace along terrace walls and beyond the crater rim as a secondary phase of ejecta emplacement (Osinski et al., 2011).

1.4 Use of Remote Sensing Datasets in Geological Interpretations

Remotely derived datasets are often used in planetary studies to understand the geology of surfaces (such as the shape, size and extent of impact craters for example), particularly when directly accessing surface rocks and conducting laboratory analyses is impossible. Remote sensing instruments are of two kinds – active and passive sensors (Joseph, 2005). Active sensors emit energy towards a target and measure the reflected radiation. Passive sensors detect natural radiation emitted or reflected by a target. Common types of remote sensing databases include photography, radar, thermal, reflectance, and emission energies recorded using different parts of the electromagnetic spectrum (ultraviolet, visible, infrared, x-ray, gamma, etc.). Using a combination of these instruments enables us to characterize the morphologies of impact craters on planetary surfaces based on the macroscopic assessments of impactites including impact melt deposits, ejecta deposits, etc.

1.4.1 Role of Spectroscopy

Reflectance spectroscopy is currently the most useful technique for remotely measuring the mineral assemblages of planetary surfaces. Regions of the electromagnetic spectrum, for example using ultraviolet, visible, and infrared spectroscopy, are commonly used to derive mineralogical information of the surface (Pieters, 1998). Elemental abundances present on a planetary surface can be gathered using spectroscopic instruments specifically designed to detect them. Each mineral or rock type has a characteristic spectral signature, absorbing energy at specific wavelengths – thereby providing an indication of the crystal structure (Fig. 1.5). Instruments aboard spacecraft can detect variations in the energy emitted or reflected by the target surface, and the information captured is used to create a spectral profile. By combining morphologic data with spectral data, we can determine the spatial context and compositional detail for an area of interest.

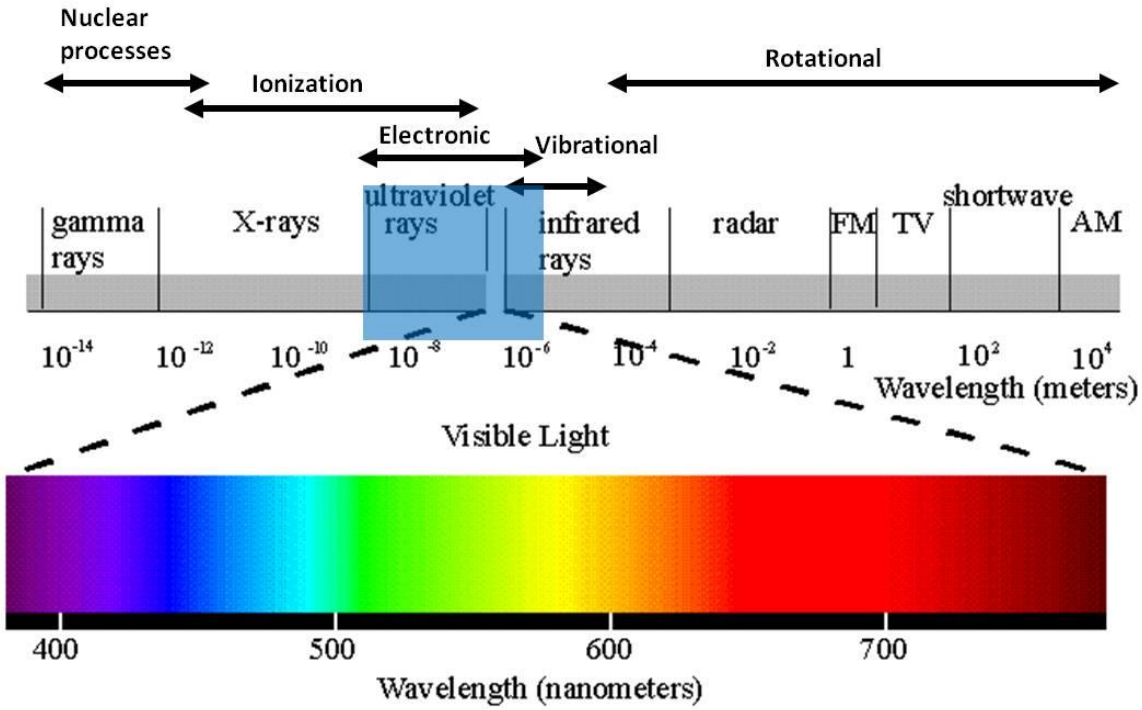

Figure 1.5: The absorption responses of elements for various parts of the electromagnetic spectrum. The cause of response is dependent on the crystal structure, or presence of any crystal defects. For example, within the ultraviolet, visible, and infrared range, the cause of absorption is due to the electronic and vibrational effects on molecules.

1.5 The Moon

The Moon is the only natural satellite of Earth, with a gravitational field 1/6th that of Earth's. Telescope data, satellite data, and analyses of samples from the Apollo missions have greatly helped scientists in their understanding of the lunar surface and geological history of the Moon (e.g., Hiesinger and Head, 2006; Lucey et al., 2006). These analyses suggest a simple dichotomy within rock types on the Moon; volcanic rich rocks and ancient crustal materials (discussed further in sections 1.5.1.1 and 1.5.1.2). The surface of the Moon is dominated by impact craters, with a wide range of morphologies and sizes. Other features on the lunar surface include lunar *regolith* (Papike et al., 1982) fine-grained and unconsolidated broken fragments of rocks subject to impacts. Constant bombardment of micrometeorites on the regolith has resulted in the formation of glassy materials called agglutinates (Morris et al., 1978). The lunar nearside (tidally locked hemisphere in view from Earth) has a greater percentage of volcanic deposits than the lunar farside.

1.5.1 The Lunar Stratigraphy

Based on remotely sensed data, it is assumed that the Moon is differentiated into a crust, mantle and possible core (Hiesinger and Head, 2006 and references therein). Within the lunar crust, the top 10 m of the lunar surface is made up of surface regolith (Fig.1.6). Regolith is fine grained (< 1cm), and forms from surface rocks that have eroded due to constant micrometeorite bombardment on the lunar surface. Beneath the regolith layer is the megaregolith layer, comprised of large-scale ejecta and structurally disturbed crust (Fig. 1.6). The ejecta deposits and fractured crust is part of large impact basins that have formed from multiple events of large impacts early in the lunar history (Hiesinger and Head, 2006). Impact basins are complex craters that exceed 150 km in diameter (see section 1.5.2 for more details on the classification of impact craters on the Moon). The ~2 km thick ejecta layer, is essentially ballistic and secondary ejecta of large impact basins and is comprised of a mixture of impactites including impact melts and displaced rocks. The rest of the crust consists of structurally disturbed crust and fractured in situ rocks (Fig. 1.6).

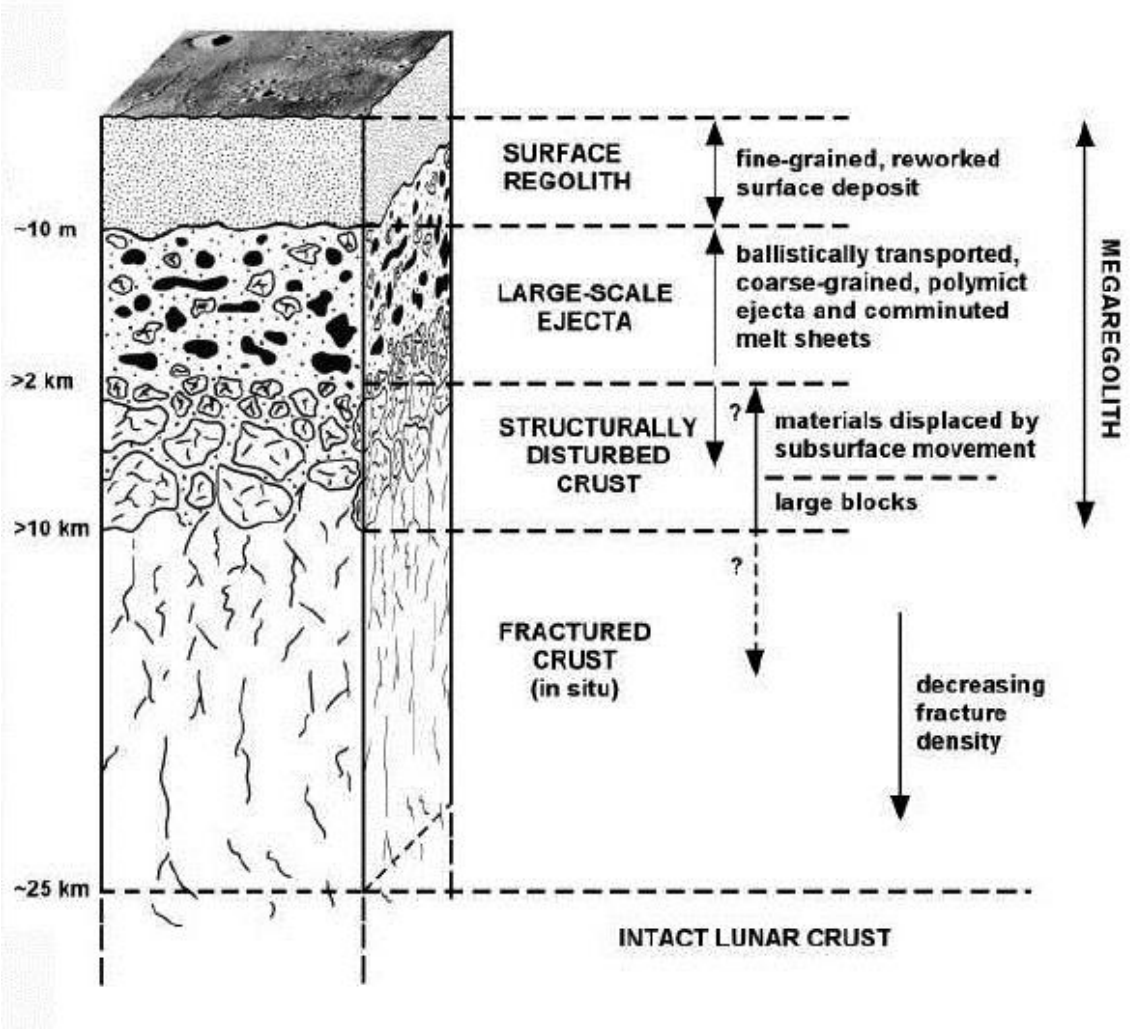

Figure 1.6: Cross sectional view of the lunar crust. The top 25 km is comprised of impactite materials emplaced from the formation of large impact basins (modified from Hiesinger et al., 2006 and references therein).

1.5.1.1 Highland crust

Generally, it is believed that the energy released from a Mars-size impactor with Earth resulted in the ejection and re-accretion of the Earth's crust and upper mantle material to form the Moon (Hartmann and Davis, 1975; Kipp and Melosh, 1986). Soon after accretion, the Moon was mostly molten with a large magma ocean (Smith et al., 1970). The cooling of this ocean led to the settling of heavy ultramafic minerals like olivine and pyroxene into the mantle. Lighter minerals such as plagioclase feldspar floated to the top levels and formed the pristine lunar crust (Smith et al., 1970; Wood et al., 1970). *Highland* rocks are heavily cratered crustal terrains comprised of brecciated rocks from large impact basins. The lunar highlands comprise of anorthosites (rocks with >90% plagioclase) and magnesian-suite rocks (Warner et al., 1976; Papike et al., 1998). Ferroan anorthosites typically have >94% anorthosite and mafic silicates with high Fe/Mg content (Warren et al., 1993). The magnesian-suite (Mg-suite) rocks have a greater Mg/Fe content and include dunites, troctolites, norites, and gabbronorites (Warren et al., 1993). The upper crust is dominated by plagioclase feldspar and low-Ca pyroxene, but the composition gets increasingly iron rich with depth (plagioclase; low and high-Ca pyroxene; and olivine) (Tompkins and Pieters, 1999).

1.5.1.2 Lunar Maria

Mare are generally smooth areas composed of basalts that have originated from the re-melting of mantle cumulates produced during differentiation of the Moon (Taylor et al., 1991). Unlike the highlands, mare regions are rich in mafic elements such as iron and titanium. Mare deposits are enriched in olivine and clinopyroxene but depleted in plagioclase (Pieters, 1978).

1.5.2 Impact Craters on the Moon

The Moon is an excellent natural laboratory to study the morphologic characteristics of impact craters. With a good impact record and lack of extensive surficial modifications, the lunar surface preserves the morphology, morphometry, and the extent of various impact materials including impact ejecta and impact melt deposits. On the Moon, impact craters excavate materials that are typically composed of either of highland anorthositic or mantle

derived Fe-rich rocks. A lower gravity means that complex craters are much deeper on the Moon than in terrestrial craters (Sharpton, 1994).

Impact craters on the Moon are recognized by their characteristic morphology (Fig. 1.7). For increasing rim diameter, the morphology of craters on the Moon varies from simple craters to complex craters and finally large impact basins (Stöffler et. al, 2006). The transition diameter from simple to complex crater on the Moon ranges from ~10 km – 25 km (Smith and Sanchez, 1973; Pike, 1980). However, further research has revealed that the transition occurs at 16 km within mare surfaces, and ~21 km in the highlands (Pike, 1980). The central uplifts within complex craters are typically central peaks (Fig. 1.7B; Hale and Head, 1979). The transition from complex to larger impact basins is marked by a series of stages characterized by a gradual increase in peak heights, and the widening of peaks to a cluster of peak hills (Hale and Head, 1979). The crater morphology further transitions into a protobasin – a crater with a central peak and peak ring (Pike 1988; Baker et al., 2011). For diameters > 200 km on the Moon, the central peak vanishes and is replaced by an inner concentric ring of irregular mountain peaks, forming a peak-ring basin (Melosh, 1989; Baker et al., 2011). Currently there are 17 known peak-ring basins and three protobasins on the Moon (Baker et al., 2011). Schrödinger basin (Fig. 1.7C) is a well preserved example of a peak-ring basin, and is the focus of Chapters 2 and 4. Beyond Peak ring basins transition to multi-ring basins – basins with more than two concentric rings within and beyond the basin rim (Pike, 1985; Melosh, 1989; Spudis, 1993; Head, 2010). Orientale basin (930 km diameter) is a well-known example of a multi-ring basin (Fig. 1.7D; Head et al., 1993). The South Pole-Aitken basin (2100 km diameter) is the second largest known basin in the solar system, and based on its size it is presumed to be a multi-ring basin (Wieczorek and Phillips, 1999). Basins get increasingly shallow with larger diameters due to gravitational (isostatic) responses and infilling during the crater modification stage (Melosh, 1989; Spudis, 1993). The interior morphologies within basins are often modified from the effects of volcanic activity, and erosion due to continual impact (meteoritic and micro-meteoritic) bombardment on the Moon.

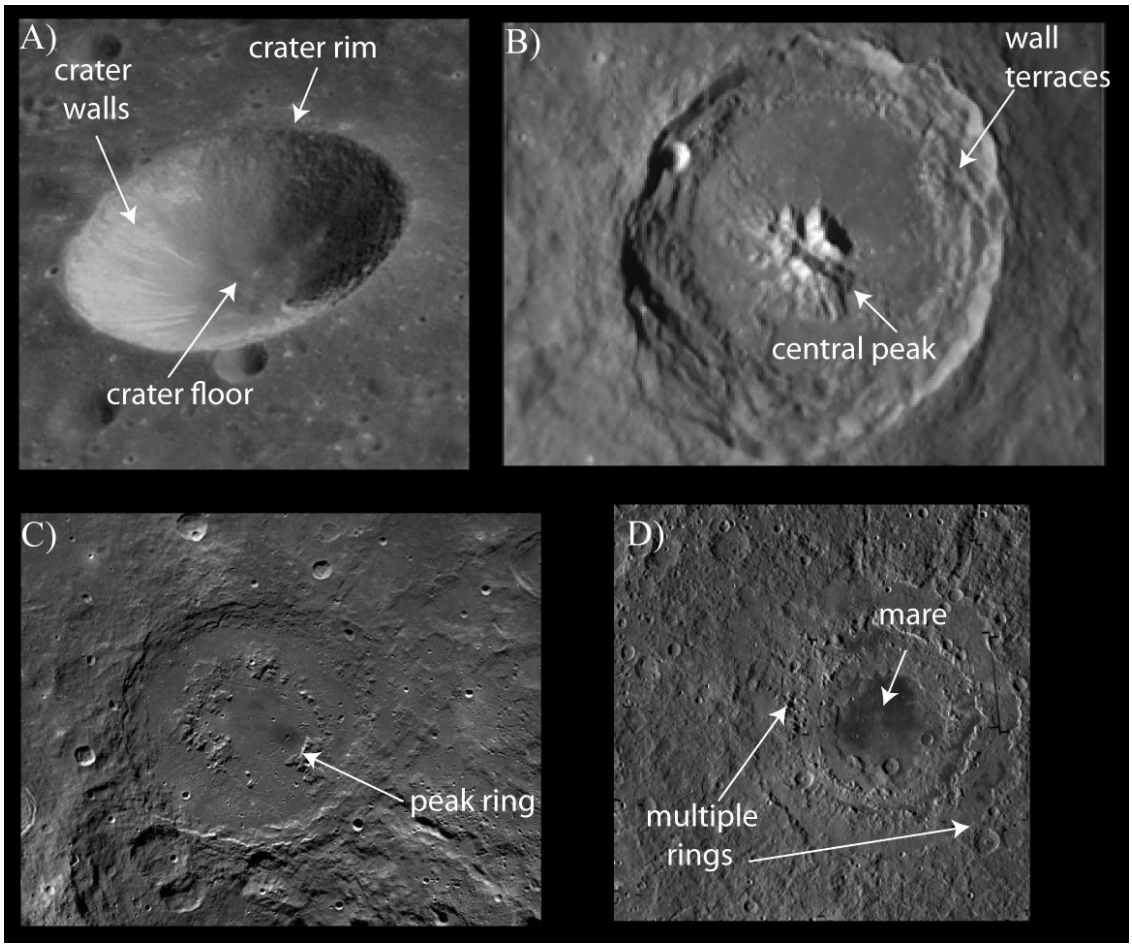

Figure 1.7: Impact craters on the Moon show a diverse range of morphologies. A) Typical simple crater (1 km diameter) displays a sharp rim, sloped walls, and inner depression. B) Theophilus crater, a 100 km complex crater, displays terraced walls, a smooth floor, and a central uplifted peak. C) Schrödinger basin is a 312 km complex crater with an interior peak ring (Chapter 2). D) Orientale basin is a ~930 km complex crater with multiple peak rings and mare deposits within the interior. [Image source: NASA/GSFC/ASU]

1.5.3 Lunar Missions

Various missions have been sent to the Moon to gather data on the topography, composition, internal structure, magnetic field, and impact flux of terrestrial surfaces (Hiesinger and Head, 2006 and references therein). Detailed data was derived from lab analyses of the Apollo mission samples. Missions since the 1990's (Clementine, Lunar Reconnaissance Orbiter, Chandrayaan-1) have acquired global coverage and added further information including the improved detail of the topographic expressions of impact craters, the identification of hidden mare deposits (Antonenko et al., 1995), and the discovery of water (Pieters et al., 2009a). The specifications and instrument details utilized in this study are summarized in Table 1 (Nozette et al., 1994; Pieters et al., 2009; Robinson et al., 2010; and Smith et al., 2010).

1.5.4 Spectral characteristics of Lunar materials

Ultraviolet and visible spectral analyses of the Apollo samples and telescopic observations in the near infrared have enabled scientists to characterize the spectral properties of various lunar materials. These particular wavelengths are useful, because they exhibit identifiable diagnostic absorptions features created by the electron transitions of ferrous iron within the crystal structure (Fig. 1.5; Burns, 1993).

Anorthosites within the lunar highlands display a diagnostic broad absorption feature at 1.3 µm, indicating the presence of plagioclase feldspar (Fig. 1.8; Smrekar and Pieters, 1985; Pieters, 1998). Mare spectra have stronger absorption features due to higher content of mafic minerals (compared to highland) (Smrekar and Pieters, 1985). Mafic minerals include olivine and pyroxene. Olivine displays a broad triple absorption feature near 1µm (Fig. 1.8; Smrekar and Pieters, 1985; Pieters, 1998). Typically, pyroxenes have distinct absorption features - near 1 and 2 µm (Fig. 1.8; Smrekar and Pieters, 1985; Pieters, 1998). Low-Ca pyroxene features typically display absorption bands centred near 0.90 – 0.93 µm (Smrekar and Pieters, 1985). High-Ca pyroxene features display absorption bands centred near 0.97 – 1 µm (Smrekar and Pieters, 1985). Rocks with a mixture of high and low-Ca pyroxene have absorption bands near 0.94 µm (Smrekar and Pieters, 1985).

As the surface matures due to constant bombardment of solar particles, there is an increase in agglutinates and the weakening of the overall strength of the absorption bands. However, the

Table 1.1: Spectral and spatial resolution details of various instruments sent on recent lunar missions with global coverage

Mission	**Clementine *[1] (1994)**	**Lunar Reconnaissance Orbiter (LRO) (2009 – present)**				**Chandrayaan-1 (2008 – 2009)**
Instrument	Ultraviolet-Visible (UV-VIS) Camera	Wide Angle Camera (WAC) *[2]	Narrow Angle Camera (NAC) *[2]	Lunar Orbiter Laser Altimetry (LOLA) *[3]	Miniature Radio Frequency (Mini-RF) *[4]	Moon Mineralogy Mapper (M^3) *[5]
# bands	5	7	1	-	2	85
Spectral Range	415, 750, 900, 950, 1000 nm	300 – 680 nm	400 – 750 nm	-	S – band (12.6 cm)	0.4 to 3 µm
Spectrum Coverage**	UV-VIS-NIR	UV-VIS	Panchromatic		Radar	UV-VIS-NIR
Spatial Resolution	~120 – 250 m/pixel	100 m/pixel	1 – 2 m/pixel	5 m (H); 10 cm (V)	30 m/pixel	140 m/pixel

*[1] Nozette et al., 1994; *[2] Robinson et al., 2010; *[3] Smith et al., 2010; *[4] Nozette et al., 2010; *[5] Pieters et al., 2009b

** *Coverage terminology follows conventions defined in the lunar literature*

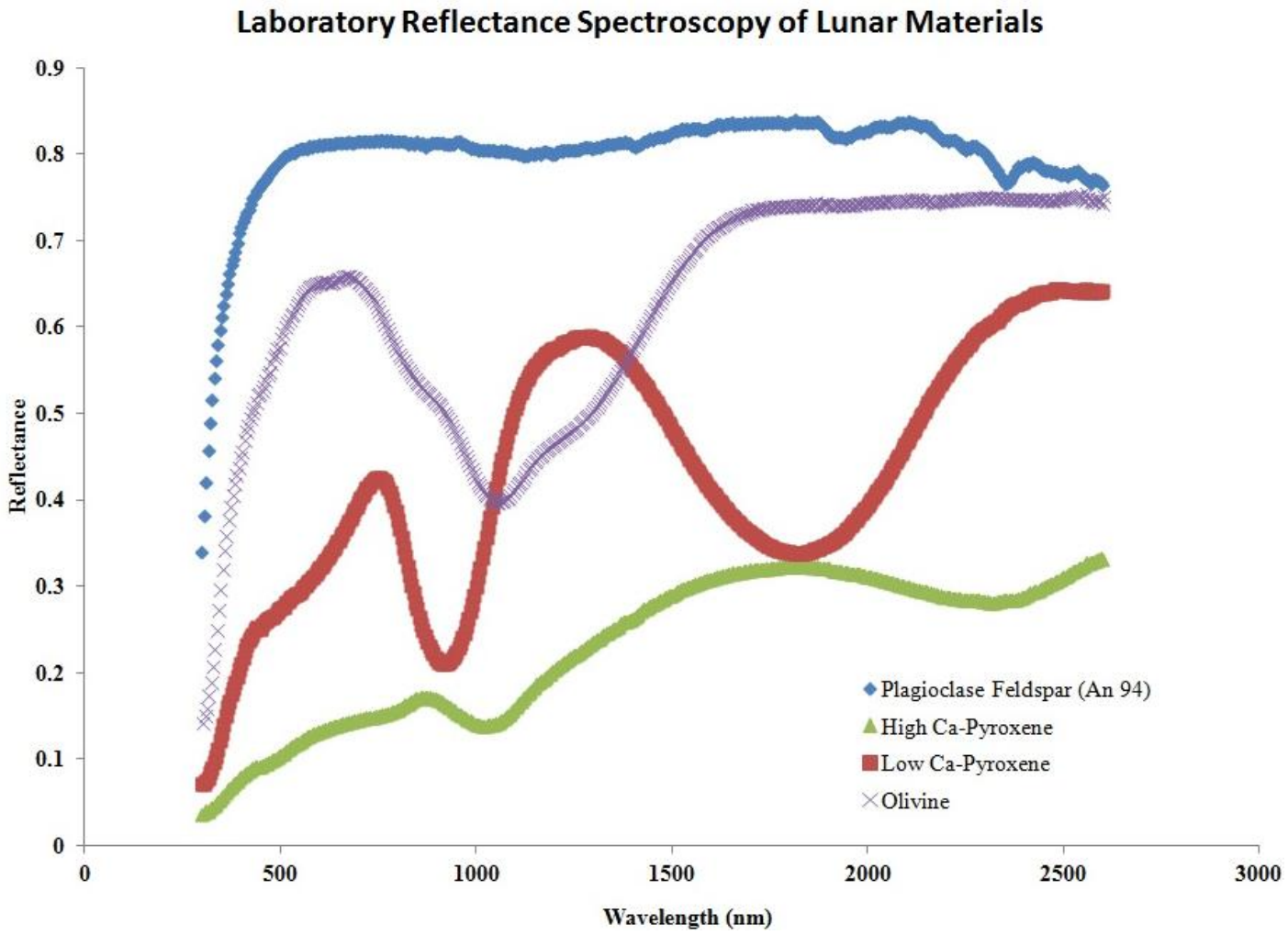

Figure 1.8: Laboratory derived spectral profiles of lunar materials [Source: RELAB Spectral Library]

location of the absorption bands remains the same making identification of minerals and rocks on the Moon possible (Adams and McCord, 1971).

1.6 Thesis Outline

In this study, both the morphological and spectral aspects of three complex impact craters have been combined to provide for a more accurate assessment of impact crater characteristics. The three craters are all located on the lunar farside, and range in diameter from 81 to ~312 km. The crater units are easily identifiable in image view, and all three craters have central uplifts with varying morphologies. The study sites are Olcott crater, Kovalevskaya crater, and Schrödinger basin.

For each crater site, the topographic expressions are assessed; the extents of impactite materials are mapped using high-resolution data at visible wavelengths. Mapped units include the crater ejecta, impact melt deposits, and central uplifts. In addition, reflectance spectral profiles of all the morphologic features within each crater are also collected using the various multispectral (UV-VIS-NIR) datasets. Particular attention is paid to the characteristics and distribution of impact melt deposits within these complex craters, to better understand the emplacement mechanisms of impactites on the Moon.

In Chapter 2, a multispectral study is conducted on Schrödinger basin. Schrödinger basin (312 km diameter), is a well preserved peak ring basin located on the lunar farside, along the rim of the much larger South Pole-Aitken (SPA) basin. The relatively young age (Lower Imbrian series, or 3.8 Gyr) of this basin has made it an ideal site to study the geology of peak ring basins in general (Shoemaker et al., 1994; Shoemaker and Robinson, 1995; O'Sullivan et al., 2011; Souchen et al., 2011), and at a broader scale, the geological history of SPA. Impact materials still recognizable include a well-defined crater rim, wall terraces, quasi-circular peak ring, and interior and exterior melt units. Several mare patches and a small pyroclastic deposit that covers a portion of the basin floor are indicative of the local volcanic activity within Schrödinger. This study uses Clementine multispectral UV-VIS data, and a limited set of higher spectral resolution Chandrayaan-1 Moon Mineralogy Mapper (M^3) data, as well as radar, camera and topography data from the Lunar Reconnaissance Orbiter to better understand Schrödinger's geology. Sampled spectral profiles and linear unmixing

models applied to the Clementine data indicate there is a heterogeneous distribution of both anorthositic and basaltic materials within the crater floor. These results challenge the traditional assumption that Schrödinger was formed in mostly highland terrain. Our assessment brings forth a new understanding regarding the placement of Schrödinger basin within SPA, and the role impact materials within SPA may have affected the compositions present within Schrödinger basin.

In Chapter 3, a complete multispectral characterization of Olcott crater is discussed. Olcott crater (81 km diameter) is a well preserved impact feature located on the central highland lunar farside and along the eastern edge of the much older, degraded Lomonosov-Fleming basin (Giguere et al., 2003). Olcott crater is similar in size to Tycho crater (85 km), a well-studied impact crater (Smrekar and Pieters, 1985; Morris et al., 2000; Hirata et al., 2009; Dhingra and Pieters, 2012; Carter et al., 2012). The preservation of impact generated morphologic features at Olcott crater makes it an ideal site to study the geology of complex craters of this crater size on the lunar farside. Impactite materials include a well-defined crater rim, wall terraces, a cluster of central peaks, and an interior melt unit. This study uses primarily higher spectral resolution Chandrayaan-1 Moon Mineralogy Mapper (M^3) data, as well as camera and topography data from the Lunar Reconnaissance Orbiter to better understand the geology of Olcott crater. Sampled spectral profiles and composite maps using M^3 and Clementine data indicate the southern half of the crater is mafic rich and dominated by pyroxene-rich materials. The strong concentration of pyroxene rich materials indicates that the crater event forming Olcott likely tapped into buried mare units within the larger Lomonosov-Fleming basin. Our assessment brings forth a new understanding regarding the placement of Olcott within Lomonosov-Fleming basin.

Chapter 4 is a comparison study on the distribution of impact melts beyond the crater floor for three complex craters – Olcott, Kovalevskaya, and Schrödinger. The characterization of impact melt deposits (beyond the crater floor) are made for both Olcott crater and Schrödinger basin following the multispectral assessments from Chapters 2 and 3. As an intermediate crater size comparison, the characterization of impact melt deposits of Kovalevskaya crater, a 113 km size complex structure on the lunar farside with a fractured interior central uplift, is also considered. This study uses mainly high resolution camera and

topography data from the Lunar Reconnaissance Orbiter and M^3 spectral data in the assessment. Furthermore, area and volume measurements of melt deposits at all three craters are calculated, and a comparison is made to model estimates (Cintala and Grieve, 1998) of melt volumes for the original transient cavities for these craters.

Chapter 5 provides a general discussion and summary reviewing the characterization of impact melt deposits from Chapters 2 to 4. The benefits and challenges in the instrument data are summarized. The discussion also re-examines the geologic histories for these craters in context with our understanding of the lunar farside. The use of data fusion techniques and its potential for future research is also discussed, particularly in their value for advancing the scientific community's understandings of the impact cratering processes on a geologically old surface.

1.7 References

Adams, J.B., and McCord, T.B. 1971. Alteration of Lunar Optical Properties: Age and Composition Effects. *Science*. **171**, 3971: 567–571.

Adams, J.B., Hörz, F., and Gibbons, R.V. 1979. Effects of shock-loading on the reflectance spectra of plagioclase, pyroxene, and glass. Proceedings, 10th Lunar and Planetary Science Conference. pp. 1–3.

Ahrens, T.J., and O'Keefe, J.D. 1972. Shock compression and vaporization of lunar rocks and minerals. *Moon*, **4**: 214–247.

Antonenko, I., Head, J.W., Mustard, J.F., and Ray Hawke, B. 1995. Criteria for the detection of lunar cryptomare. *Earth, Moon, and Planets*, **69**, 2: 141–172.

Baker, D.M.H., Head, J.W., Fassett, C.I., Kadish, S.J., Smith, D.E., Zuber, M.T., and Neumann, G.A. 2011. The transition from complex crater to peak-ring basin on the Moon: New observations from the Lunar Orbiter Laser Altimeter (LOLA) instrument. *Icarus*, **214**: 377–393.

Bray, V.J., Tornabene, L.L., Keszthelyi, L.P., McEwen, A.S., Hawke, B.R., Giguere, T.A., Kattenhorn, S.A., Garry, W.B., Rizk, B., Caudill, C.M., Gaddis, L.R., and C.H. van der Bogert. 2010. New insight into lunar impact melt mobility from the LRO camera. *Geophysical Research Letters*. **37**, 21: L21202.

Bruckenthal, E.A., and Pieters, C.M. 1984. Spectral effects of natural shock on plagioclase feldspar. 15th Lunar and Planetary Science Conference. pp. 96–97.

Burns, R.G. 1993. Mineralogical applications of crystal field theory. In *Mineralogical Applications of Crystal Field Theory*. Cambridge: Cambridge University Press. pp. 575.

Carter, L.M., Neish, C.D., Bussey, D.B.J., Spudis, P.D., Patterson, G.W., Cahill, J.T., and Raney, R.K. 2012. Initial observations of lunar impact melts and ejecta flows with the Mini-RF radar. *Journal of Geophysical Research*. **117**: E00H09.

Cintala, M.J., and Grieve, R.A. 1998. Scaling impact melting and crater dimensions: Implications for the lunar cratering record. *Meteoritics and Planetary Science*. **33**, 4: 889–912.

Dence, M.R. 1968. Shock zoning at Canadian craters: petrography and structural implications. In *Shock Metamorphism of Natural Materials*, edited by French, B.M., and Short, N.M. Baltimore: Mono Book Corporation. pp. 169–184.

Dence, M.R. 1973. Dimensional analysis of impact structures. *Meteoritics*, **8**: 343–344.

Dhingra, D., and Pieters, C.M. 2012. Spectroscopy of Impact Melts – Results from Lunar Crater Tycho. 43rd Lunar and Planetary Science Conference. Abstract #1836.

French, B. 1998. Traces of Catastrophe. *Lunar and Planetary Institute Contribution*. **954**: pp. 1–120.

Gault, D.E., Quaide, W.L., and Oberbeck, V.R. 1968. Impact cratering mechanics and structures. In *Shock Metamorphism of Natural Materials*, edited by French, B.M., and Short, N.M. Baltimore: Mono Book Corporation. pp. 87-99.

Giguere, T.A., Hawke, B.R., Blewett, D.T., Bussey, D.B.J., Lucey, P.G., Smith, G.A., Spudis, P.D., and Taylor, G.J. 2003. Remote sensing studies of the Lomonosov-Fleming region of the Moon. *Journal of Geophysical Research*. **108**, E11: 5118.

Grieve, R.A.F., Dence, M.R., and Robertson, P.B. 1977. Cratering processes: as interpreted from the occurrences of impact melts. In *Impact and Explosion Cratering*, edited by Roddy, D.J., Pepin, R.O., and Merrill, R.B. New York: Pergamon Press. pp. 791–814.

Grieve, R.A.F. and Cintala, M.J. 1981. A method for estimating the initial impact conditions of terrestrial cratering events, exemplified by its application to Brent crater, Ontario. 11th Lunar and Planetary Science Conference. pp. 1607-1621.

Grieve, R.A.F., Garvin, J.B., Coderre, J.M., and Rupert, J. 1989. Test of a geometric model for the modification stage of simple impact crater development. *Meteoritics*. **24**: 83–88.

Hale, W., and Head, J.W. 1979. Central peaks in lunar craters: Morphology and morphometry. Proceedings, 10th Lunar and Planetary Science Conference. pp. 2623–2633.

Hartmann, W.K. and Davis, D.R. 1975. Satellite-sized planetesimals and lunar origin. *Icarus*. **24**, 4: 504–515.

Hawke, B.R., and Head, J.W. 1977. Impact melt on lunar crater rims. Proceedings, Symposium on Planetary Cratering Mechanics. pp. 815–841.

Head, J., Murchie, S., Mustard, J.F., Pieters, C., Neukum, G., McEwen, A., Greeley, R., Nagel, E., and Belton, M.J.S. 1993. Lunar impact basins: New data for the western limb and far side (Orientale and South Pole-Aitken basins) from the first Galileo flyby. *Journal of Geophysical Research*. **98**, E9: 17149–17182.

Hiesinger, H., and Head, J.W. (III). 2006. New Views of Lunar Geoscience: An Introduction and Overview. In *Reviews in Mineralogy and Geochemistry*, edited by Jolliff, B.L., Wieczorek, M.A., Shearer, C.K., and Neal, C.R. **60**: 1–81.

Hirata, N., Haruyama, J., Ohtake, M., Matsunaga, T., Yokota, Y., Morota, T., Honda, C., Ogawa, Y., Sugihara, T., Miyamoto, H., Demura, H., and Asada, N. 2009. Morphological analyses of Tycho crater with Kaguya data. 40th Lunar and Planetary Science Conference. Abstract # 1514.

Hörz, F., Grieve, R., Heiken, G., Spudis, P., and Binder, A. 1991. Lunar surface processes. In *Lunar Sourcebook: A User's Guide to the Moon,* edited by Heiken, G.H., Vanima, D.T., and French, B.M. Cambridge: Cambridge University Press. pp. 85–144.

Howard, K.A. and Wilshire, H.G. 1975. Flows of impact melt in lunar craters. *Journal of Research of the U. S. Geological Survey*. **3**: 237–251.

Johnson, J. R., and Hörz, F. 2003. Visible/near-infrared spectra of experimentally shock plagioclase feldspars. *Journal of Geophysical Research*. **108**, E11: 5120 (1–6).

Joseph, G. 2005. *Fundamentals of Remote Sensing*. India: Universities Press. 486p.

Kieffer, S.W., and Simonds, C.H.H. 1980. The role of volatiles and lithology in the impact cratering process. *Reviews of Geophysics and Space Physics*. **18**, 143–181.

Kipp, M.E., and Melosh, H.J. 1986. Origin of the Moon: a preliminary numerical study of colliding planets. 17th Lunar and Planetary Science Conference. pp. 420–421.

Liu, J.G. and Mason, P.J. 2009. *Essential Image Processing for GIS and Remote Sensing.* New York: John Wiley & Sons. 460 p.

Lucey, P.G., Taylor, G. J., and Malaret, E. 1995. Global distribution of iron on the Moon and its implications for the magma ocean, crustal structure, and lunar origin. 26th Lunar and Planetary Science Conference. pp. 877–878.

Lucey, P., Korotev, R.L., Gillis, J.J., Taylor, L.A., Lawrence, D., Campbell, B.A., Elphic, R., Feldman, B., Hood, L.L., Hunten, D., Mendillo, M., Noble, S., Papike, J.J., Reedy, R.C., Lawson, S., Prettyman, T., Gasnault, O., and Maurice, S. 2006. Understanding the lunar surface and space-moon interactions. In *Reviews in Mineralogy and Geochemistry*, edited by Jolliff, B.L., Wieczorek, M.A., Shearer, C.K., and Neal, C.R.. **60**: 83–219.

Melosh, H.J. 1989. *Impact Cratering: A Geologic Process*. New York: Oxford University Press. 245p.

Melosh, H.J. and Ivanov, B. 1999. Impact Crater Collapse. *Annual Reviews of Earth Planetary Science*. **27**: 385–415.

Morris, R.V. 1978. The surface exposure (maturity) of lunar soils: Some concepts and I_s/FeO compilation. Proceedings, 9th Lunar and Planetary Science Conference. pp. 2287–2297.

Morris, A.R., Head, J.W., Margot, J-L., and Campbell, D.B. 2000. Impact melt distribution and emplacement on Tycho: A new look at an old question. 31st Lunar and Planetary Science Conference. Abstract # 1828.

Nozette, S., Rustan, P., Pleasance, L.P., Horan, D.M., Regeon, P., Shoemaker, E.M., Spudis, P.D., Acton, C.H., Baker, D.N., Blamont, J.E., Buratti, B.J., Corson, M.P., Davies, M.E., Duxbury, T.C., Elaison, E.M., Jakosky, B.M., Kordas, J.F., Lewis, I.T., Lichtenberg, C.L.,

Lucey, P.G., Malaret, E., Massie, M.A., Resnick, J.H., Rollins, C.J., Park, H.S., McEwen, A.S., Priest, R.E., Pieters, C.M., Riesse, R.A., Robinson, M.S., Simpson, R.A., Smith, D.E., Sorenson, T.C., Vorder Breugge, R.W., and Zuber, M.T. 1994. The Clementine Mission to the Moon: Scientific Overview. *Science*. **266**, 5192: 1835–1839.

Nozette, S., Spudis, P., Bussey, B., Jensen, R., Raney, K., Winters, H., Lichtenberg, C.L., Marinelli, W., Crusan, J., Gates, M., and Robinson, M. 2010. The Lunar Reconnaissance Orbiter Miniature Radio Frequency (Mini-RF) Technology Demonstration. *Space Science Reviews*. 150, 1–4: 285–302.

O'Keefe, J.D., and Ahrens, T.J. 1982. Cometary and meteorite swarm impact on planetary surfaces. *Journal of Geophysical Research*. **103**, 28607.

O'Sullivan, K.M., Kohout, T., Thaisen, K.G., and Kring, D.A., 2011. Calibrating several key lunar stratigraphic units representing 4 b.y. of lunar history within Schrödinger basin. In *Recent advances and current research issues in lunar stratigraphy*, edited by Ambrose, W.A., and Williams, D.A. Special Paper # 477. Boulder, Colorado: Geological Society of America. pp. 117–128.

Oberbeck, V. 1975. The role of ballistic erosion and sedimentation in lunar stratigraphy. *Reviews of Geophysics and Space Physics*. **13**: 337–362.

Osinski, G.R., Tornabene, L.L., and Grieve, R.A.F. 2011. Impact melt and ejecta emplacement on terrestrial planets. *Earth and Planetary Science Letters*. **310**, 3: 167–181.

Papike, J.J., Simon, S.B., and Laul, J.C. 1982. The Lunar Regolith: Chemistry, Mineralogy, and Petrology. *Reviews of Geophysics and Space Physics*. **20**, 4: 761–826.

Papike, J.J., Ryder, G., and Shearer, C.K. 1998. Lunar samples. In *Reviews in Mineralogy and Geochemistry*. Edited by Hazen, R.M., and Downs, R.T. **36**: 1–234.

Pieters, C.M. 1978. Mare basalt types on the front side of the moon: A summary of spectral reflectance data. Proceedings, 9th Lunar Planetary Science Conference. pp. 2825–2849.

Pieters, C.M. 1996. Plagioclase and maskelynite diagnostic features. 27th Lunar and Planetary Science Conference. pp. 1031–1032.

Pieters, C.M. 1998. Lunar Materials from the Visible to Mid-Infrared: The Effects of Space Weathering. *International Geology Review*. **40**:11, 981–989.

Pieters, C.M., Goswami, J.N., Clark, R.N., Annadurai, M., Boardman, J., Buratti, B., Combe, J.-P., Dyar, M.D., Green, R., Head, J.W., Hibbits, C., Hicks, M., Isaacson, P., Klima, R., Kramer, G., Kumar, S., Livo, E., Lundeen, S., Malaret, E., McCord, T., Mustard, J., Nettles, J., Petro, N., Runyon, C., Staid, M., Sunshine, J., Taylor, L.A., Tompkins, S., and Varanasi, P. 2009a. Character and spatial distribution of OH/H_2O on the surface of the Moon seen by M^3 on Chandrayaan-1. *Science*. **326**: 568–572.

Pieters, C.M., Boardman, J., Buratti, B., Chatterjee, A., Clark, R., Glavich, T., Green, R., Head (III), J., Isaacson, P., Malaret, E., McCord, T., Mustard, J., Petro, N., Runyon, C., Staid, M., Sunshine, J., Taylor, L., Tompkins, S., Varanasi, P., and White, M. 2009b. The Moon Mineralogy Mapper (M^3) on Chandrayaan-1.*Current Science*. **96**, 4: 500–505.

Pike, R.J. 1980. Control of crater morphology by gravity and target type: Mars, Earth, Moon. Proceedings, 11th Lunar and Planetary Science Conference. pp. 2159–2189.

Pike, R.J. 1985. Some morphologic systematic of complex impact structures. *Meteoritics*. **20**, 1: 49–68.

Robinson, M.S., Brylow, S.M., Tschimmel, M., Humm, D., Lawrence, S.J., Thomas, P.C., Denevi, B.W., Bowman-Cisneros, E., Zerr, J., Ravine, M.A., Caplinger, M.A., Ghaemi, F.T., Schaffner, J.A., Malin, M.C., Mahanti, P., Bartels, A., Anderson, J., Tran, T.N., Eliason, E.M., McEwen, A.S., Turtle, E., Jolliff, B.L., and Hiesinger, H. 2010. Lunar Reconnaissance Orbiter Camera (LROC) Instrument Overview. *Space Science Reviews*. **150**, 1–4: 81–124.

Sharpton, V.L. 1994. Evidence from Magellan for unexpectedly deep complex craters on Venus. In *Large Meteorite Impacts and Planetary Evolution*, edited by Dressler, B.O., Grieve, R.A.F., and Sharpton, V.L. Special Paper #293. Boulder, Colorado: Geological Society of America. pp. 19-27.

Shoemaker, E.M. 1960. Penetration mechanics of high velocity meteorites, illustrated by Meteor Crater, Arizona. In *Report of the International Geological Congress, XXI Session, Norden*. Copenhagen, Denmark: International Geological Congress, Part XVIII. pp. 418-434.

Shoemaker, E.M., Robinson, M.S., and Eliason, E. M. 1994. The South Pole region of the Moon as seen by Clementine. *Science*. **266**, 5192: 1851–1854.

Shoemaker, E.M., and Robinson, M.S. 1995. Clementine observations of melt rocks and volcanic materials in the Schrödinger Basin. 26nd Lunar and Planetary Science Conference. Abstract #1297.

Smith, J.V., Anderson, A.T., Newton, R.C., Olsen, E.J., Wyllie, P.J., Crewe, A.V., Isaacson, M.S., and Johnson, D. 1970. Petrologic history of the moon inferred from petrography, mineralogy and petrogenesis of Apollo 11 rocks. *Proceedings of the Apollo 11 Lunar Science Conference*. In *Geochimica et Cosmochimica Acta*, edited by Levinson, A.A. Supplement 1. Elmsford, N.Y.: Pergamon Press. pp. 897–925.

Smith, E.L., and Sanchez, A.G. 1973. Fresh lunar craters: Morphology as a function of diameter, a possible criterion for crater origin. *Modern Geology*. **4**: 51–59.

Smith, D.E., Zuber, M.T., Jackson, G.B., Cavanaugh, J.F., Neumann, G.A., Riris, H., Sun, X., Zellar, R.S., Coltharp, C., Connelly, J., Katz, R.B., Kleyner, I., Liiva, P., Matuszeski, A., Mazarico, E.M., McGarry, J.F., Novo-Gradac, A-M., Ott, M N., Peters, C., Ramos-Izquierdo, L.A., Ramsey, L., Rowlands, D.D., Schmidt, S., Scott, V.S., Shaw, G.B., Smith, J.C., Swinski, J-P., Torrence, M.H., Unger, G., Yu, A.W., Zagwodzki, T.W. 2010. The Lunar Orbiter Laser Altimeter Investigation on the Lunar Reconnaissance Orbiter Mission. *Space Science Reviews*. **150**, 1–4: 209–241.

Smrekar, S., and Pieters, C.M. 1985. Near-infrared spectroscopy of probable impact melt from three large lunar highland craters. *Icarus*. **63**: 442–452.

Souchen, A.L., Flahaut, J., Sharma, P., Jilly, C.E., Blanchette – Guertin, J.-F., and Kring, D.A. 2011. Suggested Landing Sites To Study Key Planetary Processes On The Moon: The Case Of Schrödinger Basin. 42nd Lunar and Planetary Science Conference. Abstract # 1791.

Spudis, P.D. 1993. *The geology of multi-ring impact basins*. Cambridge: Cambridge University Press. 277 p.

Stöffler, D. 1971. Progressive Metamorphism and Classification of Shocked and Brecciated Crystalline Rocks at Impact Craters. *Journal of Geophysical Research*. **76**, 23: 5541–5551.

Stöffler, D., Ryder, G., Ivanov, B.A., Artemieva, N.A., Cintala, M.J., and Grieve, R.A.F. 2006. Cratering history and lunar chronology. In *Reviews in Mineralogy and Geochemistry,* edited by Jolliff, B.L., Wieczorek, M.A., Shearer, C.K., and Neal, C.R. **60**: 519–596.

Stöffler, D., and Grieve, R.A.F. 2007. Impactites. In *Metamorphic Rocks,* edited by Fettes, D., and Desmons, J. Cambridge: Cambridge University Press. pp. 82–92.

Stuart-Alexander, D.1978. Geologic map of the central farside of the Moon. *United States Geological Services.* Map I-1047.

Taylor, G.J., Warren, P., Ryder, G., Delano, J., Pieters C., and Lofgren, G. 1991. Lunar rocks. . In *Lunar Sourcebook: A User's Guide to the Moon,* edited by Heiken, G.H., Vanima, D.T., and French, B.M. Cambridge: Cambridge University Press. pp. 183–284.

Tompkins, S., and Pieters, C.M. 1999. Mineralogy of the lunar crust: Results from Clementine. *Meteoritics and Planetary Science*, **34**, 25 – 41.

Warren, P.H. 1993. A concise compilation of petrologic information on possibly pristine nonmare Moon rocks. *American Mineralogist*. **78**, 360-376.

Warner, J.L., Simonds, C.H., Phinney, W.C. 1976. Genetic distinction between anorthosites and Mg-rich plutonic rocks: New data from 76255. 7th Lunar and Planetary Science Conference. pp. 915-917.

Wieczorek, M.A., and Phillips, R.J. 1999. Lunar multiring basins and the cratering process. *Icarus*. **139**, 2: 246–259.

Wood, J.A, Dickey, J.S., Marvin, U.B., Powell, B.N. 1970. Lunar anorthosites and a geophysical model of the Moon. *Proceedings of the Apollo 11 Lunar Science Conference*. In

Geochimica et Cosmochimica Acta, edited by Levinson, A.A. Supplement 1. Elmsford, N.Y.: Pergamon Press. pp. 965–988.

Chapter 2

2 A multispectral geological study of the Schrödinger impact basin

Data from the Lunar Reconnaissance Orbiter (LRO) and Chandrayaan-1 missions provide an opportunity to study lunar impact craters at previously unavailable resolutions and wavelengths (e.g., Bhandari, 2004; Goswami et al., 2006; Chin et al., 2007; Robinson et al., 2010). Various datasets, including topography (Lunar Orbiter Laser Altimetry, LOLA), multispectral imagery (Clementine ultraviolet and visible-UVVIS-Camera; LRO Camera-LROC; Moon Mineralogy Mapper-M^3), and synthetic aperture radar (Mini-RF) can be used to characterize the composition and spatial extent of impact crater materials, including impact ejecta and shocked materials. While crater materials are easily identifiable within fresh small craters, it is often hard to determine the extent of impact melt and ejecta deposits for larger craters (D > 100km). This is because most large craters are relatively old and, thus, have experienced subsequent surface "gardening" from later impact events.

The Schrödinger impact basin, located near the southern rim of the larger South Pole-Aitken (SPA) basin, is an excellent site to study the distribution of impact materials within large craters. Schrödinger materials are minimally modified in comparison to other large basins, so identifying the compositions of impact materials and characterizing their distributions can be more readily determined. Based on mapped units and crater counting, Schrödinger basin is proposed to be early Imbrian in age (3.8 Gyr) (Wilhelms, 1987). This makes it one of the youngest peak ring basins on the Moon, with a well preserved rim, terrace walls, and basin floor. In addition to being an ideal candidate for studying the formation of peak-ring basins, its location within SPA has also made it a high priority target for future lunar exploration and sample return missions (Souchen et al., 2011; O'Sullivan et al., 2011).

The goals of this study are to update our understanding of the geology of Schrödinger using the currently available multispectral datasets, with a specific emphasis on identifying and characterizing the extent of impact melt deposits beyond the crater basin rim. This will lead to a better understanding of the emplacement mechanisms of impact melts around large craters. This paper seeks to 1) characterize the compositions of previously mapped geologic

units in Schrödinger (Shoemaker et al., 1994; Mest and van Arsdall, 2008; van Arsdall and Mest, 2008; Mest, 2011) using the Clementine and Chandrayaan-1 multispectral bandsets, and 2) use new data from the Lunar Reconnaissance Orbiter and Chandrayaan-1 missions to extend the existing geologic map to include all Schrödinger impact materials, including crater ejecta and external melt deposits that are not resolvable at Clementine scale resolutions.

2.1 Geological setting of the Schrödinger impact basin

Schrödinger is a large peak-ring impact basin, with a diameter of 312 km, located near the south pole on the lunar farside at ~75°S, 130°E, at the edge of the much larger SPA basin (Fig. 2.1). SPA basin is an extremely large, possibly multi-ring, structure on the lunar farside and is considered to be the oldest (Pre–Nectarian, ~4Ga), largest (~2,600 km), and deepest (~12 km) lunar impact basin (Lucey et al., 1998; Pieters et al., 2001). While the SPA impact excavated the predominantly anorthositic upper crust, materials exposed within the basin may represent lower crustal or upper mantle materials (Pieters et al., 2001). If impact models can be extrapolated to a scale as large as SPA, it is quite likely that impact melts of SPA may lie along terraced surfaces and outside the topographic rim in addition to filling the basin floor. Over four billion years, however, subsequent impact events have worked to redistribute SPA materials in a process called "impact gardening" (Housen et al., 1979). The location of Schrödinger along the rim edge of SPA suggests that the composition of Schrödinger can give us insight into SPA materials.

The first geologic interpretations of Schrödinger were based on medium to high resolution photographs (20–60 m/pixel) taken from the Lunar Orbiter V spacecraft (Wilhelms et al., 1979; Wilhelms, 1987). From this dataset, along with later Clementine images, different geologic units were mapped in the basin interior (Fig. 2.2) and the surface age was determined from crater counts (Wilhelms et al., 1979; Shoemaker et al., 1994; Mest and van Arsdall, 2008; Mest, 2011). Identified geologic units are described in detail below.

The basin floor has most units interpreted as shock-melted materials. The melt unit on the basin floor has been mapped as two separate units (as observed using Clementine data) with

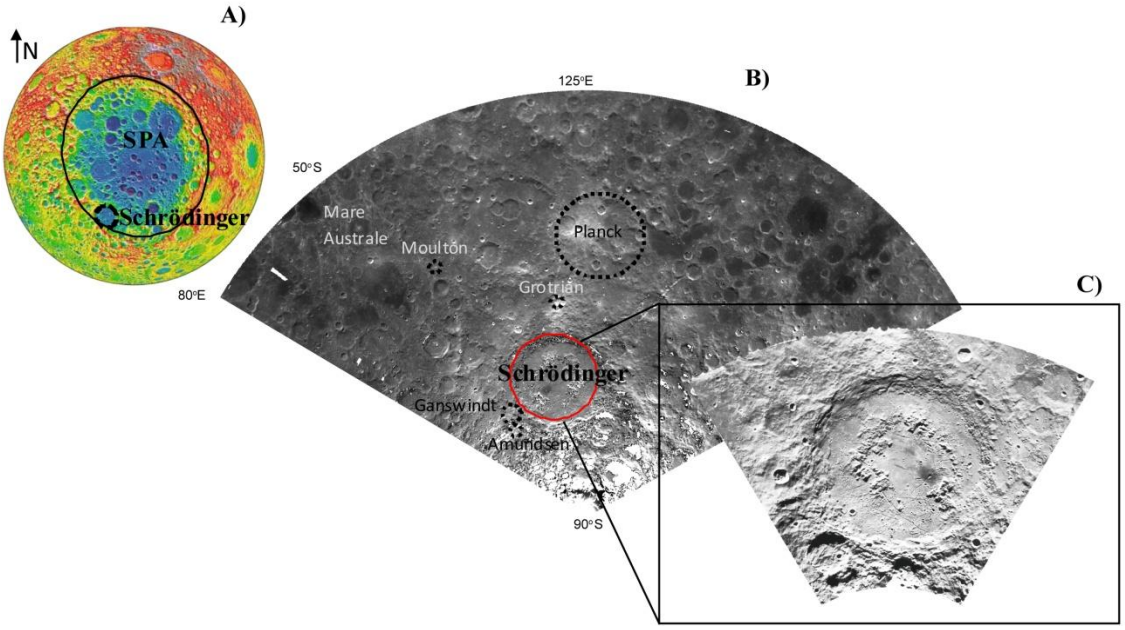

Figure 2.1: A) The location of Schrödinger (dashed circle) shown within the topographic extent of the South Pole - Aitken basin (topography using LOLA data). B) Regional view of the Schrödinger impact basin centered at 75^{o}S/130^{o}E (Clementine 750 nm band). C) A close up of Schrödinger shows a well preserved impact crater with a basin wall, terraces, peak ring, interior mare patches, and a pyroclastic deposit within the basin floor.

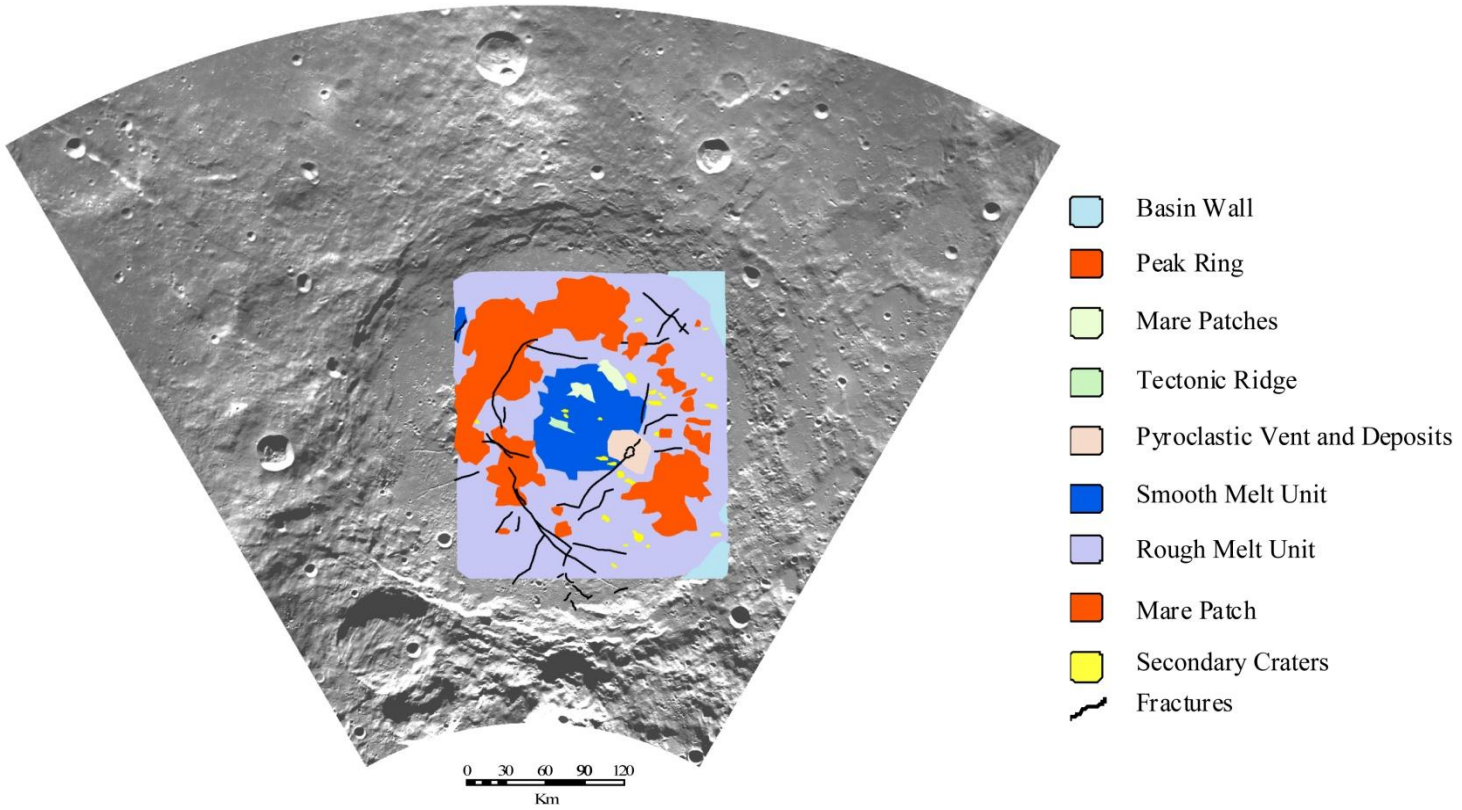

Figure 2.2: Original geologic map of Schrödinger impact basin. Adapted from Shoemaker et al. (1994).

distinct rough and smooth textures (Shoemaker et al., 1994). The rough plains unit has a hummocky texture and fills the area between the terrace walls and inner peak ring. The smooth plains unit covers a smaller part of the basin, lying mainly within the inner ring (Shoemaker et al., 1994, Shoemaker and Robinson, 1995). Fractures on the southern part of the basin floor are partly radial and extend away from a local volcanic vent (discussed further below). Graben radial to the basin have been explained as the isostatic response of the central basin area after the melt sheet was emplaced (Shoemaker et al., 1994; Schultz, 1976).

Parts of the basin floor are also covered by a low albedo pyroclastic deposit and mare patches (Shoemaker and Robinson, 1995). The pyroclastic deposit within Schrödinger covers an area of ~820 km^2 (Gaddis et al., 2003). The source for the pyroclastic deposit is a volcanic vent 4.8 km by 8.6 km in size that rises 0.5 km above the basin floor (Shoemaker et al., 1994). The cross–cutting fractures and concentrated spatial coverage of deposits near the vents indicate that the pyroclast deposits occurred after the crater forming event. Other mapped features on the basin floor include ghost craters, a lobate ridge, as well as secondary craters from the Orientale, Humboldt, and Antoniadi impacts (Shoemaker et al., 1994).

The inner peak ring on the basin floor is 150 km in diameter and rises 2.5 km above the basin floor (Shoemaker et al., 1994; Mest and van Arsdall, 2008; Cook et al., 1999). Data from the recent Kaguya and Chandrayaan–1 missions have led to the identification of pure anorthosite and olivine materials within various segments of the peak ring (Ohtake et al., 2009; Yamamoto et al., 2011; Kramer et al., 2011).

Schrödinger basin has a well-defined outer rim. The basin depth, measured from the highest rim height to the lowest part of the floor using Lunar Reconnaissance Orbiter Laser Altimer data (LRO-LOLA), is deepest (3-4 km) along the northern and western parts of the basin and shallowest along the southern and eastern sections of the basin (~ 1-2 km). Ejecta deposits lie outside the basin and are concentrated along the north east sections of the rim, extending up to 100 km from the basin rim (Hawke and Head, 1977; Shoemaker et al., 1994). Beyond the basin rim, narrow valleys (Vallis Schrödinger and Vallis Planck) start from the north-northwest corners of the rim and extend away from Schrödinger basin into the surroundings (Wilhelms et al., 1979) (Fig. 2.1).

The total mapped volume of impact melt units within the basin floor (Shoemaker et al., 1994) is much less than model calculations would estimate (Cintala and Grieve, 1998). It has been suggested that much of the impact melt may lie along terrace walls, over the peak ring, and outside the basin area (Shoemaker and Robinson, 1995; Cintala and Grieve, 1998). With the improved spectral resolutions offered from recent spacecraft missions, it is now possible to determine if there are significant melt deposits (ponds) along the walls and beyond the rim of Schrödinger.

2.2 Methods

To conduct this study, we selected an area that includes the basin interior, the rim of Schrödinger and exterior deposits extending up to 1.5 crater radii from the basin centre. The geographical extent for the area was 67–82°S and 100–160°E. We used the Clementine UV-VIS multispectral dataset to: 1) determine the spectral properties and compositions of previously identified geologic units within Schrödinger; 2) address the potential presence of deeper derived materials within Schrödinger; and 3) run spectral unmixing models to determine the fractional abundances of basalt and anorthosite in the basin. Higher resolution data from the Lunar Reconnaissance Orbiter and Chandrayaan-1 were used to compliment the regional scale Clementine data.

2.2.1 Multispectral Study

Clementine

The Clementine UV-VIS dataset was used to assess the material composition and extent of previously mapped units. The dataset was manipulated in various ways for analyses. We 1) generated composite maps to determine maturity and iron content details (Pieters et al., 1994; Lucey et al., 2000), 2) gathered sample spectra of previously identified geologic units (Shoemaker et al., 1994) and classified sampled spectra based on composition, 3) ran an automated algorithm to determine the distribution of fresh basalt spectra (Antonenko and Osinski, 2011), and 4) ran a linear–unmixing model to determine the spatial distribution of identified spectral units (Sheppard, 2005). These techniques are discussed in detail below.

False colour ratio maps (Fig. 2.3A), created using the UV-VIS data, help accentuate features that otherwise are not obvious in single-band albedo alone, such as the surface maturity and the presence of mafic materials (Pieters et al., 1994). Colour ratio maps help accentuate features that otherwise are not obvious in band images alone. An FeO weight percent map for the area was also generated using algorithms defined by Lucey et al., 2000 (Fig. 2.3B). Together, these maps were used to determine fresh surfaces and significant FeO rich areas that may be present.

Spectral profiles were derived by plotting reflectance levels at each of the five UV-VIS (415, 750, 900, 950, 1000 nm) bands of Clementine data to provide information regarding the broad material composition of different mapped units. The most common lithologies on the Moon are mare basalts and highland anorthosites; these are expected to be present within Schrödinger as well. Spectra were sampled from all geologic units previously identified by Shoemaker et al. (1994). Spectra sampling sites were typically located along sloped surfaces or freshly exposed surfaces with a 1x1 pixel window size (Clementine data has a 100-200 m/pixel spatial resolution (Nozette et al., 1994)). We avoid using weathered spectral profiles in our analyses as they are hard to distinguish. Sloped surfaces tend to expose the freshest surfaces by inhibiting regolith build-up. Freshly exposed surfaces on the slopes of smaller craters can be used to sample the immediate subsurface (McCord et al., 1981; Antonenko, 1999; Staid et al, 2000). Shadowed regions or overly bright areas (where reflectance was supersaturated) were not used for spectra selection to avoid misinterpretations. Sampled spectra were classified as basalt (defined as rocks rich in pyroxene, and which may or may not contain olivine), highland (defined as rocks rich in plagioclase), or “ambiguous”.

The distribution of pixels suggesting the spectra of fresh mafic–rich material was also derived using an algorithm defined by Antonenko and Osinski (2011). This algorithm was developed in equatorial regions to automatically identify very fresh basalt spectra using a combination of continuum slope and band depth. Since Schrödinger is located closer to the south pole, some caution is required with the use of this algorithm. Even so, high concentration areas of fresh mafic-rich material were noted to be generally consistent with the FeO dataset (Fig. 2.3B).

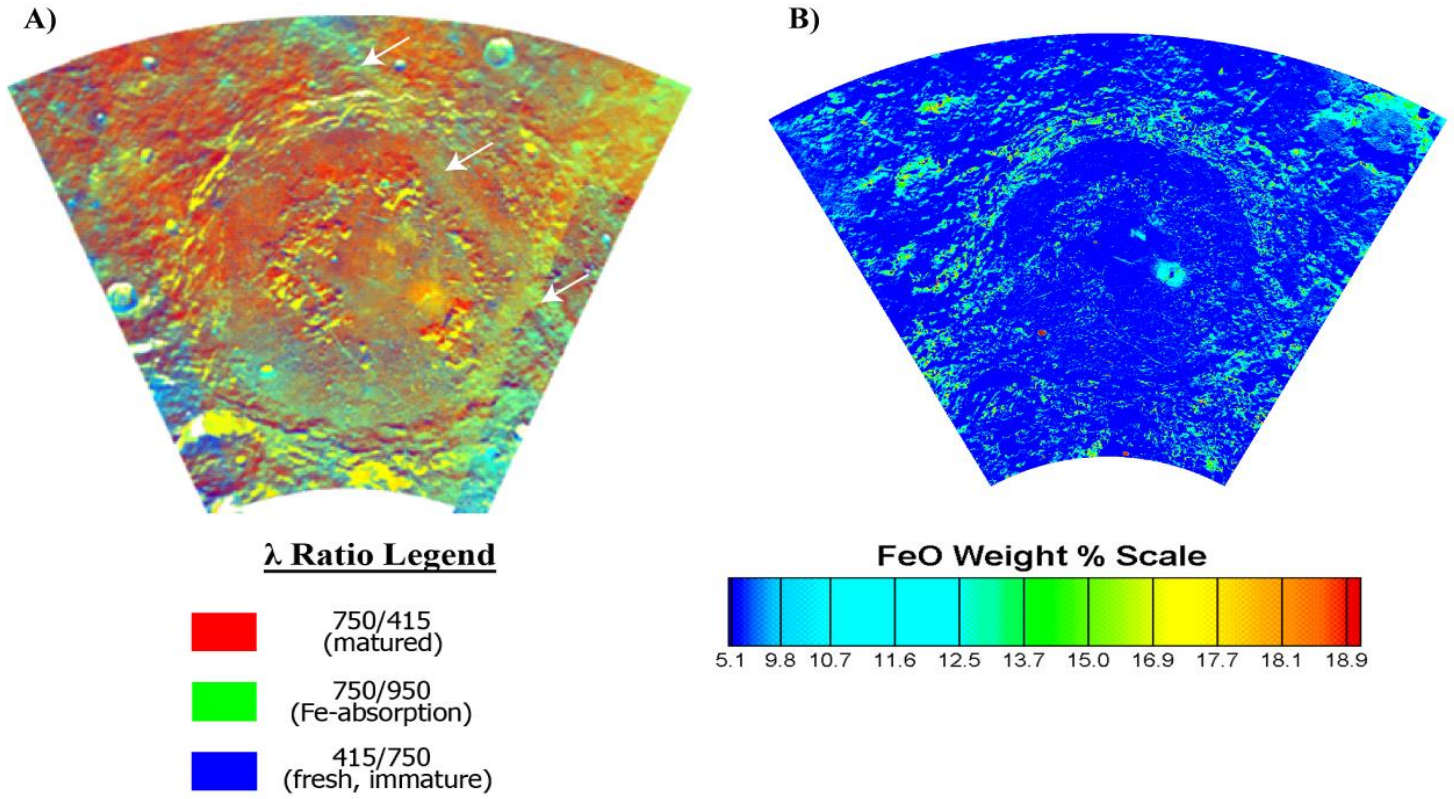

Figure 2.3: A) Clementine-derived false colour ratio composite map of the study area. The area appears to be a largely matured surface with the exception of post – Schrödinger impact craters within and around the basin. The pyroclastic deposits and mare patches are relatively mafic rich compared to the rest of the study area. B) FeO weight % map of the study area. Values were derived using algorithms defined by Lucey et al., 2000. Both the mare patches and pyroclastic deposits have higher than average FeO content. Shadowed areas also show high FeO content, but this is a known artefact.

We ran spectral unmixing models using PCI Geometrics proprietary standard algorithms ENDMEMB and SPUNMIX (Sheppard, 2005) to obtain fractional maps of basalt and anorthosite distributions for the study area. High concentration areas of basalt and anorthosite were noted for analyses in the distribution of spectral endmembers relative to geological units previously identified. A dark endmember was also included to factor in shadowed areas (Fig. 2.8E).

Chandrayaan-1 (Moon Mineralogy Mapper)

We also examined a portion of the study area using data from the Moon Mineralogy Mapper (M^3) instrument on board Chandrayaan-1 (Fig. 2.4). M^3 data covers the UV-VIS-NIR (ultraviolet-visible-near infrared) spectrum like the Clementine dataset but has improved spectral resolution and range, allowing for a more accurate evaluation of compositional information. The spatial resolution of M^3 (140 m/pixel) is comparable to that of Clementine (100 m/pixel) but the spectral resolution of global mode M^3 data is greatly improved at 20–40 nm. At the time of study, only one image strip was publicly released for the study area. The data (image # M3G20090529T013507) was used to assess the spectral properties of all the geological units present and test our Clementine results at a preliminary level. The M^3 file was originally a Level1b file (pixel-located, resampled, and calibrated data in radiance units), and radiance values were converted to reflectance, using techniques outlined by Green et al., 2010. The criteria for selecting suitable spectral sampling sites are the same as for Clementine multispectral data. The spectral coverage of M^3 ranges from 446 nm to 3000 nm. Spectra were sampled using a 3x3 pixel average. Each spectral profile acquired was compared to the M^3 spectral library (Lundeen et al., 2010) to determine mineralogy.

LRO Mini-RF Data

Complementary information can be obtained by observing Schrödinger basin at radar wavelengths. Radars use an active source to probe the lunar surface at wavelengths of several centimetres to several metres, yielding information about the topography, and roughness of the reflecting surface. Unlike visible images, radar is also capable of probing the near subsurface, to depths roughly ten times the radar wavelength (Campbell and Campbell, 2006).

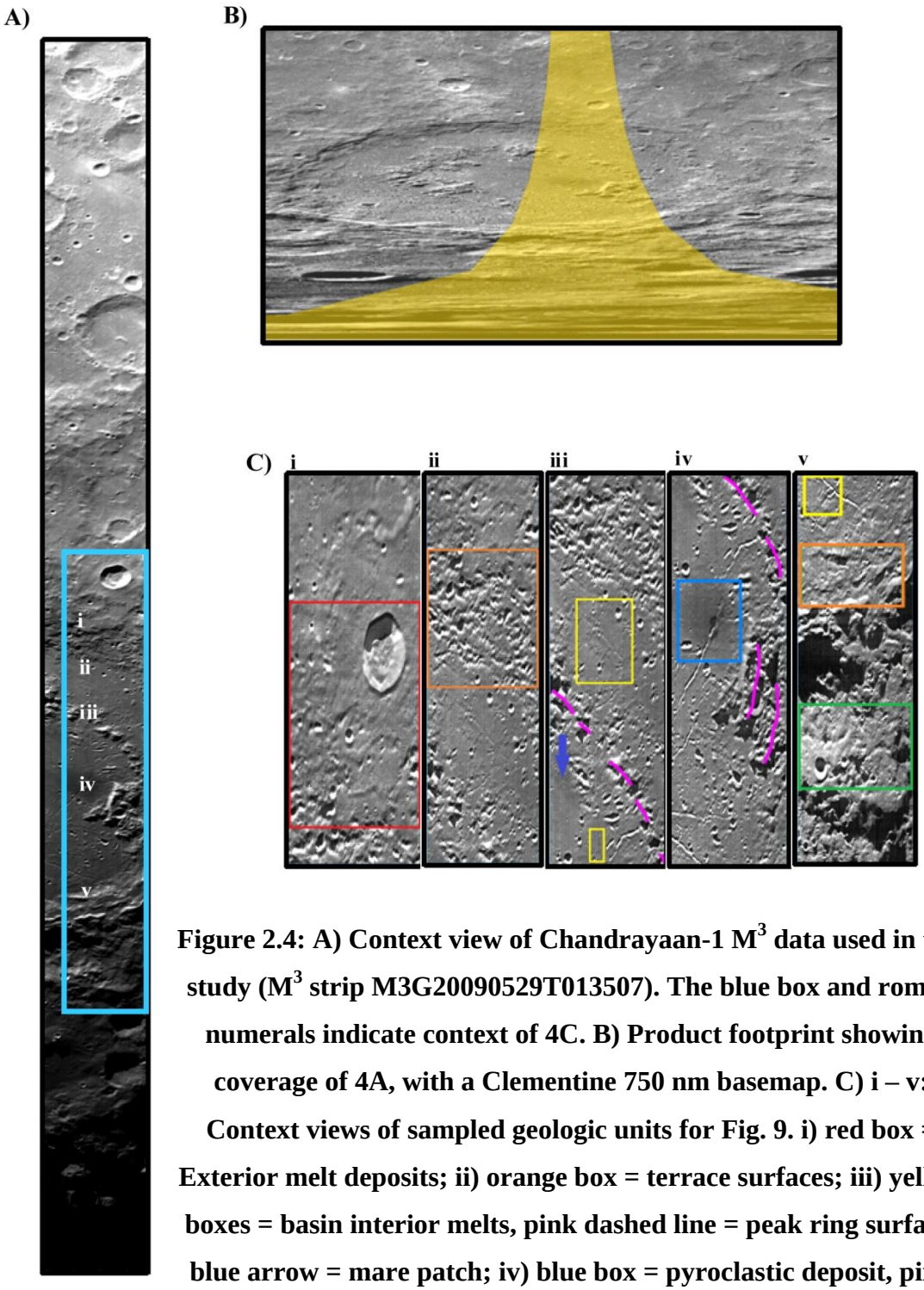

Figure 2.4: A) Context view of Chandrayaan-1 M^3 data used in this study (M^3 strip M3G20090529T013507). The blue box and roman numerals indicate context of 4C. B) Product footprint showing coverage of 4A, with a Clementine 750 nm basemap. C) i – v: Context views of sampled geologic units for Fig. 9. i) red box = Exterior melt deposits; ii) orange box = terrace surfaces; iii) yellow boxes = basin interior melts, pink dashed line = peak ring surface, blue arrow = mare patch; iv) blue box = pyroclastic deposit, pink lines = peak ring surface; v) yellow box = basin interior melts, orange box= terrace surfaces, green box= crater ejecta.

Earth-based radars have been mapping the Moon since the 1970s (e.g., Zisk et al., 1971), and advances in computer processing have made very high–resolution radar imagery of the Moon possible (on the order of tens of metres, e.g., Carter et al. (2009); Campbell et al. (2010)). However, given the synchronous rotation of the Moon about the Earth, ground–based observers have been unable to probe the lunar far side. The Mini–RF instrument on the Lunar Reconnaissance Orbiter has, therefore, provided our first view of Schrödinger basin at radar wavelengths, with a resolution of 30 m at S–Band (12.6 cm).

One of the most useful indicators of surface roughness is the circular polarization ratio (CPR). This value is defined as the ratio of the backscattered power in the same–sense circular polarization as was transmitted (SC) to the opposite–sense circular polarization (OC) (Nozette et al., 2010). When an incident circularly polarized radar wave is backscattered off an interface, the polarization state of the wave changes. Thus, flat, mirror–like surfaces, dominated by single–bounce reflections, tend to have high OC returns and low CPR values. Rough surfaces, dominated by multiple–bounce reflections, tend to have roughly equal OC and SC returns, with CPR values approaching unity. We, therefore, created both radar backscatter and CPR maps for the study area and assessed the roughness scale for several mapped units of Schrödinger.

2.2.2 Mapping exterior melt deposits

Melt pond regions are defined as smooth deposits that drape over crater ejecta or pool into low lying crevasses along crater walls, outside the outer rim, and surrounding area. Exterior melt deposits are easily recognizable as smooth surfaces with a lower albedo than the surrounding crater ejecta. Various datasets were utilized for mapping impact melts along the basin wall and outside the basin rim. Locations of different melt deposits (including ponds, veneers, and flows) were identified using the Clementine 750 nm band (data at 100 pixel per degree resolution).

We have also used extensive coverage from the Lunar Reconnaissance Orbiter datasets, including altimeter data (LOLA – 20 m along track resolution and 0.1–1.8 km cross track resolution), and camera data (panchromatic Narrow Angle Camera (NAC) at 0.5 m/pixel resolution; and multispectral Wide Angle Camera at 100 m/pixel resolutions) (Robinson et

al., 2010; Smith et al., 2010) for mapping the locations of melt deposits associated with Schrödinger.

2.3 Results

2.3.1 Regional context

The Clementine false colour ratio composite map of the study area indicates that most of the basin area and surrounding surface is mature highland material (Fig. 2.3A). Mature surfaces indicate that soils (top millimeter depth) have been exposed to space radiation on the surface for long periods of time, and likely have a high content of agglutinates (Morris et al., 1978). Typically the degree of maturity is assessed by comparing the abundance of reduced iron to the total abundance of iron (Morris et al., 1978); therefore the more mature a surface, the redder it appears in false colour. Iron- rich materials appear in shades of yellow-orange for mature materials or turquoise for fresh materials. An iron-rich crater ray feature of low maturity can also be observed in the false colour image (Fig. 2.3A). It is important to take precaution in interpreting the false colour details, particularly along topographic regions of the study area. Due to the high phase angles encountered at high latitudes, some regions (e.g., along terraced walls to the north, along the south-facing slopes of the peak ring, and shadowed craters) are subject to extreme lighting and high saturations levels (Figs. 2.1, 2.2). Therefore in the false colour map (Fig. 2.3A), shadowed areas and super-saturated areas can provide incorrect information.

The iron (FeO wt%) weight percent distribution map for the study area (Fig. 2.3B), created using algorithms defined by Lucey et al. (2000), shows that iron compositions are comparable to levels expected for that region of the South Pole–Aitken basin (Lucey et al., 1998). We find FeO rich material within the volcanic vent and mare sites, as expected. However, we use precaution in interpreting this map for the same reasons as mentioned above for the false colour map. Because of the high phase angles, we consider only regional trends in FeO distribution, not the exact FeO values. We minimize the importance of isolated anomalies where saturation may be an issue.

Spectral profiles, from Clementine data, were sampled at various locations within the basin (including peak ring, basin floor, mare patches, pyroclastic deposit, and basin ejecta). The

small number of sites sampled in this work is the result of a lack of small fresh craters resolvable using Clementine UV–VIS data. The compositional analysis indicates a slightly heterogeneous distribution of both anorthosite and basalt signatures (Figs. 2.5, 2.6).

The automated algorithm applied to the area provides an independent way to identify fresh mafic-rich areas (Fig. 2.7). As expected, pyroclastic deposits display basaltic spectra. Interestingly, much of the basin floor, particularly between the inner peak ring and basin wall, is void of much fresh mafic indicators - a factor of surface maturity. Similar to our interpretation of the FeO distribution map, we use caution and look only for clusters of mafic-rich areas due to the high phase angles encountered at these latitudes. The mafic-rich spots along the basin rim to the south, along the peak ring, and southern areas outside the basin, have very high phase angles and, therefore, may not reflect the true composition. However, there are regions where mafic-rich clusters exist and may indicate more about the composition. These regions include a small fresh crater on the southwest basin floor, two small craters on the west and north east part of the basin ejecta, and a strong cluster ~0.5 crater radius to the northeast beyond the rim. In addition, mafic-rich spectra trend along the general geographic direction as the crater ray identified in figure 2.3A.

Unmixing analyses of the study area confirm that distributions of anorthosite and basalt endmembers are not confined to specific geologic units (Fig. 2.8). Within the anorthosite fraction map (Fig. 2.8A), pyroclastic deposits and mare regions appear dark (as expected). The inverse is true in the basalt fraction map (Fig. 2.8B). The basalt fraction map also indicates that many post-Schrödinger impact craters have a strong basalt endmember signature, and the eastern half of the study area has also relatively high basalt endmember coverage. The crater ray present across the eastern half of the basin floor is clearly visible in the basalt fraction map (Fig. 2.8B) and indicates its parent crater post-dates the post-Schrödinger impact event. The dark fraction map (Fig. 2.8C) includes shadow areas as well as some geologic units (mare patches, pyroclastic deposits). Both anorthosite and dark fraction maps preserve the topographical features, indicating the need for additional endmembers (Fig. 2.8D).

With the single M^3 image used in this study, there is very little surface coverage of the various units, including the lack of tectonic ridge material available to sample (Fig. 2.2, Fig.

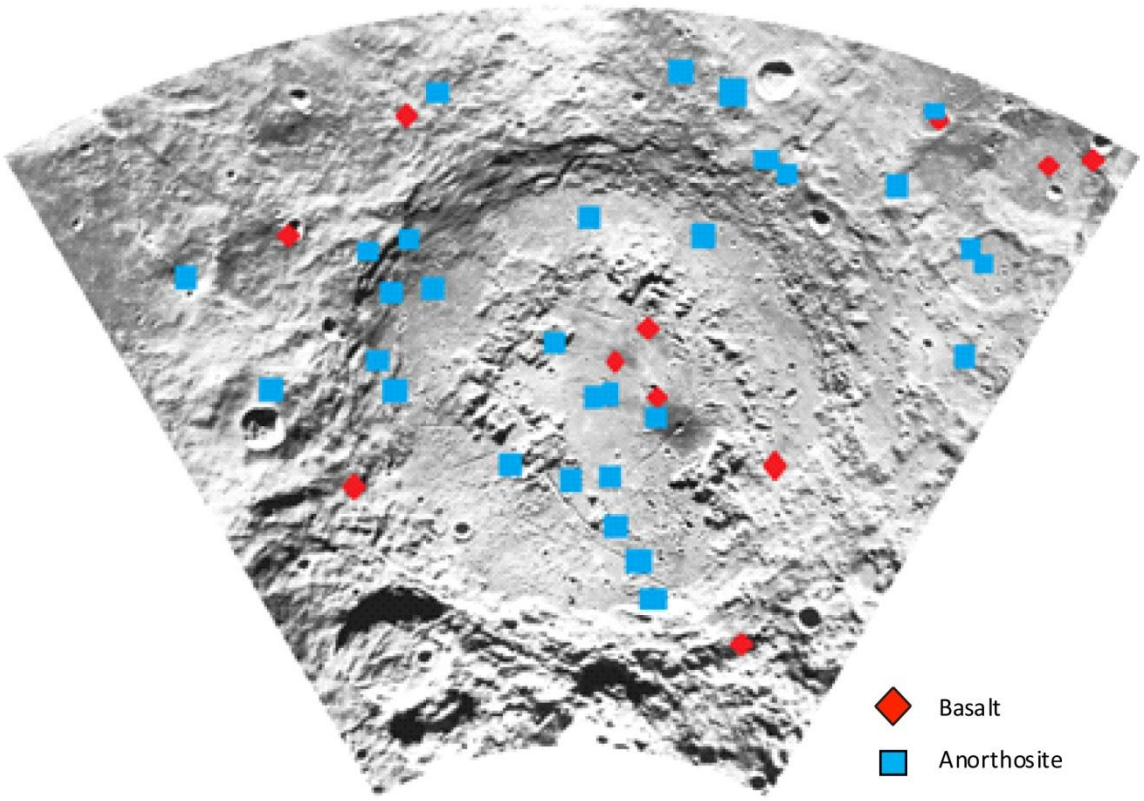

Figure 2.5: Locations of sample spectra obtained for all mapped geologic units mapped in Fig. 2.2, as well as the crater ejecta extending to the limits of this image. The sample number is low due to the lack of fresh craters resolvable within the instrument parameters. The distribution of basalt and anorthosite materials is heterogeneous.

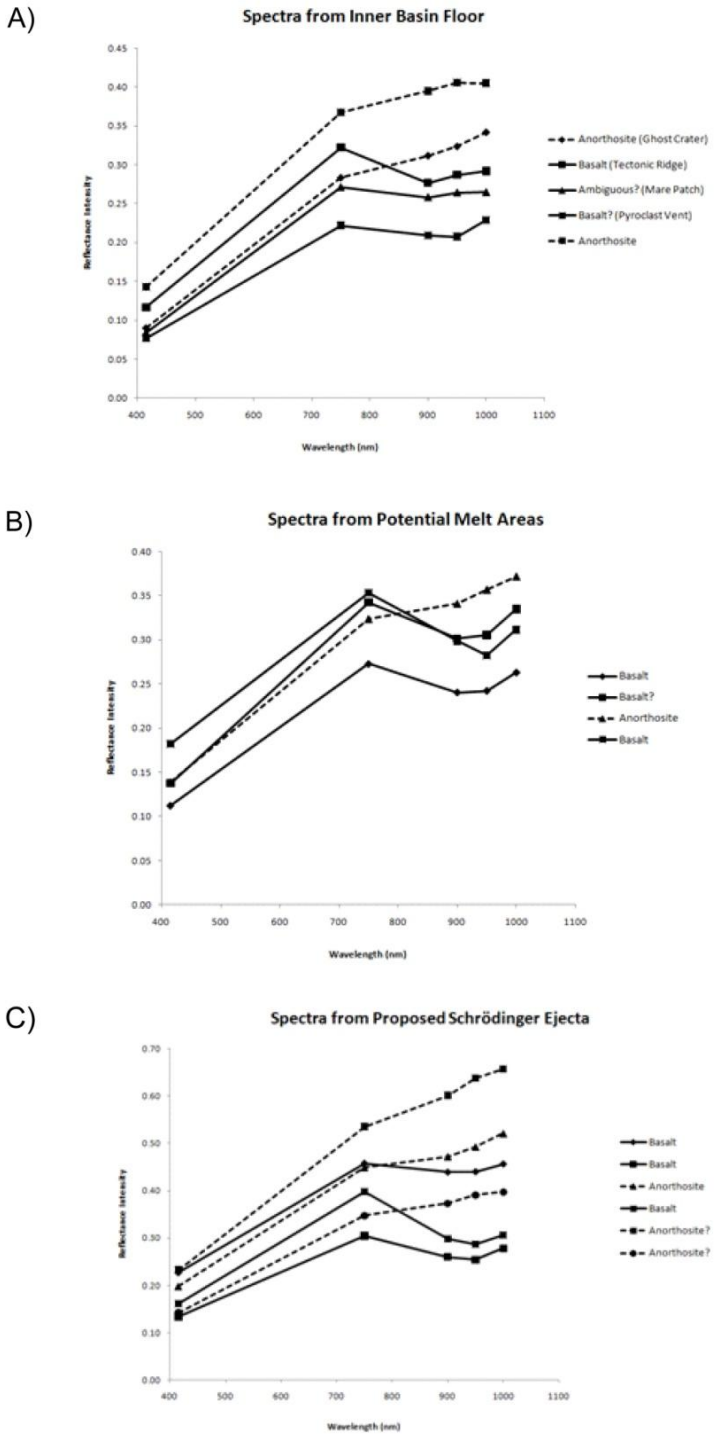

Figure 2.6: Sample spectra of mapped units in and around Schrödinger using Clementine data. A) Normalized sample spectra from the mare, pyroclastic deposits and tectonic ridge within the basin floor of Schrödinger. B) and C) Normalized sample spectra from the melt deposit units and exterior ejecta respectively.

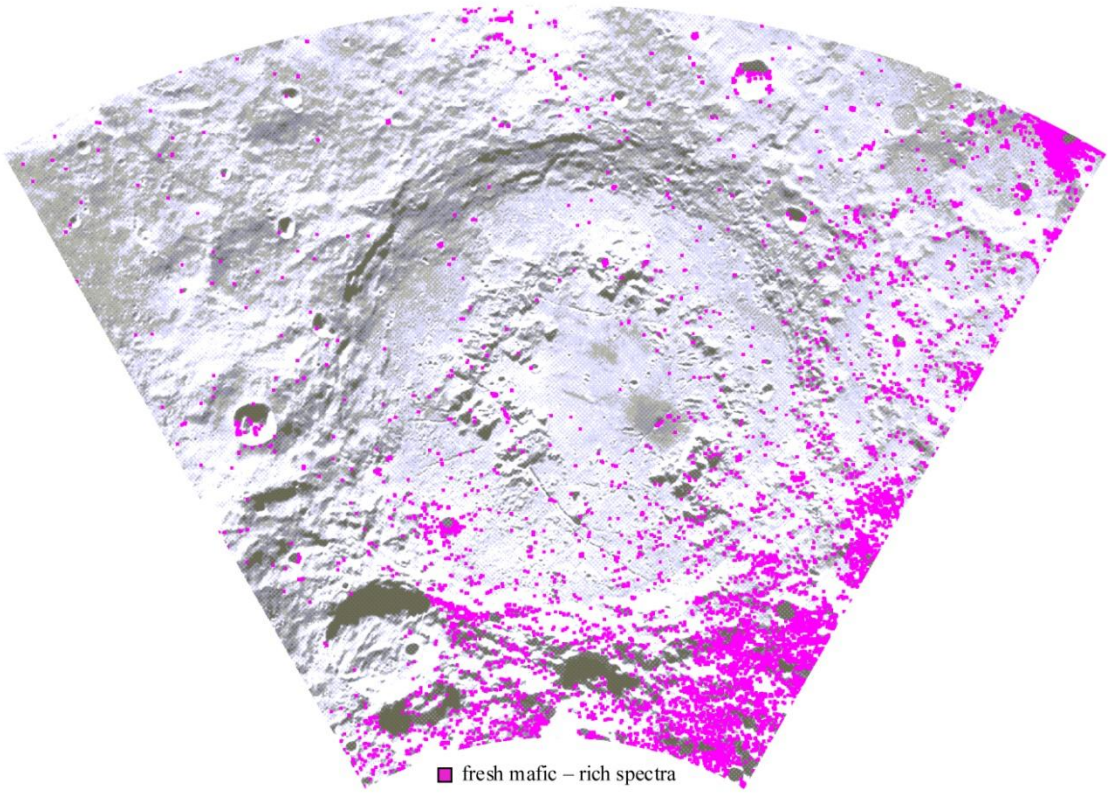

Figure 2.7: Mafic rich spectral distribution using algorithm defined by Antonenko and Osinski, 2011. The distribution shows mafic spectral content for the pyroclastic deposits on the basin floor, sporadic distribution along the peak ring, within post Schrödinger impact craters, and along the eastern half of the study area.

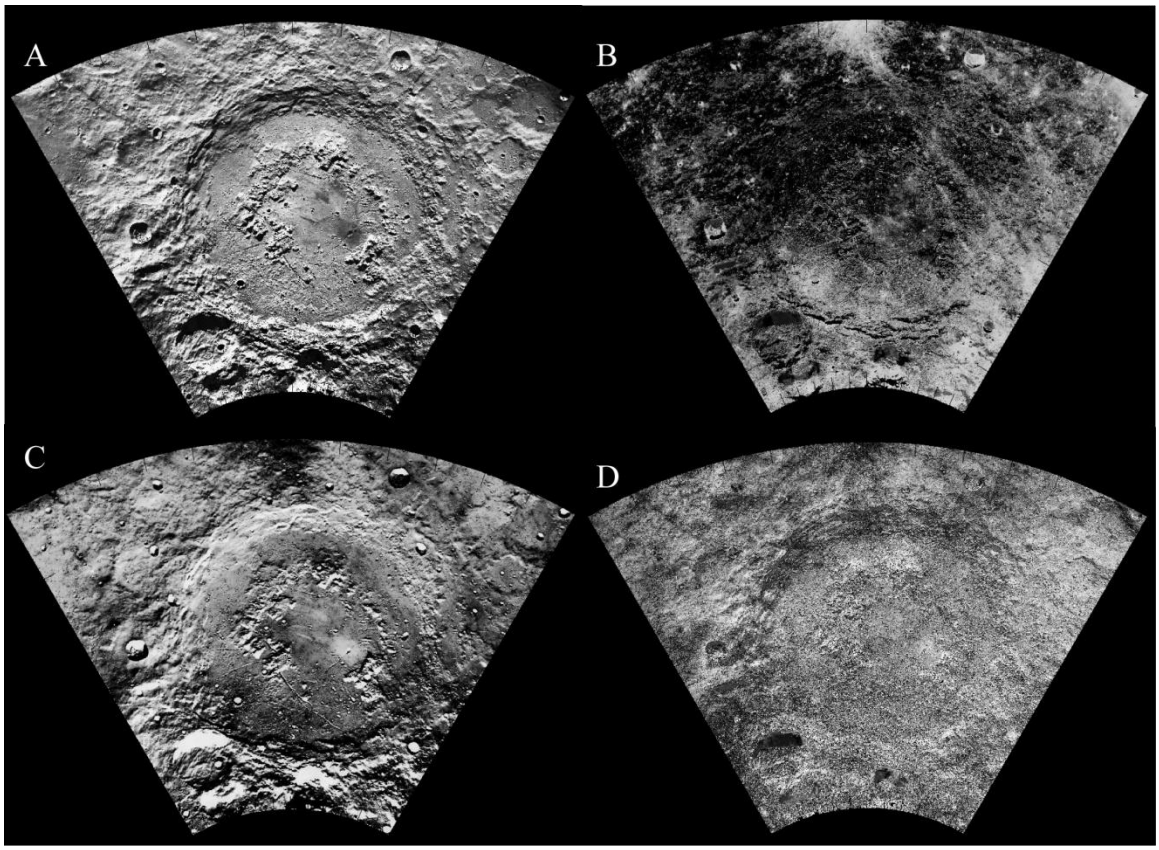

Figure 2.8: Spectral un-mixing fraction maps. A) Anorthosite distribution: most materials within and around Schrödinger are rich in anorthosite, however, topography is preserved so this endmember includes some component that is not associated with composition. B) Basalt distribution: Crater ejecta (north of basin rim), an external impact crater ray, and tectonic ridge are basalt rich. C) Dark fraction: shadow areas are well highlighted. However, both the mare patches and pyroclastic deposits are picked up as well indicating more spectral endmembers are required to accurately characterize the compositions of these units. D) Root mean square (RMS) error map of spectral un-mixing results.

2.4 for M^3 context). Spectra sampled from fresh small craters within most geologic units visible in the image file show the presence of pyroxene (Fig. 2.9). The spectra have low reflectance and display noise; therefore, it is challenging to identify the mineral or rock type present.

In Mini-RF (Fig. 2.10) S-Band data (12.6 cm), the basin interior displays an increased radar backscatter (Fig. 2.10A) and CPR (Fig. 2.10B) compared to the regions outside the crater, indicating the basin's interior surface and near-surface is rough at a scale of centimeters to decimeters. There is also a radar bright crater ray (Fig. 2.11A) that corresponds to the region of high Fe abundance as seen in Figure 3A. The pyroclastic deposits appear radar dark, which is consistent with observations of pyroclastic deposits on the near-side of the Moon (Carter et al., 2009). The average CPR of the pyroclastic deposit is near ~0.6, which is higher than that observed in near-side deposits, but may be consistent with the increase in CPR expected with increasing incidence angle (see Figure 4 in Carter et al. (2009); Mini–RF has a look angle of 48°). Alternatively, it may indicate that the deposit is relatively shallow, less than several meters thick. The two mare patches are distinguished by higher radar backscatter and CPR than the surrounding basin. Their CPR of ~0.7 is consistent with regions of similar TiO_2 content (5%) in Mare Imbrium (Campbell et al., 2010). The TiO_2 distribution is calculated using algorithms defined by Lucey et al. (1998). These high values of CPR have been attributed to abundant cm–sized rock fragments, likely from small impacts, and subsurface volume scattering (Campbell et al., 2010). The exterior impact melt deposits identified in the Clementine images do not noticeably differ in radar properties compared to the surrounding regolith, suggesting perhaps that they are buried under a lot of regolith.

We present an updated geologic map combining previously mapped units by Shoemaker et al. (1994) and Mest (2011) with the impact melt pond areas identified along the terrace walls and beyond the basin rim in this study (Fig. 2.12). Melt units within the basin floor are combined to one "inner melt" unit in contrast to other published maps due to the spectral similarities between the rough and smooth plains units as discussed further in Chapter 4, section 4.2.2.

A)

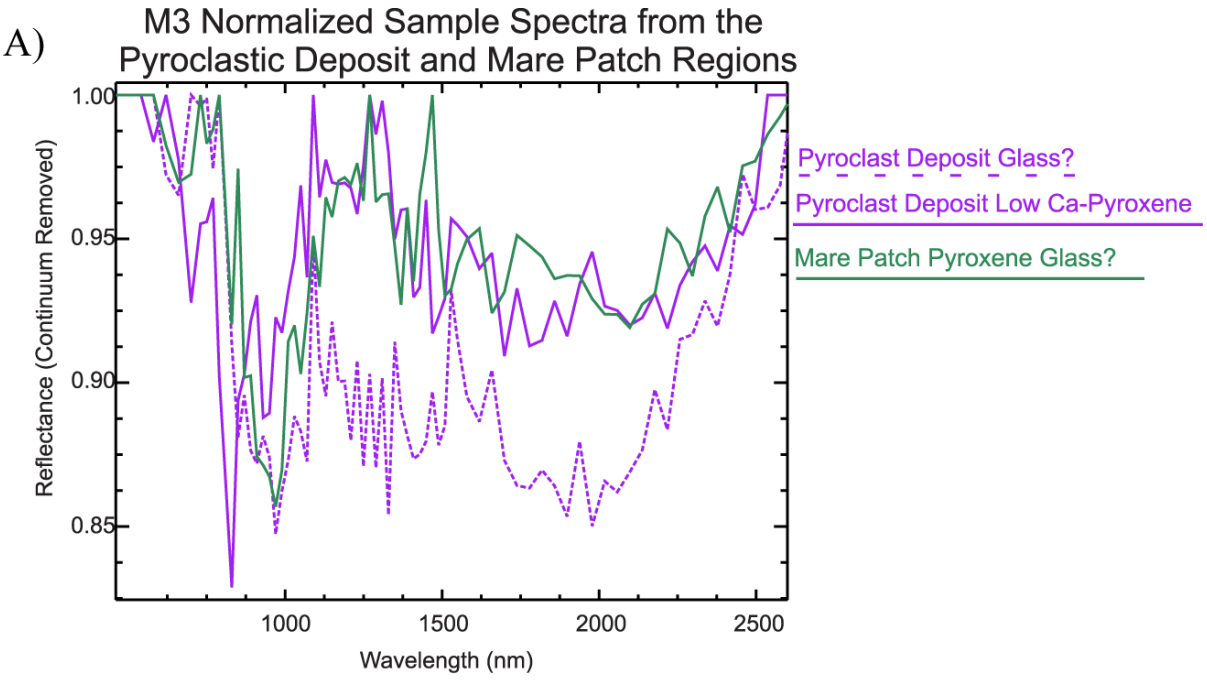

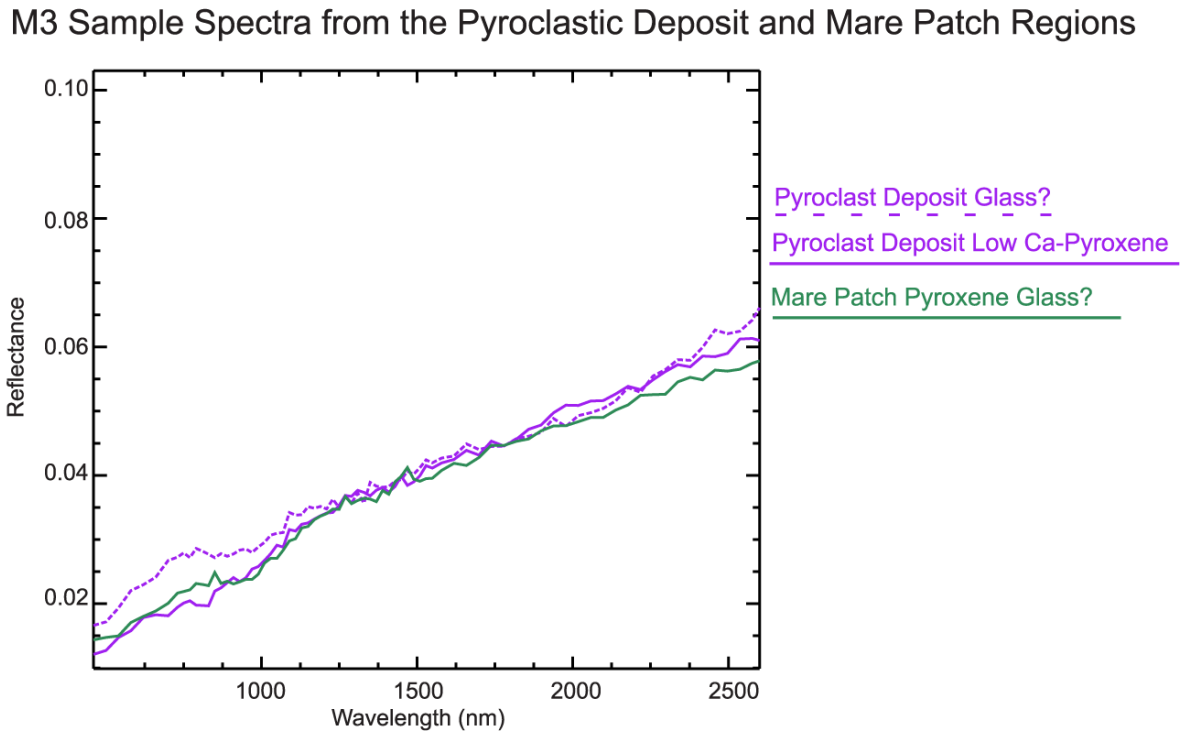

Figure 2.9A: Chandrayaan-1 M^3 derived sample spectra of basin floor pyroclastic and mare units indicate the presence of mafic minerals, as expected.

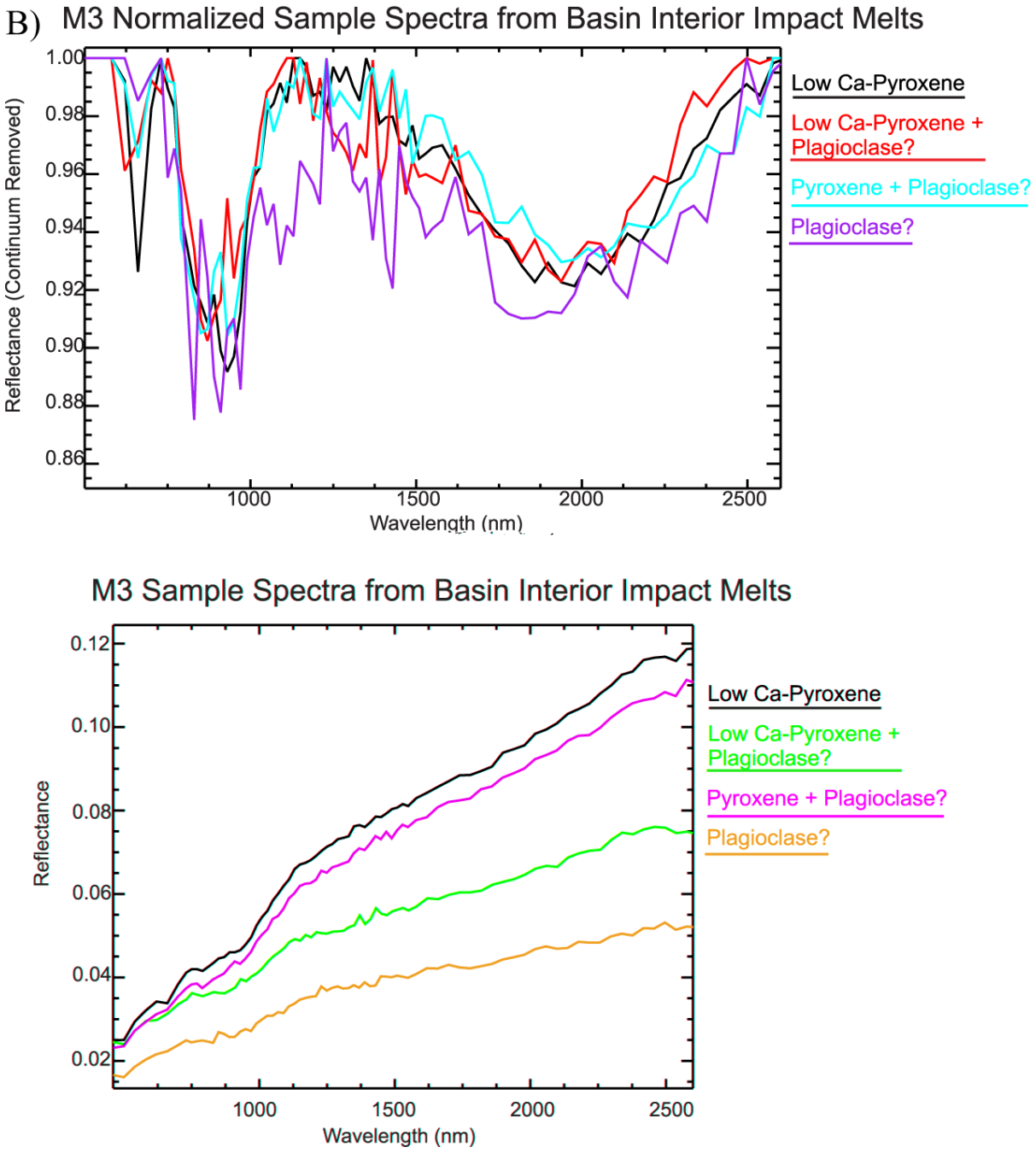

Figure 2.9B: Chandrayaan-1 M^3 derived sample spectra of the basin interior impact melt unit indicate the presence of low-Ca pyroxene and some plagioclase feldspar.

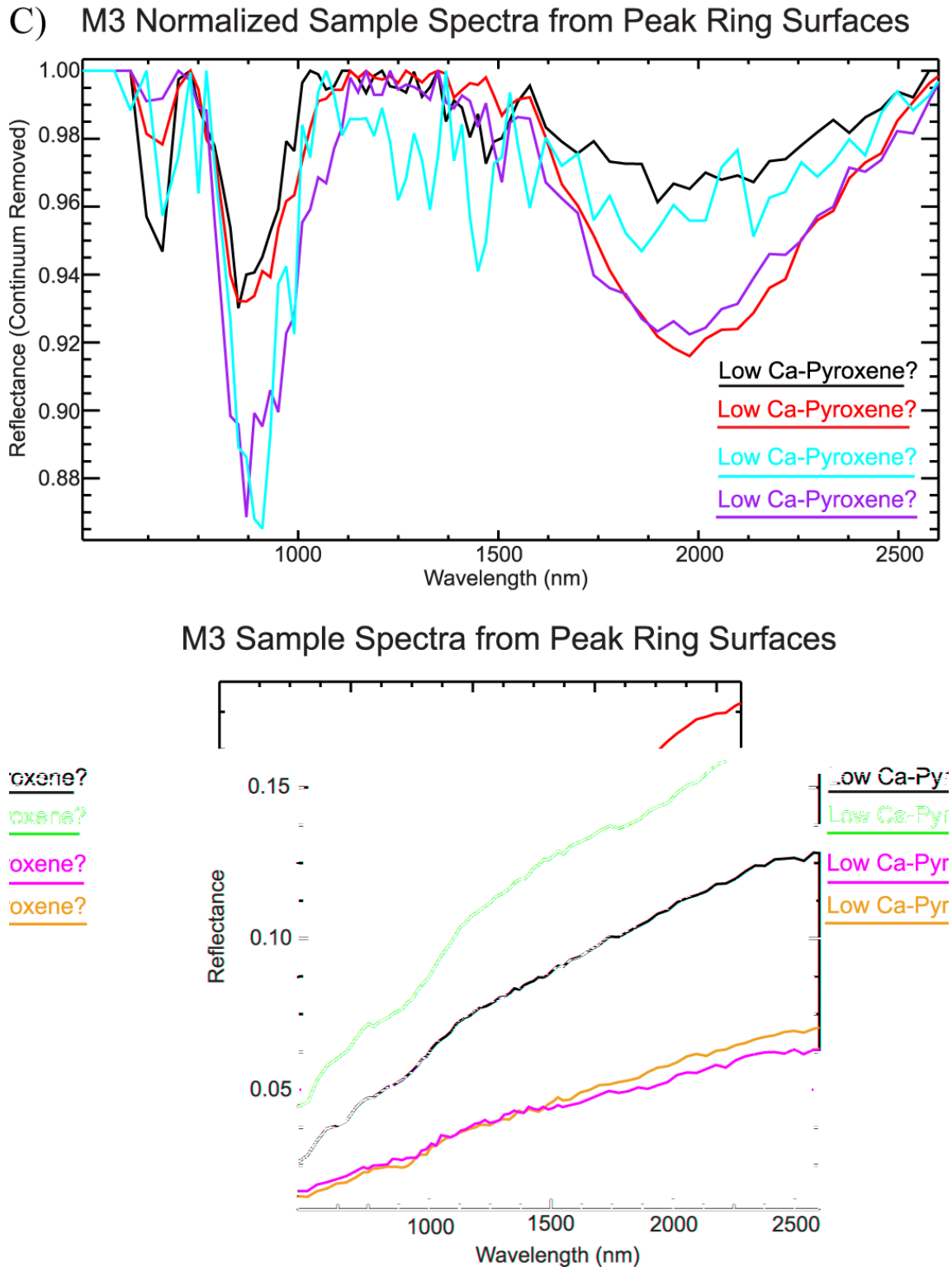

Figure 2.9C: Chandrayaan-1 M^3 derived sample spectra of the peak ring indicate the presence of mostly low-Ca pyroxene, with potentially some plagioclase feldspar.

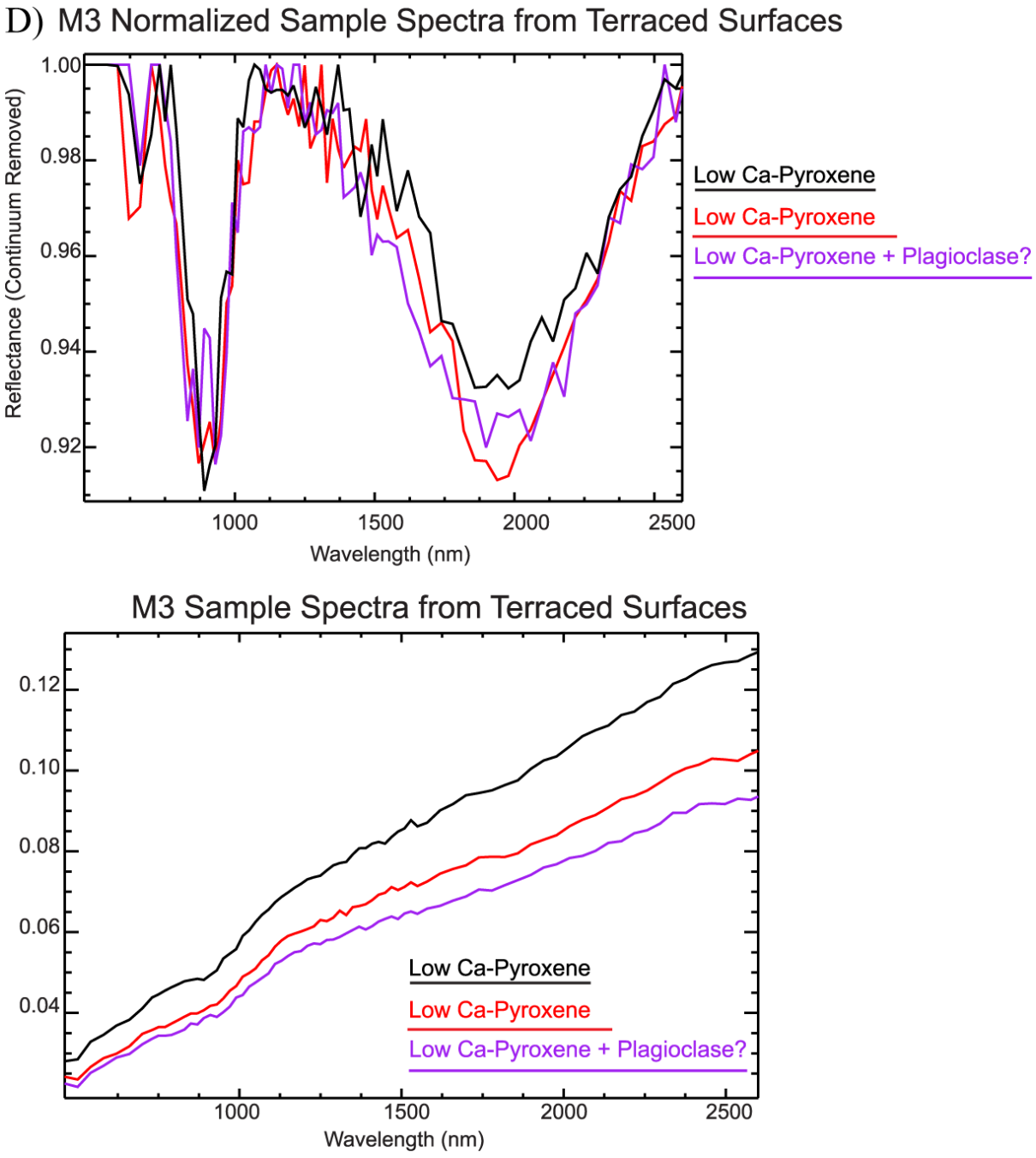

Figure 2.9D: Chandrayaan-1 M^3 derived sample spectra of the terraced surfaces indicate materials are mostly low-Ca pyroxene.

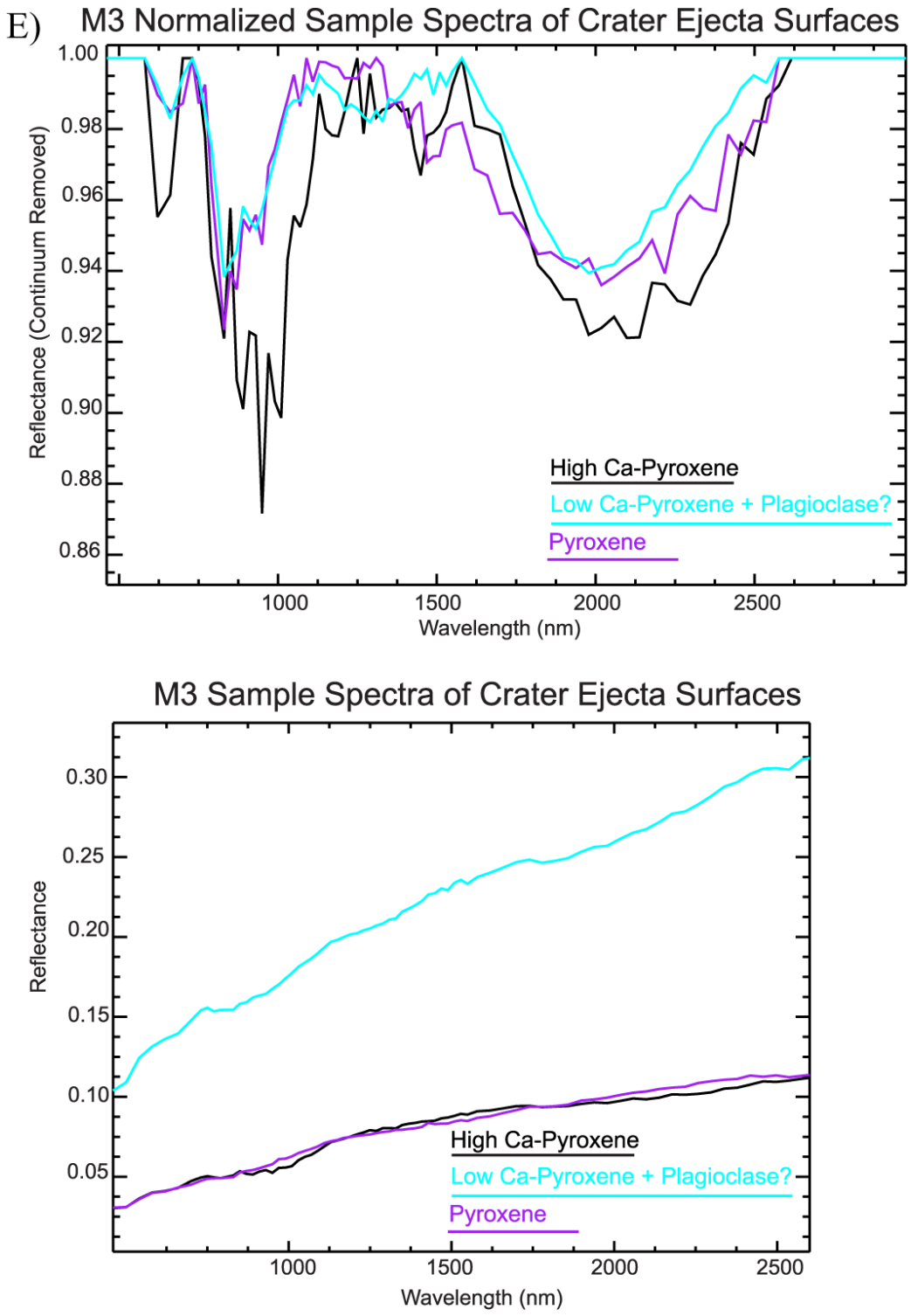

Figure 2.9E: Chandrayaan-1 M^3 derived sample spectra of the ejecta unit suggests a mixture of various materials including plagioclase feldspar and both low and high-Ca pyroxene.

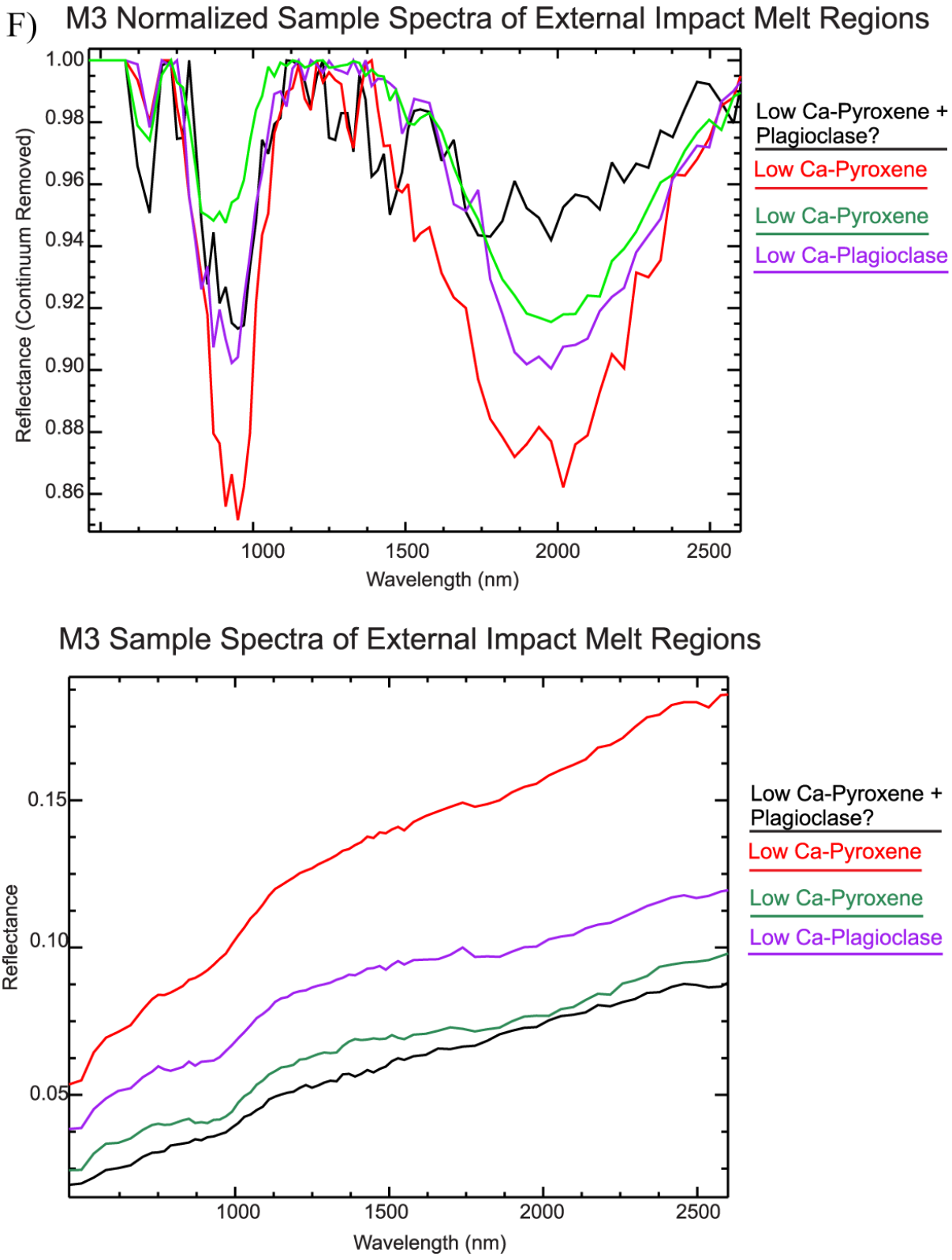

Figure 2.9F: Chandrayaan-1 M^3 derived sample spectra of the exterior melt deposits indicates a strong signature of low-Ca pyroxene.

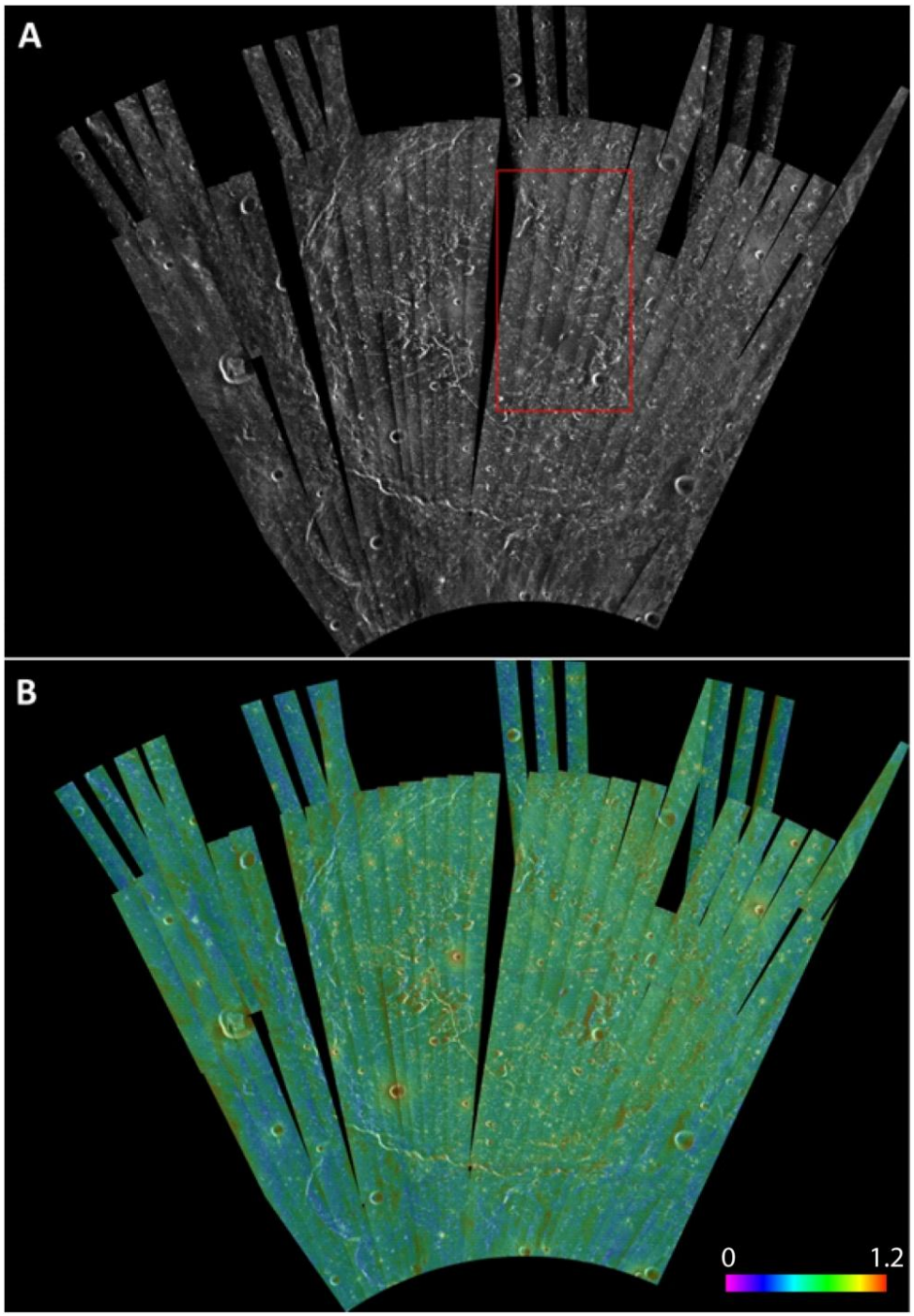

Figure 2.10: Mini-RF results of study area. (A) Total radar backscatter mosaic of Schrödinger crater in S–Band, from the mini–RF instrument aboard the Lunar Reconnaissance Orbiter. Red box outlines location of Fig. 11. (B) CPR mosaic of Schrödinger crater overlaid on a total radar backscatter mosaic. Here, the CPR has been scaled from 0 (purple) to 1.2 (red). [Image credit: ISRO/NASA/JHUAPL/LPI]

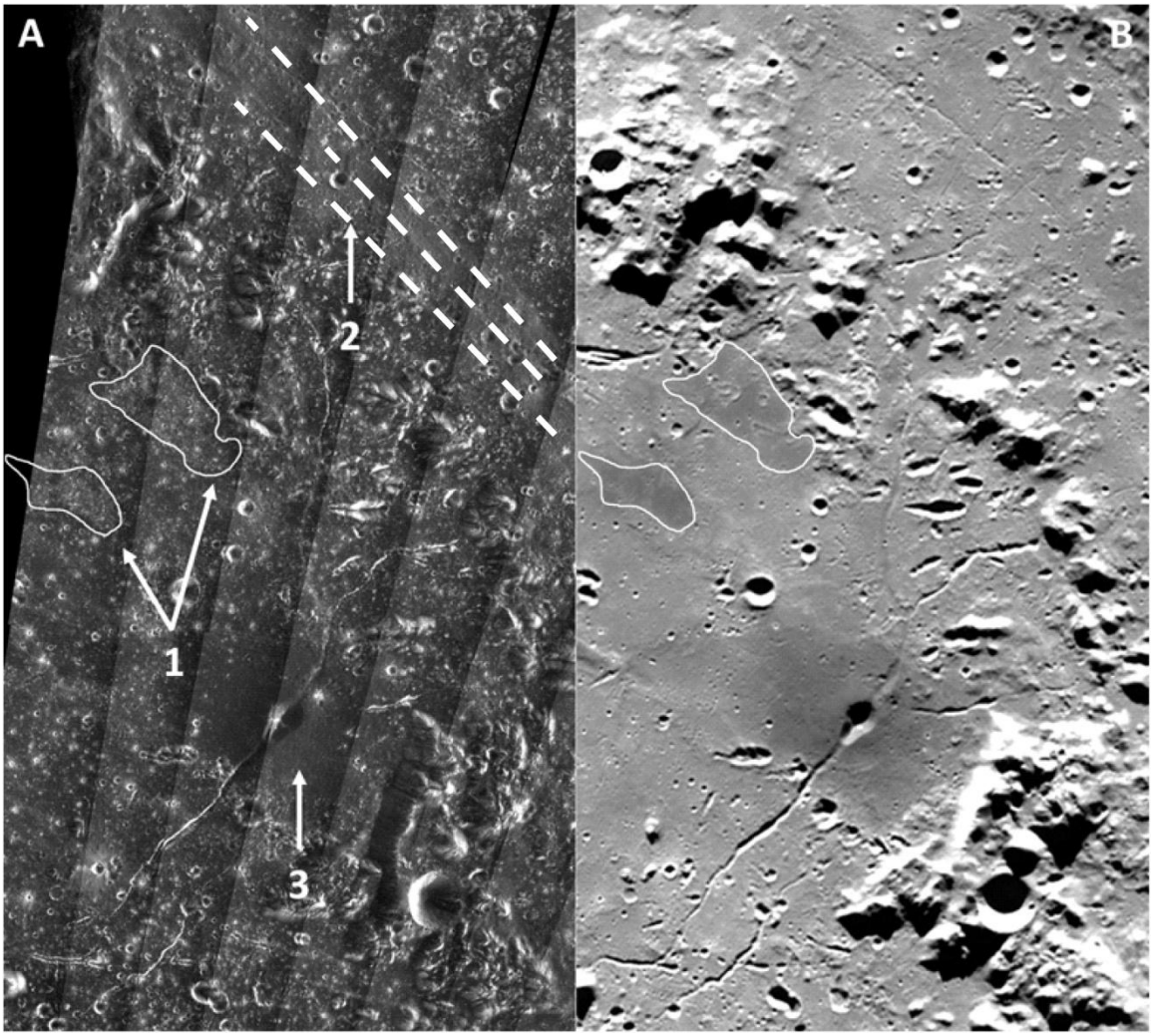

Figure 2.11: Mini-RF results of study area. A) Inset view of Fig. 2.10 showing radar properties of three sites, (1) radar bright mare patches, (2) radar bright crater ray, and (3) radar dark pyroclastic deposits. B) Clementine 750 nm band view of same area as in A).

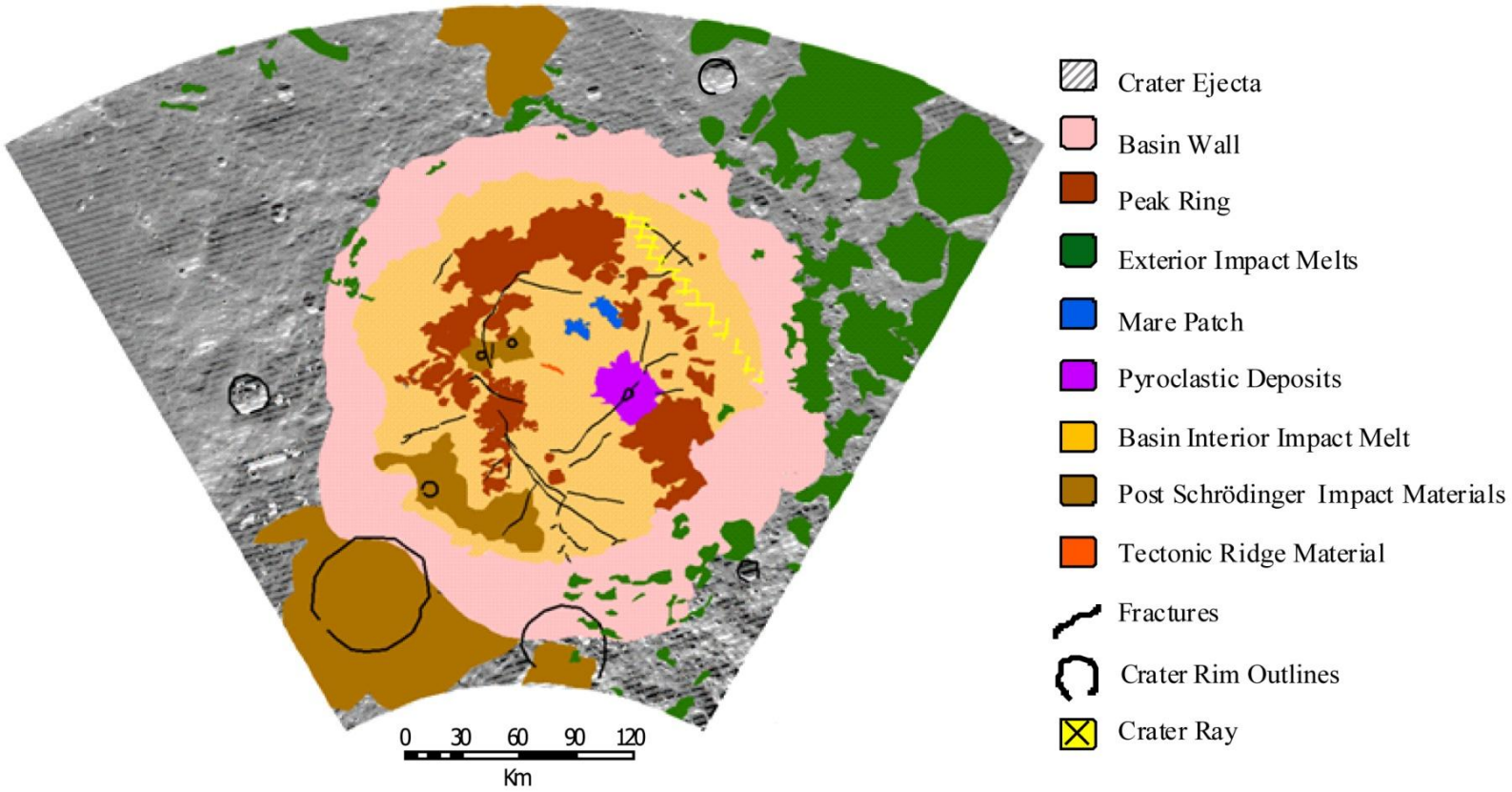

Figure 2.12: Compiled geologic map of the Schrödinger basin (building on work from Shoemaker et al. (1994), and Mest and vanArsdall (2008)) including the locations of exterior melt deposits.

2.3.2 Basin interior pyroclastic deposits, tectonic ridge, and mare patches

The pyroclastic deposits and mare patches are high in mafic content, as observed from various data products, including the false colour ratio and iron maps, Clementine-derived spectral profiles, and spectral unmixing fraction maps (Figs. 2.3, 2.5–2.8). Clementine spectral data indicates that the pyroclastic vent and deposits have a predominantly basaltic profile (Fig. 2.6A). Basalt spectra have distinctive absorption features near 1µm (indicating the presence of olivine) and absorption features near 2 µm (indicating the presence of pyroxene) (Pieters, 1978). Anorthosite spectra show increase in reflectance with increasing wavelengths, lack absorption features at 1 µm due to the absence of ferrous iron, and a weak absorption feature near1.3 µm (Pieters, 1986). Spectral profiles of the tectonic ridge unit are significantly different from mare and volcanic vent spectra. As is the case with many geological units sampled, it is difficult to accurately identify the composition of these units using the Clementine dataset, as the spectra are neither purely basalt nor anorthosite and are, therefore, termed ambiguous. M^3 spectra indicate there is pyroxene, within the small section of mare patch and within the pyroclastic deposits, however with the low reflectance values it is difficult to assess the composition more accurately (Fig. 2.9A). With M^3 data, the greater number of bands provides a more distinct spectral characteristic for both basalts and anorthosites.

2.3.3 Basin interior melt deposits

Previously, impact melt deposits beyond the peak ring have been mapped as “rough” and the innermost melts within the peak ring as being smooth (Shoemaker et al., 1994). However, from a spectral perspective, both the “rough” and “smooth” plains impact melt units show a similar spectral trend to each other (Figs. 2.6B, 2.9B). They are mostly basalt-like in character with sporadic spectra showing occurrences of anorthosite. Sampled M^3 spectra of the impact melt deposit indicate the strong presence of pyroxene (Fig. 2.9B) confirming our Clementine results (Fig. 2.6B). The absorption strengths of pyroxene at 1µm and 2µm vary in intensity suggesting variation in grain size, although

the degree of this is unknown. Mini-RF data indicates that there is a similar cm–scale roughness between the melt units (Figs. 2.10, 2.11).

2.3.4 Peak ring

From Clementine data, the peak ring unit appears to be predominantly anorthosite in composition, with few basalt profiles (Figs. 2.5, 2.7). M^3 spectra sampled along the peak ring suggest the minor presence of plagioclase with low-Ca pyroxene being more represented (Fig. 2.9C).

2.3.5 Terraces and basin wall

Several sites along the terraced basin walls were sampled for spectra using Clementine data. Clementine spectra along the basin wall suggest that the composition here consists mostly of anorthosite, with the occasional presence of basalt (Fig. 2.6C). A few craters sampled in the narrow M^3 data image strip that was available to us indicate a more pyroxene rich area than earlier inferred using Clementine data (Fig. 2.9D).

2.3.6 Exterior ejecta and impact melt deposits

Preliminary observations suggest that beyond the basin floor, impact melt deposits are also found along the basin walls and beyond the crater rim (Fig. 2.12). Using high resolution LROC data, the presence of melts is inferred from the smooth texture and low albedo characteristics (Fig. 2.13). Observations from previous publications indicate that the greatest degree of wall slumping of Schrödinger occurs on the eastern part of the basin (Hawke and Head, 1977; Shoemaker et al., 1994). This is consistent with the hypothesis that emplaced impact melt deposits can pool within topographic lows (Osinski et al., 2011). Most of the exterior impact melt deposits presently identified are located beyond the north-eastern parts of the Schrödinger rim.

High resolution LROC images of ejecta and exterior melt deposits highlight significant textural differences (Fig. 2.13). Much of the ejecta materials preserve a coarse, leathery texture, such as are seen in many places on the Moon (Schultz, 1972, Antonenko, 2012). The exterior melt regions, in contrast, are smooth and lack this leathery texture. Melts

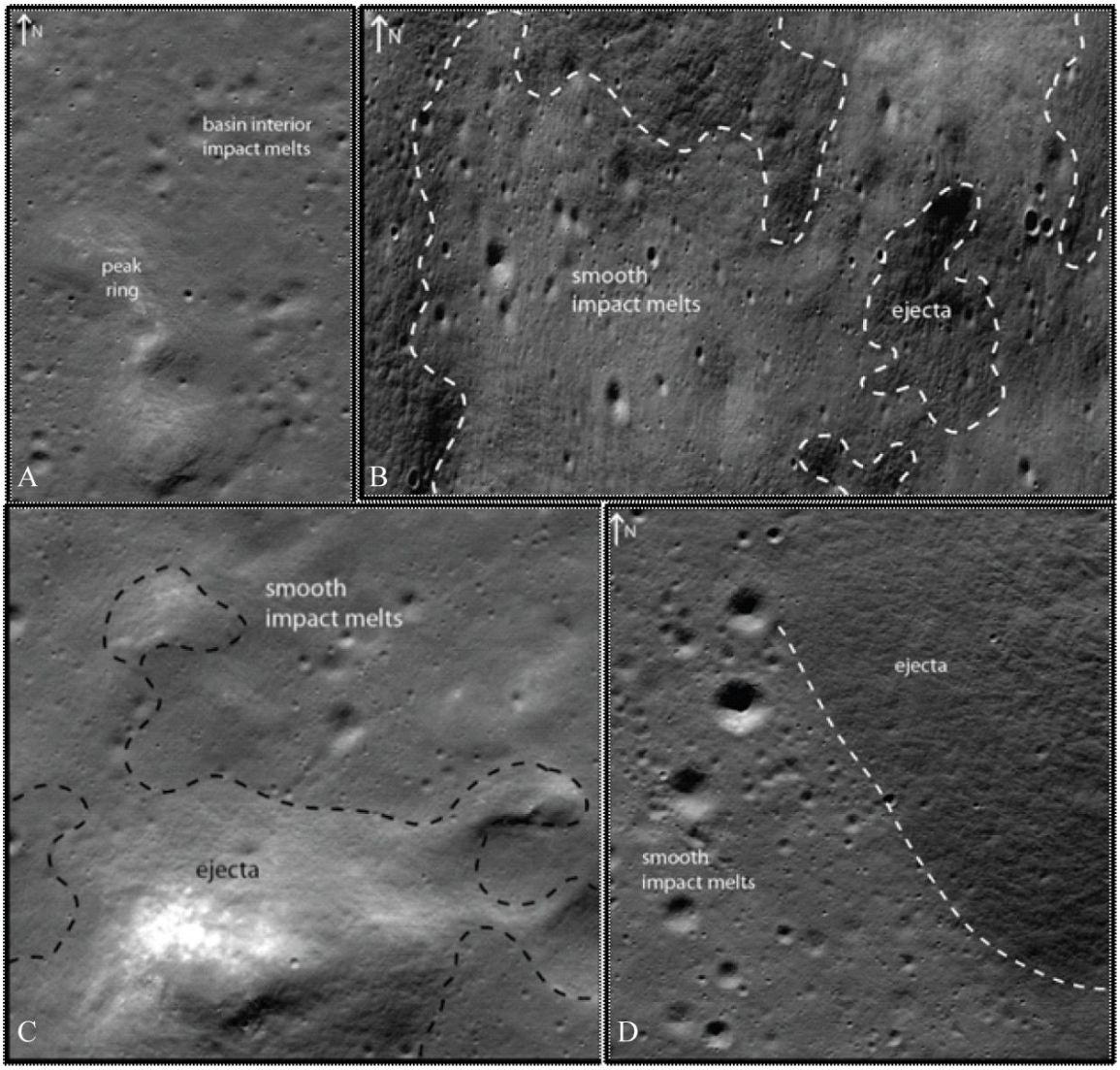

Figure 2.13: A) LROC images of inner basin melts and peak ring material that are similar in texture to the exterior deposits (product M141473253RC). B – D) LROC images of ejecta and melt deposit regions beyond Schrödinger crater rim (products M105860485LC; M141418958RC; M141473253RC).

also have a lower albedo than surrounding materials (which are interpreted to consist predominantly of Schrödinger ejecta). Sampled Clementine spectral profiles of the continuous ejecta blanket suggest the presence of both basalt and anorthosite (Fig. 2.6C). Sampled M^3 spectral profiles of basin ejecta, however, indicate a large distribution of mafic materials, particularly pyroxene (both low-Ca and high-Ca type) (Fig. 2.9E).

Exterior impact melt deposits show spectral variation in the Clementine data and suggests the presence of both basalt and anorthosite materials. The cluster of fresh basalt-rich spectra identified using the algorithm of Antonenko and Osinski (2011) suggests a stronger mafic signature beyond the basin rim along the north east section (Fig. 2.7). Both the compositions of the exterior melt deposits and basin floor melt deposits are assumed to be of the same melt material due to their spectral similarities. M^3 spectra suggest a similar spectral trend of the external melts to the ejecta material, namely an abundance of mafic minerals (exclusively pyroxene) (Figs. 2.9E, F).

2.3.7 Post-Schrödinger impact features and secondary craters

Post-Schrödinger event crater materials, both within and outside the basin rim, are well preserved with most of the associated impact materials being easily recognizable. These craters appear green to blue on the Clementine derived false colour ratio map (Fig. 2.3A) indicating a fresh surface, and the low FeO wt % (Fig. 2.3B) indicates the exposed materials to be a more feldspathic surface. From the LROC and M^3 data images, high spatial and spectral resolutions respectively allows more fresh smaller craters to be identified and spectrally sampled.

The distribution of fresh mafic material, determined using the algorithm of Antonenko and Osinski (2011), highlights ejecta deposits of a 10 km crater on the southwest part of the basin floor (Fig. 2.7), which has a strong basalt composition signature compared to the rest of the basin floor materials. This suggests that the subsurface material at that location is higher in mafic content unlike the rest of the Schrödinger basin. A possible explanation of this observation is that the Schrödinger forming impact event could be tapping into potential cryptomare areas in this section of Schrödinger's floor, or sampling

SPA impact melt materials. Using M^3 data other post–Schrödinger events spectrally sampled within the image extent show a mafic signature (e.g., along the basin peak ring, terraced surfaces, etc) where typically deeper materials are assumed to be excavated during the cratering process.

2.4 Discussion

We have provided the first detailed multispectral assessment of Schrödinger, a well-preserved peak-ring basin structure. This study focused on investigating the composition of previously mapped impactite units within and immediately surrounding the basin. The results from this study provide a foundation for determining the role of impact cratering in distributing target materials, particularly in the case of Schrödinger, but also at a wider scale in the South Pole-Aitken basin. Multispectral datasets of all scales greatly aid in piecing together the geological puzzle by combining image detail and spectral information.

2.4.1 Regional context

An interesting observation is the increased mafic content within the basin floor of Schrödinger and beyond the basin rim, as well as the lack of anorthosite with respect to the surrounding surficial target materials as evidenced by spectral profiles using M^3 data (Fig. 2.9). The simplest explanation for this is heterogeneities within the target, i.e. the pre-existing materials of the South Pole-Aitken basin.

New altimetry data (LOLA) from LRO provides improved resolution to characterize the topographic dichotomy that exists between the western and eastern half of Schrödinger (Fig. 2.14). The terrain west of Schrödinger is topographically higher than to the east. This is likely a pre-Schrödinger feature and related to the structure of the South Pole-Aitken basin rim.

It has been recognized that topography governs the movement of exterior impact melt deposits or “ponds” (e.g., Hawke and Head, 1977; Osinski et al., 2011). As such, impact materials such as exterior melt ponds may preferentially deposit into topographic lows,

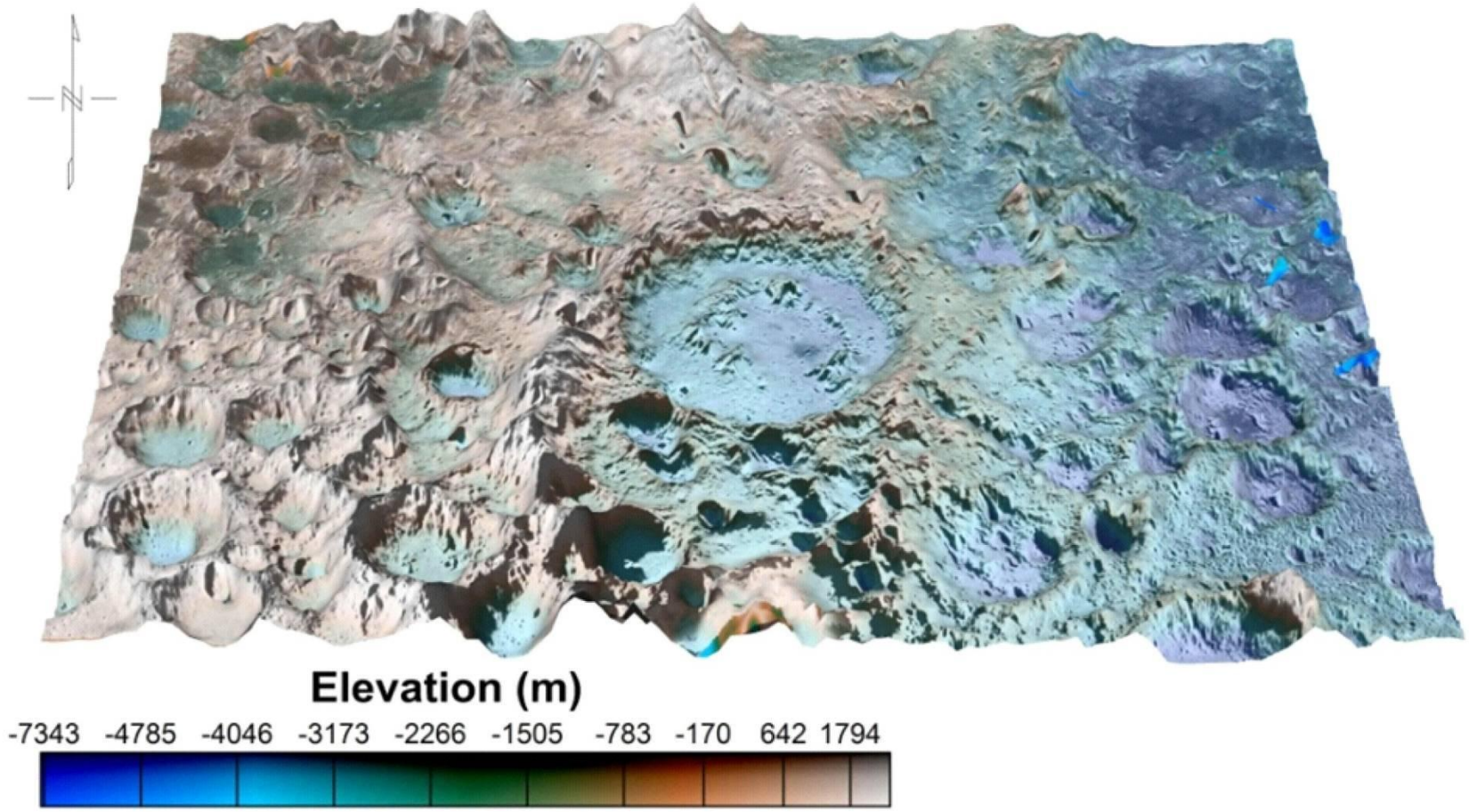

Figure 2.14: Digital Elevation Model of Schrödinger and surrounding region (with 7x vertical exaggeration, source: LOLA). Elevation decreases moving eastward and along the northern edges of the area.

with an extreme example being the large exterior melt pond in King Crater (Heather and Dunkin, 2003). With the regional dip in topography towards the north-east (Fig. 2.14), there is a high chance of impact melt exiting the basin in the eastern direction, and this study has identified and mapped large deposits of smooth materials interpreted as impact melt in the same area (Fig. 2.12). However, the possibility of an oblique impact resulting in the same observations cannot be ruled out. The high mafic concentrations (Figs. 2.7, 2.9) from the spectral analyses along the same northeast area could, therefore, indicate sampling of lower crust and/or mantle materials from the South Pole-Aitken event. This is consistent with a new impact ejecta emplacement model, which predicts that melt ponds should be derived from deeper lithologies than the underlying ballistic, continuous ejecta blanket (Osinski et al., 2011). An alternative explanation would be the presence of cryptomare material in this region.

2.4.2 Inner basin materials

The Clementine dataset provides an overall picture of the composition of Schrödinger materials. Both basaltic and highland materials exist; however, exact proportions of the two are not easily resolvable. With much of the surface being mature, both the continuum slope (415 nm/750 nm) and absorption depths in general are weakened at most of the sampled sites. At the latitude of Schrödinger, high phase angles require careful analysis of compositional information.

The lack of fresh craters uninfluenced by high phase angles makes it difficult to find reliable sites that meet our sampling criteria to sample spectra within this study area. With the currently available data, all impact material units on the basin floor show spectra that suggest compositions of both pyroxene and feldspar. Spectral profiles from M^3 data suggest that there may be a lot more pyroxene-rich materials present within the basin floor (cf., Kramer et al., 2011).

2.4.3 Mare patches and pyroclastic deposits

Most spectral profiles of these units capture the mafic absorption features well, however there is a certain degree of "spectral noise" leading to some of the interpretations being

ambiguous (Figs. 2.3B, 2.5, 2.6A). M^3 spectra sampled from the mare patch indicate the presence of pyroxene, however there is a high degree of noise.

The observation of the mare patches using radar (Mini-RF) is interesting because typically mare patches have relatively high iron and titanium content, which increases the radar loss tangent and inhibits volume scattering, and therefore should appear radar dark (Campbell et al., 1997). The relatively rough surface textures of mare patches (which exceed those of rough terrestrial lava flows at radar wavelengths) might be attributed to a relatively young surface rich in cm–sized rocks from small impacts.

2.4.4 Peak ring

The presence of both pyroxene and feldspar spectra from Clementine data, as seen in this study, within the peak ring is of great interest as it can potentially shed light into the peak ring formation process. Recent identification of olivine and pure anorthosite signatures within the peak ring using the Kaguya dataset (Yamamoto et al., 2010; Ohtake et al., 2010) provides some indication that the peak ring material may be derived from deep within the subsurface where the transient cavity reached its maximum expansion. However, the identification of mafic content along the peak ring (Figs. 2.6, 2.7, 2.8, 2.9) provides new insight into what the subsurface may be comprised of. From constant cratering activity since the formation of SPA, the pre-impact terrain of Schrödinger could possibly contain mafic rich materials (redistributing of mare materials, from other nearby crater events, or mafic content from within SPA itself).

2.4.5 Post-Schrödinger crater units

High concentrations of basalt spectra derived from the automated algorithm (Antonenko and Osinski, 2011) are located within post–Schrödinger craters on the southwest section of the basin floor and to the northeast beyond the basin rim (Fig. 2.7). These high concentrations suggests that the observed spectral features truly reflect compositional information, and are not sporadic clusters or artefacts linked to high phase angles or topography.

Making inferences on the compositions along these post-Schrödinger craters in many ways can give us insights into the pre-Schrödinger impact settings. An example of this is the distribution of fresh mafic material (determined using the algorithm of Antonenko and Osinski (2011)) within a small 10km crater on the basin floor (Fig. 2.7). The high cluster of fresh basalt spots suggest that the subsurface material at that location is high in mafic content unlike other regions of the basin floor that are filled with impact melt deposits. The crater is greatly separated from the pyroclastic deposit and mare regions of the floor, therefore making this an interesting observation. Recent preliminary analyses of the basin floor using M^3 data also picks up the largely mafic signature within post-Schrödinger-impact craters suggesting that there may be a greater depth of origin for the Schrödinger event impact materials (Kramer et al., 2011). However, this is also consistent with Schrödinger tapping and excavating large ponds of impact melt from SPA that may be mafic rich.

2.4.6 Spectral unmixing model results

The spectral distribution within Schrödinger (from un-mixing models) is difficult to assess using only two spectral endmembers (anorthosite and basalt) (Fig. 2.8). The flatness and lack of topography in the basalt fraction map (Fig. 2.8B) indicate that much of the interpretation is accurate and high areas of basalt content are not due to topographic factors. However, the inclusion of topography in the anorthosite endmember, or the inclusion of shadowed areas, maria, and pyroclastic deposit in the dark fraction endmember indicates that additional endmembers are required for more accurate assessment of the spectral distribution within Schrödinger basin. Incorporating other compositions found within the SPA basin as spectral endmembers, and using higher spectral resolution data sets (e.g. M^3) can lead to more accurate spectral distributions particular to Schrödinger (Pieters et al., 1997; Kramer et al., 2011).

2.4.7 Impact melt and ejecta deposits

In this study, we combine the previously identified textural rough and smooth units into one “inner melt” unit. This inner impact melt unit displays a common spectral trend (a heterogeneous mixture of both feldspar and pyroxene-like spectra), indicating that the

material is likely the same with only a textural difference (as expected from cratering models). Exterior melt deposits appear relatively radar smooth with the exception of overlying fresh craters with rough ejecta deposits.

For the continuous ejecta blanket beyond the basin rim, sampled Clementine spectral profiles suggests the presence of anorthosite (Fig. 2.6C). This is in agreement with the general location of Schrödinger within the farside lunar highlands. However, the low count of plagioclase feldspar–type spectral profiles from the M^3 image area, and the higher occurrence of pyroxene-type spectra are different from the Clementine results suggesting that high spectral resolution of M^3 data (85 spectral bands versus 5 spectral bands in Clementine) may be giving us more information of the material distributions.

Impact melt ponds located beyond the basin rim are concentrated on the northern and eastern parts of the study area and along the basin rim. As noted above, we suggest this may be due to the lower regional topography in this area. Previous observations found that exterior melt ponds occur within 0.70 radii of the Schrödinger rim, with most melt lying on the eastern side of the basin (Hawke and Head, 1977). These exterior melt deposits are interpreted to be Schrödinger melts that have been emplaced outside of the basin floor during the cratering process. Such deposits have been noted in numerous other smaller lunar impact craters (Hawke and Head, 1977; Osinski et al., 2011; Carter et al., 2012) and their emplacement accounted for in a new model for ejecta emplacement by Osinski et al. (2011). These impact melt regions are similar in texture to the basin interior impact melt regions (Fig. 2.13), however spectral sampling indicates there is a difference in the compositions at both of these locations. The inner basin melts show both highland and mafic signatures, but the exterior impact melt deposits show a strong mafic trend (Figs. 2.5–2.7).

Future mapping using recently-released high resolution datasets will allow us to better identify all Schrödinger-produced impact melt deposits beyond the basin interior, which will lead to a more accurate melt volume calculation and compositional assessment.

2.5 Summary and future work

The findings of this study suggest that the materials making up the Schrödinger impact basin are not homogeneous, containing some anorthosite but more mafic material than anticipated. Impact melt deposits extend beyond the basin floor, along terraced walls and are emplaced over basin ejecta. From a spectral perspective, all the interior impact melt materials are alike and therefore treated as one geologic unit. Sites of local concentrations of overly mafic-rich compositions along fresh craters on the basin floor, on the basin rim, and in the east section of basin ejecta are indicative of a more complex process involving regional surface interactions that needs further investigation.

We used the Clementine dataset as a preliminary guide and will focus on data sets with higher spectral and spatial resolutions (e.g., LRO, Chandrayaan-1, and Kaguya) in a future work to obtain more robust compositional information. With the release of further M^3 multispectral data, additional areas, both within the basin floor and outside the rim can be spectrally sampled and more can be learned about the target compositions (e.g. Kramer et al., 2011). High resolution imagery can allow us to better identify melt deposits at all scales, map the extent of deposits beyond the basin rim, and measure melt and ejecta distributions. Together, this will help us derive a better understanding of the Schrödinger basin, and, by extension, the South Pole-Aitken basin.

2.6 References

Antonenko, I. 1999. Cryptomafic Deposits on the Western Limb of the Moon: Areal Distribution and Volumetric Significance of Early Imbrian Volcanism as Determined from Dark – Haloed Impact Craters. Ph.D. thesis, Department of Geological Sciences, Brown University, Providence, R.I.

Antonenko, I., Osinski, G.R. 2011. Automated identification of basalt spectra in Clementine lunar data. *Planetary and Space Science*. **59**, 8: 715 – 721.

Antonenko, I. 2012. Leathery texture in the Bose, Bhabha, and Stoney Crater region of South Pole-Aitken basin on the Moon. 43rd Lunar and Planetary Science Conference. Abstract #2581.

Bhandari, N. 2004. Chandrayaan-1, Lunar polar orbiter. 35th COSPAR Scientific Assembly. pp. 2430.

Campbell, B.A., and Campbell, D.B. 2006. Regolith properties in the south polar region of the Moon from 70-cm radar polarimetry. *Icarus*. **180**, 1: 1–7.

Campbell, B.A., Hawke, B.R., and Thompson, T.W. 1997. Regolith composition and structure in the lunar maria: Results of long-wavelength radar studies. *Journal of Geophysical Research*. **102**, E8: 19307–19320.

Campbell, B.A., Carter, L.M., Campbell, D.B., Nolan, M., Chandler, J., Ghent, R.R., Hawke, B.R., Anderson, R.F., and Wells, K. 2010. Earth-based 12.6-cm wavelength radar mapping of the Moon: New views of impact melt distribution and mare physical properties. *Icarus*. **208**, 2: 565–573.

Carter, L.M., Campbell, B.A., Hawke, B.R., Campbell, D.B., and Nolan, M.C. 2009. Radar remote sensing of pyroclastic deposits in the southern Mare Serenitatis and Mare Vaporum regions of the Moon. *Journal of Geophysical Research*. **114**, E11004.

Carter, L.M., Neish, C.D., Bussey, D.B.J., Spudis, P.D., Patterson, G.W., Cahill, J.T., and Raney, R.K. 2012. Initial observations of lunar impact melts and ejecta flows with the Mini-RF radar. *Journal of Geophysical Research*. **117**, E00H09.

Chin, G., Brylow, S., Foote, M., Garvin, J., Kasper, J., Keller, J., Litvak, M., Mitrofanov, I., Paige, D., Raney, K., Robinson, M., Sanin, A., Smith, D., Spence, H., Spudis, P., Stern, S.A., and Zuber, M. 2007. Lunar Reconnaissance Orbiter Overview: The instrument suite and mission. *Space Science Reviews*. **129**, 4: 391–419.

Cintala, M.J., and Grieve, R.A. 1998. Scaling impact melting and crater dimensions: Implications for the lunar cratering record. *Meteoritics and Planetary Science*. **33**, 4: 889 – 912.

Cook, A.C., Spudis, P.D., Robinson, M.S., Watters, T.R., and Bussey, D.B.J. 1999. The topography of the lunar poles from digital stereo analysis. 30th Lunar and Planetary Science Conference. Abstract #1154.

Gaddis, L.R., Hawke, B.R., Robinson, M.S., and Coombs, C. 2000. Compositional analyses of small lunar pyroclastic deposits using Clementine multispectral data. *Journal of Geophysical Research*. **105**, E2: 4245 – 4262.

Gaddis, L.R., Staid, M.I., Tyburczy, J.A., Hawke, B.R., and Petro, N.E. 2003. Compositional analyses of lunar pyroclastic deposits. *Icarus*. **161**, 2: 262 – 280.

Green, R.O., Boardman, J., Pieters, C.M., Clark, R. and the M^3 Team. 2010. An algorithm for estimation and correction of the thermal emitted radiance with preservation of spectral structure in data measured by the Moon Mineralogy Mapper. 41st Lunar and Planetary Science Conference. Abstract #2331.

Goswami, J. N., Thyagarajan, K., and Annadurai, M. 2006. Chandrayaan-1: Indian Mission to Moon. 37th Lunar and Planetary Science Conference. Abstract #1704.

Hawke, B.R., and Head, J.W. 1977. Impact melt on lunar crater rims. Proceedings, Symposium on Planetary Cratering Mechanics. pp. 815–841.

Heather, D. J., and Dunkin, S. K. 2003. Geology and stratigraphy of King crater, lunar farside. *Icarus*. **163**, 2:307–329.

Housen, K.R., Wilkening, L.L., Chapman, C.R., and Greenberg, R. 1979. Asteroidal Regoliths. *Icarus*. **39**: 317–351.

Kramer, G.Y., Kring, D.A., Pieters, C.M., Head, J.W. III, Isaacson, P.J., Klima, R.L., McCord, T.B., Nettles, J.W., and Petro, N.E. 2011. Analysis of Schrödinger Basin Using Moon Mineralogy Mapper Spectra. 42nd Lunar and Planetary Science Conference. Abstract #1545.

Lucey, P.G., Taylor, G.J., Hawke, B.R., and Spudis, P.D. 1998. FeO and TiO_2 concentrations in the South Pole-Aitken basin – Implications for mantle composition and basin formation. *Journal of Geophysical Research*. **103**: 3701 – 3708.

Lucey, P.G., Blewett, D.T., Jolliff, B.L. 2000. Lunar iron and titanium abundance algorithms based on final processing of Clementine ultraviolet – visible images. *Journal of Geophysical Research*. **105**, E8: 20297 – 20306.

Lundeen, S., McLaughlin, S., Alanis, R. 2010. Moon Mineralogy Mapper: Data Product Software Interface Specification (Ver. 9.3). *http://img.pds.nasa.gov/documentation/M3_DPSIS.PDF*. 13p.

McCord, T.B., Clark, R.N., Hawke, B.R., McFadden, L.A., Owensby, P.D., and Pieters, C.M. 1981. Near-Infrared Spectral Reflectance: A First Good Look. *Journal of Geophysical Research*. **86**: 10883-10892.

Mest, S.C. 2011. The geology of Schrödinger basin: Insights from post – Lunar Orbiter data. In *Recent advances and current research issues in lunar stratigraphy*, edited by Ambrose, W.A., and Williams, D.A. Special Paper # 477. Boulder, Colorado: Geological Society of America. pp. 95–115.

Mest, S.C., and van Arsdall, L.E. 2008. Geologic Mapping of the Schrödinger Basin Area, Lunar South Pole. NLSI Lunar Science Conference, Abstract # 2089.

Morris, R.V. 1978. The surface exposure (maturity) of lunar soils: Some concepts and I_s/FeO compilation. Proceedings, 9th Lunar and Planetary Science Conference. pp. 2287–2297.

National Research Council. 2007. The Scientific Context for Exploration of the Moon. Washington, D.C: 107p.

Nozette, S., Rustan, P., Pleasance, L.P., Horan, D.M., Regeon, P., Shoemaker, E.M., Spudis, P.D., Acton, C.H., Baker, D.N., Blamont, J.E., Buratti, B.J., Corson, M.P., Davies, M.E., Duxbury, T.C., Elaison, E.M., Jakosky, B.M., Kordas, J.F., Lewis, I.T., Lichtenberg, C.L., Lucey, P.G., Malaret, E., Massie, M.A., Resnick, J.H., Rollins, C.J., Park, H.S., McEwen, A.S., Priest, R.E., Pieters, C.M., Riesse, R.A., Robinson, M.S., Simpson, R.A., Smith, D.E., Sorenson, T.C., Vorder Breugge, R.W., and Zuber, M.T. 1994. The Clementine Mission to the Moon: Scientific Overview. *Science*. **266**, 5192: 1835–1839.

Nozette, S., Spudis, P., Bussey, B., Jensen, R., Raney, K., Winters, H., Lichtenberg, C.L., Marinelli, W., Crusan, J., Gates, M., and Robinson, M. 2010. The Lunar Reconnaissance Orbiter Miniature Radio Frequency (Mini-RF) Technology Demonstration. *Space Science Reviews*. 150, 1–4: 285–302.

O'Sullivan, K.M., Kohout, T., Thaisen, K.G., and Kring, D.A., 2011. Calibrating several key lunar stratigraphic units representing 4 b.y. of lunar history within Schrödinger basin. In *Recent advances and current research issues in lunar stratigraphy*, edited by Ambrose, W.A., and Williams, D.A. Special Paper # 477. Boulder, Colorado: Geological Society of America. pp. 117–128.

Ohtake, M., Matsunaga, T., Takeda, H., Yokota, Y., Yamamoto, S., Morota, T., Ogawa, Y., Hiroi, T., Nakamura, R., and Haruyama, J. 2010. Distribution of Purest Anorthosite on the Entire Lunar Surface. 41nd Lunar and Planetary Science Conference. Abstract #1628.

Osinski, G.R., Tornabene, L.L., and Grieve, R.A.F. 2011. Impact melt and ejecta emplacement on terrestrial planets. *Earth and Planetary Science Letters*. **310**, 3: 167–181.

Pieters, C.M. 1978. Mare basalt types on the front side of the moon: A summary of spectral reflectance data. Proceedings, 9th Lunar Planetary Science Conference. pp. 2825–2849.

Pieters, C.M. 1986. Composition of the lunar highland crust from near-infrared spectroscopy. *Review of Geophysics*. **24**, 557–558.

Pieters, C.M., Staid, M.I., Fischer, E.M., Tompkins, S., and He, G. 1994. A sharper view of impact craters from Clementine data. *Science*. **266**: 1844 – 1848.

Pieters, C.M., Tompkins, S., Head, J.W., and Hess, P.C. 1997. Mineralogy of the mafic anomaly in the South Pole-Aitken Basin: Implications for excavation of the lunar mantle. *Geophysical Research Letters*. **24**, 15: 1903 – 1906.

Pieters, C.M., Gaddis, L., Jolliff, B., and Duke, M. 2001. Rock Types of South Pole - Aitken basin and extent of basaltic volcanism. *Journal of Geophysical Research*. **106**, E11: 28001 – 28022.

Robinson, M.S., Brylow, S.M., Tschimmel, M., Humm, D., Lawrence, S.J., Thomas, P.C., Denevi, B.W., Bowman-Cisneros, E., Zerr, J., Ravine, M.A., Caplinger, M.A., Ghaemi, F.T., Schaffner, J.A., Malin, M.C., Mahanti, P., Bartels, A., Anderson, J., Tran, T.N., Eliason, E.M., McEwen, A.S., Turtle, E., Jolliff, B.L., and Hiesinger, H. 2010. Lunar Reconnaissance Orbiter Camera (LROC) Instrument Overview. *Space Science Reviews*. **150**, 1–4: 81–124.

Schultz, P. H. 1972. A Preliminary Morphologic Study of the Lunar Surface. Ph.D. thesis, Dissertation Abstracts International. University of Texas at Austin, Volume 33-09. Section B, 4096.

Schultz, P.H. 1976. Floor fractured lunar craters. *The Moon*. **15**: 241 – 273.

Shepherd, P. 2005. SPUNMIX algorithm, PCI Geomatica 9. *Earth Observations Lab, Institute for Space and Terrestrial Science*, North York, Ontario, Canada.

Shoemaker, E.M., Robinson, M.S., and Eliason, E. M. 1994. The South Pole region of the Moon as seen by Clementine. *Science*. **266**, 5192: 1851–1854.

Shoemaker, E.M., and Robinson, M.S. 1995. Clementine observations of melt rocks and volcanic materials in the Schrödinger Basin. 26nd Lunar and Planetary Science Conference. Abstract #1297.

Smith, D.E., Zuber, M.T., Jackson, G.B., Cavanaugh, J.F., Neumann, G.A., Riris, H., Sun, X., Zellar, R.S., Coltharp, C., Connelly, J., Katz, R.B., Kleyner, I., Liiva, P., Matuszeski, A., Mazarico, E.M., McGarry, J.F., Novo-Gradac, A-M., Ott, M N., Peters, C., Ramos-Izquierdo, L.A., Ramsey, L., Rowlands, D.D., Schmidt, S., Scott, V.S., Shaw, G.B., Smith, J.C., Swinski, J-P., Torrence, M.H., Unger, G., Yu, A.W., Zagwodzki, T.W. 2010. The Lunar Orbiter Laser Altimeter Investigation on the Lunar Reconnaissance Orbiter Mission. *Space Science Reviews*. **150**, 1–4: 209–241.

Souchen, A.L., Flahaut, J., Sharma, P., Jilly, C.E., Blanchette – Guertin, J.-F., and Kring, D.A. 2011. Suggested Landing Sites To Study Key Planetary Processes On The Moon: The Case Of Schrödinger Basin. 42nd Lunar and Planetary Science Conference. Abstract # 1791.

Spudis, P.D. 1993. *The geology of multi-ring impact basins*. Cambridge: Cambridge University Press. 277 p.

Staid, M.I., and Pieters, C.M. 2000. Integrated Spectral Analysis of Mare Soils and Craters: Application to Eastern Nearside Basalts. *Icarus*. **145**: 122-139.

van Arsdall, L.E., and Mest, S.C. 2008. Geologic Mapping of the Schrödinger Basin Area, Lunar South Pole. 39th Lunar and Planetary Science Conference. Abstract #1706.

Wilhelms, D.E. 1987. *The geologic history of the Moon,* edited by Wilhelms, D.E., McCauley, J.F., and Trask, N.J. Professional Paper # 1348. Denver, CO: U. S. Geological Survey Printing Office. 302p.

Wilhelms, D.E., Howard, K.A., and Wilshire, H.G. 1979. *Geologic Map of South Side of the Moon*. Department of the interior United States geological survey. Map. I–1162. 1:5M scale.

Yamamoto, S., Nakamura, R., Matsunaga, T., Ogawa, Y., Ishihara, Y., Morota, T., Hirata, N., Ohtake, M., Hiroi, T., Yokota, Y., and Haruyama, J. 2012. Olivine-rich exposures in the South Pole-Aitken Basin. *Icarus*. **218**, 1: 331–344.

Zuber, M.T., Smith, D.E., Lemoine, F.G., and Neumann, G.A. 1994. The Shape and Internal Structure of the Moon from the Clementine Mission. *Science*. **266**, 5192: 1839–1843.

Chapter 3

3 Multispectral Analyses of Olcott Crater Using Current Lunar Datasets

Data from the Lunar Reconnaissance Orbiter (LRO) and Chandrayaan-1 missions provide an opportunity to study lunar impact craters at previously unavailable resolutions and wavelengths (e.g., Bhandari, 2004; Goswami et al., 2006; Chin et al., 2007; Robinson et al., 2010). Various datasets, including topography (Lunar Orbiter Laser Altimetry, LOLA), multispectral imagery (Clementine ultraviolet and visible-UVVIS-Camera; LRO Camera-LROC; Chandrayaan-1 Moon Mineralogy Mapper-M^3), and synthetic aperture radar (Mini-RF) can be used to characterize the composition and spatial extent of impact crater materials including impact ejecta and shocked materials. There is excellent evidence of impact melt features around fresh lunar craters (e.g., Bray et al., 2010; Dhingra et al., 2011; Carter et al., 2011; Osinski et al., 2011). High quality image data from instruments including the LRO Camera and Kaguya Terrain Camera, for example, show that distinct impact melt deposits including pond features, and draped melt veneers are easily recognizable (Fig. 3.1). Mini-RF data is also used to help identify sharp contrasts between smooth and rough melt deposits along crater rims (Fig. 3.1C; Carter et al., 2011).

While impact materials are easily identifiable within fresh and newly formed craters, it is often hard to determine the spatial extent of impact melt and ejecta deposits for craters that have been on the lunar surface longer. Such craters are exposed to space weathering for longer periods of time, resulting in regolith buildup, incorporation of impactite materials within the local terrain, and the redistribution of surfaces from later impact events. The fusion of various types of satellite datasets – including surface topography, reflectance spectroscopy, and radar – provides opportunities to decipher the geologic and emplacement histories of older craters. We provide the first such study of Olcott crater centred at 22^{o}N, 117^{o}E (Fig. 3.2), an 81 km diameter complex crater located on the lunar farside highlands (Wilhelms and El Baz, 1977). Olcott crater is Eratosthenian in age

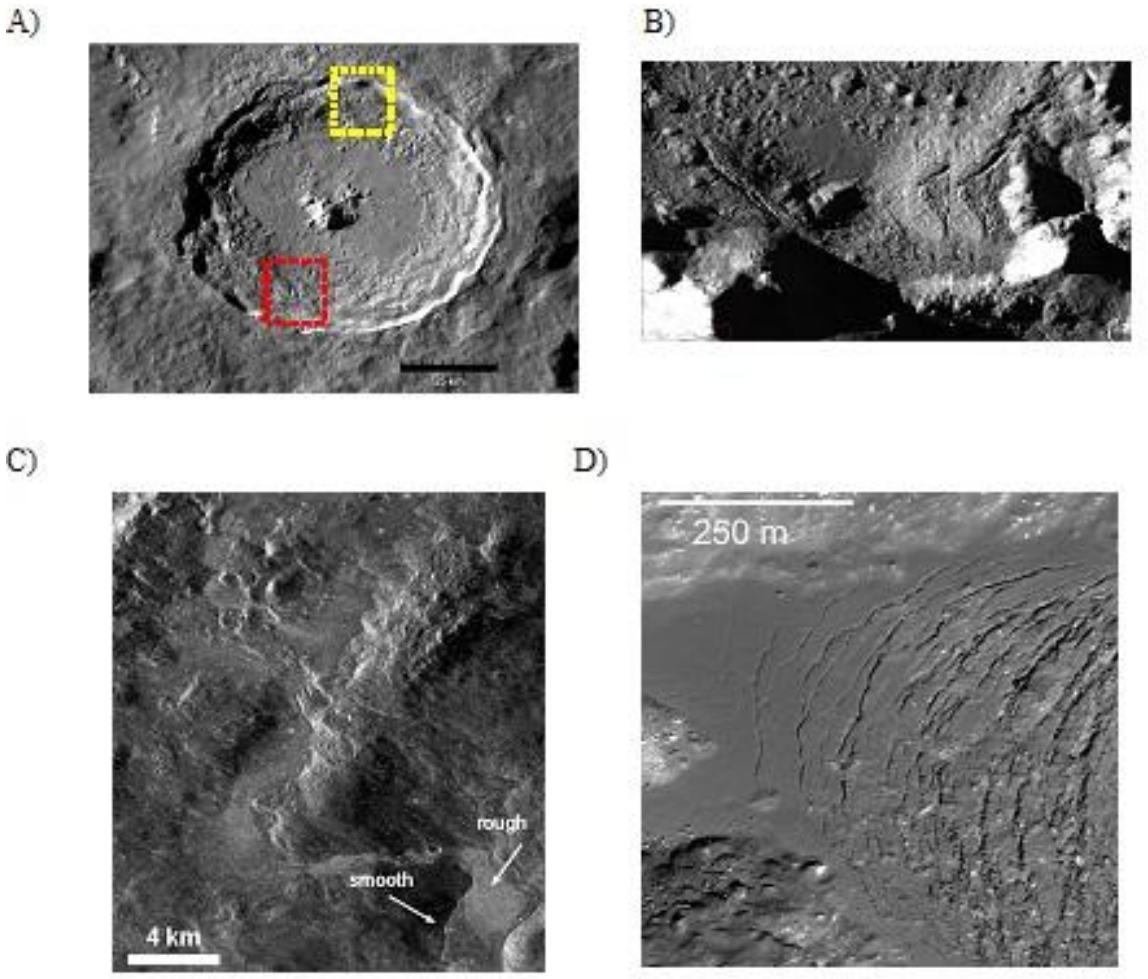

Figure 3.1: Morphological variations of lunar impact melt deposits. A) LRO WAC global mosaic context view of Tycho crater (85 km). Red and yellow boxes indicate locations of 3.1B and 3.1C respectively. B) Kaguya Terrain Camera image of impact melts along the crater floor within Tycho crater. Image credit: JAXA/SELENE. C) Mini-RF Image of Tycho crater shows the variations in texture roughness of impact melts. Image credit: Neish et al. (2011). D) LRO NAC image of the crater floor impact melt deposits within Moore F crater. [Image credit: NASA/GSFC/Arizona State University]

(Wilhelms and El Baz, 1977), with a distinct rim and a cluster of central mountains on the crater floor. However, the extent of impactite materials, including crater ejecta and impact melt deposits, is not discernible in visible view. At a regional scale, Olcott crater is located west of the much larger, older, and heavily degraded Lomonosov-Fleming (LF) basin (Fig. 3.2B). LF basin, centred on 19^{o}N/105^{o}E, has a main ring diameter of ~620 km and an average depth of ~2.4 km (Giguere et al., 2003). Estimated to be Pre-Nectarian in age, LF basin has been identified as a site of cryptomare and mare basalt deposits with variable TiO_2 content (Giguere et al., 2003).

The release of high-resolution multispectral data from the Lunar Reconnaissance Orbiter (LRO) and Chandrayaan-1 missions provides new opportunities to observe and assess both the spectral characteristics and morphology of Olcott crater in great detail. We present here results from the analyses and synthesis of Clementine, Chandrayaan-1 M^3, and LRO-Camera, and LRO-altimeter data. We use the results of this study to map and assess the distribution of impact materials, and determine how they may reflect the depths excavated by a crater of this size. Melt deposits (beyond the crater floor) are proposed to be a secondary phase of ejecta emplacement that occurs predominantly during the crater modification stage (Hawke and Head, 1977; Osinski et al., 2011). Therefore, locating and characterizing impact melt deposits relative to impact ejecta at Olcott crater can provide details on the emplacement mechanisms involved in impact cratering.

This paper seeks to 1) map the extent of impact material units, 2) characterize the compositions of mapped units in Olcott crater using the Chandrayaan-1 M^3 multispectral bandsets, and 3) use new image and altimetry data from the Lunar Reconnaissance Orbiter to identify the extent of all Olcott impact materials, including crater ejecta and external melt deposits that are not resolvable at Clementine scale resolutions.

3.1 Methods

We conducted the study within an area that extended two crater radii from the crater rim. Crater characterizations including crater diameter and depth calculations were conducted

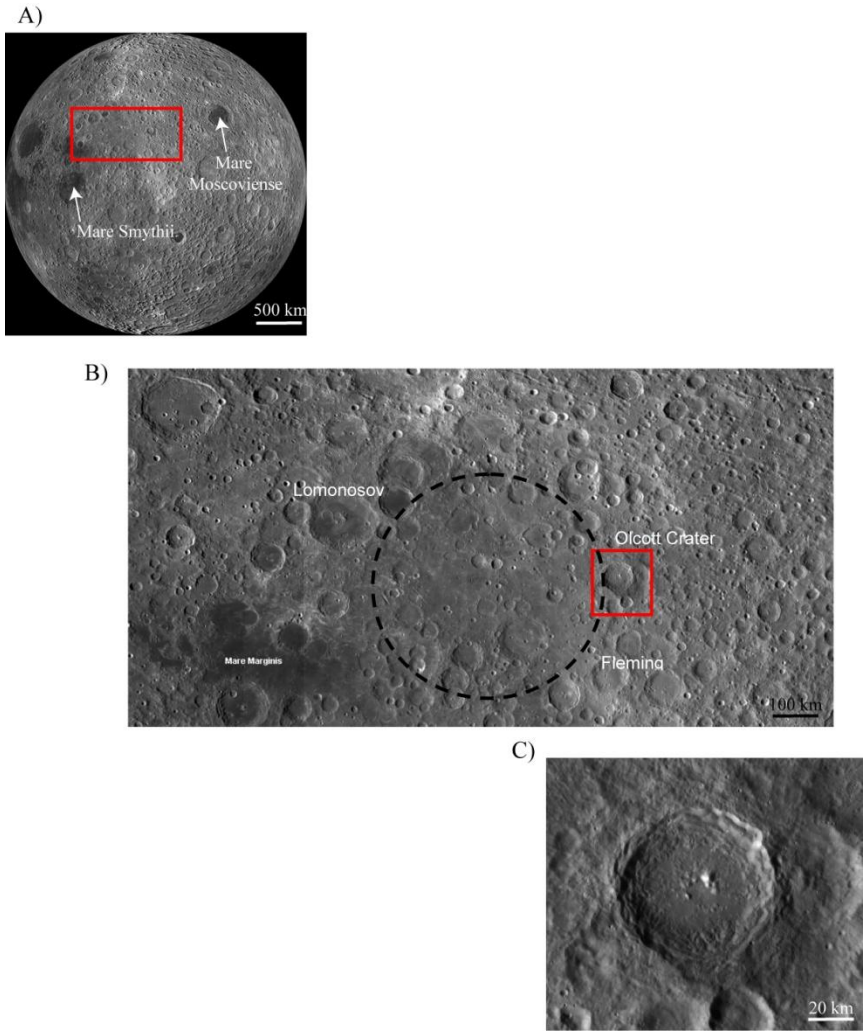

Figure 3.2: Context view of Olcott crater at various observable scales. Major mare areas are labeled for context. Image sources: NASA/GSFC/Arizona State University. A) Global context view of study region using the LRO WAC monochrome mosaic, centred at 120^{o}. Red box shows area coverage for 3.2B. B) Regional context view, using LRO WAC global mosaic, of the Lomonosov-Fleming Basin area. The main rim location of the degraded basin is outlined in black (modified from Hawke et al., 2003). LRO WAC global mosaic of Olcott crater, displaying the crater morphology. [Image credit: NASA/GSFC/Arizona State University]

using Gridded Data Record (GDR) altimeter data from the Lunar Orbiter Laser Altimeter (LOLA) instrument with 1024 pixels per degree resolution (Smith et al., 2010). The data was downloaded from the Lunar Orbital Data Explorer portal (ode.rsl.wustl.edu/moon**)**. The altimetry data were processed, calibrated, and map projected in simple cylindrical projection using mission specific scripts within the ISIS 3software.

The extent of various impact material units was mapped using coverage from the Lunar Reconnaissance Orbiter cameras; including the panchromatic Narrow Angle Camera (NAC) at 0.5 m/pixel resolution and monochrome 643 nm Wide Angle Camera (WAC) global mosaics at 100 m/pixel resolutions (Robinson et al., 2010; Speyerer et al., 2011). The goal of mapping was to determine the capability of identifying impact melt deposits at a first-order level, using the available high-resolution mapping. Producing a detailed geological map of Olcott crater was beyond the scope of the study. Impact melt deposits beyond the crater floor were identified using the following criteria: 1) deposits that are generally smooth, and have low albedo, 2) deposits that drape over wall terraces, crater ejecta, or on the crater rim, or 3) pooled deposits that are found within low lying areas along crater walls, on the outer rim, and in the surrounding areas outside the crater (Osinski et al., 2011). Locations of different melt deposits (including ponds, veneers, and flows) were identified using both the LRO WAC and NAC camera data. The integration of multiple spectral and spatial images for analyses was conducted using the JMars for Earth's Moon software (Christensen et al., 2009).

3.1.1 Multispectral Data Analyses

The multispectral aspect of the study was conducted using reflectance spectroscopy – using data from both the Clementine UV-VIS and Chandrayaan-1 Moon Mineralogy Mapper (M^3) datasets (Fig. 3.3). Clementine UV-VIS data (415, 750, 900, 950, 1000 nm) was utilized to determine the compositional information of the crater at a regional scale, including the maturity and iron content information of the surface (Pieters et al., 1994; Lucey et al., 2000). Hue, saturation, value composite maps were also generated to better visualize the distribution of compositional detail relative to topography (Fig. 3.3 A, B). In this particular application, hue and saturation parameters were obtained using the

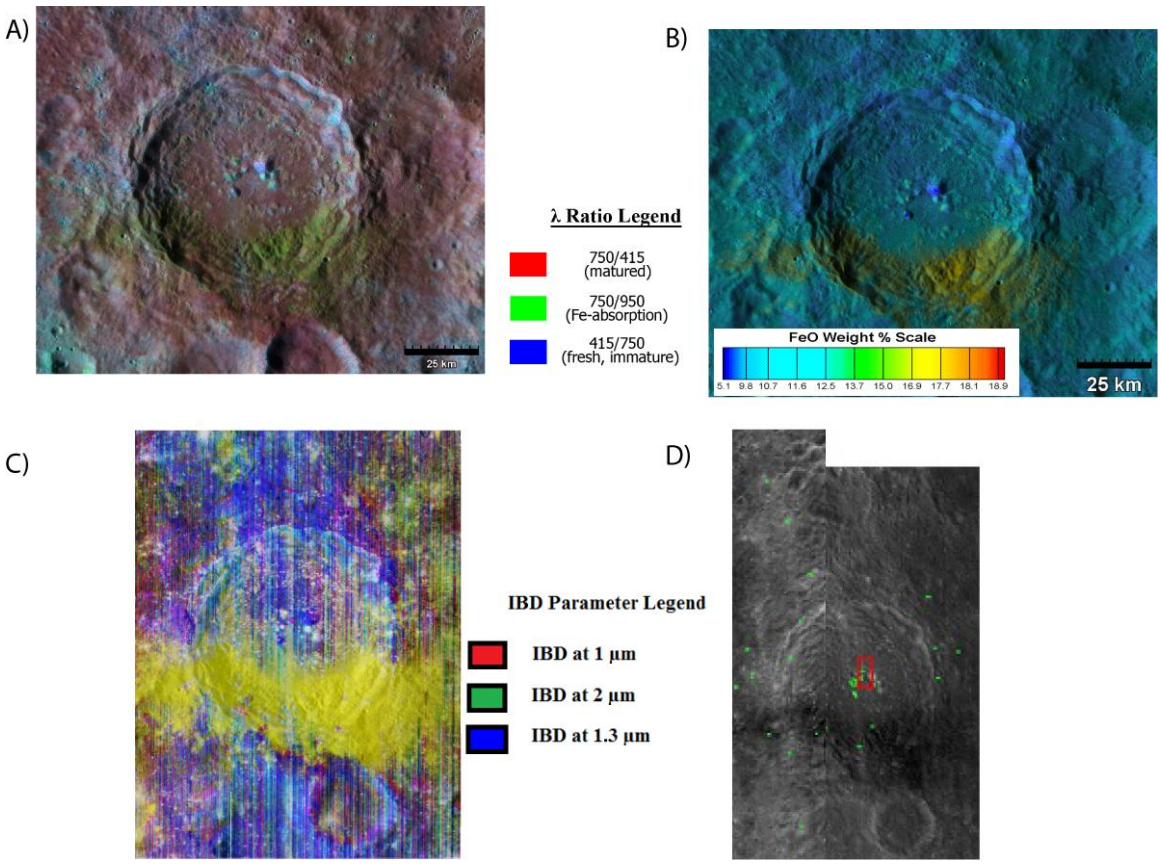

Figure 3.3: Composite maps of the study area created using various multispectral datasets overlaid on LROC WAC mosaics. The legends in Figs. 3.3A–C refer to the composite map parameters. A) Clementine false colour ratio over LROC WAC mosaic. Black boxes outline locations of high mafic content found in addition to the strong features in the southern section. B) Clementine iron content derived from Clementine data over LROC WAC mosaic. C) M^3 derived RGB spectral parameter map of the study area. The colour illustrates the occurrence of integrated band depths at 1, 2, and 1.3 µm respectively in various strengths. D) M^3 (1508nm) mosaic of Olcott crater highlighting locations where spectral profiles (green dots) were sampled. Red box refers to the context location of Fig. 3.8. [Image credit: ISRO/NASA/GSFC/Arizona State University]

Clementine composite maps; and the value parameter were obtained from LRO-WAC data. This allowed for an intuitive assessment of the spatial and spectral observations. Similarly, composite maps were generated combining the Chandrayaan-1 M^3 datasets and morphological characteristics for analyses.

The most common lithologies on the Moon are generally volcanic basalts and highland anorthositic rock types, and these rocks expected to be present within Olcott crater. Spectra of mafic minerals, such as pyroxene, have distinctive absorption features near 1 and 2 µm (Pieters, 1978). Mare basalts contain typically high-Ca pyroxenes, with absorption bands centred near 0.97 – 1 µm (Smrekar and Pieters, 1985). Highland rocks also contain pyroxenes, but typically these are low-Ca pyroxenes, with absorption bands centred near 0.9 – 0.93 µm (Smrekar and Pieters, 1985). Iron bearing plagioclase feldspar, a main component within the lunar highlands has absorption bands centred near 1.3 µm, however any content of pyroxene can mask the presence of feldspar bearing absorption bands (Crown and Pieters, 1985; Pieters, 1986). Analyses of the lunar surface using the high spectral resolution M^3 instrument on Chandrayaan-1 has led to the discovery of three new rock types, including an Mg-spinel bearing rock that has a strong absorption feature near 2 µm but has no detectable absorption near 1 µm (Pieters et al., 2011). These new rock types, located within the Moscoviense region of the lunar farside (Fig. 3.2A), are not visible in image data and are have only been observed through spectral analyses (Pieters et al., 2011).

Spectral profiles of mapped morphological units within Olcott were collected from two image strips of the 85-band Chandrayaan-1 M^3 data (Fig. 3.3D). M^3 data covers the UV-VIS-NIR (446–3000 nm) spectrum, a spectral range greater than the Clementine UV-VIS dataset and with improved spectral resolution (20 – 40 nm). This allows a more accurate evaluation of compositional information, and a more distinct spectral characteristic for both basalts and anorthosites. Due to the lack of readily available calibrated, processed and georeferenced data, the M^3 composite maps were manually processed and calibrated (more information on the data products can be found in Appendix C). Level1b M^3files (pixel-located, resampled, and calibrated data presented in radiance units) were downloaded from the Lunar Orbital Data Explorer portal (ode.rsl.wustl.edu/moon**)**, and

the radiance values converted to reflectance using techniques outlined by Green et al. (2010).

M^3 data was used to generate an RGB spectral parameter composite map (Fig. 3.3C) comparing the integrated band depth (IBD) values at 1µm, 1.3 µm, and 2µm to assess the presence of minerals typical of lunar rocks. The IBD values were calculated using algorithms defined by Mustard et al. (2011) and Donaldson Hanna et al. (2012). The colours in the map (Fig. 3.3C) indicate the various strengths of the spectral parameters. Typically, red colour indicates that the 1 µm pyroxene absorption feature is strong; green colour indicates that the 2 µm Mg-spinel absorption feature is strong; and the blue colour indicates that the 1.3 µm plagioclase feldspar feature is strong. Any other colour present indicates the combination of these three basic parameters with variable strengths. For example, yellow colour would indicate a mixture of red and green parameters; i.e. the presence of both the 1 and 2 µm absorption features – characteristic of the spectral signature of pyroxene. White colour indicates the presence of all parameters with equal strength. The IBD strength spectral parameter map (Fig. 3.3C) was used to assess the distribution of these spectral parameters at a first order crater-wide scale and also determine sampling spots for capturing individual spectral profiles representative of the various colours identified in the spectral parameter map (Fig. 3.3D). Sampling was conducted on freshly exposed surfaces using 3x3 and 5x5 pixel window sizes of individual M^3 data products.

3.2 Results

From a morphological perspective, Olcott crater materials can be classified into four major morphologically distinguishable units – 1) hummocky crater ejecta, 2) terraced walls, 3) central uplift, and 4) low albedo crater floor deposits. A simplified geological map (Fig. 3.4) of the identified units provides a visual assessment of the extent of impact materials related to Olcott crater.

The location of Olcott within the lunar highlands on the farside may suggest, at first, that much of the terrain is predominantly feldspathic. However, composite data maps indicate more diversity. The Clementine colour ratio composite image indicates that much of the

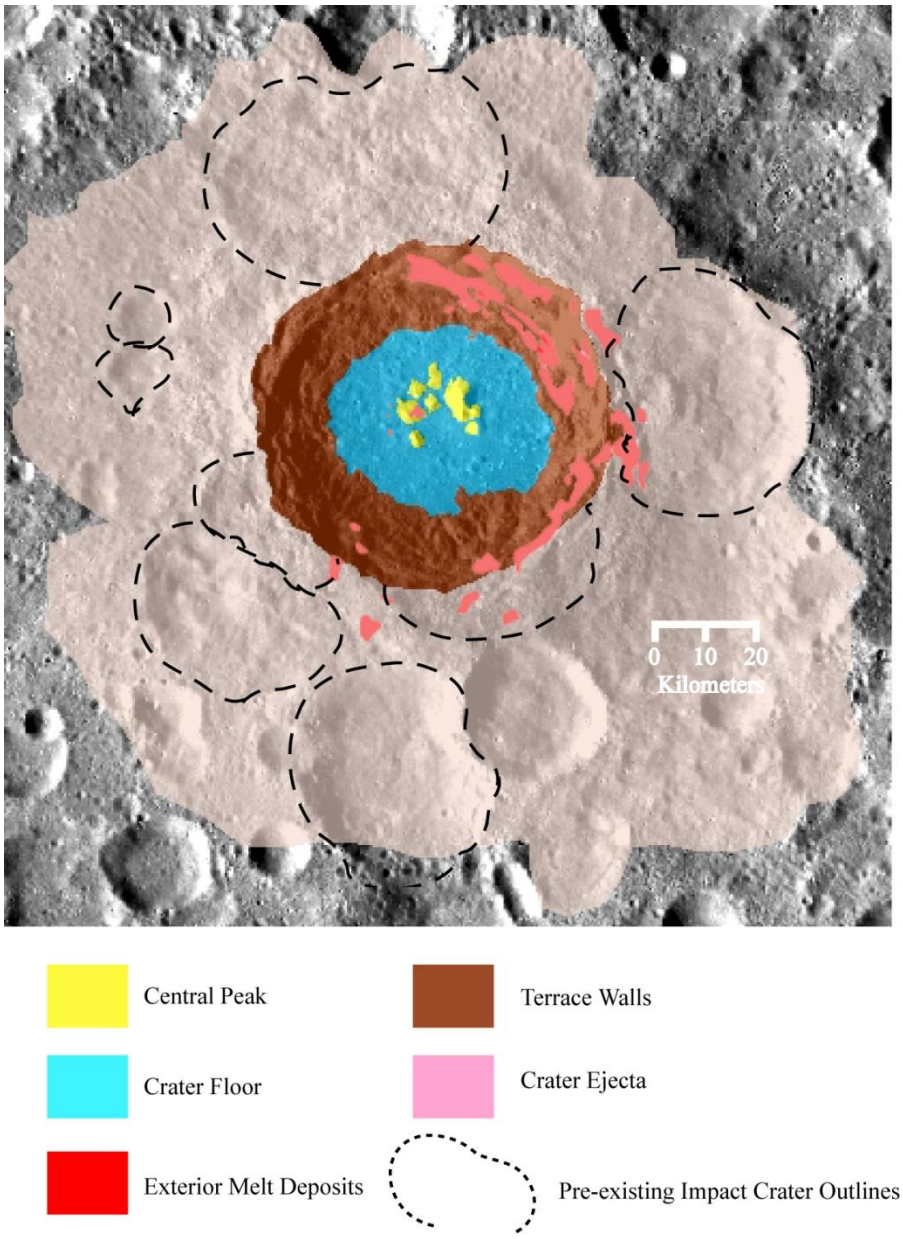

Figure 3.4: Geological sketch map of Olcott crater. [Image credit for basemap: NASA/GSFC/Arizona State University]

region in the image is mature material (Fig. 3.3A). Mature surfaces indicate that soils (top millimeter depth) have been exposed to space weathering on the surface for long periods bombardment (Morris et al., 1978). The yellow green colour along the southern wall of time, and likely have a high content of agglutinates caused by micro-meteorite terraces indicates the presence of mature mafic-rich content. The iron map (Fig. 3.3B) shows a high abundance of iron content along the southern half of the crater, identical in extent to the false colour composite map (Fig. 3.3A). In contrast, crater materials along the northern half are low in iron content. The M^3 derived IBD spectral parameter map (Fig. 3.3C) indicates a diverse distribution of materials. This includes very strong pyroxene abundance along the south crater walls (yellow colour), identical in extent to the observations made using the Clementine data. In general, the colours present in the parameter map (Fig. 3.3C) indicate the occurrence of absorption at all three parameters (1 µm, 1.3 µm, and 2 µm). There is a sharp contrast in the distribution of pyroxene within the crater, the north section of the crater is void of much pyroxene distribution (Fig. 3.3C).

Spectral profiles of the morphological units within Olcott suggest that the materials are rich in both types of pyroxenes and plagioclase feldspar (Fig. 3.5). The presence of ilmenite and water/hydroxyl is inferred by the observation of strong absorption features near 0.6 µm and 3 µm respectively (Tompkins and Pieters, 2010; Pieters et al, 2009). In the following sections, we examine the different morphological units in detail.

Crater Rim and Ejecta:

Olcott crater has a well-defined outer rim, easily recognizable from the global mosaic (Fig. 3.2B). The basin depth, measured from the highest rim height to the lowest part of the floor using the altimetry data (LRO-LOLA) indicates a crater depth of 4 km (Fig. 3.6). Beyond the rim, crater ejecta extend 1 to 1.5 crater radii into the surrounding terrain. The crater ejecta is comprised of rough hummocky materials with boulders. Crater ejecta materials along the eastern and southern sections around the rim superimpose nearby older craters (Fig. 3.4).

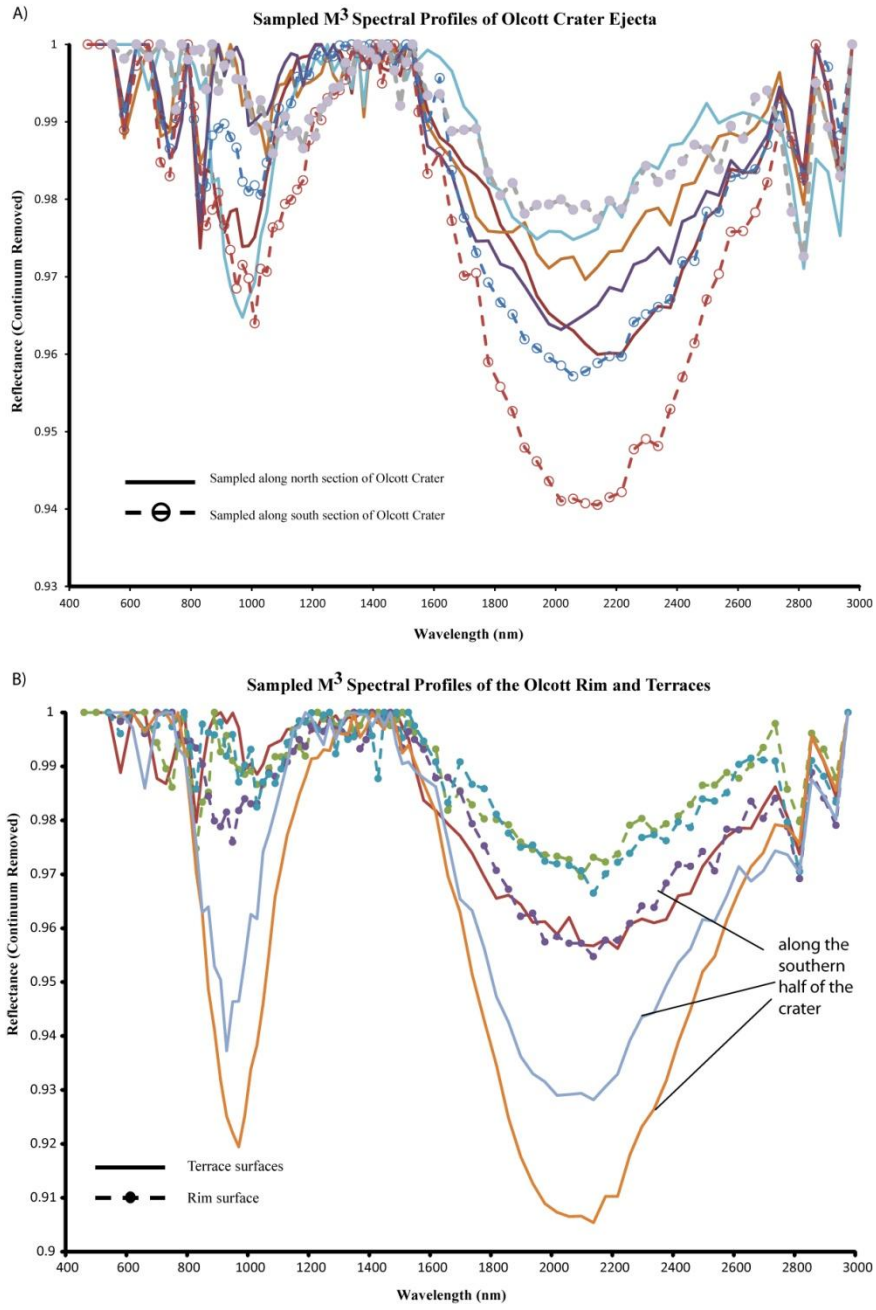

Figure 3.5: Chandrayaan-1 Moon Mineralogy Mapper (M^3) derived spectral profiles of morphological units identified for Olcott crater. A) Spectral profiles of the crater ejecta indicate the presence of plagioclase feldspar, and low-Ca pyroxene within the northern ejecta deposits; and high-Ca pyroxene within the southern ejecta deposits. B) Spectral profiles of the rim and terraces of Olcott indicate the presence of plagioclase feldspar, low-Ca, and a strong signature of high-Ca pyroxene along the southern area of the crater.

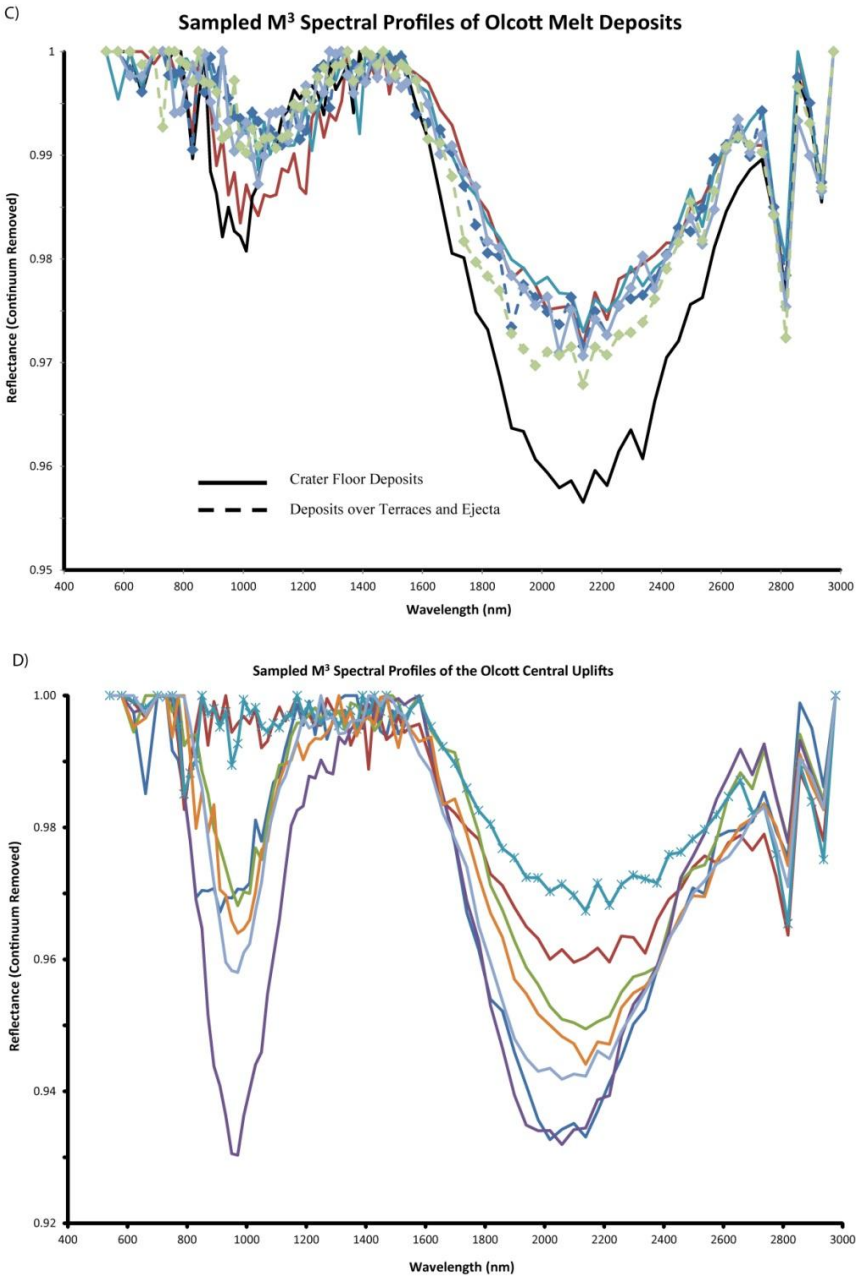

Figure 3.5 (cont'd): Chandrayaan-1 Moon Mineralogy Mapper (M^3) derived spectral profiles of morphological units identified for Olcott crater. C) Spectral profiles of the melt deposits within and beyond the crater floor indicate the presence of high-Ca pyroxene. Weak absorption features indicating plagioclase feldspar are detected within the crater floor deposits. D) Spectral profiles of the central uplifts within the crater indicate the presence of high-Ca pyroxene and plagioclase feldspar. This indicates a varied morphology within the central uplifts.

Compositional information indicates that the ejecta and rim are comprised of both mafic rich and mafic poor minerals (Fig. 3.5A, B). Along the northern half of the crater, the ejecta typically contain mature material (Fig. 3.3A). Spectral profiles along the north section of the crater (Fig. 3.5A, B) indicate the presence of low-Ca pyroxene (absorption bands centred near 0.90 μm and Fe bearing plagioclase feldspar (weak absorption bands near 1.3 μm). The south section of Olcott crater is also a matured surface, but is rich in iron-rich mafic materials (Fig. 3.3A, B). Many sampled sites of crater ejecta along the southern wall and floor indicate the presence of high-Ca pyroxene with absorption features between 0.97 and 1 μm (Fig. 3.5A, B). Spectral profiles taken around the crater rim indicates the presence of both low-Ca pyroxene and high-Ca pyroxene (Fig. 3.5B).

Crater Walls and Terraces:

The crater walls along Olcott are well defined. Elevation information is derived using LRO-LOLA data indicate that along the NW-SE profile (Fig. 3.6A), the wall slope is greatest along the northwest wall. The slope along the south-facing wall is more gradual near the rim – i.e. terrace floors are easily distinguishable in cross section (Fig. 3.6A). Along the W-E profile (Fig. 3.6B), the eastern crater wall is lower by ~200 m than the west wall. LRO Camera images indicate materials along the terraces have variable textures including blocky boulders and smooth deposits.

The Clementine-derived false colour ratio composite and iron distribution maps indicate the southern crater walls to be dominated with stronger mafic signatures than the rest of the crater area (Fig. 3.3A, B). Similar observations are made with both the spectral parameter map (Fig. 3.3C) and spectral profiling of the area using M^3 data (Fig. 3.5B). Absorption bands are centred near 0.9 μm and 1 μm indicating the presence of both low-Ca and high-Ca pyroxenes (Fig. 3.5B). There is a little plagioclase feldspar (band centred near 1.3 μm) that is visible, however, the crater walls are dominated with pyroxene signatures in the south therefore it is hard to assess the complete extent of plagioclase feldspar (Fig. 3.5B).

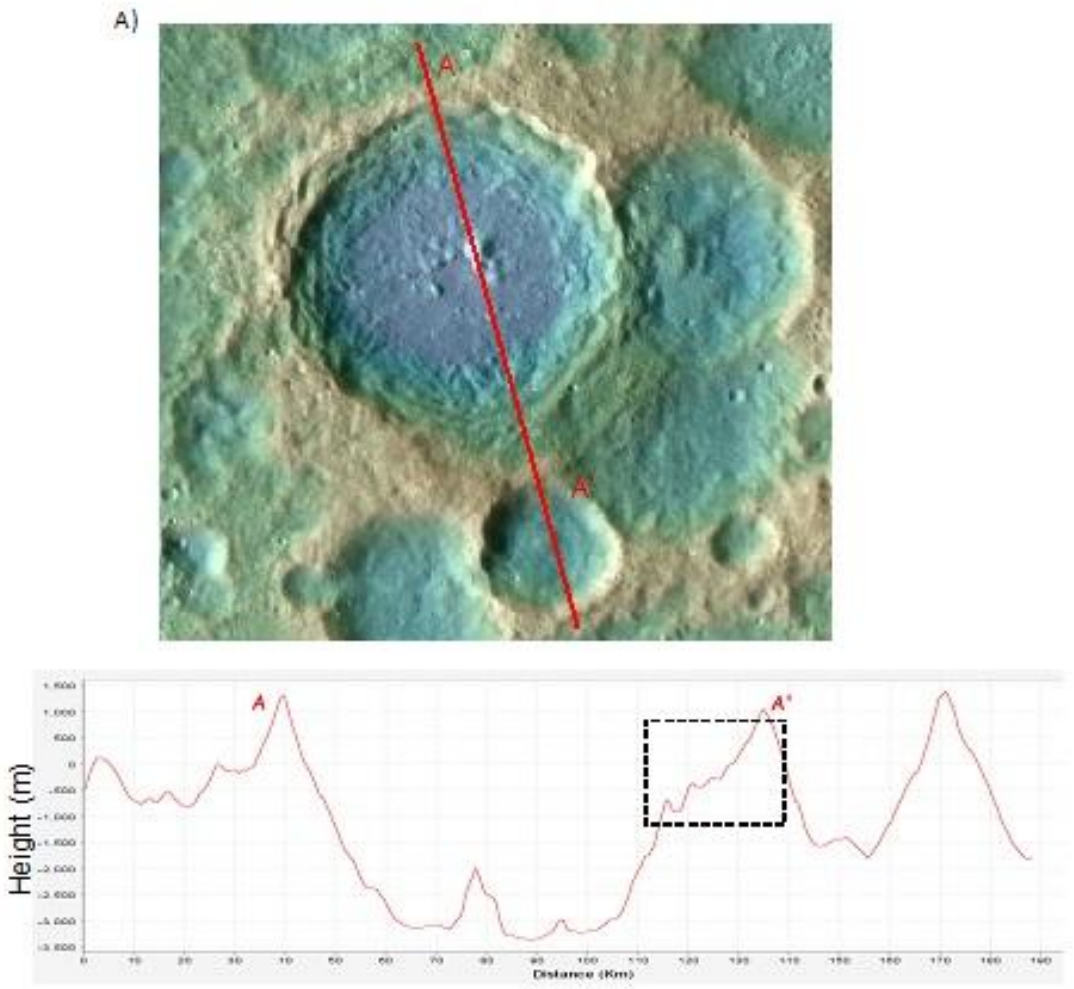

Figure 3.6A: Topography detail of Olcott crater along the NW-SE direction. (Top) LRO LOLA shaded relief map with context view of the profiled area. The topographic expressions of many pre-existing craters are recognizable in this dataset. (Bottom) LRO-LOLA derived topographic profile. The crater walls along the SE part near the crater rim (black box) have greater slumping closer to the rim, different from the NW crater wall. This may be due to the presence of a pre-existing feature that was obliterated during the Olcott forming crater event. [Image credit: MIT/NASA]

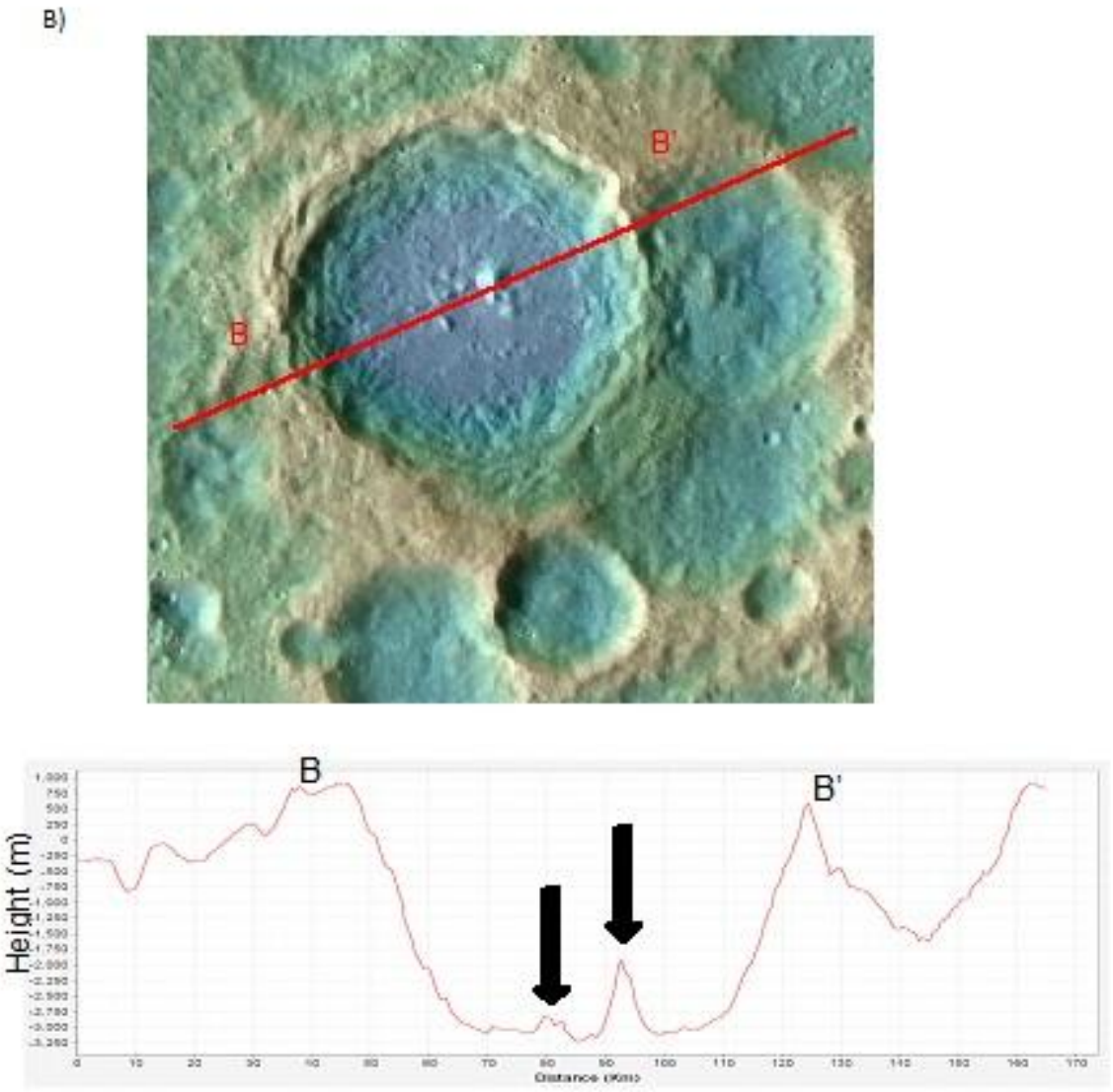

Figure 3.6B: Topography detail of Olcott crater along the W-E direction. (Top) LRO LOLA shaded relief map with context view of the profiled area. (Bottom) The central uplifts on the crater floor range in height from ~200 m to 1 km (black arrows). [Image credit: MIT/NASA]

Crater Floor, Melt deposits, and Central Uplift:

Impact melt deposits have been identified throughout the crater surface (Fig. 3.7) including the crater floor, and as deposits over terraces and crater ejecta (Fig. 3.7A). Details on the morphological characteristics, spectral signatures, and extent are described in this section. The crater floor fill is a dark toned, smooth region with occasional hummocky materials and in general is interpreted as impact melt-rich deposits (Fig. 3.7B). From a spectral perspective, the crater floor is greatly matured, particularly within the northern parts (Fig. 3.3A) and has variable iron content (Fig. 3.3B). Spectral profiles indicate that much of the crater floor is predominantly high-Ca pyroxenes with band centres near 0.98 µm. Weak absorptions near 1.3 µm (plagioclase feldspar) are also observed. Interestingly, the M^3 IBD spectral parameter map (Fig. 3.3C) shows a wider spatial distribution of pyroxene rich materials along the southern crater floor than regional composite maps from Clementine data indicate (Fig. 3.3A, B). However, this needs further verification due to the current unavailability of georeferenced M^3 datasets for a more accurate spatial analysis of the pyroxene rich distribution.

Beyond the crater floor, several deposits of dark toned, smooth materials are identified along the terrace walls and beyond the crater ejecta (Fig. 3.7A). These deposits occur predominantly as thin veneers draped over terrace floors (Fig. 3.7D–G), but can also occur as pooled deposits. Spectral profiles indicate that absorption features have band centres near 0.97 – 1 µm with variable absorption depths suggesting the presence of high-Ca pyroxenes (Fig. 3.5C). Absorption features near 1.3 µm are rare in occurrence. These exterior deposits are assumed to be of impact melt origin due to their similarity in spectral characteristics with crater fill deposits particularly with the common occurrence of high-Ca pyroxene (Fig. 3.5B, C).

The crater uplift is comprised of a partial ring of hills protruding through the crater floor deposits (Fig. 3.2B, 3.4). LRO-LOLA derived altimetry data indicate that the hills have heights that vary between 200 and 1000 m above the crater floor (Fig. 3.6). The surfaces of many of the hills consist of blocky rocks and boulders, high in albedo (Fig. 3.7B, C). The surfaces of the central hills are also rugged and display a rough “elephant-skin”

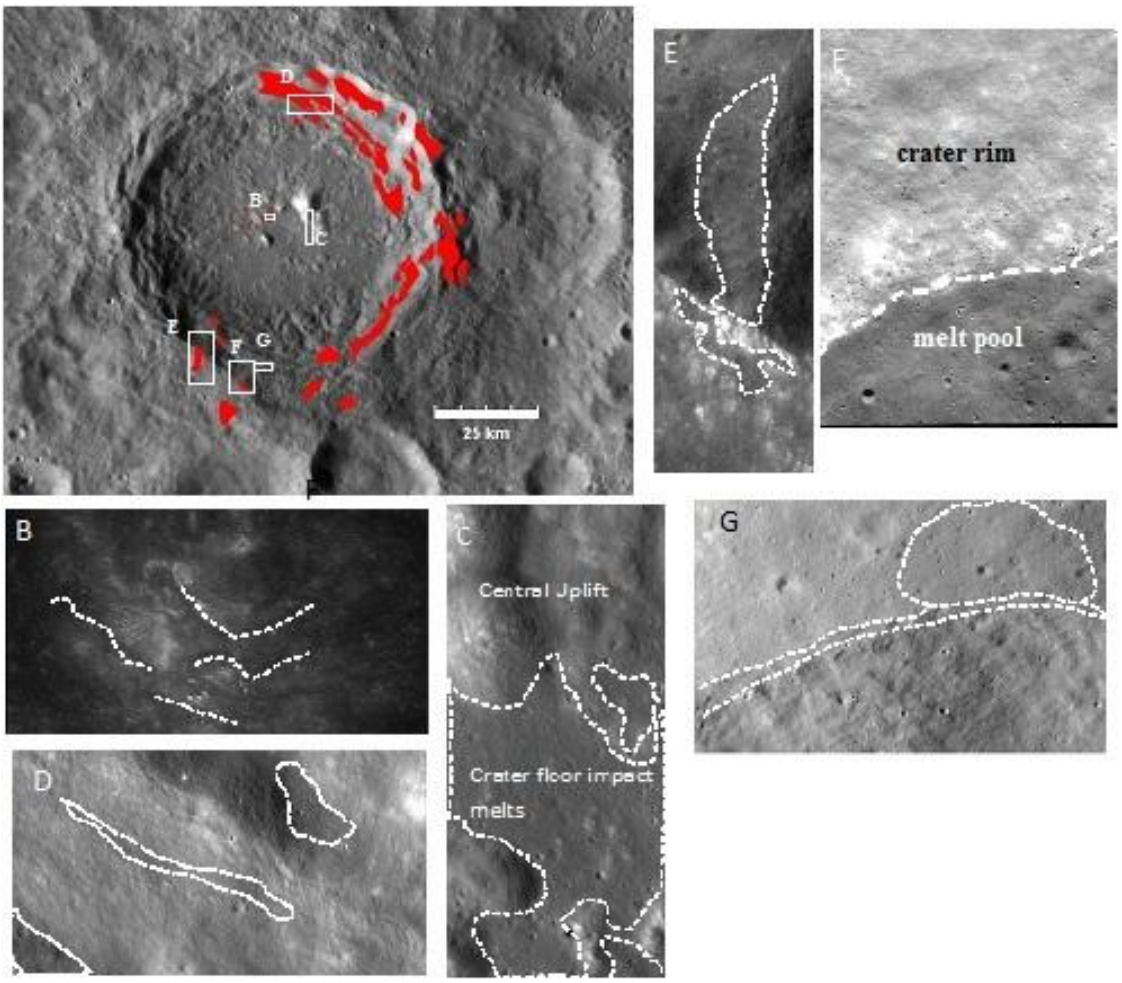

Figure 3.7: A) Context view of Olcott crater highlighting areas where occurrences of impact melts are mapped (red polygons). Marked boxes are context views for close-ups of melt deposits in Fig. 3.7B–G. The image widths for 3.7B–G are 2.5 km. B) Impact melt deposits atop central uplifts are long and narrow, and appear superposed and embayed. LRO Camera NAC image M108460950LC. C) Impact melt deposits on the crater floor are smooth and have low albedo when compared to the central uplift materials which appear rugged. LRO Camera NAC image M103739096RC. D)–G) Impact melts along the crater walls and terrace zones appear as thin veneers. LRO Camera NAC images M103739096RC; M159189508LC; M115543039RC; M161544383RC. [Image credit: NASA/GSFC/Arizona State University]

texture. Smooth dark toned deposits are draped over peaks, indicating they are superposed, and are most likely impact melt deposits (Fig. 3.7B). The Clementine derived composite maps indicate that the uplifted hills display varying levels of maturity and iron content (Fig. 3.3A, B). M^3 derived spectral parameter map suggest the presence of both mafic rich and mafic poor materials (Fig. 3.3C). Spectral profiles indicate the presence of high-Ca pyroxene and a weak signal of plagioclase feldspar (Fig. 3.5D).

3.3 Discussion

The use of multispectral datasets greatly assists us in piecing together the geological history of Olcott crater by combining image detail and spectral information with high spatial and spectral resolutions respectively. Using high resolution LROC camera data, we are able to assess the extent of various impactite materials and characterize their morphology. The improved spectral detail from 85 bands in the UV-VIS range of M^3 helps to assess the spectral properties of the terrain. This detail also allows the comparison of Olcott's characteristics to other complex craters of similar diameters. In particular, with a crater diameter of 81 km, Olcott is almost identical to Tycho (~85 km in diameter), a well-studied complex crater. Tycho crater has a sharp crater rim, terrace walls, and a distinct central uplift; and is located on the lunar nearside, on feldspathic terrain (Fig. 3.1). Many occurrences of well-preserved impact melt deposits have been identified beyond the crater floor of Tycho (Howard and Wilshire, 1973). Studies have indicated that the mineralogy within Tycho is a combination of high-Ca pyroxene and plagioclase feldspar (Hawke et al., 1986; Pieters, 1986; Dhingra and Pieters, 2012). Where applicable, the results from Olcott crater have been compared to those of Tycho crater and are discussed further below.

3.3.1 Effects of pre-existing topography on crater formation

Pre-existing faults on a planetary surface play a key role in affecting the final shape of an impact crater, and this has been well documented in the literature for terrestrial craters (e.g., Shoemaker and Kieffer, 1974; Spray et al., 2004; Osinski and Spray, 2005). We observe similar trends with regard to Olcott crater. Subdued impact crater features, presumed to be pre-existing due to the high level of crater modification, are identified

within 1 crater radii beyond the rim of Olcott (Fig. 3.4). These craters range in diameter from ~12 km to 45 km. The effects of pre-existing topography on Olcott can be seen from the cross-sectional topographic profiles (Fig. 3.6A). Altimetry data indicate the wall slope of Olcott crater along the southeast section is not as steep as on the opposite facing wall. There is greater wall slumping near the crater rim of the southeast section, with several topographic lows along the crater wall which correlate with areas where exterior melt deposits have been mapped (Fig. 3.7A). There is evidence of crater features being present in the local region prior to the Olcott forming event (Fig. 3.4). It is quite likely that the south half of the transient cavity of Olcott was near one of these pre-existing features which resulted in a greater level of wall collapse during the modification stages of the crater formation (Chapter 1, section 1.1).

3.3.2 Nature of the central uplift at Olcott crater

For lunar complex impact craters the size of Olcott (81 km), the morphology typically includes a rim, terraced walls, and an uplifted coherent central peak on the crater floor (Chapter 1, section 1.5.2). The morphologies of central peaks can be *simple* with a single peak, or *complex* with a cluster of peaks (Hale and Head, 1979).

The central uplift at Olcott crater is a cluster of peaks with variable heights (Fig. 3.2, 3.6B), and can be classified as a complex central uplift, with a ring-like central peak (Baker et al., 2011). This could indicate a transitional state of the crater, with an initial central peak collapsing to form a ring feature due to gravitational effects. Hydrocode simulations suggest that the formation of peak rings involves two mechanisms – the collapse of the crater rim inwards and the collapse of the central uplift outwards (Collins et al., 2002). However, the crater diameter size of Olcott at 81 km is far less than the crater diameter where the transition from a central peak to a peak ring occurs (diameters > 200 km; Baker et al., 2011) therefore this is unlikely to be the case. An alternative explanation is that the target surface where the Olcott event occurred is not homogeneous highland terrain, but instead a heterogeneous target. Modeling results and studies of terrestrial craters indicate that much of the crater collapse during the final modification stages depends on the strength of the target materials (Melosh, 1989). Parameters including the extent of ejecta deposits, depth of the crater floor, and heights of uplifted

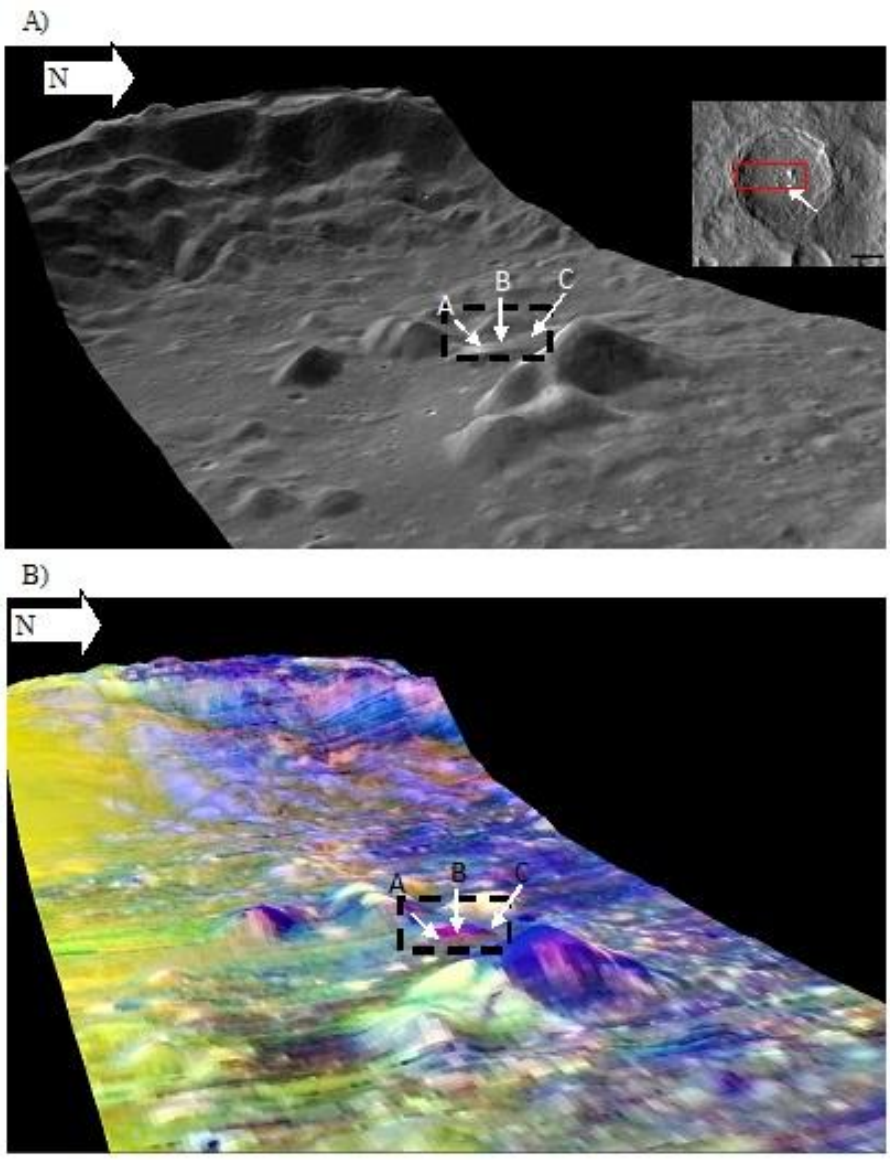

Figure 3.8: 3-D views of the central peak hills within Olcott crater. The black dashed rectangle refers to the location of the central peak hill discussed in the text, and featured in Fig. 3.8C. The lettered legend refers to the location of spectral profiles in Fig. 3.8D. A) This is a LRO-WAC context view of central uplift area discussed in 3.8C, D (10x vertical exaggeration). Image width is ~55 km. White arrow refers to location of spectral sampling in Fig. 3.8C. B) M^3 derived IBD parameter map of the area in Fig. 3.8A (10x vertical exaggeration). Image width is ~55 km. [Image credit: ISRO/NASA/GSFC/Arizona State University]

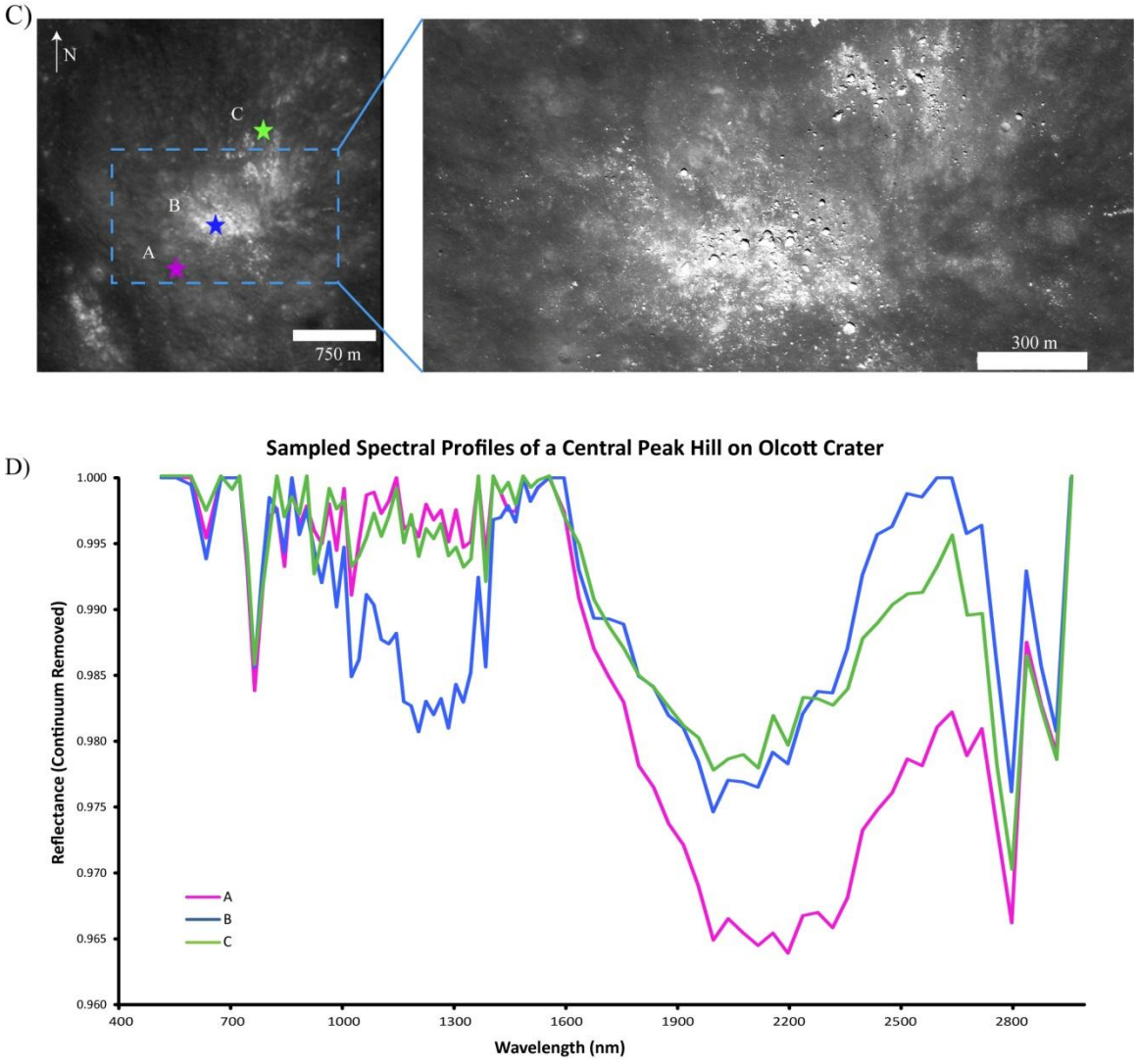

Figure 3.8 (cont'd): Image and spectral characterizations of a central peak hill at Olcott crater. C) LRO NAC (product # M108460950RC) of the central peak hill discussed in text and highlighted in Fig. 3.8A, B. The surface texture is similar to that characterized in Figure 3.7B. Image width is 2.5 km across. The letters refer to sample spectral profiles in Fig. 3.8D. D) Sample spectral profiles of spots identified in Fig. 3.8C. There are variable absorption strengths near 1 µm, 1.3 µm and 2 µm suggesting the presence of high-Ca pyroxene, Mg-spinel and plagioclase feldspar at this central peak hill. [Image credit: NASA/GSFC/Arizona State University]

sections are dependent on the pre-impact target layering (Collins et al., 2008). Crater morphologies with ring-like central peaks have been observed for craters between 50 and 205 km, however in these cases, there are also coherent peaks on the crater floor thereby classifying the features as protobasins (Baker et al., 2011). However, it is unknown at this point, if the target is heterogeneous at those crater sites. By fusing the spectral detail from M^3 IBD parameter map over topographic LOLA data, we observe that many areas within the Olcott central uplift have multiple colour variations indicating the possibility of multiple spectral trends (Fig. 3.3D, 3.8). From the sample spectral profiles using M^3 data (Fig. 3.5D, 3.8D), we note the presence of both pyroxene-rich and pyroxene poor materials in the central uplifts. Image data of the uplifts at Olcott crater display a mixture of rough, blocky materials (boulders) and thin impact melt deposits draped along the surface (Fig. 3.8C). This variability in surface texture may explain the variation in spectral properties. This observation is further investigated, using one of the peaks as an example, to assess both the spatial and spectral information and determine the connection if any. The spectral parameter composite map (Fig. 3.3D, 3.8B) indicates that the mineralogical content on one of the uplifted peaks, a 1 km feature (black dashed box in Fig. 3.8), has variable intensities of the individual parameters, indicating a potential variation in spectral characteristics and types of absorption features found. Spectral profiles sampled along the peak surface (Fig. 3.8D) indicate in general the weak occurrence of a 1 μm absorption, and strong 2 μm abundance. At sample sites "A" and "B", there is a lack of an absorption feature at 1 μm and a broad absorption feature observed at 2 μm, suggesting the presence of Mg-spinel (Pieters et al., 2011). At sample spot "B", absorption features of both plagioclase feldspar and Mg-spinel can be observed (Fig. 3.8D). The presence of an absorption feature at 1.3 μm is typical of Fe-bearing plagioclase feldspar. This occurrence of Mg-spinel on the central hill is similar to observations made on the central uplift region of Theophilus crater, 100 km complex crater on the lunar nearside (Dhingra et al., 2011). It is interesting to note that while this central uplift feature discussed here shows signs of the occurrence of Mg-spinel, other areas, spectrally sampled, within the central uplifts do not show a similar spectral signature (Fig. 3.5D). A more detailed investigation and thorough spectral sampling of

the central uplifts is required for a better assessment on the distribution of Mg-spinel rich areas within Olcott crater.

The identification of Mg-spinel within the central uplifts at Olcott crater is a significant observation. Mg-spinel has only been observed at two other locations on the Moon – Theophilus crater on the lunar nearside, and Moscovience basin on the lunar farside (Pieters et al., 2011; Dhingra et al., 2011). These studies propose that Mg-spinel is present within the lunar crust and is excavated from great depth. Olcott crater is ~735 km south west of the western edge of Mare Moscoviense – a known volcanic mare patch on the lunar farside. This new observation of Mg-spinel at these distances provides new estimates on the lateral and vertical extent of the Mg-spinel rock type within the lunar crust. An addition of a new "data point" of Olcott crater to the global dataset of Mg-spinel bearing complex craters will help better constrain the origin for this rock type.

3.3.3 Recognition of impact melt deposits

The presence of impact melt deposits beyond the crater floor is inferred from the smooth texture and low albedo compared to the surrounding regolith. Many instances of smooth deposits (resembling veneers and small pools) are observed within the ejecta deposits beyond the crater rim and along terrace walls, and are interpreted to be impact melt deposits (Fig. 3.7A, C–F). The spectral trends of both the exterior melt deposits and basin floor melt deposits are similar (high-Ca pyroxene; Fig. 3.5C) and, therefore, assumed to consist of the same material. Several instances of impact melt deposits on terrace zones and extending beyond the crater rim, have been recorded around many fresh lunar craters including Tycho, Giordano Bruno, King, etc. (Hirata et al., 2009; Plescia et al., 2010; Ashley et al., 2011). Morphologies of melt deposits at these craters range from melt flow lobes, to veneers, and melt ponds (Bray et al., 2010).

Observations of impact melt deposits beyond the crater floor of Olcott crater (Fig. 3.7A) can help us understand more about the stages of crater formation, particularly the emplacement of ejecta deposits (Chapter 1, section 1.3.1). Continuous ejecta deposits are emplaced through ballistic sedimentation during the crater excavation stage, and extend 1–2 crater radii beyond the crater rim with ejecta around large craters incorporating local

material (Oberbeck, 1975). Hummocky and block ejecta form much of the continuous ejecta deposits around Olcott crater, and extend 1 – 1.5 crater radii into the surroundings (Fig. 3.4). The evidence of a later stage of ejecta emplacement (Chapter 1, section 1.3.1) is found in the form of melt pools lining terrace walls to thin deposits draped over the continuous ejecta deposits (Fig. 3.4, 3.7). This is similar to results from studies of other craters on the terrestrial planets that suggest the emplacement of crater ejecta is likely a multi-stage process (Osinski et al., 2011). The role of pre-existing topography affecting the emplacement process is observed Olcott crater. There is a concentration of identified impact melt deposits beyond the central floor towards the eastern and southern parts of Olcott crater (Fig. 3.7A). The presence of pre-existing crater features to the east and south (Fig. 3.4) may explain this observation. However, further image mapping is required using the LRO Camera data suite at Olcott crater to assess if the entire distribution of impact melt deposits.

A goal of this study is to determine if by fusing multiple datasets, we can use spectral characteristics in identifying impact melt units around older complex craters. Optically, such impact melt deposits would be degraded, and appear less distinct, due to regolith buildup. With the use of M^3 data, we have documented multiple instances of localized regions in the IBD spectral parameter map (Fig. 3.3C) that have distinct and contrasting characteristics, when compared to the surrounding regions (Fig. 3.9). This is particularly striking along the southern crater walls and terrace zones (Fig. 3.9A, B, D). Whether these areas represent impact melts that are in some way obscured from identification in image view or represent another type of crater morphology is further investigated and discussed here. Spectral profiles of these areas are acquired (Fig. 3.9C), and the spectral information is compared to visible LRO NAC image detail (Fig. 3.9D). The spectral characteristics indicate the material in these areas is mafic rich, with both low-Ca pyroxene and high-Ca pyroxene signatures evident (Fig. 3.9C). There is, however, no direct indication suggesting the presence of Mg-spinel unlike within the central peak hill discussed earlier (Section 3.3.2), or even plagioclase feldspar. On close inspection of LRO NAC images (Fig. 3.9D), the sites appear to be variable in morphologies – they appear to be impact melt deposit areas (near sites i and ii), and a combination of ejecta deposits of fresh craters near the rough crater wall terrain (at site iii) (Fig. 3.9D). While

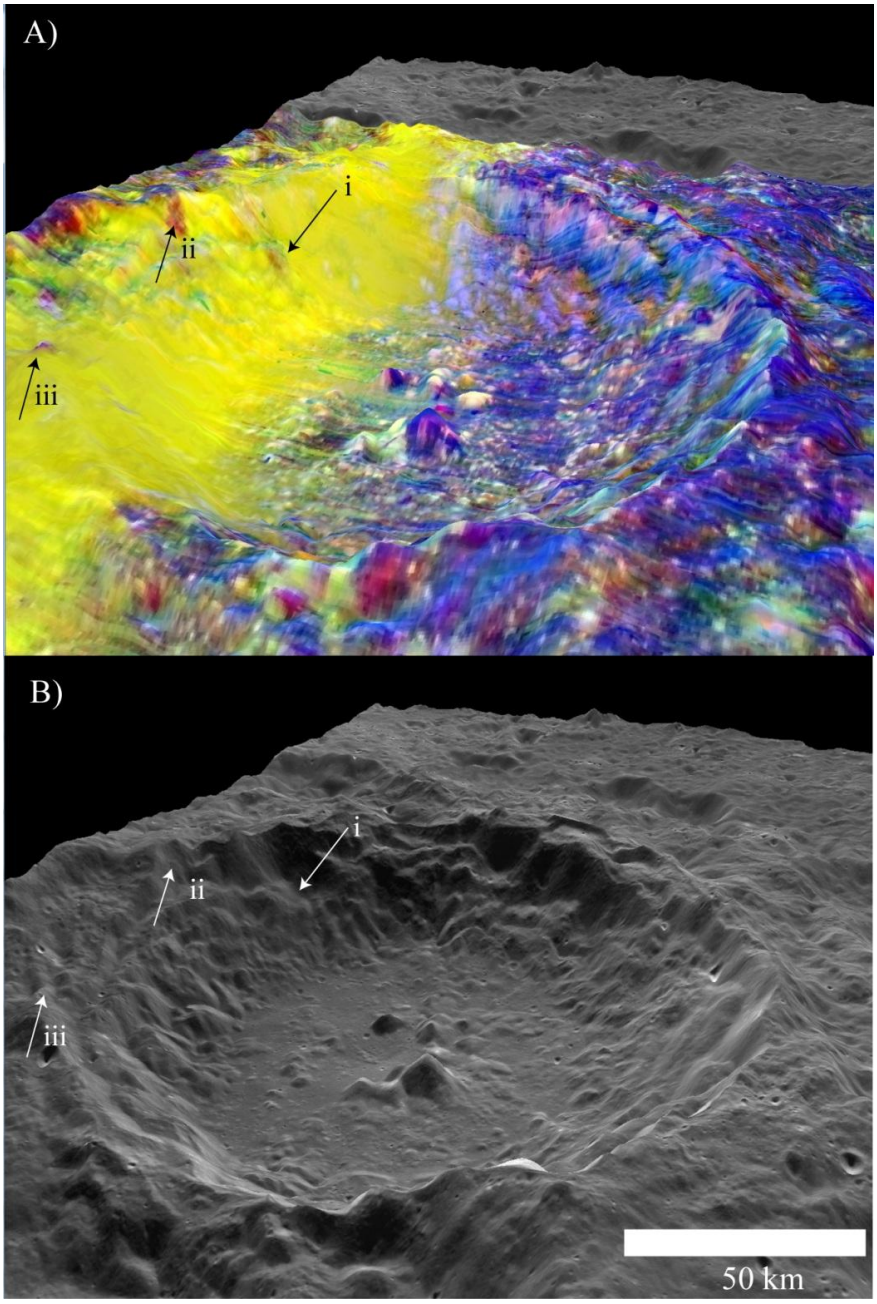

Figure 3.9: 3-D views of Olcott crater looking towards the southeast direction. A) 3-D view of the M^3 IBD spectral parameter map draped over LRO-LOLA altimetry data (512ppd resolution and15x vertical exaggeration). Numbered annotations refer to sites with colour anomalies as discussed in the text. B) 3-D image view of the same area as Fig. 3.9A. LRO-WAC global mosaic draped over LRO-LOLA altimetry data (512ppd resolution, 15x vertical exaggeration). [Image credit: NASA/GSFC/Arizona State University]

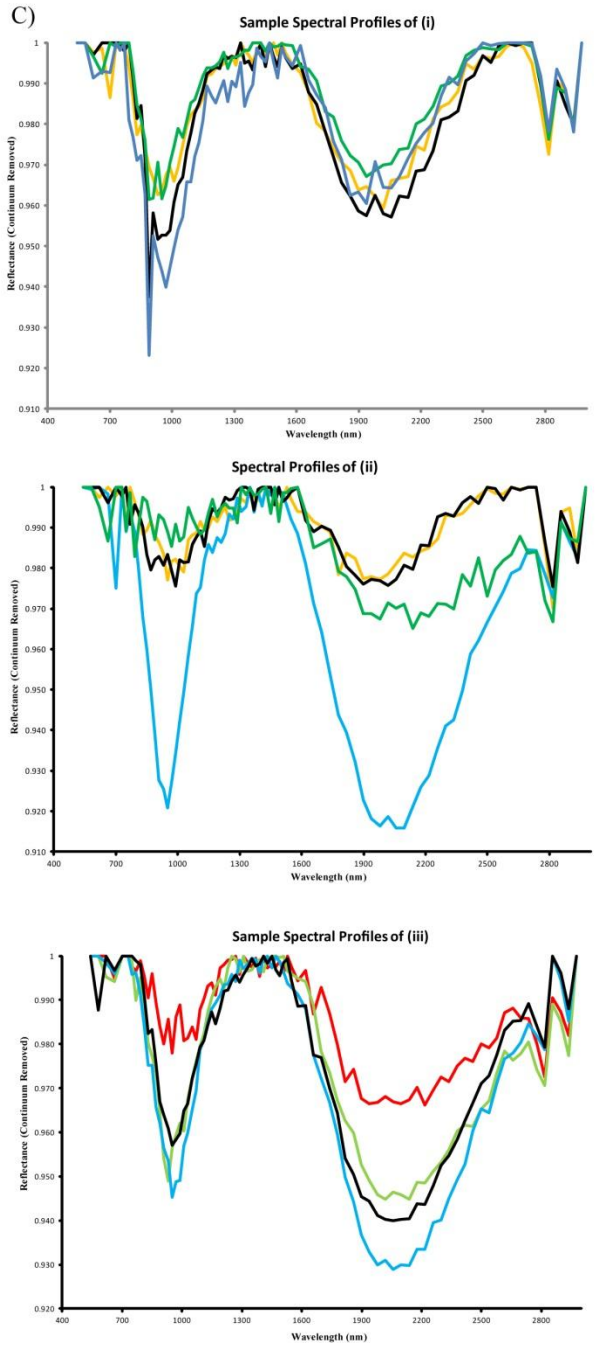

Figure 3.9 (cont'd): C) Sampled spectral profiles of the three sites (i-iii). The profiles indicate a pyroxene-rich terrain, with absorption features near 1 and 2 µm. There is minimal presence of plagioclase feldspar indicated (lack of absorption feature near 1.3 µm).

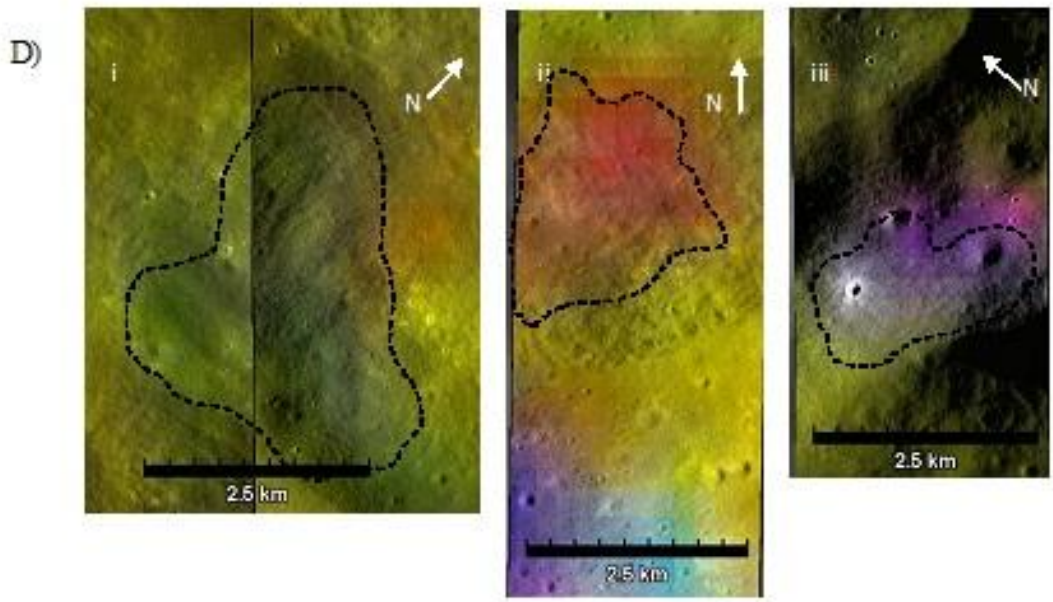

Figure 3.9 (cont'd): Closeups of the spectral anomalies. D) M^3 IBD parameter map overlaid on LRO NAC views of the three sites discussed in Fig. 3.9A–C. Black dashed lines highlight the colour anomalies identified. The ratio of spectral parameters varies significantly compared to the immediate surrounding areas, resulting in the different colours in the IBD map of these three sites. The morphologies vary between all three locations, with smooth low albedo impact melt deposits (site i), crater wall material with variable textures (site ii), and a freshly excavated crater with exposed ejecta deposits (site iii). LRO NAC images: M159189508LC and M115543039RC for site i, M161544383RC for site ii, and M115536257LC for site iii. [Image credit: ISRO/NASA/GSFC/Arizona State University]

the focused areas are in shadow-free zones, we also avoid making the general assumption that all anomalous areas in the IBD spectral parameter map have similar morphologies to those observed in figure 3.9D. As explained in the methods section (3.3.1), M^3 data had to be manually calibrated and georeferenced with respect to the camera data. At a crater-wide scale, the offset in georeferencing is minimal (Fig. 3.3C). However, for the zoomed in areas (at the scale of Fig. 3.9D), there is room for error in georeferencing. Further work is needed to account for all the possibilities of the spectral anomalies, including the presence of shadow areas, instrument resolution, etc.

3.3.4 Olcott as a window into the subsurface

Recognizing the proximity of Olcott crater to the Lomonosov-Fleming region may aid in the understanding of spectral variations observed from both the Clementine derived composite maps (Figs. 3.3A, B) and M^3 derived spectral information (Figs. 3.3C, 3.5). Although the crater lies in the lunar highlands, the compositional trends indicate there is a very strong mafic signature. This is particularly true along the southern half of Olcott crater. The concentration of mafic materials over the southern crater ejecta, crater wall, and crater floor suggests that the excavated material is emplaced as a result of mechanical mixing of the target layer. The high mafic signature in spectral profiles (Fig. 3.5) from the southern half of the crater provides evidence that the Olcott impact event may have struck a heterogeneous target, possibly a cryptomare deposit from the nearby Lomonosov-Fleming basin (Fig. 3.10). This is similar to the excavation hypothesis of observed materials proposed at Aristarchus crater (Mustard et al., 2010). The diversity in spectral compositions observed along the central peak hills of Olcott crater (Figs. 3.5D, 3.8D) supports the hypothesis that the Olcott crater event may have occurred within a heterogeneous target. Therefore, possibility of Olcott striking a heterogeneous target results in: 1) re-evaluating the total diameter of the Lomonosov-Fleming basin and 2) including Olcott crater within the basin rim. It is quite likely that the size of the Lomonosov-Fleming basin is much larger, at approximately 700 km, and the edge of the basin extends further eastward than earlier indicated by Giguere et al. (2003). However, the buried mafic-rich material can be of a buried magmatic origin. The distinction

Figure 3.10: Illustration of the proposed pre-impact stratigraphy in the Olcott crater region. The impact event occurred within a heterogeneous target, potentially tapping into buried mafic rich materials, likely from the Lomonosov-Fleming basin.

between determining if the mafic content is of cryptomare or magmatic origin is impossible at present using available spectral and spatial datasets. The proximity of Olcott crater to the Lomonosov-Fleming basin makes the cryptomare origin hypothesis more likely.

3.4 Summary

The findings of this study suggest that the section of lunar farside at Olcott crater is, like in the case of Schrödinger basin (Chapter 2), a heterogeneous target. There is a distinct split in the types of lunar materials found at Olcott crater. The north is largely comprised of low-Ca pyroxene, and plagioclase feldspar (norite) rich materials. The south is, however, dominated by low and high-Ca pyroxenes with little occurrence of plagioclase feldspar. The source of the mafic rich materials on the southern section of the crater is likely from buried mafic deposits excavated from the larger, and older Lomonosov-Fleming basin (a known region that contains cryptomare deposits; Giguere et al., 2003). Spectral observations also reveal that the heterogeneity of the target is best captured within the central uplifts, peak hills in this case The spectral variety of mafic rich materials present (from the range in pyroxene types to the occurrence of Mg-spinel) provides some perspective on the depths to which mafic materials may be present within the subsurface. This study also highlights the benefits of fusing various types of data together in order to determine the geological history of older complex craters. With multispectral and topographic datasets, we are able to characterize the spatial and spectral properties of Olcott crater impactites – particularly identify the spatial extent of impact melt deposits. Impact melt deposits occur as veneers draped over wall terraces and peak hills, and as melt ponds filling low lying areas along the crater rim. The fusion of spatial and topographic datasets further reveals that the distribution of impact melt deposits beyond the crater floor is largely driven by the pre-existing topography. Multispectral datasets reveal that the spectral properties of the impact melt deposits are the same both within and beyond the crater floor. The results from this multispectral study of Olcott crater provide a new perspective on the crater formation processes within a heterogeneous target, and about the regional geology particularly of the Lomonosov-Fleming basin.

3.5 References

Ashley, J.W., DiCarlo, N., Enns, A.C., Hawke, B.R., Hiesinger, H., Robinson, M.S., Sato, H., Speyerer, E.J., van der Bogert, C.H., Wagner, R.V., Young, K.E., and the LROC Science Team. 2011. Geologic mapping of the King crater region with an emphasis on melt pond anatomy – evidence for subsurface drainage on the Moon. Proceedings, 42nd Lunar Planetary Science Conference. Abstract # 2437.

Baker, D.M.H., Head, J.W., Fassett, C.I., Kadish, S.J., Smith, D.E., Zuber, M.T., and Neumann, G.A. 2011. The transition from complex crater to peak-ring basin on the Moon: New observations from the Lunar Orbiter Laser Altimeter (LOLA) instrument. *Icarus*, **214**: 377–393.

Bhandari, N. 2004. Chandrayaan-1, Lunar polar orbiter. 35th COSPAR Scientific Assembly. pp. 2430.

Bray, V.J., Tornabene, L.L., Keszthelyi, L.P., McEwen, A.S., Hawke, B.R., Giguere, T.A., Kattenhorn, S.A., Garry, W.B., Rizk, B., Caudill, C.M., Gaddis, L.R., and C.H. van der Bogert. 2010. New insight into lunar impact melt mobility from the LRO camera. *Geophysical Research Letters*. **37**, 21: L21202.

Carter, L.M., Neish, C.D., Bussey, D.B.J., Spudis, P.D., Patterson, G.W., Cahill, J.T., and Raney, R.K. 2012. Initial observations of lunar impact melts and ejecta flows with the Mini-RF radar. *Journal of Geophysical Research*. **117**, E00H09.

Chin, G., Brylow, S., Foote, M., Garvin, J., Kasper, J., Keller, J., Litvak, M., Mitrofanov, I., Paige, D., Raney, K., Robinson, M., Sanin, A., Smith, D., Spence, H., Spudis, P., Stern, S.A., and Zuber, M. 2007. Lunar Reconnaissance Orbiter Overview: The instrument suite and mission. *Space Science Reviews*. **129**, 4: 391–419.

Christensen, P.R., Engle, E., Anwar, S., Dickenshied, S., Noss, D., Gorelick, N. and Weiss-Malik, M. 2009. JMARS – A Planetary GIS. American Geophysical Union Fall Meeting. Abstract # IN22A-06.

Collins, G.S., Melosh, H.J., Morgan, J-V., and Warner, M.R. 2002. Hydrocode simulations of Chicxulub crater collapse and peak-ring formation. *Icarus*. **157**: 24–33.

Collins, G.S., Kenkmann, T., Osinski, G.R., and Wünnemann, K. 2008. Mid-sized complex crater formation in mixed crystalline-sedimentary targets: Insight from modeling and observation. *Meteoritics and Planetary Science*. **44**. 12: 1955–1977.

Crown, D.A., and Pieters, C.M. 1985. Spectral properties of plagioclase and pyroxene mixtures. 16th Lunar and Planetary Science Conference. 158–159.

Dhingra, D., Pieters, C.M., Boardman, J.W., Head, J.W., Isaacson, P.J., and Taylor, L.A. 2011. Compositional diversity at Theophilus Crater: Understanding the geological context of Mg-spinel bearing central peaks. *Geophysical Research Letters*. **38**, 11: L11201.

Dhingra, D., and Pieters, C.M. 2012. Spectroscopy of Impact Melts – Results from Lunar Crater Tycho. 43rd Lunar and Planetary Science Conference. Abstract #1836.

Donaldson Hanna, K.L., Cheek, L.C., Pieters, C.M., Mustard, J.F., Wyatt, M.B., and Greehangen, B.T. 2012. Global identification of crystalline plagioclase across the lunar surface using M^3 and Diviner data. 43rd Lunar and Planetary Science Conference. Abstract # 1968.

Giguere, T.A., Hawke, B.R., Blewett, D.T., Bussey, D.B.J., Lucey, P.G., Smith, G.A., Spudis, P.D., and Taylor, G.J. 2003. Remote sensing studies of the Lomonosov-Fleming region of the Moon. *Journal of Geophysical Research*. **108**, E11: 5118.

Goswami, J. N., Thyagarajan, K., and Annadurai, M. 2006. Chandrayaan-1: Indian Mission to Moon. 37th Lunar and Planetary Science Conference. Abstract #1704.

Green, R.O., Boardman, J., Pieters, C.M., Clark, R. and the M^3 Team. 2010. An algorithm for estimation and correction of the thermal emitted radiance with preservation of spectral structure in data measured by the Moon Mineralogy Mapper. 41st Lunar and Planetary Science Conference. Abstract #2331.

Hale, W., and Head, J.W. 1979. Central peaks in lunar craters: Morphology and morphometry. Proceedings, 10th Lunar and Planetary Science Conference. pp. 2623–2633.

Hawke, B.R., and Head, J.W. 1977. Impact melt on lunar crater rims. Proceedings, Symposium on Planetary Cratering Mechanics. pp. 815–841.

Hawke, B.R., Lucey, P.G., Bell, J.F. Jaumann, R., and Neukum, G. 1986. Spectral reflectance studies of Tycho Crater: Preliminary Results. 17th Lunar and Planetary Science Conference. pp. 999-1000.

Hiesinger, H., and Head, J.W. (III). 2006. New Views of Lunar Geoscience: An Introduction and Overview. In *Reviews in Mineralogy and Geochemistry*, edited by Jolliff, B.L., Wieczorek, M.A., Shearer, C.K., and Neal, C.R. **60**: 1–81.

Hirata, N., Haruyama, J., Ohtake, M., Matsunaga, T., Yokota, Y., Morota, T., Honda, C., Ogawa, Y., Sugihara, T., Miyamoto, H., Demura, H., and Asada, N. 2009. Morphological analyses of Tycho crater with Kaguya data. 40th Lunar and Planetary Science Conference. Abstract # 1514.

Howard, K.A. and Wilshire, H.G. 1975. Flows of impact melt in lunar craters. *Journal of Research of the U. S. Geological Survey*. **3**: 237–251.

Klima, R.L., Pieters, C.M., Isaacson, P.J., Head, J.W., Staid, M., Taylor, L.A., Petro, N.E., and Sunshine, J.M. 2011. Global distribution and composition of Low-Ca pyroxenes on the Moon as viewed by the Moon Mineralogy Mapper. 41st Lunar and Planetary Science Conference. Abstract #1533.

Lucey, P.G., Blewett, D.T., Jolliff, B.L. 2000. Lunar iron and titanium abundance algorithms based on final processing of Clementine ultraviolet – visible images. *Journal of Geophysical Research*. **105**, E8: 20297–20306.

Melosh, H.J. 1989. *Impact Cratering: A Geologic Process*. New York: Oxford University Press. 245p.

Morris, R.V. 1978. The surface exposure (maturity) of lunar soils: Some concepts and I_s/FeO compilation. Proceedings, 9th Lunar and Planetary Science Conference. pp. 2287–2297.

Mustard, J.F., Pieters, C.M., Issacson, P.J., Head, J.W., Besse, S., Clark, R.N., Klima, R.L., Petro, N.E., Staid, M.I., Sunshine J.M., Runyon, C.J., and Tompkins, S. 2011. Compositional diversity and geologic insights of the Aristarchus crater from Moon Mineralogy Mapper data. *Journal of Geophysical Research*. **116**: E00G12.

Oberbeck, V. 1975. The role of ballistic erosion and sedimentation in lunar stratigraphy. *Reviews of Geophysics and Space Physics*. **13**: 337–362.

Osinski, G.R., and Spray, J.G. 2005. Tectonics of complex crater formation as revealed by the Haughton impact structure, Devon Island, Canadian High Arctic. *Meteoritics and Planetary Science*. **40**, 12: 1813–1834.

Osinski, G.R., Tornabene, L.L., and Grieve, R.A.F. 2011. Impact melt and ejecta emplacement on terrestrial planets. *Earth and Planetary Science Letters*. **310**, 3: 167–181.

Pieters, C.M. 1978. Mare basalt types on the front side of the moon: A summary of spectral reflectance data. Proceedings, 9th Lunar Planetary Science Conference. pp. 2825–2849.

Pieters, C.M. 1986. Composition of the lunar highland crust from near-infrared spectroscopy. *Review of Geophysics*. **24**, 557–558.

Pieters, C.M., Staid, M.I., Fischer, E.M., Tompkins, S., and He, G. 1994. A sharper view of impact craters from Clementine data. *Science*. **266**: 1844 – 1848.

Pieters, C.M., Goswami, J.N., Clark, R.N., Annadurai, M., Boardman, J., Buratti, B., Combe, J.-P., Dyar, M.D., Green, R., Head, J.W., Hibbits, C., Hicks, M., Isaacson, P., Klima, R., Kramer, G., Kumar, S., Livo, E., Lundeen, S., Malaret, E., McCord, T., Mustard, J., Nettles, J., Petro, N., Runyon, C., Staid, M., Sunshine, J., Taylor, L.A.,

Tompkins, S., and Varanasi, P. 2009. Character and spatial distribution of OH/H_2O on the surface of the Moon seen by M^3 on Chandrayaan-1. *Science*. **326**: 568–572.

Pieters, C.M., Besse, S., Boardman, J., Buratti, B., Cheek, L., Clark, R.N., Combe, J.P., Dhingra, D., Goswami, J.N., Green, R.O., Head, J.W., Isaacson, P., Klima, R., Kramer, G., Lundeen, S., Malaret, E., McCord, T., Mustard, J., Nettles, J., Petro, N., Runyon, C., Staid, M., Sunshine, J., Taylor, L.A., Thaisen, K., Tompkins, S., and Whitten, J. 2011. Mg-spinel lithology: A new rock type on the lunar farside. *Journal of Geophysical Research.* **116**: E00G08.

Pike, R.J. 1983. Large craters or small basins on the Moon. Proceedings, 14th Lunar Planetary Science Conference. pp. 610–611.

Plescia, J.B., Robinson, M.S., and Paige, D.A. 2010. Giordano Bruno: the young and the restless. Proceedings, 41st Lunar Planetary Science Conference. Abstract # 2038.

Robinson, M.S., Brylow, S.M., Tschimmel, M., Humm, D., Lawrence, S.J., Thomas, P.C., Denevi, B.W., Bowman-Cisneros, E., Zerr, J., Ravine, M.A., Caplinger, M.A., Ghaemi, F.T., Schaffner, J.A., Malin, M.C., Mahanti, P., Bartels, A., Anderson, J., Tran, T.N., Eliason, E.M., McEwen, A.S., Turtle, E., Jolliff, B.L., and Hiesinger, H. 2010. Lunar Reconnaissance Orbiter Camera (LROC) Instrument Overview. *Space Science Reviews*. **150**, 1–4: 81–124.

Smith, D.E., Zuber, M.T., Jackson, G.B., Cavanaugh, J.F., Neumann, G.A., Riris, H., Sun, X., Zellar, R.S., Coltharp, C., Connelly, J., Katz, R.B., Kleyner, I., Liiva, P., Matuszeski, A., Mazarico, E.M., McGarry, J.F., Novo-Gradac, A-M., Ott, M N., Peters, C., Ramos-Izquierdo, L.A., Ramsey, L., Rowlands, D.D., Schmidt, S., Scott, V.S., Shaw, G.B., Smith, J.C., Swinski, J-P., Torrence, M.H., Unger, G., Yu, A.W., Zagwodzki, T.W. 2010. The Lunar Orbiter Laser Altimeter Investigation on the Lunar Reconnaissance Orbiter Mission. *Space Science Reviews*. **150**, 1–4: 209–241.

Speyerer, E.J., Robinson, M.S., Denevi, B.W., and the LROC Science Team. 2011. Lunar Reconnaissance Orbiter camera global morphological map of the Moon. 42nd Lunar and Planetary Science Conference. Abstract # 2387.

Tompkins, S., and Pieters, C.M. 2010. Spectral characteristics of lunar impact melts and inferred mineralogy. *Meteoritics and Planetary Science*. **45**, 7: 1152–1169.

Wilhelms, D.E., and El-Baz, F. 1977. *Geologic Map of the east side of the Moon*. Department of the interior United States geological survey. Map. I–948. 1:5M scale.

Chapter 4

4 Identification and Distribution of Impact Melt Deposits surrounding Complex Impact Craters on the Lunar Farside: A comparison between different crater sizes

The early stages of impact cratering involve the shock melting of target stemming from the passage of shock waves through a target surface following a catastrophic, hypervelocity impact onto a rocky planet (Chapter 1, section 1.1). The target rocks are subject to extreme pressures and temperatures in short spans of time (Fig. 1.1) that result in the vapourization and melting of target rocks. Throughout most of the crater forming process, melted rocks remain within a growing and temporal transient cavity (Fig. 4.1). Materials within the displaced zone (Melosh, 1989; French, 1998) of the transient cavity (Fig. 4.1A, B) are subjected to a range of shock pressures (Chapter 1, section 1.3), and typically a mixture of melt and fractured rocks line the floor of the transient cavity (Fig. 4.1B–D). Melted rocks within a transient cavity that eventually form a simple crater tends to remain within the crater floor and overlie the fractured crater floor (Fig. 1.3D).

The formation of a central structural uplift within a transient cavity results in the movement of impact generated melt within the displaced zone - moving downward and outward towards the walls and rim of the transient cavity (Fig. 4.1C). The final modification phase of crater formation (Chapter 1, section 1.1.3) determines where much of the impact melts are concentrated (Melosh, 1989; Osinski et al., 2011). At this late stage, modelling and terrestrial observations suggest the collapse of crater walls and central uplifts within the transient cavity result in the movement of some melt materials (Fig. 4.1D) beyond the crater rim (Collins et al., 2002; Osinski and Spray, 2005). In a process of multi-stage ejecta emplacement, impact melt deposits within complex craters can be emplaced along terrace surfaces, or coating continuous ejecta deposits beyond the terraced rim structure (Fig. 4.1E; Osinski et al., 2011). Models suggest that as the magnitude of the crater event increases, the relative volume of melt generated will also increase (Cintala and Grieve, 1998).

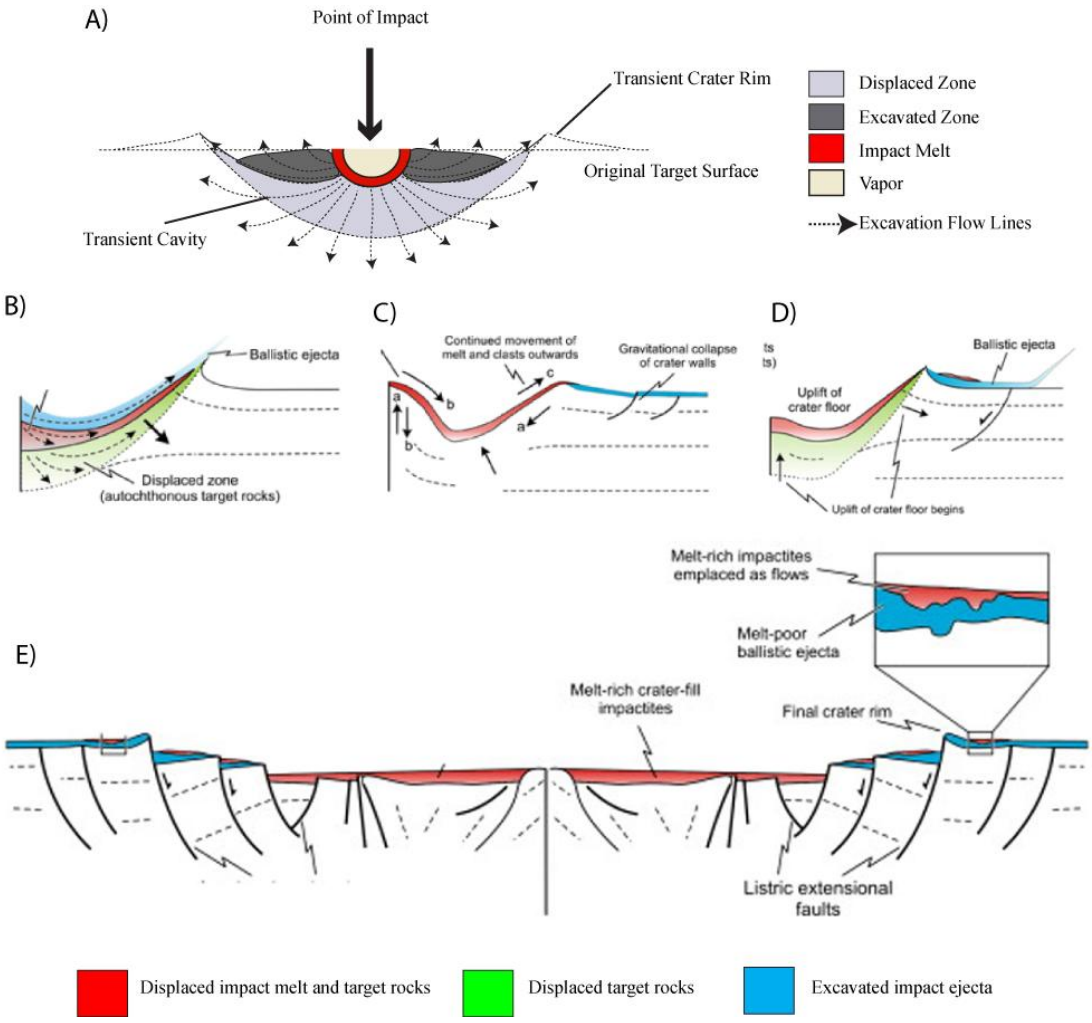

Figure 4.1: Cross sectional sketches of the impact cratering process and the emplacement of melt deposits within complex impact craters. A) Zones within an expanding transient cavity. B - D) The location of impact melt within sections of the transient cavity during the evolving stages of crater formation. E) The final crater morphology of a complex crater, with the location of impact melts within both the inner crater fill and beyond the crater rim as ponded deposits. Modified from Melosh, 1989 and Osinski et al., 2011.

Impact craters on the Moon preserve a range of melt morphologies. Within the interior of simple craters, melt deposits are typically thin melt veneers (Hawke and Head, 1977). Many examples of well-preserved impact melt deposits have also been recorded around lunar complex craters including Giordano Bruno, Necho, Jackson, and Tycho craters (Fig. 4.2). Melt deposit morphologies within complex craters include: 1) melt sheets that fill the crater floor; 2) viscous flow features; 3) thin veneers draped over wall terraces; and 4) melt pools or ponds that fill depression areas within wall terraces and continuous ejecta deposits (Howards and Wilshire, 1975; Hawke and Head, 1977; Bray et al., 2010). In addition to the visible characterization of lunar melt deposits, several studies have analyzed the characterization of impact melts surrounding various craters using reflectance spectroscopy and radar techniques (Smrekar and Pieters, 1985; Campbell et al., 2010; Tompkins and Pieters, 2010; Dhingra and Pieters, 2012). Together with lab analyses on Apollo samples and lunar meteorites, there is some understanding about: 1) the effects of shock in melt generation (Schaal et al., 1979); 2) the compositions of lunar impact melt deposits (Smrekar and Pieters, 1985; Tompkins and Pieters, 2010; Dhingra and Pieters, 2012); and 3) the distribution of rock clasts within lunar impact melts (Campbell et al., 2010; Carter et al., 2012; Neish et al., 2012).

The current understanding of impact melt rocks is increasing through: 1) the continued research on lunar meteorites and Apollo samples; and 2) the identification of melt deposits around lunar craters through the use of recent higher resolution camera imagery from the Lunar Reconnaissance Orbiter (Denevi et al., 2012). However, a gap still exists in tying the spatial observations of impact melt deposits surrounding large older complex craters, and model estimates on the impact melt volume within the original transient cavity. Much of the early studies on impact melts has been based on photogeologic studies (e.g., Howard and Wilshire, 1975; Hawke and Head, 1977). Visible image observations of melt deposits around well-preserved lunar craters and terrestrial observations have led to model estimates on the melt volume generated within lunar craters (Grieve and Cintala, 1992; Cintala and Grieve, 1998). The model has also been used to estimate the maximum depth of crater excavation, and depth of melting for a range of crater morphologies within the lunar target (Cintala and Grieve, 1998). As a result, the approximation on melt volumes around a lunar crater, in general, is estimated

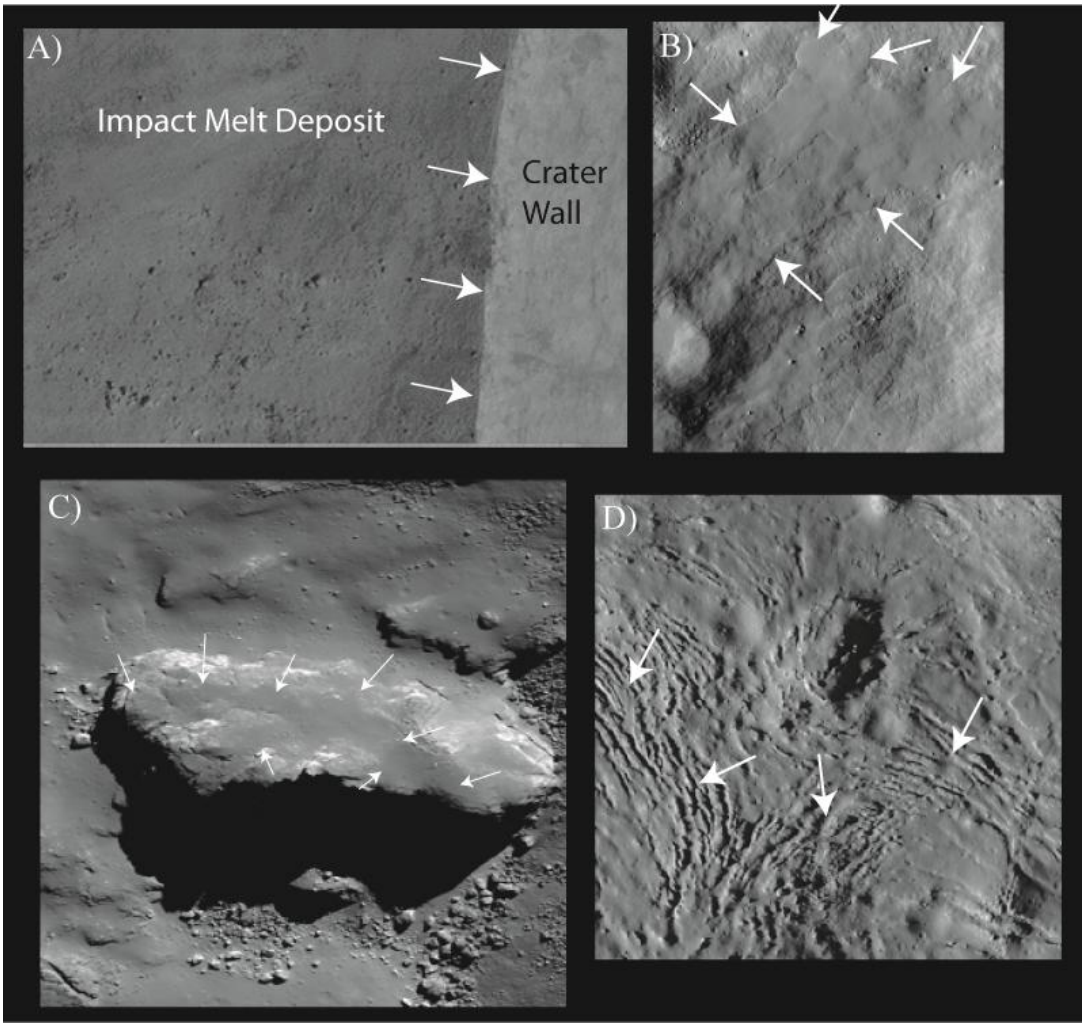

Figure 4.2: **Examples of pristine impact melt deposits within complex lunar impact craters taken by the Narrow Angle Camera (NAC) aboard the Lunar Reconnaissance Orbiter (LRO). All images acquired by NASA/GSFC/Arizona State University. A) Smooth impact melt deposit along the rim of the 22 km Giordano Bruno (LRO - NAC image M113282954RE; image width is ~1 km). B) Impact melt flow features at the 30 km Necho crater (LRO – NAC mosaic of M134374642L and R images; image width is 5 km). C) Thin, smooth veneer of impact melt draped over an ejecta block in the 85 km Tycho crater (LRO – NAC image M142334392R; image width is ~400 m). D) Fractures within a melt pond on the 71 km Jackson crater (LRO – NAC image M118560367L; image width is ~ 700 m). [Image credit: NASA/GSFC/Arizona State University]**

using the *differential scaling* property – i.e. as the crater event increases: 1) the size of the transient cavity increases, 2) the volume of melt generated increases unaffected by gravitational effects, and 3) a larger proportion of this melt will be preserved inside the crater rim, along terrace surfaces, and fill the crater floor (Cintala and Grieve, 1998). The release of high resolution multispectral data (with improved spatial and spectral detail) from the Lunar Reconnaissance Orbiter (LRO) and Chandrayaan-1 missions provides new opportunities to assess the morphologies and spectral characteristics of impact melt deposits surrounding lunar complex craters in great detail. At a simplistic, first order approach, the volume of melt produced within a transient cavity should be similar (at the least, within an order of magnitude) to the volumes of observed melt deposits around the craters.

This study discusses the distribution of impact melt deposits identified around three complex craters with varying central uplift morphologies. These craters are all located on the lunar farside, a lunar hemisphere that has minimal surface modifications caused by lunar volcanism affecting the preservations of complex craters (Hiesinger and Head, 2006 and references therein). Complex craters on the lunar farside range from complex craters with consolidated peaks, protobasins, peak ring basins, and multi-ring basins (Chapter 1, section 1.5). Therefore, the distribution of impact melt deposits at these locations can be properly be assessed. Melt volumes are estimated for each crater site using the areal extent of the deposits, and a range of thicknesses based on the individual melt morphology at each site. The results are next compared to model estimates that use the differential scaling methods approach in calculating melt volume (Cintala and Grieve, 1998). The areal extent of the melt deposits is also assessed at each site to compare the differential scaling model (Cintala and Grieve, 1998) with the multi-stage ejecta emplacement model (Osinski et al., 2011). The former proposes that much of the melt generated remains within the crater interior for large events, while the latter proposes that the collapse of central uplifts provides added momentum for melt deposits to emplace beyond the crater rim during the crater modification process.

We present results from the analysis and synthesis of Clementine (UV-VIS), Chandrayaan-1 Moon Mineralogy Mapper (M^3), LRO altimetry (LOLA), LRO radar (Mini-RF), and both LRO- Wide Angle and Narrow Angle Camera (WAC, NAC) data on three complex craters on the lunar farside – Olcott, Kovalevskaya, and Schrödinger (81, 113, and 312 km rim-rim diameters, respectively). The results are used to characterize impact melt deposits - particularly beyond the crater floor, map the distribution of identified impact melt deposits, and calculate melt volumes (as discussed above). The results can be used to better assess the distribution of impact melt deposits within large complex craters on the Moon.

4.1 Study Sites

Our understanding of the lunar farside has only advanced with the acquisition of global datasets from the photographic Lunar Orbiter (Bowker and Hughes, 1971) and multispectral Clementine missions (Nozette et al., 1994). With improved spatial and spectral resolutions, it is possible to identify the composition and distribution of impactites. This includes identifying the distribution of impact melt deposits around complex craters and testing the hypothesis that impact melt deposits beyond the crater rim are emplaced as part of a proposed multi-stage ejecta emplacement process (Osinski et al., 2011). The lunar highlands are comprised of crustal highland rocks – rich in anorthosites (predominantly plagioclase feldspar, with little mafic assemblage of low-Ca pyroxene; Smrekar and Pieters, 1985). The farside is also void of much volcanic activity – only ~1 % of the farside has volcanic basalt mare units (Hiesinger and Head, 2006 and references therein).

We identify impact melt deposits for three complex craters (Olcott, Kovalevskaya, and Schrödinger) all with increasing diameters and different morphologies (Fig. 4.3). Olcott crater, (22^oN, 117^oE), is an 81 km diameter complex crater located on the lunar farside highlands (Chapter 3). Eratosthenian in age (Wilhelms and El Baz, 1977), Olcott crater is located on the edge of the degraded Lomonosov-Fleming basin (Giguere et al., 2003). The crater morphology includes a sharp rim, crater walls with terraces, and a cluster of central peaks on the crater floor (Fig. 4.3A). Kovalevskaya crater (30^oN, 129^oW), Eratosthenian in age (Scott et al., 1977), is a 113 km complex crater located in the

western farside, and ~85 km north west of the Cordillera mountains of Orientale basin. Kovalevskaya has a well preserved crater rim, terraced walls, and a flat crater floor with a central uplift (Fig. 4.3B). The central uplift comprises of two peaks with variable heights. The final complex crater analyzed in this study is Schrödinger basin (75°S, 130°E; 312 km in diameter), located near the southern rim of the larger South Pole-Aitken basin (Chapter 2). Schrödinger basin has a well preserved rim, terrace walls, and smooth basin floor. Schrödinger basin is proposed to be early Imbrian in age (Wilhelms, 1987). There is evidence of later volcanism around a local volcanic vent on the eastern section of the inner basin floor (Chapter 2; section 2.1). However, the distribution of pyroclastic deposits occupies a small area of the floor and does not modify the characteristics of impact melt within the rest of the basin floor (Shoemaker and Robinson, 1995; Mest et al., 2011). Schrödinger basin is classified as a peak ring complex crater as the central uplift on the basin floor is a near concentric peak ring (Fig. 4.3C).

4.2 Methods

In order to assess the relationship between impact melt deposits and their topographic expressions within craters of increasing complexity on the lunar farside, the identification and characterization of impact melt deposits was conducted through the fusion of multiple lunar datasets – combining spatial, spectral, radar and topographic details. The integration of spatial, spectral, radar, and topographic datasets in this study was compiled using the USGS Integrated Software for Imagers and Spectrometers (ISIS v.3; Gaddis et al., 1997), ENVI version 4.8 (Exelis Visual Information Solutions, Boulder, Colorado), JMars for Earth's Moon (Christensen et al., 2009), and ArcGIS® (www.esri.com) software packages.

4.2.1 Identification of impact melt deposits

Impact melt deposits were identified primarily based on their visible characteristics - smooth, low albedo deposits that show obvious contrast when compared to their immediate surroundings, and deposits that do not have a volcanic source of origin (Hawke and Head, 1977). The identification of melt deposits was done using both the monochrome 643 nm LRO Wide Angle Camera (WAC) global mosaics at 100m/pixel

resolution (Robinson et al., 2010; Speyerer et al., 2011), and high resolution panchromatic images from the Narrow Angle Camera (NAC, 0.5 m/pixel; Robinson et al., 2010) instruments on the Lunar Reconnaissance Orbiter (LRO). Geologic sketch maps were created from observations obtained using a combination of WAC and NAC images outlining the spatial extent of impactite units around each crater. The map projection of the data was polar stereographic at Schrödinger basin, and simple cylindrical at Olcott and Kovalevskaya craters.

The topographic information of each crater (Fig. 4.3) and of identified impact melt deposits were acquired using data from the LRO Lunar Orbiter Laser Altimeter (LOLA) instrument (Smith et al., 2010). Gridded Data Record (GDR) files with 1024 pixels per degree resolution were downloaded from the Lunar Orbital Data Explorer portal (ode.rsl.wustl.edu/moon**)**. The altimetry data were processed, calibrated, and map projected using mission specific scripts within the ISIS v.3 software.

Multispectral data, including radar and reflectance spectroscopy, was used to characterize the impact melt deposits at each of the crater sites. The utility of each of the datasets in identifying impact melts are briefly discussed here. The spectral characterization of identified impact melt deposits was made using UV-VIS-NIR reflectance spectroscopy data from both the Clementine and Chandrayaan-1 Moon Mineralogy Mapper (M^3) instruments (Figs. 4.4, 4.5). The most common lithologies on the Moon are generally iron-rich mare basalts and highland anorthositic rock types. Spectra from the mare regions have strong absorption features representing mafic minerals, including pyroxene, with distinctive absorption features near 1 and 2 μm (Pieters, 1978). Mare areas contain typically high-Ca pyroxenes, with absorption bands centred near 0.97 – 1 μm (Smrekar and Pieters, 1985). Highland anorthosites typically contain low-Ca pyroxenes, with absorption bands centred near 0.9 – 0.93 μm (Smrekar and Pieters, 1985). Iron bearing plagioclase feldspar has absorption bands centred near 1.3 μm, however any content of pyroxene can mask the presence of feldspar bearing absorption bands (Crown and Pieters, 1985; Pieters, 1986).

The 5-band UV-VIS data (415, 750, 900, 950, 1000 nm) from the Clementine mission

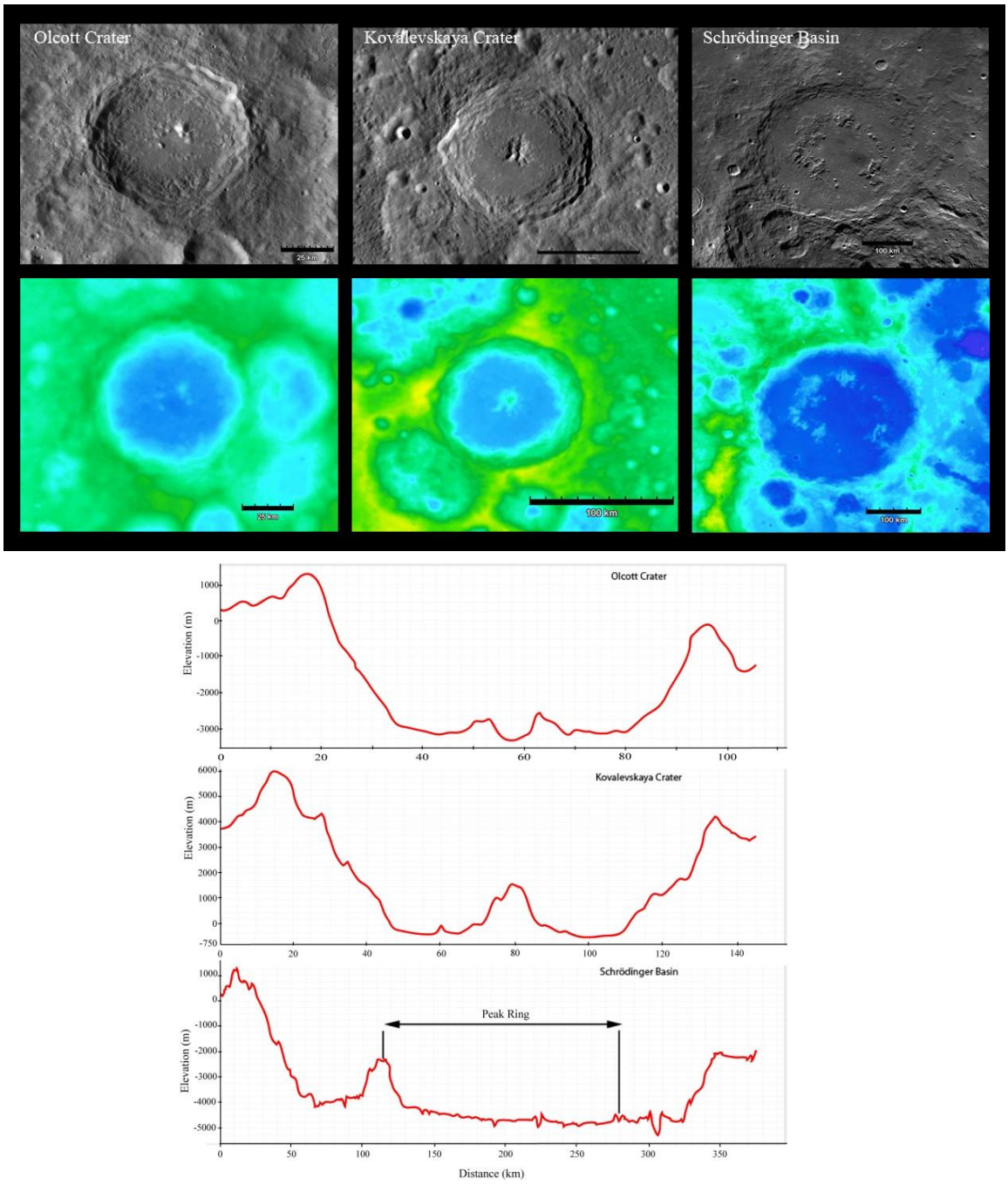

Figure 4.3: (Top) Lunar Reconnaissance Orbiter Wide Angle Camera greyscale mosaics of the three crater sites selected for this study – (A) Olcott crater, (B) Kovalevskaya crater, and (C) Schrödinger basin. (Bottom) Topographic profiles of the complex craters, data acquired from the Lunar Orbiter Laser Altimeter instrument. Topography values are relative to a lunar radius of 1737.4 km. [Image credit: MIT/NASA/GSFC/Arizona State University]

were used to characterize spectral detail of the craters at a regional scale. The optical maturity information of surfaces (Pieters et al., 1994) was inferred from colour ratio composite maps (Fig. 4.4A–C). In the colour ratio composite map, red surfaces are interpreted as mature surfaces; blue indicates a fresh surface; and green indicates the presence of a mafic component. The presence of other colours indicates a mixture of these basic parameters in variable proportions and can therefore be used in assessing the surface maturity and mafic content. The iron weight percent distribution composite map (Lucey et al., 2000) was used to gauge the level of iron content present at each of the study sites (Fig. 4.4 D–F). Typically the lunar farside is known to have very little evidence of surface volcanism and, therefore, low levels of iron on the lunar surface (Gilles and Spudis, 1996; Hiesinger and Head, 2006).

M^3 data covers the UV-VIS-NIR (446–3000 nm) spectrum like the Clementine dataset but has improved spectral resolution (20–40 nm), allowing for a more detailed evaluation of compositional information, providing a more distinct spectral characterization for both basalts and anorthosites. Level1b M^3files (pixel-located, resampled, and calibrated data in radiance units) were downloaded from the Lunar Orbital Data Explorer portal (ode.rsl.wustl.edu/moon**)**, and the radiance values converted to reflectance using techniques outlined by Green et al. (2010). M^3 data was used to generate an RGB spectral parameter composite map comparing the integrated band depth (IBD) values at 1 µm, 1.3 µm, and 2 µm (Fig. 4.5) to assess the mineral compositions on the lunar surface. The IBD values were calculated using algorithms defined by Mustard et al. (2011) and Donaldson Hanna et al. (2012). More information about the individual data products and processing details can be found in Appendix C.

The colours in the IBD spectral parameter maps (Fig. 4.5) indicate the various strengths of the spectral parameters. Typically, red indicates that the 1 µm absorption feature is strong; green indicates that the 2 µm absorption feature is strong; and the blue colour indicates that the 1.3 µm feature is strong. Other colours indicate the combination of these three basic parameters with variable strengths. For example, yellow indicates a mixture of red and green parameters; i.e., the presence of both the 1 and 2 µm absorption features – characteristic of the spectral signature of pyroxene. White indicates the

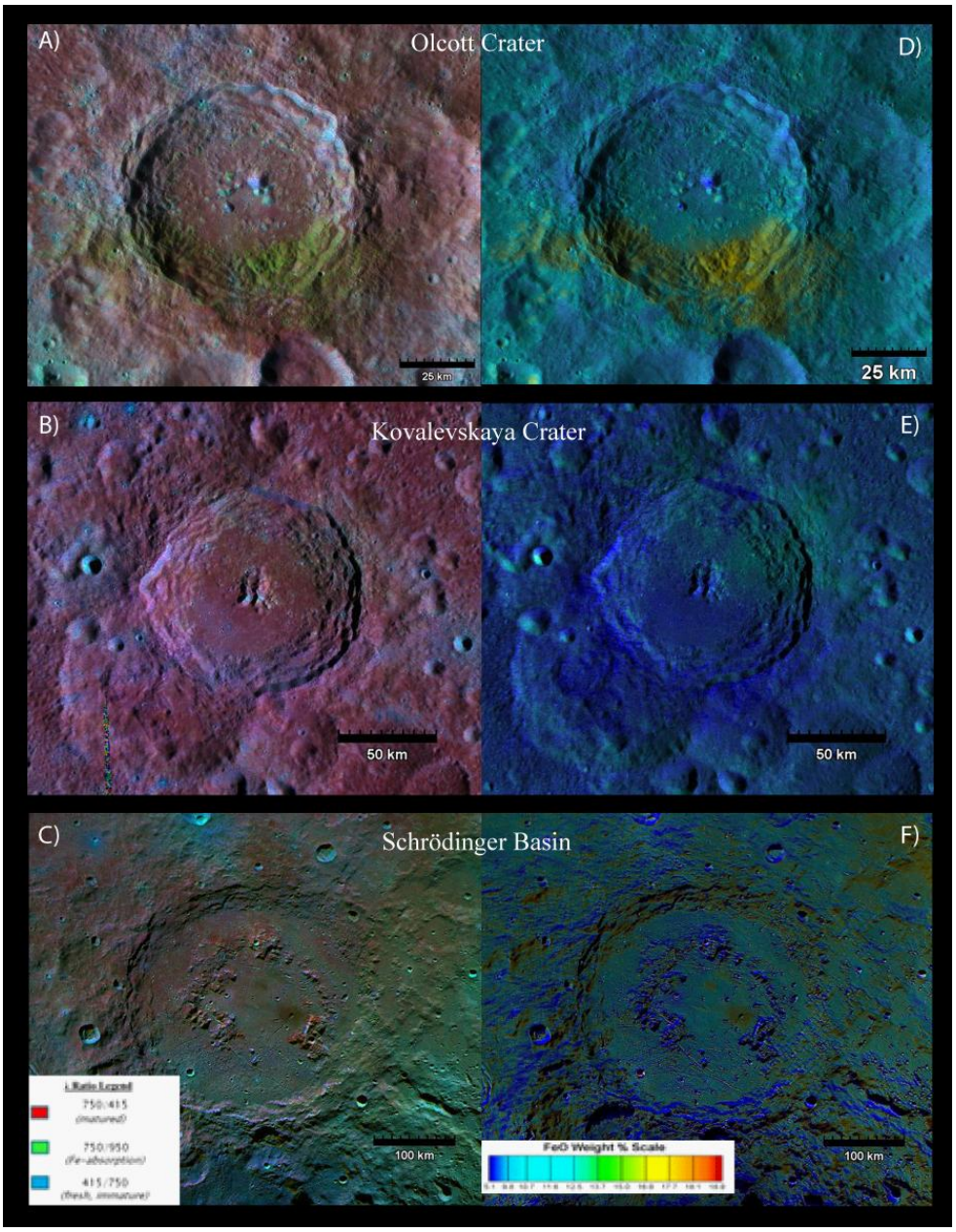

Figure 4.4: Composite maps of the study sites derived from Clementine UV-VIS data overlaid on LROC WAC mosaics. A) - C) Colour ratio composite maps highlight the distribution of mature (red) and fresh (blue) surfaces, and the presence of mafic content (green). D) - F) FeO weight % maps of each site. Iron rich regions of Olcott and Kovalevskaya craters spatially match the mafic rich areas of the colour ratio composite maps. The range of iron content within Schrödinger is likely skewed due to the high phase angles likely present at the latitude range of the basin. [Image credit: ISRO/NASA/GSFC/Arizona State University]

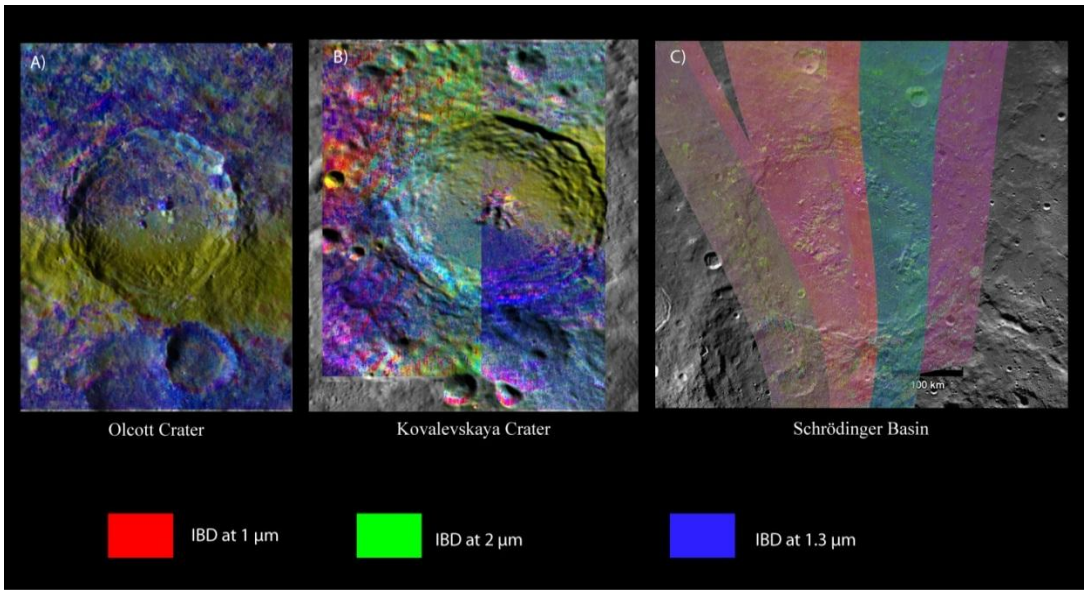

Figure 4.5: Integrated Band Depth (IBD) composite parameter maps derived from Chandrayaan-1 M^3 data for each of the study sites overlie LRO Wide Angle Camera (WAC) global mosaics to accentuate the distribution of absorption band features over impact related morphological features. [Image credit: ISRO/NASA/GSFC/Arizona State University]

presence of all parameters with equal strength. The IBD strength spectral parameter map was used to assess the distribution of these spectral parameters at a first order crater scale and also determine sample spots for capturing individual spectral profiles representative of the various colours identified in the spectral parameter map. Sampling was conducted on freshly exposed surfaces using 3x3 and 5x5 pixel window sizes of individual M^3 data products. The IBD map for Schrödinger basin is not reliable in its results and is not used in the interpretations (Fig. 4.5C). The extreme range of spectral parameters in the IBD parameter map is due to the lack of sufficient instrument calibration of the original product file that was available during the study. Therefore, the sites selected for spectral profiling at Schrödinger basin are selected based on observations using LRO WAC and NAC data.

The radar instrument (Mini-RF) on the Lunar Reconnaissance Orbiter has identified around craters (greater than 50 km in diameter) a variety of impact melt deposits, including pools and flow features, that are not discernible in image data (Neish et al., 2011; Carter et al., 2012). The surfaces of these melt deposits appear rough at the centimeter to decimeter scale, whereas the same feature appears smooth in image data. The range in radar roughness exhibited within these deposits are linked to the changes in the melt morphology – such as the clast to melt ratio, type of flow feature, or deposition of blocky material (Carter et al., 2011 and references therein). Mini-RF transmits circular-polarized radar waves and receives back polarization data in both the horizontal and vertical polarization (Nozette et al., 2010). The roughness of a surface can be determined from the circular polarization ratio (CPR) factor – a comparison between radar with similar polarization as the transmitted beam, and radar with opposite polarization as the transmitted (Nozette et al., 2010). Mini-RF captures data in the S-band wavelength (12.6 cm; with a resolution of 15 m/pixel), and is sensitive to changes in the surface and subsurface at the centimeter to decimeter scales (Carter et al., 2012).

Stokes parameters are a set of values that describe the polarization state of electromagnetic radiation, i.e., the level of radar backscatter received by the instrument. Transmitted radar waves in the S-band range can penetrate approximately 1 m below the

surface (Carter et al., 2012). This means that radar can still identify buried impact melt deposits that have been subsequently buried under regolith or have matured due to exposure to solar radiation (Campbell et al., 2010). In this study, only the first Stokes parameter (*S-1)* is used in analysis, as it measures the total radar backscatter (Carter et al., 2012 and references therein). Both the CPR and total backscatter (S-1) band data are combined to generate colourized radar mosaics (Fig. 4.6). This helps in understanding the roughness of the surface. Colourized mosaics are also used because they help enhance radar characteristics that may not obvious individually in grayscale view, e.g., impact melts with different ranges in clast content are observable at the centimetre and decimetre scale in colourized mosaics (Carter et al., 2012).

Map-Projected Calibrated Data Record (MAPCDR) files of the circular polarisation ratio and the total radar backscatter (S-1 band) were downloaded from the Lunar Orbital Data Explorer portal (ode.rsl.wustl.edu/moon). Radar data was processed, calibrated, and map projected using mission specific scripts within the ISIS v.3software. CPR data was overlaid on total radar backscatter using Adobe Photoshop to generate colourized radar mosaics of Olcott and Kovalevskaya craters (Fig. 4.6), similar to techniques outlined in Chapter 2, section 2.2.1 for Schrödinger basin. Individual greyscale radar mosaics of the CPR and S-1 bands for each of the craters can be found in Appendix A.

4.2.2 Calculating melt volumes

The calculated impact melt volume around each selected complex crater (Table 4.1) was calculated with a combination of techniques. At each crater site, the dimensions of the original transient cavity, and the proposed melt volume were first calculated using model estimates (Cintala and Grieve, 1998). The next step was to calculate the areal extent and melt volumes of identified melt deposits around each crater site. The methods of calculating these values are discussed further below.

Dimensions of transient cavity (Table 4.1), including the diameter and depth, volume of impact melt generated within the cavity, and percentage of impact ejected or retained within the cavity were calculated with techniques defined by Cintala and Grieve (1998).

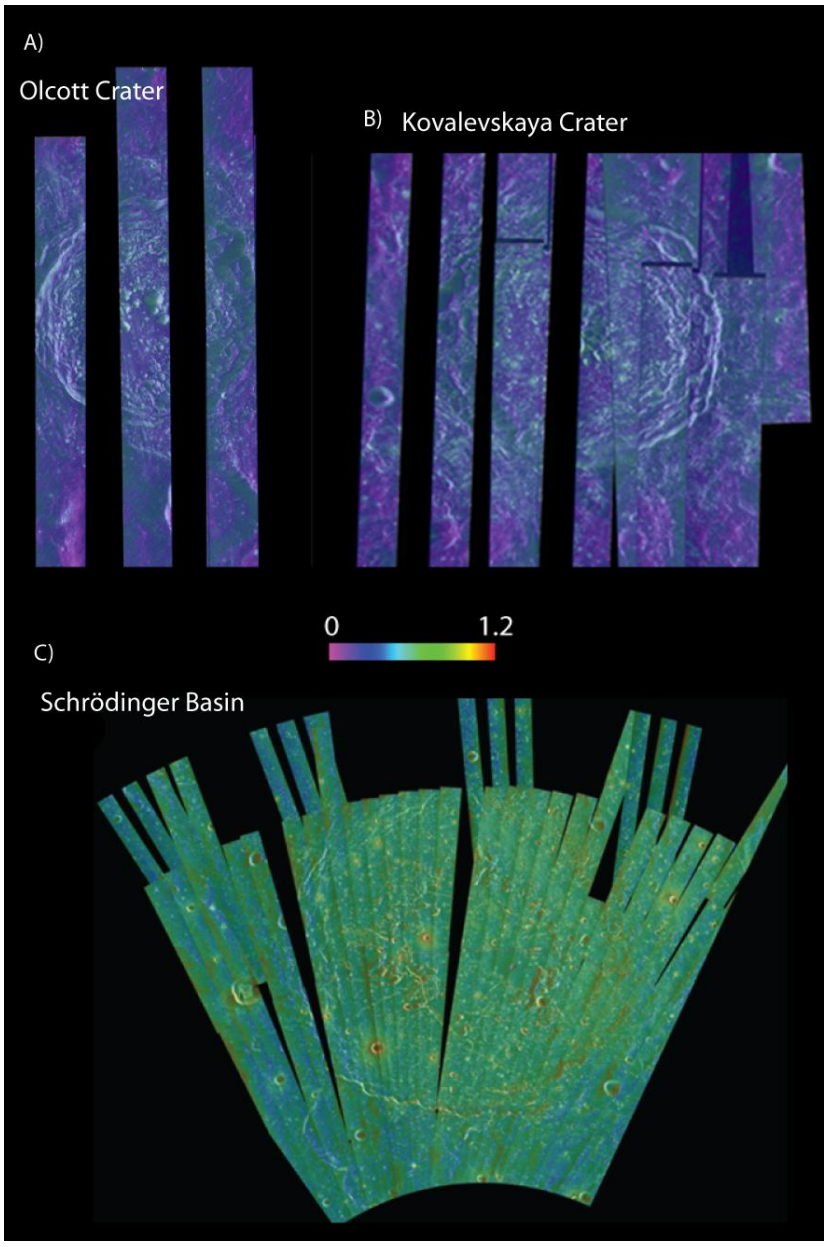

Figure 4.6: Circular polarization ratio (CPR) mosaics overlaid on total radar backscatter mosaics to generate colourized radar mosaics for the study sites (from the Mini-RF instrument aboard LRO). The colour bar refers to the unitless range in circular polarization ratio. Smooth surfaces have low CPR and total backscatter, appearing purple in the colour mosaics. Rough surfaces have high CPR and total backscatter levels, and appear red in the colour mosaics. [Image credit: ISRO/NASA/JHUAPL/LPI]

In each case, the impact event was assumed to be generated by a chondritic projectile striking onto an anorthosite target at 16.1 km s^{-1}, same as the values used by Cintala and Grieve (1998) in estimating melt volumes for a variety of simple and complex craters.

The diameter of the transient cavity was calculated using

$$D_{TC} = 1.16\left(\frac{\rho P}{\rho t}\right) dp^{0.78} vi^{0.44} g^{-0.22} \quad \text{(Equation 1)},$$

where D_{TC} is the diameter of the transient cavity; ρP is the density of the projectile; ρt is the density of the target; dp is the diameter of the projectile; v_i is the impact velocity; and g refers to lunar gravity. The values used for each of these parameters are summarized in Table 4.2.

The diameter of the projectile was calculated using

$$dp = 0.828 Dsc^{0.20} \left(\frac{\rho P}{\rho t}\right)^{-0.42} Dr^{1.09} vi^{-0.56} g^{0.28} \quad \text{(Equation 2)},$$

where D_{SC} is the diameter of the simple to complex crater transition; ρP is the density of the projectile; ρt is the density of the target; Dr is the final crater diameter; v_i is the impact velocity; and g refers to lunar gravity. The values used for each of these parameters are summarized in Table 4.2.

The volume of impact melt generated relative to the transient cavity diameter was calculated using

$$Vm = cD_{tc}^{d} \quad \text{(Equation 3)},$$

where c and d are constants are listed in Table 4.2. The depth of excavation and depth of melting of materials within the transient cavity is derived from Fig. 4.7. The percentages of melt ejected or retained (Fig. 4.8) within the transient cavity were estimated using the

Table 4.1: Numerical Calculations of the Transient Cavity for the study sites

Feature	Rim-Rim Crater Diameter (km)	Transient Cavity Diameter *[1] (km)	Transient cavity Depth*[2] (km)	Total Volume of Impact Melt within Transient Cavity *[3] (km^3)	Transient Cavity Depth of Melting *[4] (km)	Transient Cavity Depth of Excavation *[4] (km)	% of melt retained within Transient Cavity *[5]	% of melt ejected from Transient Cavity *[5]	Volume of melt retained within Transient Cavity (km^3) *[6]	Volume of melt ejected from Transient Cavity (km^3) *[7]
Olcott Crater	81	68.2	22.7	1632.3	~16	10	50	50	816.1	816.1
Kovalevskaya Crater	113	92.6	30.9	5288.8	20	~12	53	47	2803.1	2485.7
Schrödinger Basin	312	214.7	71.5	1.35E+05	60	30	59	41	7.9E+04	5.5E+04

*1. Equation 1 in this chapter

*2. Transient Cavity Depth = 1/3 Transient Cavity diameter (Dence, 1973; Grieve et al., 1989)

*3. Equation 3 in this chapter

*4. Figure 7 in this chapter

*5. Figure 8 in this chapter

*6. Total melt volume in cavity x % of melt retained within cavity

*7. Total melt volume in cavity x % of melt ejected from cavity

Table 4.1 (cont'd): Numerical Calculations of the Impact Melt Volume for the study sites

Feature	Area of observed melt on the crater floor (sq. km)	Measured thickness of melt on the crater floor *[8] (m)	Volume of observed melt within crater floor (km^3) *[9]	Area of observed melt on terraces (sq. km)	Measured thickness of observed melt on terraces *[8] (m)	Volume of observed melt on terraces (km^3) *[10]	Area of melt deposits beyond crater rim (sq. km)	Measured thickness of melt deposits beyond crater rim *[8] (m)	Volume of melt deposits beyond crater rim (km^3) *[11]	Area of melt deposit on central uplift (sq. km)	Measured thickness of melt deposits on central uplift *[8] (m)	Volume of melt deposits on central uplift (km^3) *[12]	Total observed impact melt volume (km^3)
Olcott Crater	1500	2900 to 4300	4.35E+03 to 6.45E+03	45.2	10 to 45	4.1E-01 to 1	40	80	3.2	0.34	20 to 40	6.8E-03	4.35E+03 to 6.45E+03
Kovale-vskaya Crater	3378	5900 to 6700	1.99E+04 to 2.26E+04	340	100	3.4E+01	1224	80 - 220	97 - 270	1.75	15	2.6E-02	2.02E+04 to 2.29E+04
Schrödi-nger Basin	5.1E+04	600 to 2000	3.10E+04 to 7.23E+04	1.07E+04	400 to 450	4.28E+03 to 4.82E+03	3.05E+04	1500	4.58E+04	670	200 to 400	130 to 270	1.18E+05 to 1.49E+05

*8. See Appendix B for calculation methods

*9. Melt thickness x crater floor area

*10. Melt thickness x area of melt on terrace

*11. Melt thickness x area of melt pond

*12. Melt thickness x area of melt veneer

Table 4.2: Parameter values used for transient cavity and impact melt calculations

Parameter	Value	Source
Simple to Complex crater transition diameter	21 km	Pike, 1980
ρp	3.58 (chondrite)	Cintala and Grieve, 1998
ρt	2.734 (anorthosite)	Cintala and Grieve, 1998
v_i	16.1 m/s	Shoemaker and Wolfe, 1987
g	1.63 m/s^2	
c	1.42 x 10^{-4}	Cintala and Grieve, 1998
d	3.85	Cintala and Grieve, 1998

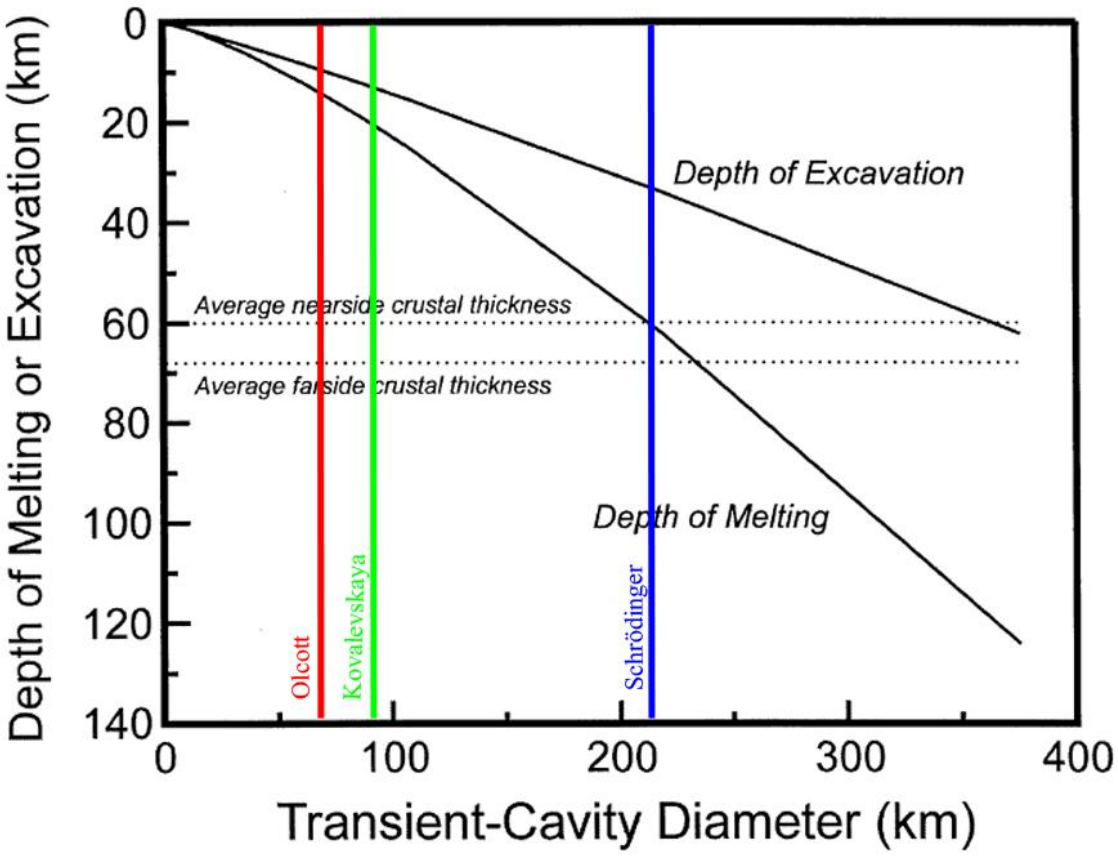

Figure 4.7: Estimates on the depth of excavation and depth of melting for materials within a transient cavity with increasing diameter size. For reference, the locations of the three study sites are plotted on the figure. Modified from Cintala and Grieve (1998).

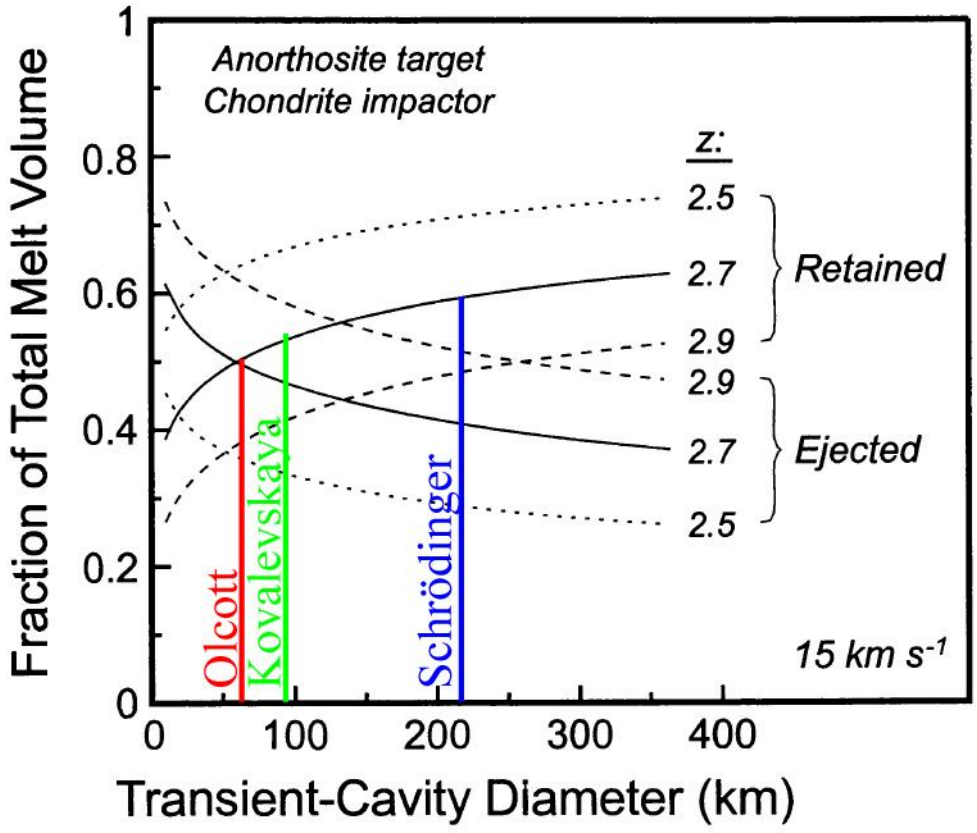

Figure 4.8: Percentage of total melt volume retained within a transient cavity or ejected from the transient cavity. For reference, the locations of the three study sites are plotted on the figure. Modified from Cintala and Grieve (1998).

assumption that the excavation flow field has a unit less value of 2.7, as stated by Cintala and Grieve (Fig. 16; 1998) in their calculations. The next step was to calculate the volume of the melt deposits identified in this study. This included calculating the area and thickness of the melt deposits on the crater floor, along the terraced walls and overlying ejecta deposits. Areal values were calculated using built-in scripts within JMars for Earth's Moon and ArcGIS® software.

With a combination of LOLA altimetry data, LRO Camera imagery data, and spectral characterization of the impactite units, a variety of techniques were used in calculating the thickness of melts depending on their location with respect to the crater (the exact methods can be found in Appendix B. The thickness of the melt sheet on the crater floor was calculated in two ways: 1) extrapolating the slopes of the crater walls to a point of intersection to obtain the true crater depth. Melt thickness was then calculated as the difference the observed depth and calculated depth; and 2) looking for any anomalies in the spectral representation of post-event crater features when compared to the general spectral content of the crater floor (using composite maps, and sample spectral profiles). This provided a range in the melt thickness of the crater floor.

The thickness of melts within the wall terraces, and beyond the crater rim in ponded deposits were individually calculated using LRO LOLA data (Appendix B), following techniques used in the melt volume calculations at King crater (Heather and Graham, 2003; Ashley et al., 2012). Regardless of the technique used, the assumption made was that at all locations, the slopes surrounding the melt deposits and the original floor surface were topographically smooth (regardless of location within the crater), i.e., the presence of faults typical of complex craters was not factored into the thickness and volume calculations. Finally, the volume of observed melt was the product of the areal extent of the mapped melt unit, and the calculated melt thickness (Table 4.1).

4.3 Results

The craters in this study are well-preserved with major the major crater morphology and impactite units easily identifiable - e.g., crater ejecta, sharp rims, terrace walls and crater

floors with central uplifts. Geological sketch maps illustrate the extent of each of the identified units at the three study sites (Fig. 4.9). Exterior impact melt deposits in the map floors with central uplifts. Geological sketch maps illustrate the extent of each of the identified units at the three study sites (Fig. 4.9). Exterior impact melt deposits in the map (Fig. 4.9) refer to the observation of melt deposits beyond the crater floor (this includes deposits over central uplifts, on terrace surfaces, and beyond the crater rim). From image data, impact melt deposits are identified both within and beyond the crater floor at each of the study sites. Impact melt deposits are smooth, have low albedo, and fill in around much of the hummocky terrain on the crater floor (Fig. 4.9). Melt deposits are found as thin veneers along each of the central uplifts, and as pooled deposits over crater terraces. Pooled deposits are also identified beyond the crater rim overlying crater ejecta (Fig. 4.9). UV-VIS-NIR reflectance data reveals great detail about the rock compositions present at each crater site, and the degree of surface maturity. Clementine colour ratio composite images (Fig. 4.4A–C) indicate that the terrain is mostly mature, due to exposure to solar radiation for much of the lunar history. The presence of some mafic component is discernible in colour ratio composite maps, particularly at Olcott (Fig. 4.4A), and Kovalevskya crater (Fig. 4.4B). The iron distribution maps highlight the presence of notable mafic areas within the feldspathic terrain much better than the colour ratio composite maps (Fig. 4.4D–F). As noted in Chapter 2 – section 2.3.1, the effects of high phase angles encountered by the Clementine instrument at the latitudes of Schrödinger are taken into account when interpreting the information from the iron distribution map (Fig. 4.4F). M^3 derived IBD parameter maps (Fig. 4.5) and sampled spectral profiles (Fig. 4.10) of the morphological units within each of the craters suggest a heterogeneous distribution of mafic and anorthosite materials. Sampled spectral profiles (Fig. 4.10) of the morphological units within each of the craters indicate the presence of both low and high-Ca pyroxenes and plagioclase feldspar. While the distribution of mafic material is not ubiquitous, it alludes to the complexity of the target subsurface (as seen in Olcott crater and Schrödinger basin in previous chapters).

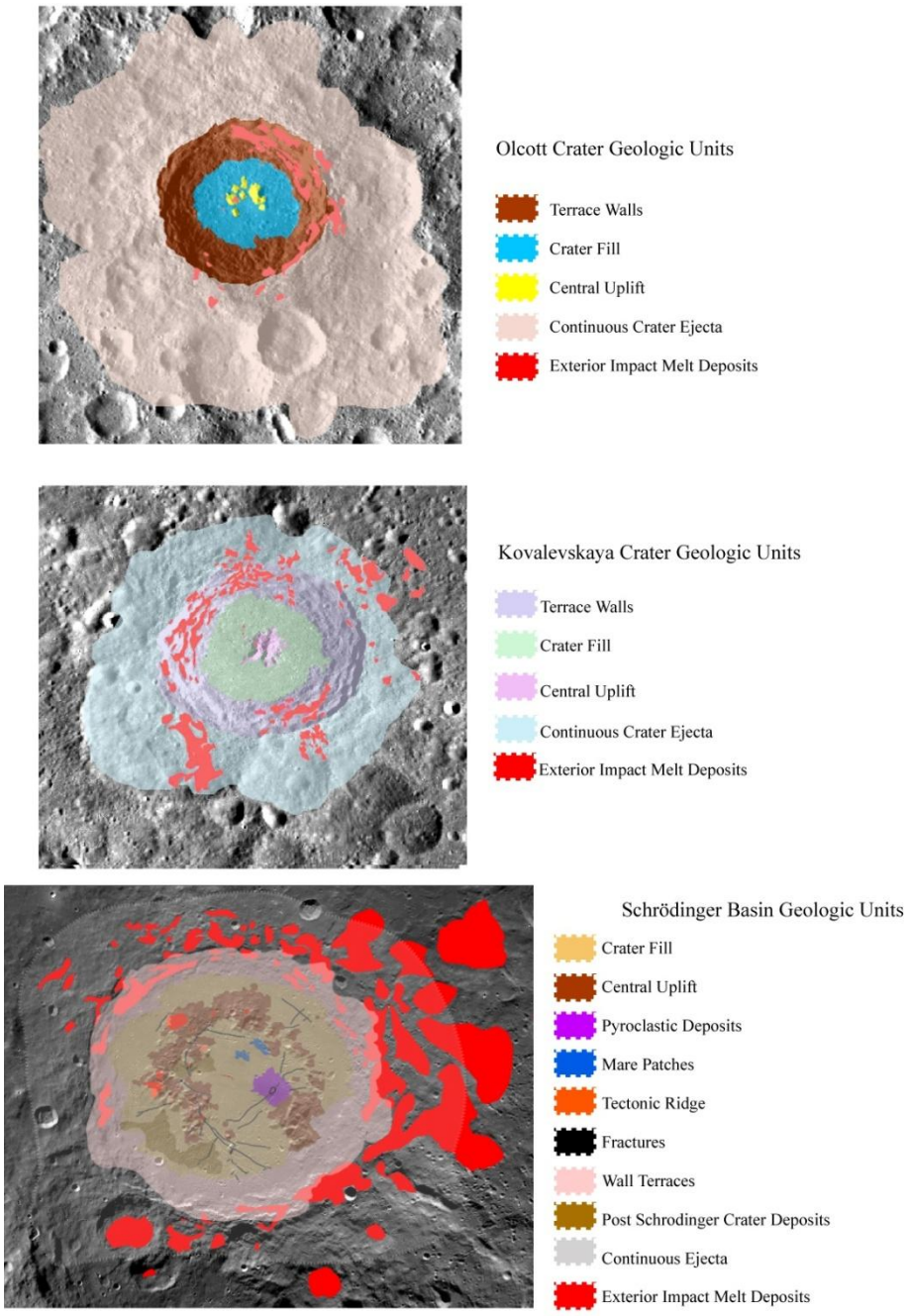

Figure 4.9: Geological sketch maps of Olcott crater, Kovalevskaya crater, and Schrödinger basin focusing on the distribution of impact melt deposits recognized beyond the crater floor. The basemap is a global mosaic derived from the Lunar Reconnaissance Orbiter Wide Angle Camera. The distribution maps for Olcott crater and Schrödinger basin are modified from versions included in Chapters 2 and 3. [Image credit for basemaps: NASA/GSFC/Arizona State University]

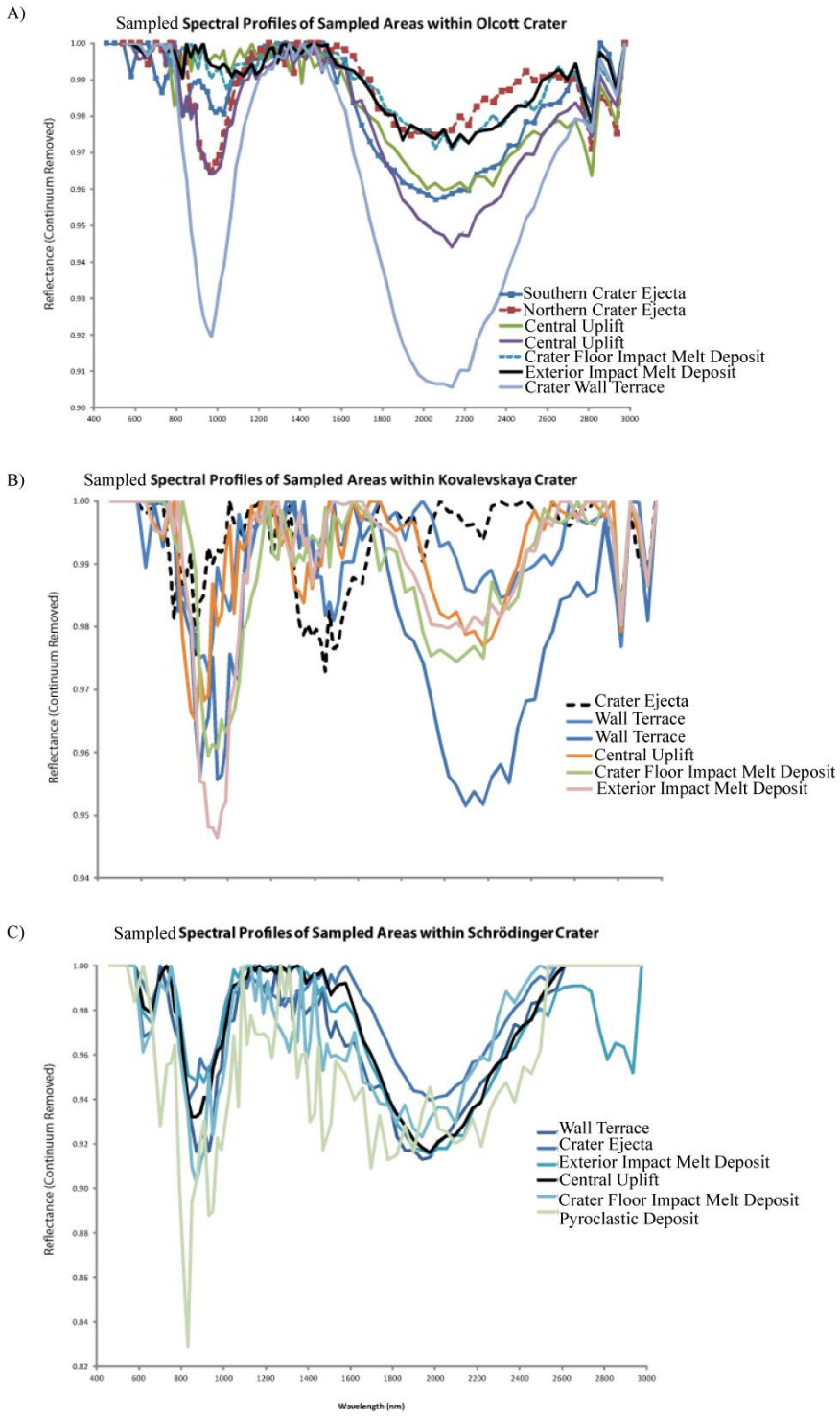

Figure 4.10: Chandrayaan-1 M^3 derived spectral profiles of sampled geological units for Olcott crater, Kovalevskaya crater, and Schrödinger basin. There is a strong presence of low-Ca pyroxenes in all craters, but some areas indicate the presence of plagioclase feldspar and high-Ca pyroxene rich materials.

With radar data, high CPR and radar backscatter values are indicative of a rough surface (Carter et al., 2012), appearing bright and red on the colour radar mosaic (Fig. 4.6). Smooth surfaces have low backscatter and low CPR and, therefore, appear dark and purple on the colour mosaics (Fig. 4.6). The radar characteristics of Olcott and Kovalevskaya craters at a regional scale reveal that much of the terrain has low CPR and total backscatter (Fig. 4.6A, B). Radar data also does not show any variations in the smoothness or roughness of the exterior impact melt deposits when compared to the surrounding terrain (Figs. 4.4, 4.12, 4.13; Appendix A).

The characterizations of melt deposits at each crater site (Figs. 4.11, 4.13, 4.15) are further detailed in sections 4.3.1 – 4.3.3.

4.3.1 Impact Melt Deposits within Olcott Crater

As stated earlier, impact melt deposits are located within various crater units of Olcott crater (Fig. 4.11). The floor of Olcott crater is filled with a mixture of smooth and hummocky terrain (Fig. 4.11A). Smooth surfaces (interpreted as impact melt deposits due to the lack of association with any nearby volcanic areas) are also found as low albedo pond deposits draped over terraced walls and concentrated along the eastern section of the crater (Fig. 4.9A, 4.11 B–D). As stated in Chapter 3, an investigation of the available LRO NAC images indicates multiple instances of impact melt veneers draped over some of the central peaks (Fig. 4.11E). The maximum extent of mapped melt deposits is approximately 43.9 km beyond the crater rim (or 1 crater radius distance) (Fig. 4.9A).

Composite maps using multispectral datasets indicate a strong mafic presence along the southern crater floor and wall (Figs. 4.4A, D; 4.5A; Chapter 3). The spectral profiles indicate there is both low and high-Ca pyroxene, and plagioclase feldspar (Fig. 4.10A; Chapter 3). Surface roughness maps of the crater reveal that impact melt deposits within the crater walls and on the floor appear smooth (Figs. 4.6A, 4.12, Appendix A). However, it is unknown at this point if the smooth texture of the surface is due to the presence of melts, a difference in the levels of regolith thickness between the smooth and rough surfaces, or topographic effect. The effects of topography or material composition

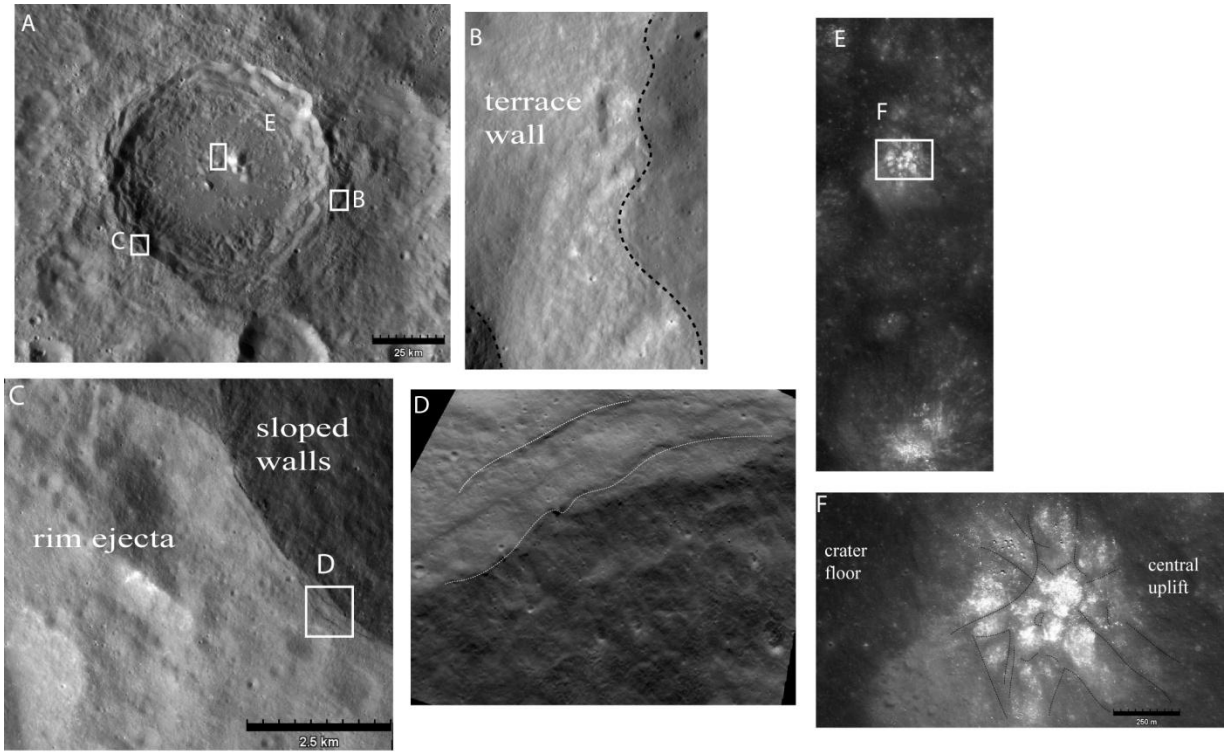

Figure 4.11: Impact melt deposits of Olcott crater. A) LRO WAC mosaic context view of melt deposits highlighted in 4.11B–F. B) Smooth, low albedo impact melt deposit near the crater rim. NAC M130870650LC. C) Crater rim area and context view for Fig. 4.11D. NAC M182767638LC. D) 3-D view of thin impact melt veneers drape over the crater ejecta just beyond the rim, 100x vertical exaggeration. E) Smooth low albedo melt fill areas between the central uplifts on the crater floor. Image width is 2.5km. NAC M108460950RC. F) Smooth, low albedo melt is draped over much of the peak surface, with some exposures of bright, presumably blocky, peak material. [Image credit: NASA/GSFC/Arizona State University]

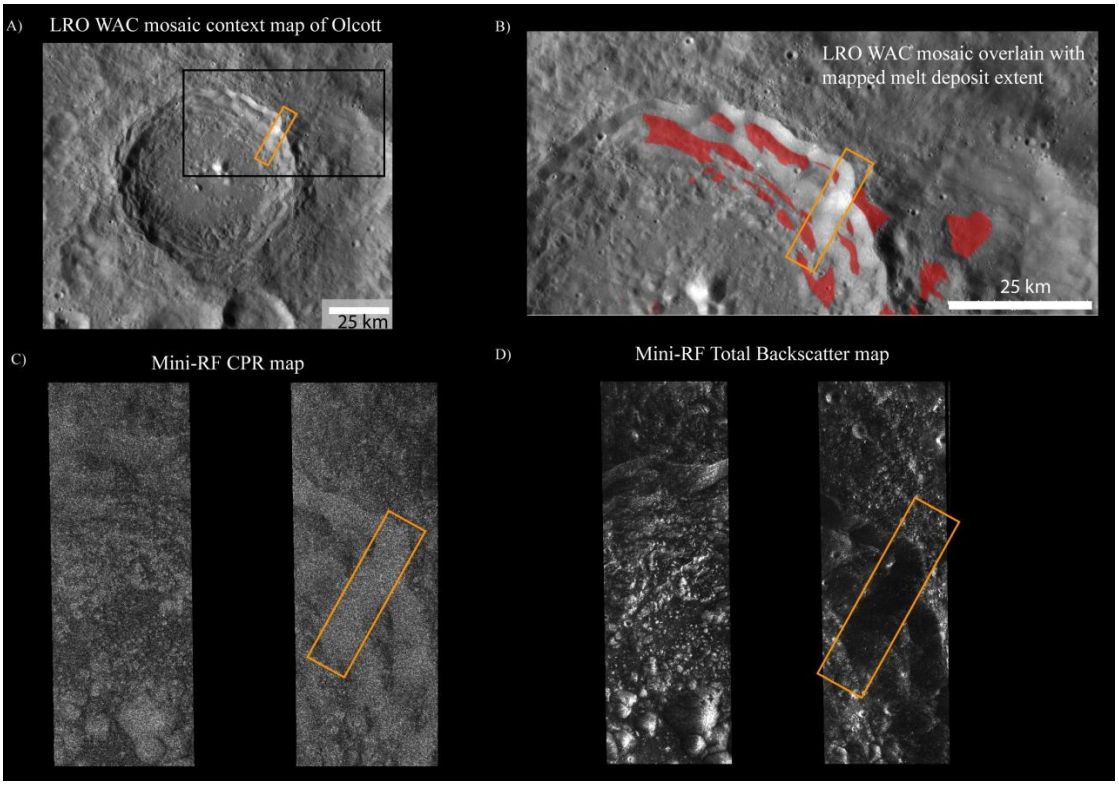

Figure 4.12: Comparison between the radar and visible observations of impact melt deposits around Olcott crater. A) LRO WAC global context view of the crater area. Black box outlines the context location of Fig. 4.12 B–D. Orange box provides a context location of the bright wall slope for reference in Fig. 4.12B–D. B) Mapped melt deposits (red polygons) overlaid on LRO WAC image mosaic. Image modified from Fig. 4.9A. C) Circular polarization radar map of the area within 4.12B. Much of the melt deposits (where data is available) have low CPR. D) Total radar backscatter map of the area within 4.12B. Much of the area including the melt deposits is radar dark, with the exception of some of the central uplifts on the crater floor. [Image credit: ISRO/NASA/JHUAPL/LPI]

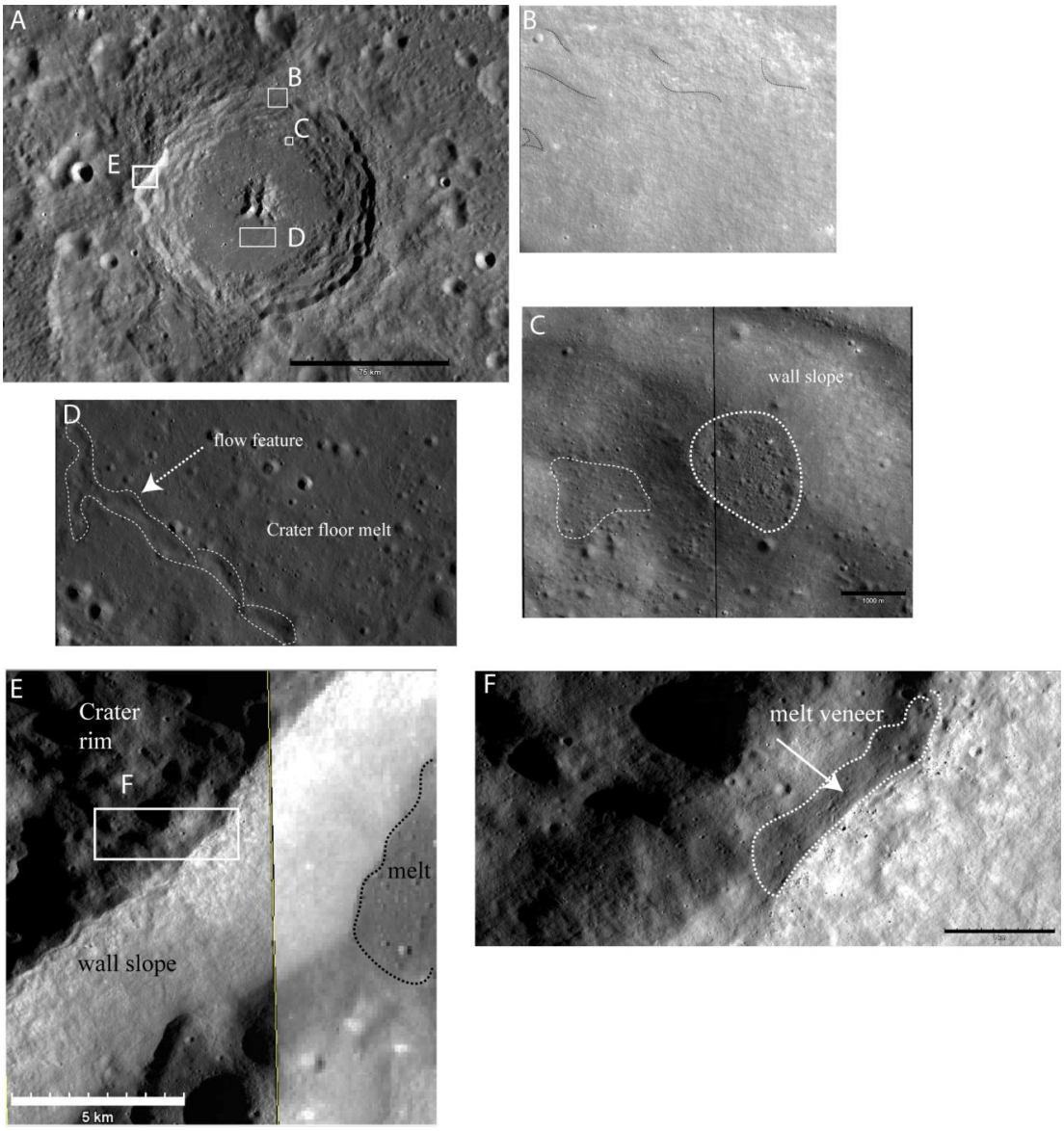

Figure 4.13: Impact melt deposits of Kovalevskaya crater. A) LRO WAC mosaic context view of melt deposits highlighted in Fig. 4.12 B–F. B) Thin melt veneers drape wall slopes and terrace surfaces. LRO NAC M136029701LC. C) A pooled melt deposit (within white dash polygon) is observed along the crater wall, close to the crater floor. NAC mosaic M136029701LC; RC. D) Sinuous feature on the crater floor, either indicative of melt flow or a scarp: LRO NAC M103001717LC. E) Smooth melt deposits on terrace floor. LRO WAC global mosaic basemap; LRO NAC M178488703LC. F) Melt veneers draped along the crater rim edge. LRO NAC M178488703LC. [Image credit: NASA/GSFC/Arizona State University]

draped over parts of the central uplift and crater walls (Fig. 4.9B; 4.13B, E, F). Beyond the crater floor, melt deposits appear as pooled deposits filling low-lying depressions within terrace surfaces (Fig. 4.13C, E). Pooled deposits also overlie on crater ejecta beyond the crater rim (Fig. 4.9B), and the extent is more widespread than at Olcott crater (Fig. 4.9A). The maximum extent of impact melt deposits is 97 km beyond the crater rim (~2 crater radii).

The multispectral datasets reveal a surface much like what is observed at Olcott crater (section 4.3.1). Composite maps reveal a concentrated presence of pyroxene rich materials along the north east section of the crater floor, terrace, and rim (Figs. 4.4B, E; 4.5B).The M^3 derived IBD spectral parameter map (Fig. 4.5B) and sampled spectral profiles (Fig. 4.10B) indicates the diverse distribution of both low and high-Ca pyroxene, and plagioclase feldspar (Fig. 4.8B). Much like the observations at Olcott crater (Fig. 4.12), radar coverage of Kovalevskaya show impact melt deposits as radar smooth features at the centimetre to decimetre scale (Fig. 4.6B; Fig. 4.14, Appendix A), when compared to the surrounding surface. As mentioned earlier for Olcott crater, it is unknown at this point if the smooth areas of the surface are as they appear due to topographic, or compositional effects, or are characteristic of the impact melt deposits.

In addition to the above observations, a sinuous feature has also been observed on the crater floor (Fig. 4.13D). This feature appears near the southern edge of the central uplift, and extends 11 km south west towards the crater terrace walls. The lack of volcanic evidence suggests this feature to be impact melt in origin, possibly a lobe flow feature. Radar data does not show any change in surface roughness associated with this feature (Fig. 4.6B, 4.14, Appendix A). The M^3 IBD spectral parameter map (Fig. 4.5B) for Kovalevskaya crater does not show any spectral characteristics unique within this feature when compared to the remainder of the crater. This is different from the results of an observation made within Copernicus crater (Dhingra et al., 2012) – a 96 km diameter complex crater that would be considered similar in size to Kovalevskaya crater. A 30 km flow feature has been observed on the floor of Copernicus crater, and shows up distinctly in the IBD spectral parameter map (Dhingra et al., 2012). The interpretation is that the feature within Copernicus crater is that it may represent a late stage flow event triggered

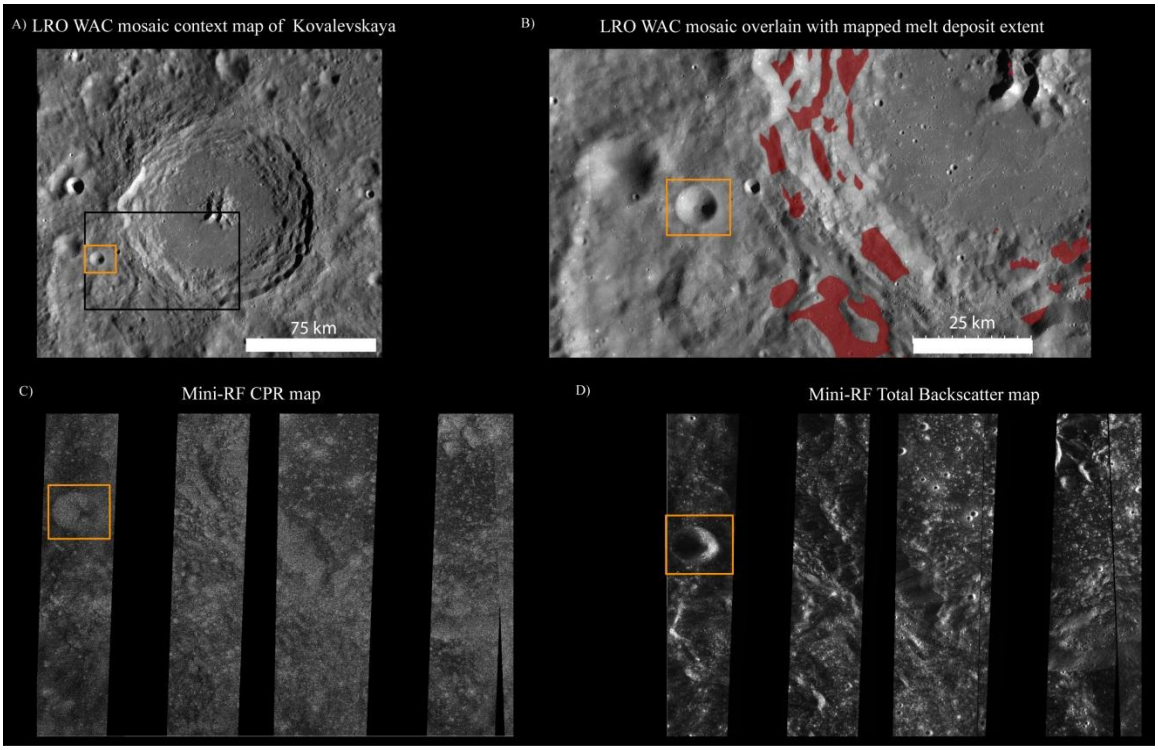

Figure 4.14: Comparison between the radar and visible observations of impact melt deposits around Kovalevskaya crater. A) LRO WAC global context view of the crater area. Black box outlines the context location of Fig. 4.14B–D. Orange box provides a context location of the simple crater for reference in Fig. 4.13 B–D. B) Mapped melt deposits (red polygons) overlaid on LRO WAC image mosaic. Image modified from Fig. 4.9B. C) Circular polarization radar map of the area within Fig. 4.14B. Much of the melt deposits (where data is available) have low CPR. D) Total radar backscatter map of the area within Fig. 4.14B. Much of the area including the melt deposits is radar dark, with the exception of materials on the crater floor. [Image credit: ISRO/NASA/JHUAPL/LPI]

by the breach of pooled melt (Dhingra et al., 2012). As this is not observed within Kovalevskaya crater, another mode of formation is that perhaps this is a result of tectonic responses of extension and contraction.

4.3.2 Impact Melt Deposits associated with Schrödinger Basin

The basin floor of Schrödinger is filled with a mixture of smooth and hummocky terrains interpreted to be impact melt rocks (see Chapter 2). As part of this study, a combination of photographic evidence from the LRO WAC data and LOLA topography has led to the visual identification of impact melt deposits beyond the crater floor (Fig. 4.15). Further to the study discussed in Chapter 2, the mapping of exterior impact melt deposits has continued and the results are summarized here (Fig. 4.9C). At the LRO WAC image scale, melt deposits show visible contrast when compared to the immediate surroundings (the deposits are not within the pre-identified mare patch, volcanic deposit regions), are smooth and low in albedo, and fill depression areas (Fig. 4.15 B–F). Impact melt appears largely as pooled deposits that fill low-lying areas within the central peak ring, terrace surfaces, and overlie ejecta deposits (Figs. 4.9, 4.15). The identification of deposits at the LRO NAC image scale is more challenging, unlike the case for the previous two craters. While visible contrasts exist along the terraced surfaces to make the identification possible, much of the areas beyond the basin rim show similar textural characteristics as the surrounding ejecta material (e.g. Fig. 4.15F). Therefore, the mapping and characterization of the melt deposits discussed here are based on observations using LRO WAC global mosaics. Much of the exterior melt deposits are located along the eastern rim of the basin (Fig. 4.9C). The maximum extent of impact melt deposits is 387 km from crater centre (or 3 crater radii).

From a spectral perspective, the profiles of the various crater units (Fig. 4.9C) indicate the presence of low-Ca pyroxene materials (Fig. 4.10C). The distribution of the occurrence of fresh mafic-rich spectra, as identified using the automated basalt algorithm on Clementine data (Fig. 2.7), indicates that there are still many areas beyond the basin rim that have a mafic signature different from the remainder of the basin. This is even after accounting for the effects of high-phase angle for latitudes near Schrödinger basin. Many of these basalt rich areas are within pooled melt deposits over continuous ejecta, as

mapped in this study (Fig. 4.9C). So far, M^3 derived spectral profiles within the available coverage areas (Fig. 4.5C) have not yielded anything unique to confirm the results from Clementine data. However, due to instrument calibration issues and the high pixel volume of M^3 data to sort through this has made the spectral characterization of impact melt deposits within Schrödinger basin challenging. It is also unknown at this point if the impact melt deposits of Schrödinger represent materials that are part of the terrace wall or the impact melt deposits of the larger South Pole-Aitken basin.

For the basin area that has available radar coverage (Fig. 4.6C, Appendix A; Fig. 2.10), impact melt deposits identified both within and beyond the basin rim (Fig. 4.9C) do not noticeably differ in radar properties when compared to the surrounding regolith. The regional extent appears radar rough. This suggests that perhaps the melt deposits are covered by regolith thick enough to affect their radar brightness (Appendix A).

4.3.3 Estimates on the volume of melt present around complex craters

Calculations of the transient cavity diameter, depth, and volume of melt generated; and the estimates on the areal extent and volume of observed melt deposits within each crater are summarized in Table 1. The areal extent of impact melt deposits increase as the crater diameter increases (Fig. 4.9). This matches model predictions that state the relative volume of melt generation increases as the crater event increases (Cintala and Grieve, 1998). The difference between the volume calculations from this study and model estimates are in the amount of melt that either remains within the crater or is ejected beyond the crater rim. The volume of identified melt deposits around Olcott crater is 2x the model estimate (Table 4.1), and a look at the distribution of identified melt deposits reveals that most of the melt remains within the crater interior. The fraction of observed melt retained within the crater interior is much higher (90% retained, ~10% ejected) than the model prediction of 50:50. The volume of identified melt deposits around Kovalevskaya crater is ~ 8-10 x the model estimate (Table 4.1). However, according to the mapping calculations, the volume of melt that is ejected represents only a percentage of the entire melt volume. The volume of identified melt deposits around Schrödinger basin models well with estimates with minimal difference (the mapped melt deposits are

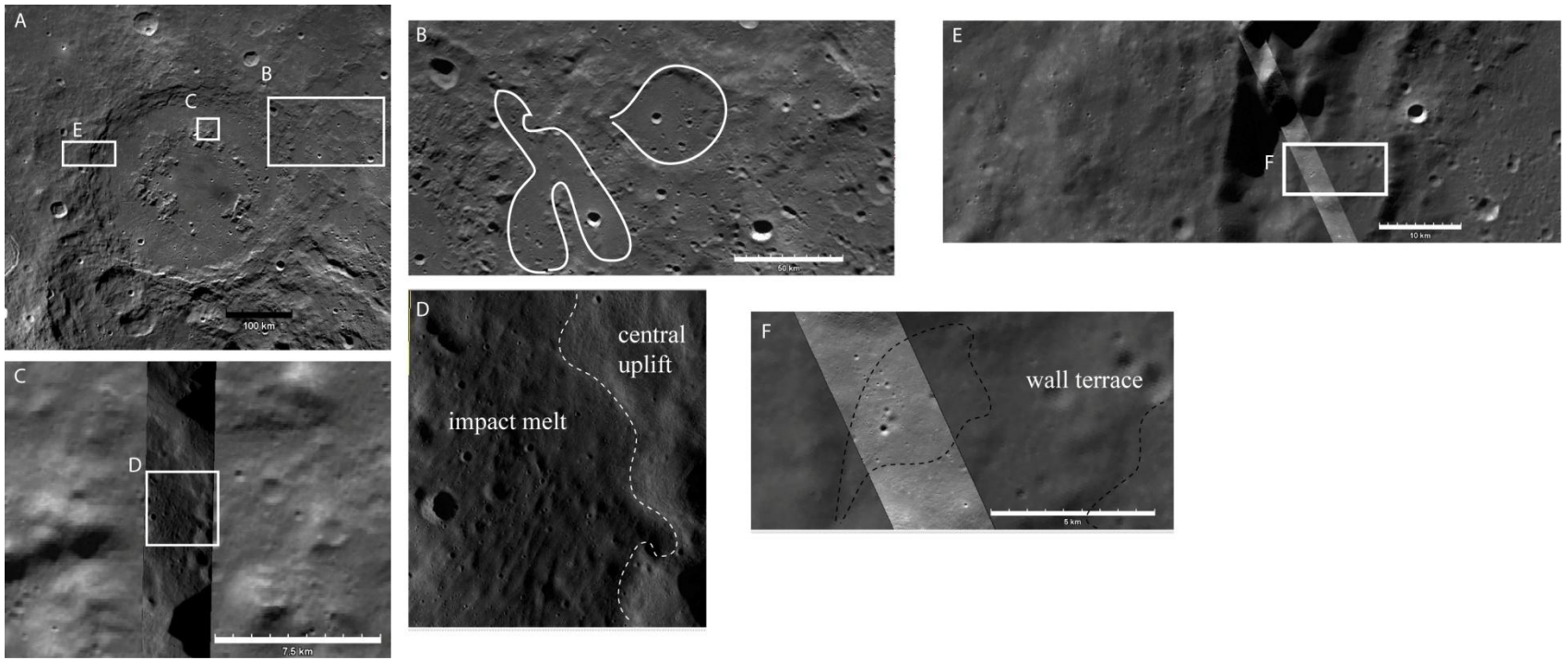

Figure 4.15: Impact melt deposits of Schrödinger basin. A) LRO WAC mosaic context view of melt deposits highlighted in 13 B–F. B) Melt ponds (within white polygons) beyond the basin rim appear smooth and fill pre-existing crater depressions, NAC M115422614LC. C) Impact melt deposits draped over the central uplifts and along the basin floor, NAC M115422614LC. D) Smooth deposit nestled in a topographic low within the central uplift. E) Melt deposits along wall terraces on the western rim, LRO WAC basemap, NAC M172182757RC. F) Comparison of the appearance of impact melts between the global WAC and high resolution NAC data. With optimal phase angles, the presence of melt deposits can be identified at latitudes of Schrödinger basin. [Image credit: NASA/GSFC/Arizona State University]

10% greater than the model estimates; Table 4.1). The amount of melt retained within the crater is only slightly larger than model estimates (70% of mapped melts are within the crater, compared to the model predictions of 60%). The potential discrepancies in the calculation methods of observed and modeled melts are detailed in section 4.4.2.

4.4 Discussion

The fusion of multiple datasets provides a unique way to recognize and characterize impact melt deposits, particularly around impact craters that have been exposed to solar radiation and on a surface that has experienced impact bombardment much of the surface history. As can be seen from this study, all the selected craters are located within the lunar highlands – assumed to consist of predominantly anorthosite (Chapter 1, section 1.5.1.1). However, the spectral trends seen within Schrödinger basin (Chapter 2), Olcott crater (Chapter 3), and Kovalevskaya crater (this chapter) indicate a strong mafic presence, one that is not uniform. This diverse distribution in mafic minerals could be the result of either 1) continuous redistribution of target materials from other subsequent impact events on the Moon, perhaps mafic material from a volcanic region from another part of the Moon was deposited at these crater sites; or 2) is indicative of the presence of mafic rich material within the target subsurface. Material that is subsequently covered by highland ejecta from later impact events on the Moon. The regional location of lunar craters also determines the types of mineral materials that may be excavated, as seen with Schrödinger basin that is on the edge of the South Pole-Aitken basin (Chapter 2), and Olcott crater that is within the larger Lomonosov-Fleming basin (Chapter 3). It is unknown at this point if Kovalevskaya crater lies within any older, degraded impact basin of any type to explain the presence of mafic-rich deposits to the north east section of the crater terraces and floor. The geological history of this crater is required however it is beyond the scope of this study. The presence of pre-existing topography and the diversity in target layers can affect the distribution of various impactite materials including the emplacement of late-stage impact melt and ejecta deposits.

4.4.1 The identification of exterior melt deposits

The purpose of this study has been to determine the advantages of conducting multispectral analyses of impact craters, and testing the effectiveness in identifying impact melt deposits

beyond the crater floor with these datasets. The craters in this study are either Erastothenian or Imbrian in age (ranging from 1.1–3.5 Gyr; Wilhelms, 1987), exposed to solar radiation and subsequent impact history. Impact melts along wall terraces and beyond the rims on lunar craters have long been characterized as: 1) smooth deposits with low albedo that pool within depressions, 2) occur with various morphologies such as veneers, and melt ponds, and 3) are not associated with any volcanic origin of source (Hawke and Head, 1977). LRO Wide Angle (WAC) and Narrow Angle (NAC) camera data provides the highest resolution available yet to identify impact melt deposits around complex craters that are moderately aged (Fig. 4.9). However, the identification of impact melt deposits around complex impact craters is challenging, and is limited only to visible datasets. Multispectral datasets (as explained further below) are useful in broadly determining the compositional and surface texture details of impact melts within the craters. The identification of melt deposits strictly using reflectance spectroscopy is not possible (explained further in Chapter 5, section 5.2.1).

The intent of using radar data in the analyses of characterizing impact melt deposits around complex craters is to determine if impact melt deposits can be identified with radar, in addition to what is already observable with visible image data. Radar data (Fig. 4.6) of the study sites do not show much variation in the roughness factor of the exterior impact melt deposits (at the centimetre and decimetre scales). This is different from the results from other recent simple and complex craters, where radar detects excellent variations in the surface roughness of impact melts, and where radar data has been greatly useful in identifying impact melts not recognized in photographic datasets (Carter et al, 2012). While there is room for error in calculating the exact values for CPR and total backscatter at Olcott and Kovalevskaya craters, the general trends in surface roughness and radar detail is still used in our interpretations. The data gaps in radar coverage of the study areas make it challenging to characterize impact melts throughout the crater area. The lack of radar roughness within impact melt deposits at these study sites may be due to the effects of topography, composition, or non-pristine state of impact melts (as discussed in sections 4.3.1–4.3.3).

Reflectance spectroscopy, in this study, has been useful in broadly identifying the compositional detail of the study area, and determining if any mafic materials exist. The high spectral resolution M^3 data provides details on the location of the band absorptions. Colour ratio maps using both the Clementine and M^3 datasets highlight the complexity of target

materials (Figs. 4.5, 4.6). Reflectance values of profiles at all sites are typically low and are normalized to determine the spectral characteristics of units (Fig. 4.10), highlighting of the effects of maturity on the intensity of the absorption features. The presence of the absorption feature at specific wavelengths in the UV-VIS-NIR confirms the occurrence of lunar minerals such as pyroxene, plagioclase feldspar, etc. However, the spectral characteristics of the exterior melt deposits are undistinguishable from spectral characteristics of the crater floor. This is an indication that the melts emplaced beyond the crater floor are the same materials as the crater floor melts, and that the compositional variation in the target surface extends to depth.

4.4.2 Melt Volumes

With the availability of high resolution of image data, identifying the extent of impact melt deposits has provided better opportunities to estimate the total melt volume within lunar craters (Mazarico et al., 2011; Denevi et al., 2012). This study uses the combination of LRO Camera data and topography to estimate (at a very simple first-order approach) the observed volume of melt deposits around each crater and compare it with model estimates on the volume of melt that is generated within the transient cavity. The effects of melt differentiation are not considered in our analyses. It is interesting to note that, while differential scaling is observed with respect to the total volume of melt generated within a transient cavity (i.e. the volume increases as the transient cavity diameter increases; Cintala and Grieve, 1998), there is also a spatial correlation that as the final crater size grows, a significant amount of melt deposits are emplaced beyond the crater rim (Fig. 4.9). The increasing scale of crater modification with crater wall collapse and central uplift modification and the role of pre-existing topography is providing added momentum for melt deposits to emplace beyond the crater rim (Osinski et al., 2011).

The thickness of the melt sheet on the crater floor of Olcott has been determined using the depth-diameter ratio of complex craters (Croft, 1980; Appendix B). Using equations for calculating the dimensions of the transient cavity (Eqs. 1 – 3), model melt volumes are estimated for each of the craters, including the percentage of melt retained or ejected relative to the transient cavity (section 4.3.4). While the total volume of mapped melt rocks is within an order of magnitude of model estimates (Table 4.1), the more interesting fact is that the

faction of observed melt retained within the crater (i.e., on the crater floor, and along terrace and central hill surfaces) comprises roughly 90% of the total mapped melt volume. This may be due to the lack of identification of melt deposits beyond the crater rim. The distribution of the melt deposits beyond the crater rim is at present limited. This highlights the need for further and detailed mapping of the melt deposits within Olcott crater to assess if the observation is of accurate measure. The high amount of image data presently available from the Lunar Reconnaissance Orbiter instrument suite for the study area has made it challenging to filter through all the images and takes up time beyond the scope of this project.

At Kovalevskaya crater, the mapped melt volume is as much as seven times than model predictions (Table 4.1). Not many post-Kovalevskaya event impact craters are identified within the melt deposits of Kovalevskaya, craters that may be excavating materials from beneath the crater floor. It is particularly difficult to gain topographic profile of crater features that are identifiable at the scale LRO NAC imagery, but not resolvable at the LOLA altimetry level in order to get melt thickness values of any of the melt morphologies.

Schrödinger basin does have the largest areal extent of melt deposits beyond the crater rim (Fig. 4.9), when compared to the other two study sites. The volume of mapped melt deposits are also the highest between the three craters. This is expected given the scale of the impact event, and the greater depths of excavation and melting estimates (Fig. 4.7). The large range in the total volume of mapped melt deposits at Schrödinger basin (Table 4.1) is due to the varied range of melt thicknesses assumed for the crater floor. As detailed in Appendix B, two approaches were taken to estimate the thickness: one using the measurements of smaller simple craters on the crater floor to estimate a minimum thickness; and the other approach by extrapolating the shape of the original basin to gauge the crater floor melt thickness (Fig. B.1). The minimum and maximum thicknesses are used in calculating the volume – which results to a wide range.

According to the calculations from this study, melt deposits ejected beyond the basin rim are identified for Schrödinger basin and represent ~30 – 50% of the total melt volume. This is close to the approximation from models estimates (~41%; Table 4.1). If model estimates on the scaling of impact melt volumes are consistent, then the results from this study indicate that the identification of impact melt deposits beyond the rim of Schrödinger basin are

accurate at the image scale, and that the extent of impact melt deposits beyond the crater rim as identified here should be considered for future studies, particularly in understanding the crater dynamics and emplacement theories of impactites at the scale of a peak-ring basin.

One potential aspect that can explain the differences between model and observed volumes of melt deposits is the thickness measurements of melt deposits used in calculating volumes of different melt morphologies. As seen in Table 4.1, there is a range in thicknesses for the mapped melt deposits. The methods used here are very simplistic, and thickness estimates for smaller fresher lunar craters are now starting to be studied using high resolution altimetry and image data (e.g., Ashley et al., 2010; Denevi et al, 2012). Ideally, the thickness of melts would have to be calculated for each and every deposit, and those values would be used to get an accurate estimate on the volume. However, measuring the thicknesses for each deposit is beyond the scope of the project. Therefore, the value of melt thicknesses used is the average thickness between the smallest and largest deposits of the same morphology where present. In principle, small melt deposit would have the thinnest melt layer, and the largest deposit would have the thickest melt layer. Nevertheless, the results of this study are meant to be a starting point in addressing this question on how the distribution of melt deposits relate to model calculations. For large areal deposits that cover a wide area of the target surface, multiple topographic profiles can be taken thereby giving an accurate estimate on the depth of melt. However for smaller deposits, where the resolution of LRO Camera (NAC) data is higher than the spatial resolution of LOLA data –the depths of many melt deposits are not resolvable at the scale of the topographic data from LOLA. Therefore, an average thickness measurement is taken, which is not totally representative of each deposit.

The values of melt deposit thicknesses surrounding lunar craters are not well understood. Models have helped gain perspective on the process, however much of our understanding on the thickness of melt deposits is still based on terrestrial observations (Grieve and Cintala, 1992). Even then the melt thickness around terrestrial craters vary – depending on the regional topography, effects of erosion (Grieve and Cintala, 1992), and target rock compositions (Osinski et al., 2008). Spectral characteristics of the crater area do provide a good constrain on the amount of melt present. As seen with Schrödinger basin (Appendix B), the observation of a spectrally different area on the crater floor (Fig. 2.7) provides an endmember on the amount of melt present within a crater floor. The effects of pre-existing

regional topography many also explain the range in melt thicknesses (Chapter 3, section 3.3.1). The spectral details of post-crater events within Olcott and Kovalevskaya are not that different from spectral details of the remainder of the crater floor, therefore there is a possibility that post-event craters measured on melt deposits are not tapping through the entire melt sheet. Therefore, the approach to use the depth-diameter ratio of complex craters is used (Fig. B.1), and the estimates on melt thickness and melt volume is, a very basic value. Modelling parameters (Table 4.2) need to account for target heterogeneity. At present, the model calculations are based on a chondrite projectile striking an anorthosite target (Cintala and Grieve, 1998). However, as is seen in this study, the target surface is heterogeneous, with mafic rich materials being excavated at depth (Chapter 2; Chapter 3; this chapter section 4.3.2).

4.5 Summary

This study investigates the distribution of impact melt deposits around complex craters. This study shows that for larger craters, the amount of melt generated increases, and the extent of impact melt deposits present beyond the crater floor also increases. Similarly, the amount of impact melt volume generated also increases. For determining the compositional makeup and extent of impactite materials, reflectance spectroscopy datasets are essential tools. This provides a complimentary tool in understanding the impact cratering process.

The combination of multiple datasets including image, altimetry, and reflectance spectroscopy prove to be a useful tool in mapping the distribution of melt deposits within and beyond the crater floor. Furthermore, the availability of high resolution spatial and topographic data provides new opportunities to estimate the thickness of melt deposits and depth estimates of the crater floor. This allows for an estimate on the melt volume around large complex lunar craters. However, various assumptions are made in the calculations of impact melt thicknesses, and crater floor depths which lead to a large range in impact volume estimates. More efforts are required in making more accurate measurements for melt thicknesses, and better model experiments on the depths of impact craters – both simple and complex.

4.6 References:

Ashley, J.W., Robinson, M.S., Hawke, B.R., van der Bogert, C.H., Hiesinger, H., Sato, H., Speyerer, E.J., Enns, A.C., Wagner, R.V., Young, K.E., and Burns, K.N. 2012. Geology of the King crater region: New insights into impact melt dynamics on the Moon. *Journal of Geophysical Research*. **117**: E00H29.

Bowker, D.E., and Hughes, J.K. 1971. Lunar Orbiter Photographic Atlas of the Moon. National Aeronautics and Space Administration, Special paper. **206**, 1 – 45.

Bray, V.J., Tornabene, L.L., Keszthelyi, L.P., McEwen, A.S., Hawke, B.R., Giguere, T.A., Kattenhorn, S.A., Garry, W.B., Rizk, B., Caudill, C.M., Gaddis, L.R., and C.H. van der Bogert. 2010. New insight into lunar impact melt mobility from the LRO camera. *Geophysical Research Letters*. **37**, 21: L21202.

Campbell, B.A., Carter, L.M., Campbell, D.B., Nolan, M., Chandler, J., Ghent, R.R., Hawke, B.R., Anderson, R.F., and Wells, K. 2010. Earth-based 12.6-cm wavelength radar mapping of the Moon: New views of impact melt distribution and mare physical properties. *Icarus*. **208**, 2: 565–573.

Carter, L.M., Neish, C.D., Bussey, D.B.J., Spudis, P.D., Patterson, G.W., Cahill, J.T., and Raney, R.K. 2012. Initial observations of lunar impact melts and ejecta flows with the Mini-RF radar. *Journal of Geophysical Research*. **117**, E00H09.

Christensen, P.R., Engle, E., Anwar, S., Dickenshied, S., Noss, D., Gorelick, N. and Weiss-Malik, M. 2009. JMARS – A Planetary GIS. American Geophysical Union Fall Meeting. Abstract # IN22A-06.

Cintala, M.J., and Grieve, R.A. 1998. Scaling impact melting and crater dimensions: Implications for the lunar cratering record. *Meteoritics and Planetary Science*. **33**, 4: 889–912.

Croft, S.K. 1980. Cratering flow fields: implications for the excavation and transient expansion stages of crater formation. Proceedings, 11th Lunar and Planetary Science Conference. pp. 2347-2378.

Crown, D.A., and Pieters, C.M. 1985. Spectral properties of plagioclase and pyroxene mixtures. 16th Lunar and Planetary Science Conference. 158–159.

Dence, M.R. 1973. Dimensional analysis of impact structures. *Meteoritics*, **8**: 343–344.

Denevi, B.W., Koeber, S.D., Robinson, M.S., Garry, W.B., Hawke, B.R., Tran, T.N., Lawrence, S.J., Keszthelyi, L.P., Barnouin, O.S., Ernst, C.M., and Tornabene, L.L. 2012. Physical constraints on impact melt properties from Lunar Reconnaissance Orbiter Camera images. *Icarus*. **219**, 2: 665–675.

Dhingra, D., and Pieters, C.M. 2012. Spectroscopy of Impact Melts – Results from Lunar Crater Tycho. 43rd Lunar and Planetary Science Conference. Abstract #1836.

Dhingra, D., Pieters, C.M., Head, J.W., and Isaacson, P.J. 2012. Large flow feature at Copernicus Crater – Implications for impact melt evolution and emplacement chronology. 43rd Annual Lunar and Planetary Science Conference. Abstract #2339.

Donaldson Hanna, K.L., Cheek, L.C., Pieters, C.M., Mustard, J.F., Wyatt, M.B., and Greehangen, B.T. 2012. Global identification of crystalline plagioclase across the lunar surface using M^3 and Diviner data. 43rd Lunar and Planetary Science Conference. Abstract # 1968.

French, B. 1998. Traces of Catastrophe. *Lunar and Planetary Institute Contribution.*. **954**: pp. 1–120.

Gaddis, L., Anderson, J., Becker, K., Becker, T., Cook, D., Edwards, K., Eliason, E., Hare, T., Kieffer, H., Lee, E.M., Mathews, J., Soderblom, L., Sucharski, T., Torson, J., McEwen, A., and Robinson, M. 1997. An overview of the integrated software for imaging spectrometers (ISIS). Proceedings, 27th Lunar and Planetary Science Conference. Abstract # 1226.

Giguere, T.A., Hawke, B.R., Blewett, D.T., Bussey, D.B.J., Lucey, P.G., Smith, G.A., Spudis, P.D., and Taylor, G.J. 2003. Remote sensing studies of the Lomonosov-Fleming region of the Moon. *Journal of Geophysical Research*. **108**, E11: 5118.

Gillis, J.J., and Spudis, P.D. 1996. The composition and geologic setting of lunar far side maria. 27th Lunar and Planetary Science Conference. pp. 413 - 414.

Green, R.O., Boardman, J., Pieters, C.M., Clark, R. and the M^3 Team. 2010. An algorithm for estimation and correction of the thermal emitted radiance with preservation of spectral structure in data measured by the Moon Mineralogy Mapper. 41st Lunar and Planetary Science Conference. Abstract #2331.

Grieve, R.A.F., Garvin, J.B., Coderre, J.M., and Rupert, J. 1989. Test of a geometric model for the modification stage of simple impact crater development. *Meteoritics*. **24**: 83–88.

Grieve, R.A.F., and Cintala, M.J. 1992. An analysis of differential impact melt-crater scaling and implications for the terrestrial impact record. *Meteoritics*. **27**: 526–538.

Hawke, B.R., and Head, J.W. 1977. Impact melt on lunar crater rims. Proceedings, Symposium on Planetary Cratering Mechanics. pp. 815–841.

Heather, D. J., and Dunkin, S. K. 2003. Geology and stratigraphy of King crater, lunar farside. *Icarus*. **163**, 2:307–329.

Hiesinger, H., and Head, J.W. (III). 2006. New Views of Lunar Geoscience: An Introduction and Overview. In *Reviews in Mineralogy and Geochemistry*, edited by Jolliff, B.L., Wieczorek, M.A., Shearer, C.K., and Neal, C.R. **60**: 1–81.

Howard, K.A. and Wilshire, H.G. 1975. Flows of impact melt in lunar craters. *Journal of Research of the U. S. Geological Survey*. **3**: 237–251.

Lucey, P.G., Blewett, D.T., Jolliff, B.L. 2000. Lunar iron and titanium abundance algorithms based on final processing of Clementine ultraviolet – visible images. *Journal of Geophysical Research*. **105**, E8: 20297–20306.

Mazarico, E., Barnouin, O.S., Salamunićcar, G., and Zuber, M.T. 2011. Impact melt volume estimates of small- to medium-sized lunar craters from Lunar Reconnaissance Orbiter data. 42nd Lunar and Planetary Science Conference. Abstract # 2075.

Melosh, H.J. 1989. *Impact Cratering: A Geologic Process*. New York: Oxford University Press. 245p.

Mest, S.C. 2011. The geology of Schrödinger basin: Insights from post – Lunar Orbiter data. In *Recent advances and current research issues in lunar stratigraphy*, edited by Ambrose, W.A., and Williams, D.A. Special Paper # 477. Boulder, Colorado: Geological Society of America. pp. 95–115.

Mustard, J.F., Pieters, C.M., Issacson, P.J., Head, J.W., Besse, S., Clark, R.N., Klima, R.L., Petro, N.E., Staid, M.I., Sunshine J.M., Runyon, C.J., and Tompkins, S. 2011. Compositional diversity and geologic insights of the Aristarchus crater from Moon Mineralogy Mapper data. *Journal of Geophysical Research*. **116**: E00G12.

Neish, C.D., Carter, L., Bussey, D.B.J., Cahill, J., Thomson, B., Barnouin, O., and the Mini-RF team. 2011. Correlation between surface roughness and slope on a lunar impact melt. 42nd Lunar and Planetary Science Conference. Abstract # 1881.

Neish, C.D., Glines, N., Carter, L.N., Bray, V.J., Hawke, B.R., Bussey, D.B.J., and the Mini-RF Science Team. 2012. New lunar impact melt flows as revealed by Mini-RF on LRO. 43rd Lunar and Planetary Science Conference. Abstract # 1659.

Nozette, S., Spudis, P., Bussey, B., Jensen, R., Raney, K., Winters, H., Lichtenberg, C.L., Marinelli, W., Crusan, J., Gates, M., and Robinson, M. 2010. The Lunar Reconnaissance Orbiter Miniature Radio Frequency (Mini-RF) Technology Demonstration. *Space Science Reviews*. 150, 1–4: 285–302.

Osinski, G.R., and Spray, J.G. 2005. Tectonics of complex crater formation as revealed by the Haughton impact structure, Devon Island, Canadian High Arctic. *Meteoritics and Planetary Science*. **40**, 12: 1813–1834.

Osinski, G.R., Grieve, R.A.F., Collins, G.S., Marion, C., and Sylvester, P. 2008. The effect of target lithology on the products of impact melting. *Meteoritics and Planetary Science*. **43**, 12: 1939 – 1954.

Osinski, G.R., Tornabene, L.L., and Grieve, R.A.F. 2011. Impact melt and ejecta emplacement on terrestrial planets. *Earth and Planetary Science Letters*. **310**, 3: 167–181.

Pieters, C.M. 1978. Mare basalt types on the front side of the moon: A summary of spectral reflectance data. Proceedings, 9th Lunar Planetary Science Conference. pp. 2825–2849.

Pieters, C.M. 1986. Composition of the lunar highland crust from near-infrared spectroscopy. *Review of Geophysics*. **24**: 557–558.

Pieters, C.M., Staid, M.I., Fischer, E.M., Tompkins, S., and He, G. 1994. A sharper view of impact craters from Clementine data. *Science*. **266**: 1844 – 1848.

Pike, R.J. 1980. Control of crater morphology by gravity and target type: Mars, Earth, Moon. Proceedings, 11th Lunar and Planetary Science Conference. pp. 2159–2189.

Robinson, M.S., Brylow, S.M., Tschimmel, M., Humm, D., Lawrence, S.J., Thomas, P.C., Denevi, B.W., Bowman-Cisneros, E., Zerr, J., Ravine, M.A., Caplinger, M.A., Ghaemi, F.T., Schaffner, J.A., Malin, M.C., Mahanti, P., Bartels, A., Anderson, J., Tran, T.N., Eliason, E.M., McEwen, A.S., Turtle, E., Jolliff, B.L., and Hiesinger, H. 2010. Lunar Reconnaissance Orbiter Camera (LROC) Instrument Overview. *Space Science Reviews*. **150**, 1–4: 81–124.

Schaal, R.B., Hörz, F., Thompson, T.D., and Bauer, J.F. 1979. Shock metamorphism of granulated lunar basalt. Proceedings, 10th Lunar and Planetary Science Conference. pp. 2547–2571.

Scott, D.H., McCauley, J.F., and West, M.N. 1977. *Geologic atlas of the west side of the Moon*. United States Geological Services. Map I-1034. 1:5M scale.

Shoemaker, E.M., and Wolfe, R.F. 1987. Crater production on Venus and Earth by asteroid and comet impact. 18th Lunar and Planetary Science Conference. pp. 918-919.

Shoemaker, E.M., and Robinson, M.S. 1995. Clementine observations of melt rocks and volcanic materials in the Schrödinger Basin. 26nd Lunar and Planetary Science Conference. Abstract #1297.

Smith, D.E., Zuber, M.T., Jackson, G.B., Cavanaugh, J.F., Neumann, G.A., Riris, H., Sun, X., Zellar, R.S., Coltharp, C., Connelly, J., Katz, R.B., Kleyner, I., Liiva, P., Matuszeski, A., Mazarico, E.M., McGarry, J.F., Novo-Gradac, A-M., Ott, M N., Peters, C., Ramos-Izquierdo, L.A., Ramsey, L., Rowlands, D.D., Schmidt, S., Scott, V.S., Shaw, G.B., Smith, J.C., Swinski, J-P., Torrence, M.H., Unger, G., Yu, A.W., Zagwodzki, T.W. 2010. The Lunar Orbiter Laser Altimeter Investigation on the Lunar Reconnaissance Orbiter Mission. *Space Science Reviews*. **150**, 1–4: 209–241.

Smrekar, S., and Pieters, C.M. 1985. Near-infrared spectroscopy of probable impact melt from three large lunar highland craters. *Icarus*. **63**: 442–452.

Speyerer, E.J., Robinson, M.S., Denevi, B.W., and the LROC Science Team. 2011. Lunar Reconnaissance Orbiter camera global morphological map of the Moon. 42nd Lunar and Planetary Science Conference. Abstract # 2387.

Tompkins, S., and Pieters, C.M. 2010. Spectral characteristics of lunar impact melts and inferred mineralogy. *Meteoritics and Planetary Science*. **45**, 7: 1152–1169.

Wilhelms, D.E., and El-Baz, F. 1977. *Geologic Map of the east side of the Moon*. Department of the interior United States geological survey. Map. I–948. 1:5M scale.

Wilhelms, D.E. 1987. *The geologic history of the Moon,* edited by Wilhelms, D.E., McCauley, J.F., and Trask, N.J. Professional Paper # 1348. Denver, CO: U. S. Geological Survey Printing Office. 302p.

Chapter 5

5 Discussion on the spectral and spatial characteristics of Impact Melt Deposits surrounding lunar complex craters

The Moon has a heavily cratered surface with varying impact crater morphologies. The minimal effects of erosion and the lack of an atmosphere make it an excellent location to study the characteristics of impact craters and the impact cratering process, in general. Constant bombardment of space rocks on the lunar surface has resulted in the record of both simple and complex craters (Chapter 1, section 1.5). The lunar farside has a good preservation of impactite features around large complex craters such as Olcott crater, Kovalevskaya crater, and Schrödinger basin (Chapters 2 – 4) with minimal modifications from later volcanism. Each of the complex craters included in this study have well preserved crater features (Fig. 4.3) including a sharp rim, walls terraces, and a diverse variety of central uplifts that range from peaks, to peak clusters, and peak ring (Fig. 4.3).

Increasing usage of remote sensing satellite instruments including the high-resolution multispectral datasets from the Lunar Reconnaissance Orbiter and Chandrayaan-1 mission instruments provides researchers with excellent new methods for understanding the distribution of various impactites. Camera data is particularly useful in the identification of impact melt deposits associated with each crater. Typically, impact melt deposits are smooth features with low albedo, and the morphologies range from coherent sheets filling the floor of complex craters, or as thin veneers, or pooled deposits that fill depression areas (Figs. 4.11, 4.13, 4.15). The influence to local topography plays a large role in the crater modification stage (Chapter 1, section 1.1.3) and provides added momentum for impact melt deposits to be displaced beyond the crater rim (Fig. 4.9). While the identification capabilities of impact melt deposits are improving, determining the extent of impact ejecta at sites such as Olcott crater, Kovalevskaya crater, and Schrödinger basin is more challenging. The long exposure of the crater terrain to subsequent micrometeorite bombardment, and later impact events is the likely explanation for this.

Impact craters also provide details about the lunar crust through the excavation of subsurface materials. The technique of fusing together high-resolution multispectral and spatial datasets

provides a unique opportunity to compare the compositional aspects of the target surface and the emplacement locations of different rock types over various impactites. The lunar farside has long been assumed to be comprised of mainly lunar highland (i.e., anorthositic and Mg-suite) materials, with minimal amounts of mare volcanism or mafic minerals including spinel or olivine that would be derived from depth (Gilles and Spudis, 1996; Hiesinger and Head, 2006 and references therein). However, from this study it is observed that both Olcott crater (Figs. 3.5C, 4.5) and Kovalevskaya crater (Figs. 4.5, 4.10) display unique distributions of mafic-rich rocks (high-Ca pyroxene, Mg-spinel) that are unlike the compositions of the regional highland terrains. Furthermore, the distributions of the mafic rich minerals are not isolated to a particular feature but rather a result of mechanical mixing. In the case of Olcott crater (Chapter 3), the proximity of to the larger Lomonosov-Fleming basin provides a reasonable assumption that the source of the mafic-rich rocks are from buried cryptomare (Chapter 3, section 3.3.4). At present, the source for the mafic rich exposure at Kovalevskaya crater (Fig. 4.5) is not attributed to any known pre-existing source of mare presence. However, the identification of this anomaly provides researchers with added detail about the immediate subsurface at Kovalevskaya. Schrödinger basin also displays a diverse distribution of mafic-rich minerals over many parts of the basin (Figs. 2.7, 2.9), which has been attributed to the proximity to the South Pole-Aitken basin (Chapter 2, section 2.4.1). This makes it increasingly apparent that the lunar farside crust is not a homogeneous layer of crustal low-Ca pyroxene and anorthosite materials, and instead is more likely interlaced with mafic minerals including high-Ca pyroxene, and Mg-spinel originating at depth.

In addition to the detailed characterizations of impact melt deposits within the crater floor for each of the sites, the availability of high resolution data provides improved opportunities in identifying and characterizing impact crater deposits beyond the crater floor. Later sections in this chapter discuss the capabilities and challenges faced in identifying such melt deposits. The discussion also looks at the role this study provides in the broader scope of impact crater studies and lunar exploration.

5.1 The distribution of impact melt deposits beyond the crater rim

One of the major topics of this study has been to assess the distribution of impact melt deposits around complex craters on the lunar farside, particularly craters that are not fresh and that are moderately aged. Impact melt deposits have long been recognized around young (Copernican age) lunar craters with image data, going back to the Lunar Orbiter (1966–1967) and Clementine (1994) missions. Impact melt sheets fill the crater floor of all the craters (Stöffler et al., 2006), and are emplaced during the crater excavation and modification stages (Osinski et al., 2011). Impact melt deposits beyond the crater floor range from thin veneers on terrace walls to pooled deposits within topographic lows (Figs. 4.9, 4.11–4.13). The availability of high resolution datasets at the scales captured by Lunar Reconnaissance Orbiter (LRO) Wide Angle Camera (WAC) and Narrow Angle Camera (NAC) data makes the identification process much easier; thereby, making the assessment of melt distribution more accurate. For example, large impact melt deposits beyond the rim of Schrödinger basin were recognizable using Clementine data (Shoemaker and Robinson, 1995). However, this study has shown that melt deposits occur along the wall terraces around the crater, and beyond the basin rim both to the south (which were in shadow during previous missions) and east (Chapters 2, 4). The identification of melt deposits around Olcott (Chapter 2) and Kovalevskaya craters has also been successful in this study, for the first time, because of the ability in the instruments to resolve features at those scales (Fig. 4.9).

This work shows that the presence of pre-existing topography affects the distribution of various impactite materials, particularly impact melt deposits around the rims of complex craters studied (Chapters 2 – 4). Earlier studies using model calculations and observations have proposed that much of the melt deposits of Schrödinger basin lie concentrated beyond the eastern rim (Hawke and Head, 1977; Cintala and Grieve, 1998). Mapping of the melts (Chapters 2, 4) reveals that the extent of the melt deposits observed beyond the crater rim is largely concentrated along the north east section of the basin (Fig. 4.9C). Schrödinger basin is located along the terrace walls of the South Pole-Aitken basin (Fig. 2.14). Topography of the South Pole-Aitken basin indicates a drop in elevation throughout the area around Schrödinger basin, particularly to the north east direction (Fig. 2.14). Collapse of the basin walls during crater modification would have made it easier for the impact melts to escape

from the transient cavity and be emplaced beyond the rim. Similar observations have been made at Kovalevskaya and Olcott craters, melt deposits are found beyond the crater rim (Fig. 4.9). From LOLA topography, a number of pre-existing feature outlines can be observed at locations where impact melt deposits are found (Fig. 4.3).

5.2 The role of multispectral datasets in identifying impact melt deposits

Identifying impact melt deposits solely with the use of multispectral datasets is challenging. Image data is needed to first identify melt deposits. Once the extent of melt deposits is determined using image data, reflectance spectroscopy is very useful in determining the compositional characteristics of the deposits and the crater terrain in general. Spectral composite maps together with topography are useful in defining aerial extent of spectral units (Smrekar and Pieters, 1985).

The absorption wavelengths captured by UV-VIS-NIR data in the M^3 data provide excellent detail to determine the types of lunar minerals present at each crater site. Each of the craters investigated in this study are located in lunar highlands, and spectral profiles of their impactite materials indicate the presence of low-Ca pyroxene and plagioclase feldspar (Chapters 2 – 4). The intensities of the plagioclase feldspar absorptions are weak, which is expected because of the dominance of the pyroxene absorptions (Crown and Pieters, 1985; Pieters, 1986). Spectral profiles in this study indicate the presence of mafic rich minerals – particularly high-Ca pyroxene and Mg-spinel (Chapter 2 – 4). This adds a new perspective on the level of mafic activity within the lunar farside because very little evidence of volcanism is present on the surface (Gilles and Spudis, 1996; Hiesinger and Head, 2006 and references therein). This work shows that crater-forming events at the scale of these complex craters excavated mafic-rich materials, and emplaced them within and around the craters (Chapters 2 – 4). This provides details not just about the individual craters, but also about the local geological history and depths to which mafic rich layers may be present within the farside crust.

The spectral characteristics of the impact melt deposits are, however, similar to the general spectral characteristics of the crater. From this study, nothing in the remotely derived spectral detail stands out as being intrinsically characteristic of impact melts. This suggests that the

impact melts emplaced beyond the crater floor are composed of the same materials as the bulk target surface; therefore supporting the suggestion that melts can be emplaced as a secondary ejecta layer phase during the crater modification process (Osinski et al., 2011).

This work has shown that radar data is not particularly useful in identifying impact melt deposits around older complex craters, in contrast to observations around younger craters (Neish et al., 2011; Carter et al., 2012). Radar mosaics of the study areas reveal that much of the impact melt deposits appear the same in radar roughness as the rest of the crater (Fig. 4.4; Appendix B).

5.2.1 Challenges in using the multispectral datasets

At all crater sites in this study, the spectral characterization of impactite units has been limited to sampling at locations that best represent fresh sloped surfaces for an accurate result. Sloped surfaces provide the freshest surfaces that are least affected by regolith build-up. Until the release of the LRO image data in 2009, it was challenging to find fresh rock outcrops to sample spectra from. Clementine UV-VIS data and the Clementine elevation maps were the only multispectral and topographic datasets available during the study on Schrödinger basin (Chapter 2). The geographical location of Schrödinger basin near the South Pole made the identification of fresh surface candidates for spectral sampling limited. The automated algorithm used in identifying fresh surfaces with high mafic content (Antonenko and Osinski, 2011) helped filter through the large UV-VIS dataset of the study area for the identification of mafic rich areas. But the results were limited to identifying fresh basalt locations (Fig. 2.7) – and not to the extent of particularly defining the type of mafic mineral present. M^3 data provides better spectral resolutions in defining the presence of low or high-Ca pyroxene, olivine, and plagioclase feldspar. Due to the unavailability of M^3 data products for the entire basin, conducting an extensive analysis of the Schrödinger basin using this dataset was beyond the scope of the project. Other studies have been published subsequently on the characterization of materials within Schrödinger basin floor using M^3 and LOLA data (Kramer et al., 2011; Kramer et al., 2012).

With the availability of M^3 and LRO image and altimetry data, the spectral and spatial resolutions of the datasets greatly improved (Chapter 1, Table 1.1). Thereby, the potential of finding fresh exposed surfaces or sloped regions increased. However, new challenges arose

due to the different spatial resolutions between the LRO image data (WAC, NAC) and M^3 multispectral dataset. Fresh exposed surfaces that were detectable using image data were not resolvable at the instrument resolution of M^3. This limited the number of sites suitable for spectral sampling. With the large data volumes of the M^3 and LRO camera suite, the process of analyzing each and every image product for identifying melt deposits or sampling every pixel is not possible without the aid of automated scripts. This, therefore, limited the number of individual NAC images that could be processed and investigated in search of melt deposits.

5.3 Central Uplifts of Complex Craters - Assessing the depths of excavation and melting

One aspect of combining various image and multispectral datasets is the ability to determine estimates on the source depth of the materials excavated during these impact events. A crater feature particularly relevant in determining the maximum depths of excavation are central uplifts within complex craters. The general-held view is that minimum depth of origin of the central uplift material coincides with the maximum depth of melting within the transient cavity (Cintala and Grieve, 1998; Figure 1.4). This would indicate that compositions making up the central uplift unit should show spectral characteristics that reflect the maximum depth sampled by the crater event. This provides us a better constraint on the depths at which mafic rich layers may exist; particularly at sites where spectral parameters indicate a strong signature of mafic content yet volcanic activity is not evident on the surface (for example, at Olcott and Kovalevskaya craters.

The depths of excavation and depths of melting for the three study sites are highlighted in Fig. 4.7 and Table 4.1. It is noted that the depths of melting exceeds the depths of excavation for each of the three crater sites as predicted in model calculations (Cintala and Grieve, 1998; Fig. 4.7). The depths of melting range from 16 km for Olcott, 20 km for Kovalevskaya, to 60 km for Schrödinger basin. Current interpretations of the lunar subsurface are that the crust is ~90 km thick on the lunar farside, though much thinner (~40 km) near the South Pole-Aitken basin (Wieczorek et al., 2006). The lunar crust is composed of the regolith, megaregolith, and crustal anorthosites (Fig. 1.6). The upper crust is dominated by plagioclase feldspar and low-Ca pyroxene, but the composition gets increasingly iron rich with depth (plagioclase; low and

high-Ca pyroxene; and olivine) (Tompkins and Pieters, 1999). The depths of melting for Olcott crater and Kovalevskaya crater are within the lunar crust. However, Schrödinger is located near the crust-mantle boundary, therefore some of the mafic enriched materials may be derived from the lunar mantle. However, determining if the mafic source is mantle-derived or represents impact melt deposits associated with the South Pole-Aitken basin are not possible using remote datasets.

5.3.1 The central uplift at Olcott crater

The central uplift of Olcott crater comprises a cluster of hills, with a lack of a central peak (Fig. 3.4). According to complex crater morphology classification scheme (Chapter 1, section 1.5.2), this would categorize Olcott crater as a peak ring. If it is a peak ring, this would be the smallest crater diameter recorded so far, and this would increase the number of peak ring basins identified on the Moon (Baker et al., 2011). As the depth of melting approaches the depth of the transient cavity, the weakness in rock strength within the transient cavity will result in the lack of a central peak and the onset of a peak ring (Grieve and Cintala, 1992; Head, 2010). In the case of Olcott, the depth of melting does exceed the depth of excavation (Fig. 4.7). This may explain the lack of a central peak at Olcott crater. As the size of the transient cavity increases, more melt is generated according to model estimates (Cintala and Grieve, 1998). However the volume of melt observed at Olcott is far less than model estimates for that size of a transient cavity (Chapter 4, Table 4.1). From a compositional perspective; the spectral profiles within all the central hills show a variation in the type of absorption features present (Chapter 3, section 3.3.4). Spectral profiles of the central uplifts indicate the presence of plagioclase feldspar, high-Ca pyroxene, and Mg-spinel (Figs. 3.5D, 3.8D). Mineral absorption features identified from the IBD spectral parameter map overlaid on altimetry (Fig. 3.8D) indicates a non-preferential distribution of the compositional materials. The variability in compositions within the central hills suggest that either: 1) the depths of origin for this hill cluster are from the mafic-rich part of the lunar crust; or 2) the target is heterogeneous, and the response of rock deformation to shock pressures is variable depending on rock rheologies. It has been observed that the transition of simple to complex crater within mare units occurs at smaller crater diameters than within the highlands (Pike, 1980; Chapter 1, section 1.5.2). Terrestrial studies also note that the transition between simple to complex occurs earlier within a sedimentary target than it does within a crystalline

target (Pike, 1980). A similar rationale can be assumed that the crater collapse within a heterogeneous target may result in different rates of collapse dependent on the rock rheologies. This may explain the difference in peak heights for the hill cluster.

It has been proposed that a cluster of peaks with variable heights reflects a range of depths for the origin of the peaks; that lower peaks may originate at shallower depths (Cintala and Grieve, 1998). This cannot be confirmed nor denied based on the current findings in this study due to the variability in compositions as discussed earlier. Detailed topographic profiles are needed, along with detailed spectral profiling of each of the central uplifts to address the question if shallow peaks originate at shallow depths. The compositions of the central peaks are similar to the compositions of the impact melt deposits; both units show the presence of high-Ca pyroxene and plagioclase feldspar (Fig. 3.5C, D). The identification of Mg-spinel (Chapter 3, section 3.3.4) does provide a better constrain on the depth estimate. Studies on the characterization of the Mg-spinel rock unit propose that such rocks are part of a magmatic intrusion or are excavated from depths near the crust-mantle boundary (Pieters et al., 2011). The multispectral assessment of Olcott crater has determined that the crater forming event excavated buried mafic materials from Lomonosov-Fleming basin including high-Ca pyroxene and Mg-spinel (Chapter 3, section 3.3.4). This adds yet another perspective on the characterization of mafic materials within Lomonosov-Fleming basin since no other observation of Mg-spinel has been made to date within the basin.

5.3.2 The central uplift at Kovalevskaya crater

In contrast to Olcott crater, the central uplift at Kovalevskaya crater is one consolidated peak making it a classic complex crater (Chapter 1, section 1.5.2). There is evidence of slumping on the western section of the peak (Fig. 4.3). Spectral profiling of the central peak area indicates the presence of low-Ca pyroxene (Fig. 4.10). The M^3 IBD parameter map for this crater however indicates the presence of the 1.3 μm absorption feature and other parameter combinations that have not yet been effectively sampled (Fig. 4.5B). Spectral sampling was limited to identifying the compositions of the geologic units throughout the crater and not for central uplifts specifically. There are some locations that may indicate the presence of Mg-spinel based on similar absorption intensities within the IBD parameter map (Fig. 5.1); however investigating this is beyond the scope of the current project and should be

considered for future work. With Mg-spinel being identified within the central uplifts at Olcott crater, and with an estimated 20 km depth of melting, it is possible that Mg-spinel may be present within Kovalevskaya as well. Therefore, detailed spectral profiles are needed to determine the overall characterization of the central uplift units of Kovalevskaya crater.

5.3.3 Central peak ring within Schrödinger basin

Schrödinger basin is the only basin on the Moon with a well-preserved peak ring basin central uplift (Fig. 2.12). Depths of melting are estimated at 60 km, close to the crust-mantle boundary, therefore the materials excavated and located within the central uplifts should spectrally represent materials typical of this depth namely mafic rich minerals (plagioclase feldspar, low-Ca pyroxene, high-Ca pyroxene, and olivine). Furthermore, if model estimates are accurate and the depth of the farside crust is ~40 km near the South Pole-Aitken basin, this means that melted materials and the source of the peak ring would be within the mantle section of the Moon.

Spectral sampling of the peak ring indicates that much of the peak ring material is composed of low-Ca pyroxene and plagioclase feldspar, i.e., highland rocks (Fig. 2.9C). This study found a strong basalt signature on the north edge of the peak ring (within a 7 km crater) using the automated algorithm (Fig. 2.7). M^3 data further validates this observation and the high spectral resolution of the data shows that most of the mafic content is dominated by high-Ca pyroxene, and olivine (Kramer et al., 2011; Kramer et al., 2012). Independent studies have also noted the presence of olivine and pure anorthosite sites on the peak ring (Ohtake et al., 2009; Yamamoto et al., 2012). It is challenging to determine if any Mg-spinel may exist due to the mosaic of the M^3 IBD parameter map for Schrödinger basin being spectrally uncalibrated (Fig. 4.5C).

5.4 Implications

The results from this study provide a new understanding on the distribution of melt deposits around older complex impact craters on the Moon. The improved spatial resolutions allow for a more detailed look at the emplacement of melt deposits beyond the crater floor. Improved spectral resolutions allow better characterization of the lunar materials within

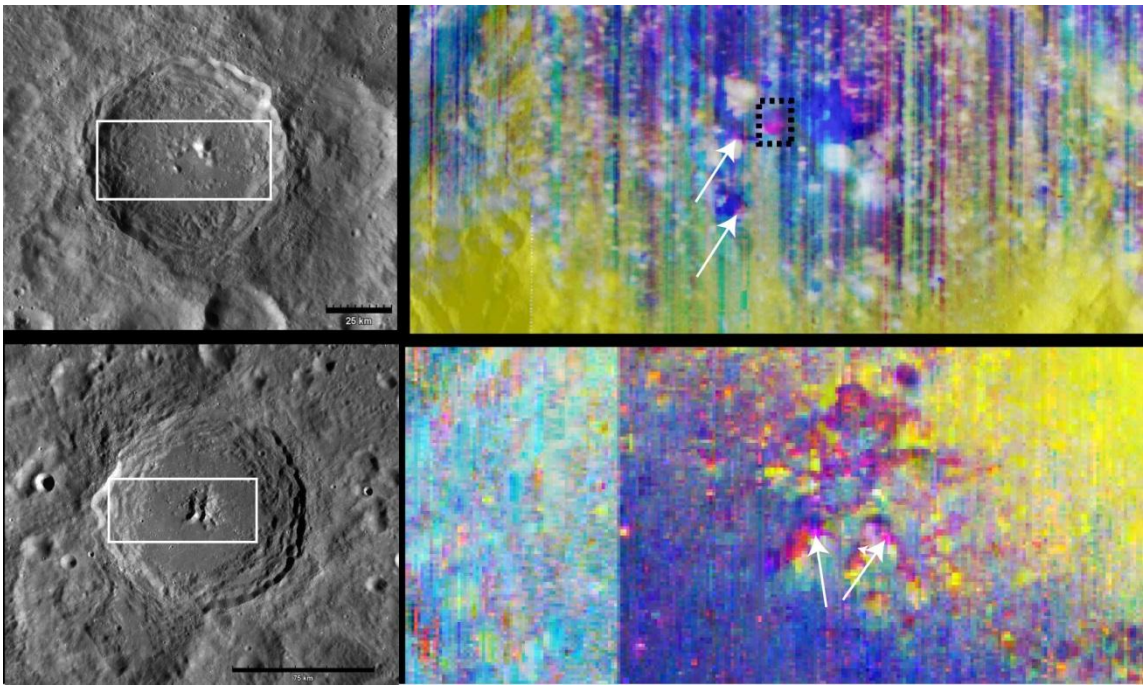

Figure 5.1: Comparison of the M^3 IBD parameter maps of the central uplift area for Olcott (top) and Kovalevskaya (bottom) craters. (Left) LRO WAC global mosaics of the craters with context views (white boxes) for the IBD parameter maps. (Right) M^3 IBD parameter maps highlighting the known (black dash box) and potential locations (white arrows) of absorption features indicative possibly of Mg-spinel. [Image credit: ISRO/NASA/GSFC/Arizona State University]

craters. Relating the spectral signature with the depths of melting provide new constraints on the crater excavation and modification processes.

Identifying the total spectral extent of observed compositions and determining if these compositions are tied to observed morphologies within a crater is not currently possible to do. This is largely due differences in spatial resolutions between spectral and image datasets, and issues with geospatial registration. The very recent release of the findings from the Gravity Recovery and Interior Laboratory (GRAIL) suggest that the crustal thickness on the Moon is much thinner (30 km; Wieczorek et al., 2012) than earlier estimated (60 km). This has widespread implications on 1) the Moon forming event, 2) the gravitational response of the target materials during the crater forming process, and 3) the depths of excavation and melting potentially tapped into during an impact event. The rates and scales at which crater walls may collapse, and the extent of melt deposits that may leave the crater floor may greatly vary from what is currently known and assumed.

5.5 Future Work

- Detailed investigation of impact melts and other impact units is essential. High resolution image data from the LRO camera network is now available, and the spatial extent of impact melt deposits beyond the crater floor at other complex craters can be determined more accurately.

- Detailed mapping of melt deposits is also needed to accurately obtain melt thicknesses within various crater units. This can better constrain models estimates on melt generation within a transient cavity. Detailed mapping can also provide a better assessment on the spatial and volumetric amount of melt generation within heterogeneous targets.

- In this study, M^3 data was manually georeferenced in order to combine the IBD spectral parameter maps with morphologic data. 3D overlays of these maps were also done manually, thereby increasing the room for error in identifying spectrally unique sites. Therefore, a better correlation between the spectral and spatial datasets is

essential to make accurate assessments on the characterization of impact melt deposits.

- The inclusion of other types of multispectral datasets, particularly high resolution image and multispectral data from the JAXA Kaguya mission (Ohtake et al., 2008) . The *Lunar Imager/Spectrometer* suite of instruments on Kaguya can add more scientific detail to various aspects of this study, including the identification of melt deposits. Multispectral and spatial data are available from the Multiband Imager (MI), Spectral Profiler (SP), Terrain Camera (TC), and Laser Altimeter (LALT) instruments at resolutions comparable to the Lunar Reconnaissance Orbiter (LRO) and Chandrayaan-1 mission instruments.

5.6 References

Antonenko, I., Osinski, G.R. 2011. Automated identification of basalt spectra in Clementine lunar data. *Planetary and Space Science*. **59**, 8: 715 – 721.

Baker, D.M.H., Head, J.W., Fassett, C.I., Kadish, S.J., Smith, D.E., Zuber, M.T., and Neumann, G.A. 2011. The transition from complex crater to peak-ring basin on the Moon: New observations from the Lunar Orbiter Laser Altimeter (LOLA) instrument. *Icarus*, **214**: 377–393.

Carter, L.M., Neish, C.D., Bussey, D.B.J., Spudis, P.D., Patterson, G.W., Cahill, J.T., and Raney, R.K. 2012. Initial observations of lunar impact melts and ejecta flows with the Mini-RF radar. *Journal of Geophysical Research*. **117**, E00H09.

Cintala, M.J., and Grieve, R.A. 1998. Scaling impact melting and crater dimensions: Implications for the lunar cratering record. *Meteoritics and Planetary Science*. **33**, 4: 889–912.

Crown, D.A., and Pieters, C.M. 1985. Spectral properties of plagioclase and pyroxene mixtures. 16th Lunar and Planetary Science Conference. 158–159.

Gillis, J.J., and Spudis, P.D. 1996. The composition and geologic setting of lunar far side maria. 27th Lunar and Planetary Science Conference. pp. 413 - 414.

Grieve, R.A.F., and Cintala, M.J. 1992. An analysis of differential impact melt-crater scaling and implications for the terrestrial impact record. *Meteoritics*. **27**: 526–538.

Hawke, B.R., and Head, J.W. 1977. Impact melt on lunar crater rims. Proceedings, Symposium on Planetary Cratering Mechanics. pp. 815–841.

Head, J.W. 2010. Transition from complex craters to multi-ringed basins on terrestrial planetary bodies: Scale-dependent role of the expanding melt cavity and progressive interaction with the displaced zone. *Geophysical Research Letters*. **37**: L022003.

Hiesinger, H., and Head, J.W. (III). 2006. New Views of Lunar Geoscience: An Introduction and Overview. In *Reviews in Mineralogy and Geochemistry*, edited by Jolliff, B.L., Wieczorek, M.A., Shearer, C.K., and Neal, C.R. **60**: 1–81.

Kramer, G.Y., Kring, D.A., Pieters, C.M., Head, J.W. III, Isaacson, P.J., Klima, R.L., McCord, T.B., Nettles, J.W., and Petro, N.E. 2011. Analysis of Schrödinger Basin Using Moon Mineralogy Mapper Spectra. 42nd Lunar and Planetary Science Conference. Abstract #1545.

Kramer, G.Y., Kring, D.A., and Pieters, C.M. 2012. Deep crust/mantle mineralogy exposed in the uplifted peak ring and basin walls of Schrödinger. 2nd Conference on the Lunar Highlands Crust. Abstract #9013.

Neish, C.D., Carter, L., Bussey, D.B.J., Cahill, J., Thomson, B., Barnouin, O., and the Mini-RF team. 2011. Correlation between surface roughness and slope on a lunar impact melt. 42nd Lunar and Planetary Science Conference. Abstract # 1881.

Ohtake, M., Haruyama, J., Matsunaga, T., Yokota, Y., Morota, T., Honda, C., and the LISM team. 2008. Performance and scientific objectives of the SELENE (KAGUYA) Multiband Imager. *Earth, Planets, and Space*. **60**: 257–264.

Ohtake, M., Matsunaga, T., Haruyama, J., Yokota, Y., Morota, T., Honda, C., Ogawa, Y., Torii, M., Miyamoto, H., Arai, T., Hirata, N., Iwasaki, A., Nakamura, R., Hiroi, T., Sugihara, T., Takeda, H., Otake, H., Pieters, C.M., Saiki, K., Kitazato, K., Abe, M., Asada, N., Demura, H., Yamaguchi, Y., Sasaki, S., Kodama, S., Terazono, J., Shirao, M., Yamaji, A., Minami, S., Akiyama, H., and Josset, J.L. 2009. The global distribution of pure anorthosite on the Moon. *Nature*. **461**: 236 – 240.

Osinski, G.R., Lee, P., Spray, J.G., Parnell, J., Lim, D.S.S., Bunch, T.E., Cockell, C.S., and Glass, B. 2005. Geological overview and cratering model for the Haughton impact structure, Devon Island, Canadian High Arctic. *Meteoritics and Planetary Science*. **40,** 12: 1759 – 1776.

Osinski, G.R., Tornabene, L.L., and Grieve, R.A.F. 2011. Impact melt and ejecta emplacement on terrestrial planets. *Earth and Planetary Science Letters*. **310**, 3: 167–181.

Pieters, C.M. 1986. Composition of the lunar highland crust from near-infrared spectroscopy. *Review of Geophysics*. **24**, 557–558.

Pieters, C.M. 1998. Lunar Materials from the Visible to Mid-Infrared: The Effects of Space Weathering. *International Geology Review*. **40**:11, 981 – 989.

Pieters, C.M., Besse, S., Boardman, J., Buratti, B., Cheek, L., Clark, R.N., Combe, J.P., Dhingra, D., Goswami, J.N., Green, R.O., Head, J.W., Isaacson, P., Klima, R., Kramer, G., Lundeen, S., Malaret, E., McCord, T., Mustard, J., Nettles, J., Petro, N., Runyon, C., Staid, M., Sunshine, J., Taylor, L.A., Thaisen, K., Tompkins, S., and Whitten, J. 2011. Mg-spinel lithology: A new rock type on the lunar farside. *Journal of Geophysical Research.* **116**, E00G08.

Pike, R.J. 1980. Control of crater morphology by gravity and target type: Mars, Earth, Moon. Proceedings, 11th Lunar and Planetary Science Conference. pp. 2159–2189.

Shoemaker, E.M., and Robinson, M.S. 1995. Clementine observations of melt rocks and volcanic materials in the Schrödinger Basin. 26nd Lunar and Planetary Science Conference. Abstract #1297.

Smrekar, S., and Pieters, C.M. 1985. Near-infrared spectroscopy of probable impact melt from three large lunar highland craters. *Icarus*. **63**: 442–452.

Tompkins, S., and Pieters, C.M. 1999. Mineralogy of the lunar crust: Results from Clementine. *Meteoritics and Planetary Science*, **34**, 25 – 41.

Wieczorek, M.A., Jolliff, B.L., Khan, A., Pritchard, M.E., Weiss, B.P., Williams, J.G., Hood, L.L., Righter, K., Neal, C.R., Shearer, C.K., McCallum, S.I., Tompkins, S., Hawke, B.R., Peterson, C., Gillis, J.J., and Bussey, B. 2006. The constitution and structure of the lunar interior. *Reviews in Mineralogy and Geochemistry*. **60**: 221–264.

Wieczorek, M.A., Neumann, G.A., Nimmo, F., Walter, K.S., Taylor, G.J., Melosh, H.J., Phillips, R.J., Solomon, S.C., Andrews-Hanna, J.C., Asmar, S.W., Konopliv, A.S., Lemoine, F.G., Smith, D.E., Watkins, M.M., Williams, J.G., and Zuber, M.T. 2012. The crust of the Moon as seen by GRAIL. *Science*. **338**: pp. 6112

Yamamoto, S., Nakamura, R., Matsunaga, T., Ogawa, Y., Ishihara, Y., Morota, T., Hirata, N., Ohtake, M., Hiroi, T., Yokota, Y., and Haruyama, J. 2012.Olivine-rich exposures in the South Pole-Aitken Basin. *Icarus*. **218**, 1: 331-344.

Appendices

Appendix A: Mini-RF grayscale Circular Polarization Ratio (CPR) and total backscatter mosaic maps for the study sites

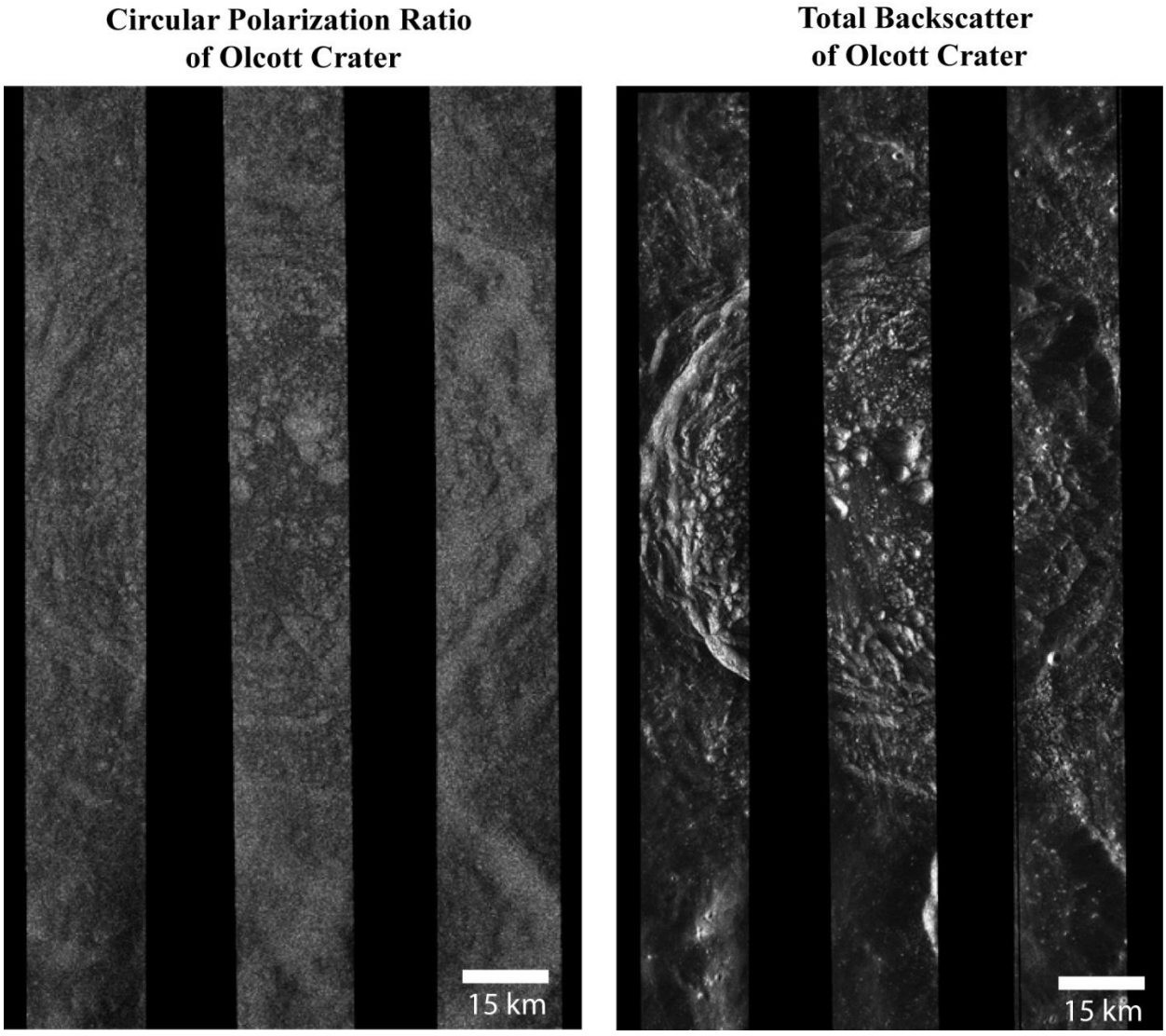

Figure A.1: Grayscale Mini-RF radar maps of Olcott crater. [Image credit: ISRO/NASA/JHUAPL/LPI]

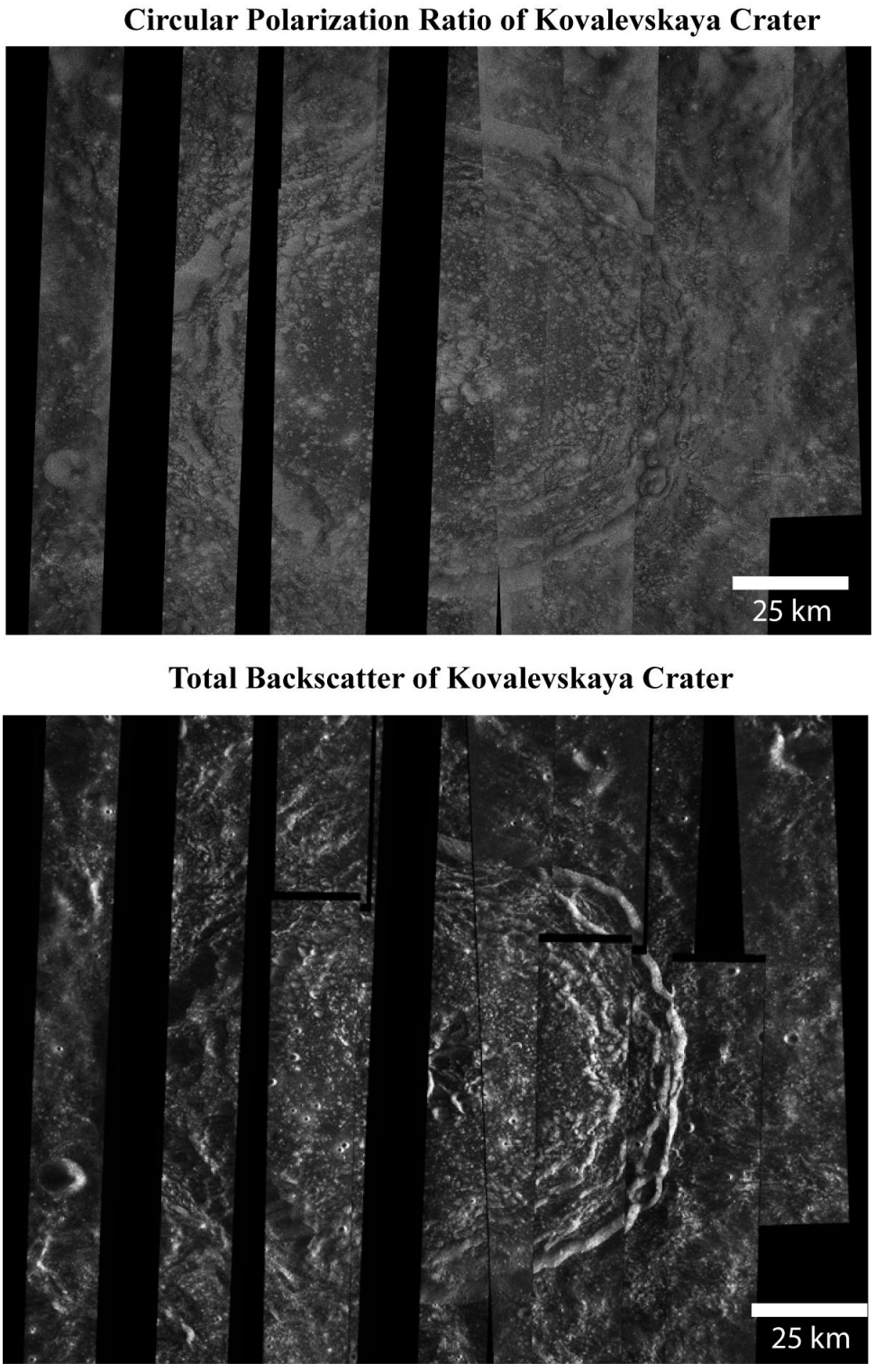

Figure A.2: Grayscale Mini-RF radar maps of Kovalevskaya crater. [Image credit: ISRO/NASA/JHUAPL/LPI]

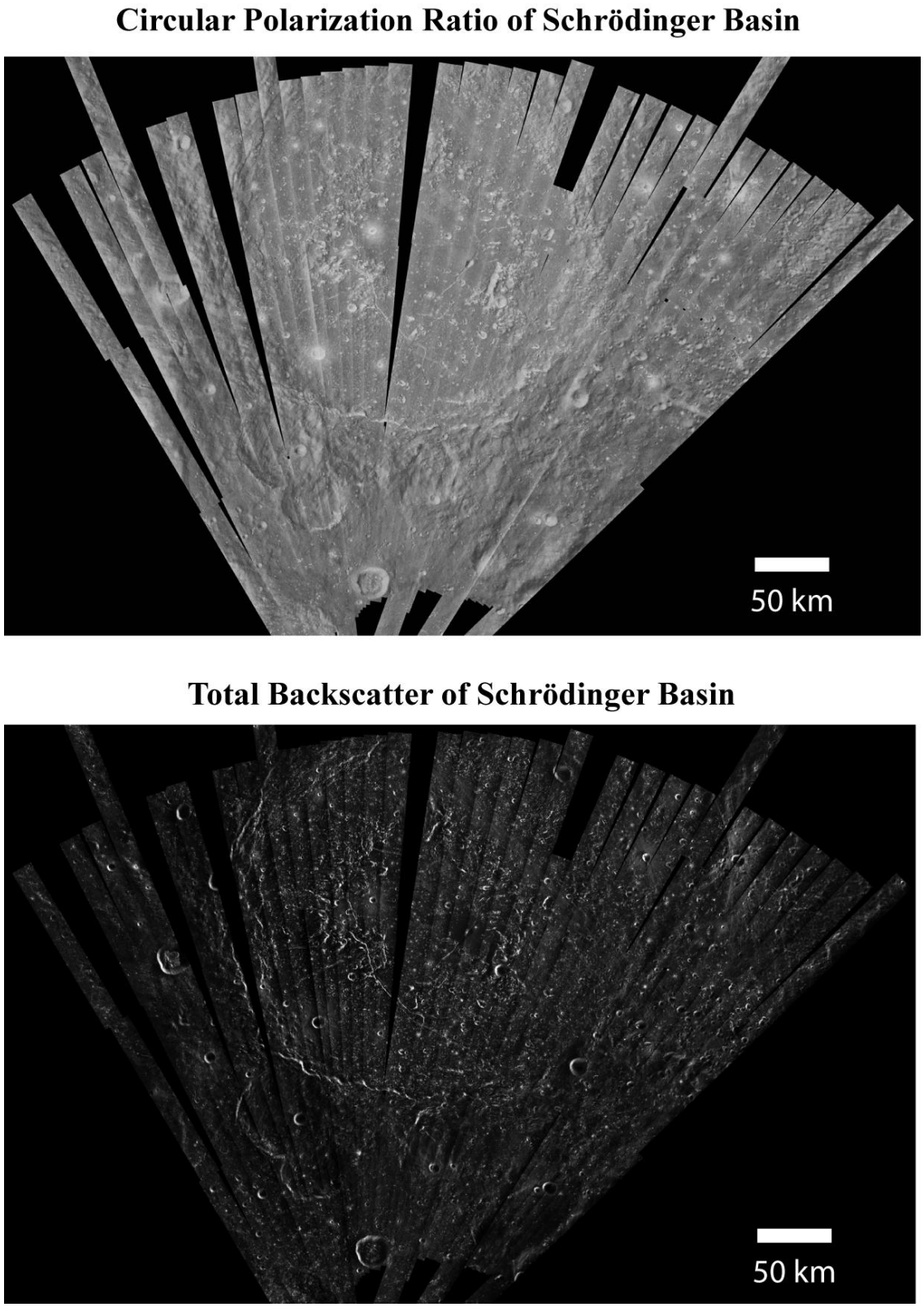

Figure A.3: Grayscale Mini-RF radar maps of Schrödinger basin. [Image credit: ISRO/NASA/JHUAPL/LPI]

Appendix B: Techniques for Calculating the Thickness of Observed Impact Melt Deposits within Lunar Complex Craters

The extent of impact melt deposits associated with each crater was identified using Lunar Reconnaissance Orbiter Camera suite (WAC and NAC). Lunar Orbiter Laser Altimeter (LOLA) data at a 1024 pixel per degree (ppd) resolution was used to derive topographical profiles of melt deposits in order to get a thickness value. The thickness of the different morphologies of impact melt deposits were estimated by assuming that the slopes surrounding a melt deposit (pond, veneer, or melt sheet) and the original crater floor surface were directly connected, and that the crater floor was smooth as well.

B.1. *Thickness of the melt sheet on the crater floor:*

At Olcott and Kovalevskaya craters, the thickness of the melt sheet on the crater floor were estimated by subtracting the current crater depth (using LOLA altimetry data at 1024 ppd resolution), from the true crater depth (Fig. B.1). Current crater depth is assumed to be an apparent crater depth, i.e., the crater floor is filled with a layer of melt sheet overlying the brecciated crater floor (Chapter 1, section 1.2). The true crater depth is estimated by assuming a smooth and direct connection between the crater wall slopes and the crater floor. By extrapolation process, the point of intersection was assumed to reflect the true crater depth (e.g. Fig. B.2). The calculated impact melt thickness on the crater floor would represent the maximum value when determining impact melt volumes.

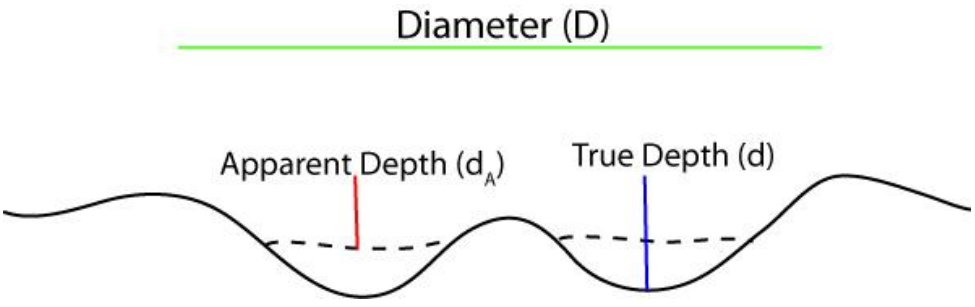

Figure B.1: Cross section of a complex crater showing the apparent and true depth- diameter relation (modified from Croft, 1980).

In the case of Schrödinger basin, a different approach was used to calculate the melt sheet thickness on the basin floor. Previously, model calculations have estimated that the melt thickness lining the transient cavity of Schrödinger basin would be 1.4 km thick (Cintala and Grieve, 1998). Even if a significant percent of melt remains within the transient cavity as models estimate (Table 4.1), the collapse of crater walls and central uplifts during the crater modification phase would result in some of the melts being emplaced over terraces and the peak ring at Schrödinger basin, in addition to the melt sheet on the crater floor. Therefore, this value of 1.4 km is not used in estimating the current melt thicknesses on the basin floor. The melt thickness was, instead, estimated using the depth-diameter ratio of a 10 km simple crater located on the southwest section of the crater floor (Fig. 2.7). The spectral characterization of impactites of this simple crater is different (more mafic-rich) from the rest of the Schrödinger basin floor, as summarized in Chapter 2 (section 2.3.1). It was interpreted that this simple crater was excavating materials at depth, possibly sampling impact melt from the South Pole-Aitken basin (Chapter 2, section 2.4.5). No other post-Schrödinger crater feature show similar spectral variations on the basin floor (Figs. 2.7, 2.8B, 2.9B; section 2.3.7). Therefore, the melt thickness calculated using this technique provides a maximum value on the melt thickness within the basin floor.

B.2. *Thickness of impact melt deposits along terrace surfaces, melt ponds, and melt veneers:*

At each crater site, the volume was estimated through a series of steps. First, topographic profiles were extracted of surfaces perpendicular to the melt deposit surface. LRO – LOLA data was used to derive topographic information (1024 ppd resolution). The next step was to assume that the slopes surrounding the deposit were smoothly connected to the surface beneath as done earlier for calculating the thickness on the crater floor. Slopes were extrapolated on either sides of the deposits, and the point of intersection was assumed to be the depth of the original terrace surface. The depth of the melt deposit was calculated by subtracting the depth of the current pond surface from the depth of the terrace floor (Fig. B.2). Multiple topographic profiles were extracted at locations with a range in the size of the melt morphology. This way a range of melt thicknesses could be obtained to better constrain the melt volume. The melt thickness within melt ponds are estimated the same way as above in the case of terraces.

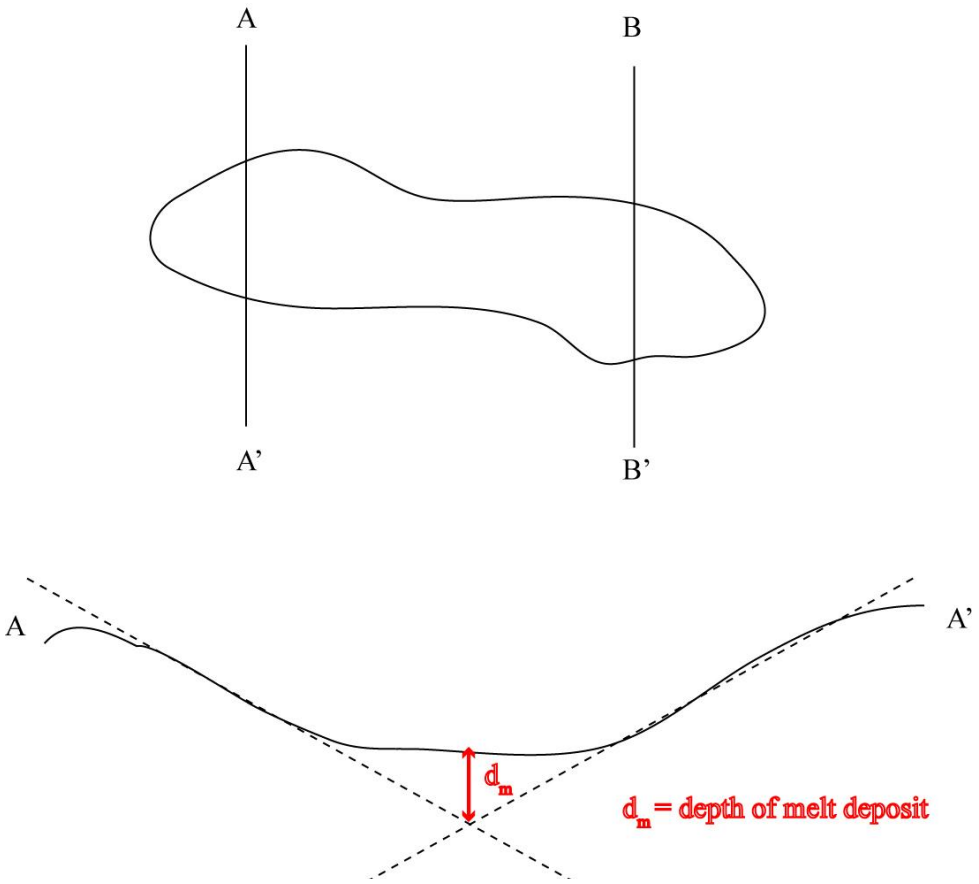

Figure B.24: Cross section view of a pooled deposit along terraces or beyond the crater rim. The depth of the melt deposit is the same as melt thickness. Where available multiple topographic profiles are taken to acquire a potential range in melt thickness to better constrain the melt volume.

The thickness of melt veneers were estimated in a different way that methods listed earlier. Once the extent of melt veneers was determined, the LROC NAC image database was further searched to locate examples of veneer outcrops. For a coherent veneer outcrop, the shadow height along a vertical scarp face was taken as a measure of the thickness (e.g. Fig. B.3).

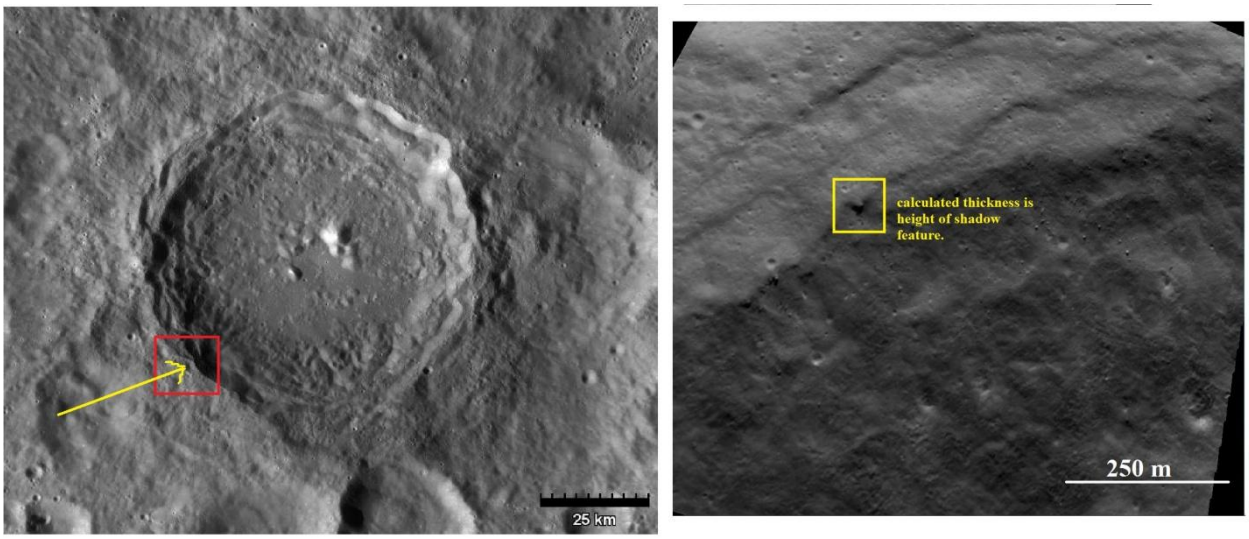

Figure B.3: An example of calculating the thickness of a melt veneer at Olcott crater. The measure height of shadow near a rim scarp provides a minimum estimate on the melt thickness of the deposit. [Image credit: NASA/GSFC/Arizona State University]

Appendix C: Moon Mineralogy Mapper (M^3) Data Product List and Processing Summary

The Moon Mineralogy Mapper (M^3) data from the Chandrayaan-1 mission was extensively used to characterize the mineralogical information for each of the study sites. This included generating false colour composite maps. Such composite maps typically highlight the strengths of the absorption bands at particularly at integrated band depths characteristic of lunar minerals. Such maps are known as *IBD Composite Maps*. The other utility of M^3 data was in obtaining individual reflectance spectral profiles for sites of interest.

Due to the lack of readily available, calibrated, and georeferenced data, raw M^3 data had to be processed in multiple ways to extract individual spectral profiles and generate IBD composite maps. Details of the individual M^3 product types and the various stages of data processing conducted for each of the study sites are summarized in Sections C.1 – C.2.

Spectral Profiles presented in Chapters 2–4 (Figs. 2.9, 3.5, 3.8D, 3.9, and 4.10) display continuum removed profiles. Continuum removal is typically used to normalize reflectance spectra to compare individual absorption features from a common baseline (Joseph, 2005). The continuum is a straight-line that connects spectral maxima at spectral wavelength range of interest. The default continuum removal algorithm available in ENVI v. 4.8 (Exelis Visual Information Solutions, Boulder, Colorado) was utilized in analysis for this study.

C.1. Deriving individual reflectance absorption spectral profiles each of the study sites

Olcott Crater

For Olcott crater, three M^3 products (Table C.1) were downloaded from the Lunar Orbital Data Explorer portal (ode.rsl.wustl.edu/moon). Since M^3 product tiles typically cover a large swath of the lunar surface (specify the width and height), each reflectance data product file was brought into ENVI version 4.8 (Exelis Visual Information Solutions, Boulder, Colorado) and later cropped to the necessary size dimensions for the analysis. Typically, the area for analysis included Olcott crater and a surrounding surface extending one crater diameter beyond the crater rim that was visible in the product file.

Table C.1: M^3 Product Information for Olcott Crater

Product ID	Product Level	Product Level Description
M3G20081231T113333_V01_RFL	Level 2	pixel located, thermal corrected, photometry corrected, reflectance data
M3G20090530T160828_V01_RFL	Level 2	pixel located, thermal corrected, photometry corrected, reflectance data
M3G20090530T201123_V01_RFL	Level 2	pixel located, thermal corrected, photometry corrected, reflectance data

By default the downloaded data is band interleaved (BIL). In order to view reflectance data and extract spectral profiles, the data would have to be in band sequential format (BSQ). The data conversion was possible using the built-in conversion feature in ENVI v. 4.8 (located within the *Basic Tools* menu).

Following the conversion to BSQ, data values for each of the individual band filters were read in using the Oasis Montaj (Geosoft Inc., Toronto, Ontario). Spectra sampling sites were typically located along sloped surfaces or freshly exposed surfaces. Due to the calibration issues stemming from the thermal effects and instrumentation artefacts, the spectral range typically plotted to derive spectral plots were limited to band filters 3 (540 nm) – 85 (2936 nm). Spectra were sampled using a 3x3or 5x5 pixel averages. Each spectral profile acquired was compared to the M^3 spectral library (Lundeen et al., 2010) to determine mineralogy. weathered spectral profiles in our analyses as they are hard to distinguish. Sloped surfaces tend to expose the freshest surfaces by inhibiting regolith build-up. Freshly exposed surfaces on the slopes of smaller craters can be used to sample the immediate subsurface (McCord et al., 1981; Antonenko, 1999; Staid et al, 2000). Shadowed regions or overly bright areas (where reflectance was supersaturated) were not used for spectra selection to avoid misinterpretations.

Kovalevskaya Crater

Two M^3 products (Table C.2) over the Kovalevskaya crater region were downloaded from the Lunar Orbital Data Explorer portal (ode.rsl.wustl.edu/moon). The data processing and sample selection processes were similar to those described for Olcott crater (above).

Table C.2: M^3 Product Information for Kovalevskaya Crater

Product ID	Product Level	Product Level Description
M3G20090812T071513_V01_RFL	Level 2	pixel located, thermal corrected, photometry corrected, reflectance data
M3G20090618T112223_V01_RFL	Level 2	pixel located, thermal corrected, photometry corrected, reflectance data

Schrödinger Basin

A single M^3 product (Table C.3) crossing through a section of the Schrödinger basin was downloaded from the Lunar Orbital Data Explorer portal (ode.rsl.wustl.edu/moon). Radiance data was converted into reflectance data using the processes described in (Green et al., 2010).

Table C.3: M^3 Product Information for Schrödinger Basin

Product ID	Product Level	Product Level Description
M3G20090529T013507_V01_RDN	Level 1B	pixel located, resampled, calibrated, radiance data

C.2. Generating Integrated Band Depth (IBD) Composite Maps

Spectral parameter IBD maps were generated at each of the crater sites to: 1) assess the distribution of these spectral parameters at a first order crater-wide scale, and 2) determine sampling spots for capturing individual spectral profiles that would be representative of the various colours identified in the spectral parameter map. For this study, the band

concentrations at 1 µm, 1.3 µm, and 2 µm were selected to determine the presence of low- and high-Ca pyroxene, olivine, spinel, and plagioclase feldspar on the surface.

The generation of IBD composite maps involved an elaborate series of steps, where certain band filter channels were manipulated using algorithms defined by Mustard et al. (2011) and Donaldson Hanna et al. (2012). The exact steps are summarized below.

The IBD value at 1 µm (olivine) was calculated using the following algorithm (Mustard et al., 2011).

$$\sum_{n=0}^{26} 1 - \frac{R(789+20n)}{Rc(789+20n)} \qquad \text{Equation C.1.}$$

where R = reflectance at given wavelength; Rc = continuum reflectance i.e. a straight line across the absorption band

The IBD value at 2 µm (spinel) was calculated using the following algorithm (Mustard et al., 2011).

$$\sum_{n=0}^{21} 1 - \frac{R(1658+40n)}{Rc(1658+40n)} \qquad \text{Equation C.2.}$$

where R = reflectance at given wavelength; Rc = continuum reflectance i.e. a straight line across the absorption band

The IBD value at 1.3 µm (plagioclase feldspar) was calculated using the algorithm defined by Donaldson Hanna et al. (2012).

$$\sum_{n=0}^{26} 1 - \frac{R(1029+20n)}{Rc(1029+20n)} \qquad \text{Equation C.2.}$$

where R = reflectance at given wavelength; Rc = continuum reflectance i.e. a straight line across the absorption band

Once the values for each of the IBD parameters were calculated, the composite maps were combined in RGB mode with the 1 μm in the red channel, 2 μm in the green channel, and 1.3 μm in the blue channel to generate composite maps as seen in Fig. 4.5.

C.3. References

Antonenko, I. 1999. Cryptomafic Deposits on the Western Limb of the Moon: Areal Distribution and Volumetric Significance of Early Imbrian Volcanism as Determined from Dark – Haloed Impact Craters. Ph.D. thesis, Department of Geological Sciences, Brown University, Providence, R.I.

Donaldson Hanna, K.L., Cheek, L.C., Pieters, C.M., Mustard, J.F., Wyatt, M.B., and Greehangen, B.T. 2012. Global identification of crystalline plagioclase across the lunar surface using M^3 and Diviner data. 43rd Lunar and Planetary Science Conference. Abstract # 1968.

Green, R.O., Boardman, J., Pieters, C.M., Clark, R. and the M^3 Team. 2010. An algorithm for estimation and correction of the thermal emitted radiance with preservation of spectral structure in data measured by the Moon Mineralogy Mapper. 41st Lunar and Planetary Science Conference. Abstract #2331.

Joseph, G. 2005. *Fundamentals of Remote Sensing*. India: Universities Press. 486p.

Lundeen, S., McLaughlin, S., Alanis, R. 2010. Moon Mineralogy Mapper: Data Product Software Interface Specification (Ver. 9.3). *http://img.pds.nasa.gov/documentation/M3_DPSIS.PDF*. 13p.

McCord, T.B., Clark, R.N., Hawke, B.R., McFadden, L.A., Owensby, P.D., and Pieters, C.M. 1981. Near-Infrared Spectral Reflectance: A First Good Look. *Journal of Geophysical Research*. **86**: 10883-10892.

Mustard, J.F., Pieters, C.M., Issacson, P.J., Head, J.W., Besse, S., Clark, R.N., Klima, R.L., Petro, N.E., Staid, M.I., Sunshine J.M., Runyon, C.J., and Tompkins, S. 2011. Compositional diversity and geologic insights of the Aristarchus crater from Moon Mineralogy Mapper data. *Journal of Geophysical Research*. **116**: E00G12.

Staid, M.I., and Pieters, C.M. 2000. Integrated Spectral Analysis of Mare Soils and Craters: Application to Eastern Nearside Basalts. *Icarus*. **145**: 122-139.

Curriculum Vitae

Name: Bhairavi Shankar

Post-secondary Education and Degrees:

University of Toronto
Toronto, Ontario, Canada
2002-2006 B.Sc.

The University of Minnesota - Duluth
Duluth, Minnesota, USA
2006-2008 M.Sc.

The University of Western Ontario
London, Ontario, Canada
2008-present Ph.D.

Honours and University Awards:

Robert & Ruth Lumsden Graduate Award in Earth Sciences, of Western Ontario
2011-2012

Lunar Planetary Institute (LPI) Career Development (Travel) Award
2012

Graduate Thesis Research Award – University of Western Ontario, Dept. of Earth Sciences
2008

Related Work Experience

Teaching Assistant – Outreach and Education
Centre of Planetary Science and Exploration
The University of Western Ontario
2011-2012

GIS Lead – ILSR Analogue Mission
Centre of Planetary Science and Exploration
The University of Western Ontario
2010-2011

Teaching Assistant
Department of Earth Sciences
The University of Western Ontario
2008-2011

Publications:

(2013)

Shankar, B., Osinski, G.R., Antonenko, I., and Tornabene, L.L. (2013). A Multispectral Assessment of the Schrödinger impact basin. Canadian Journal of Earth Sciences, in press.

Shankar B., Osinski G. R., and Antonenko I. (2013). Multispectral analyses of Kovalevskaya crater on the Lunar Farside (abstract #2094). 44th Lunar and Planetary Science Conference.

Gilbert A., Osinski G. R., Harrison, T. N., Mader M., Nuhn, A., **Shankar B.**, and Tornabene, L.L. (2013). Interactive Mapping of the Planets using the Google Earth Platform (abstract #2045). 44th Lunar and Planetary Science Conference.

(2012)

Shankar B., Osinski G. R., Antonenko I., and Tornabene L. L. (2012). Multispectral analyses of Olcott crater with recent high resolution data (abstract #1357). 43rd Lunar and Planetary Science Conference.

Shankar B., Osinski G. R., Abou-Aly S., Beauchamp M., Blain S., Chanou A., Clayton J., Francis R., Kerrigan M., Mader M. M., Marion C., McCullough E., Moores J. E., Pickersgill A. E., Pontefract A., Preston L. J., and Tornabene L. L. (2012). Lunar Analogue Mission: Overview of the site selection and traverse planning process for a human sortie mission at the Mistastin Lake Impact Structure, Labrador, Canada (abstract #1143). 43rd Lunar and Planetary Science Conference.

Kerrigan M. C., **Shankar B.**, Marion C., Francis R., Pickersgill A. E., Capitan R. D., Osinski G. R., and the ILSR Team (2012). Real-time Mission Control Tracking of Astronaut Positions during Analogue Missions (abstract #2756). 43rd Lunar and Planetary Science Conference.

McCullough E., Pickersgill A. E., Francis R., Bassi A., **Shankar B.**, Mader M., Beauchamp M., Osinski G. R., and the KRASH science and operations teams. (2012). Scientific Application of Visual Systems Instrumentation used during Lunar Sample Return Analogue Missions (abstract #2687). 43rd Lunar and Planetary Science Conference.

Chanou A., Tornabene L. L., Osinski G. R., Zanetti M., Pickersgill A. E., **Shankar B.**, Marion C., Mader M. M., Souders K. A., Sylvester P., Jolliff B. L., Shaver C., and the KRASH science and operations teams (2012). Impact Melt-Pond Scenario Tested During the KRASH 2011 Analogue Mission at Kamestastin Impact Structure (abstract #2580). 43rd Lunar and Planetary Science Conference.

Gilbert A., Osinski G. R., August T., Mader M., McCullough E., Pontefract A., **Shankar B.**, and Singleton A. (2012). The continued growth of the education and outreach program at the Centre for Planetary Science and Exploration (abstract #1626). 43rd Lunar and Planetary Science Conference.

Mader M. M., McCullough E., Beauchamp M., Clayton J., Marion C. L., Moores J., Pickersgill A. E., Preston L. J., **Shankar B.**, Osinski G. R., and ILSR team. (2012). Science data management during real-time geological lunar analogue missions to the Sudbury and Mistastin Lake impact structures: Recommendations for future ground data systems (abstract #1842). 43rd Lunar and Planetary Science Conference.

Pickersgill A. E., Osinski G. R., Beauchamp M., Marion C., Mader M. M., Francis R., McCullough E., **Shankar B.**, Barfoot T., Bondy M., Chanou A., Daly M., Dong H., Furgale P., Gammell J., Ghafoor N., Hussein M., Jasiobedzki P., Lambert A., Leung K., McManus C., Ng H. K., Pontefract A., Stenning B., Tornabene L. L., Tripp J., and the ILSR Team. (2012). Scientific Instrumentation for a Lunar Sample Return Analogue Mission (abstract #2657). 43rd Lunar and Planetary Science Conference.

Marion C. L., Osinski G. R., Abou-Aly S., Antonenko I., Barfoot T., Barry N., Bassi A., Battler M., Beauchamp M., Bondy M., Blain S., Capitan R., Cloutis E., Cupelli L., Chanou A., Clayton J., Daly M., Dong H., Ferrière L., Flemming R., Flynn L., Francis R., Furgale P., Gammell J., Garbino A., Ghafoor N., Grieve R. A. F., Hodges K., Hussein M., Jasiobedzki P., Jolliff B. L.,

Kerrigan M. C., Lambert A., Leung K., Mader M. M., McCullough E., McManus C., Moores J., Ng H.K., Otto C., Ozaruk A., Pickersgill A. E., Pontefract A., Preston L. J., Redman D., Sapers H., **Shankar B.**, Shaver C., Singleton A., Souders K., Stenning B., Stooke P., Sylvester P., Tripp J., Tornabene L. L., Unrau T., Veillette D., Young K., Zanetti M. (2012). A Series of robotic and human analogue missions in support of lunar sample return (abstract #2333). 43rd Lunar and Planetary Science Conference.

(2011)

Shankar B., Antonenko I., Osinski G. R., Mader M. M., Preston L. Battler M., Beauchamp M., Chanou A., Cupelli L., Francis R., Marion C., McCullough E. Pickersgill A., Unrau T., and Veilliette D. (2011). Lunar Analogue Mission – Overview of the Site Selection Process at Mistastin Lake Impact Structure, Labrador, Canada. (Abstract#2594). 42nd Lunar and Planetary Science Conference.

Mader M. M., Antonenko I., Osinski G. R., Battler M., Beauchamp M., Cupelli L., Chanou A., Francis R., Marion C., McCullough E., Preston L. , **Shankar B.**, Unrau T., and Veillette D. (2011). Optimizing Lunar Sample Return: Lessons Learned from a Robotic Precursor Lunar Analogue Mission at the Mistastin Impact Structure, Labrador, Canada. *The Importance of Solar System Sample Return Missions to the Future of Planetary Science Workshop.*

Marion C., Osinski G. R., Antonenko I. , Barfoot T., Battler M., Beauchamp M., Cloutis E., Cupelli L., Chanou A., Daly M., Ferrière L., Flemming R., Francis R., Ghafoor N., Grieve R. A. F., Hodges K., Hussain M., Jolliff B. L., Mader M. M., McCullough E., Otto C., Preston L. , Redman D., **Shankar B.**, Singleton A., Stooke P., Sylvester P., Tornabene L. L., Unrau T., and Veillette D. (2011). A Lunar Analogue Mission: Sample Return to the South Pole–Aitken Basin. (Abstract #2515). 42nd Lunar and Planetary Science Conference.

Kring D. A., Balcerski J., Blair D. M., Chojnacki M., Donohue P. H., Drummond S. A, Garber J. M., Hopkins M., Huber M. S., Jaret S. J., Losiak A., Maier A, Mitchell J., Ong L., Ostrach L. R., O'Sullivan K. M., Potter R. W. K., Robbins S., **Shankar B.**, Shea E. K., Singer K. N., Sori M., Sturm S., Willmes M., Zanetti M., and Wittmann A. (2011). Fold hinge in overturned Coconino Sandstone and its structural displacement during the formation of Barringer Meteorite Crater (aka Meteor Crater). 42nd Lunar and Planetary Science Conference.

Kring D. A., Balcerski J., Blair D. M., Chojnacki M., Donohue P. H., Drummond S. A , Garber J. M., Hopkins M., Huber M. S., Jaret S. J., Losiak A., Maier A, Mitchell J., Ong L., Ostrach L. R., O'Sullivan K. M., Potter R. W. K., Robbins S., **Shankar B.,** Shea E. K. ,Singer K. N., Sori M., Sturm S., Willmes M., Zanetti M., and Wittmann A. (2011). Asymmetrical Distribution of Impact Ejected Lithologies at Barringer Meteorite Crater (aka Meteor Crater). 42nd Lunar and Planetary Science Conference.

(2010)

Shankar B., Antonenko I., Osinski G. R., and Stooke P. J. (2010). Revisiting the Geology of the Schrödinger Impact Basin. NLSI- Third Annual Lunar Science Conference.

Shankar B., Antonenko I., Osinski G. R., and Stooke P. J. (2010). Revisiting the Geology of the Schrödinger Impact Basin. 2nd Annual Lunar Scientists and Engineers Workshop.

Shankar B., Antonenko I., and Osinski G. R. (2010). Characterizing impact melt deposits within the Schrödinger Impact Basin. First Lunar Graduate Conference.

Shankar B., Antonenko I., Osinski G. R., Stooke P. J., and Mest S. (2010). Multispectral Study of the Schrödinger Impact Basin. *(*Abstract #2542). 41st Lunar and Planetary Science Conference

Mader M. M., Osinski G. R., Marion C., Dammeier R., **Shankar B.**, and Sylvester P. (2010). Mistastin impact structure, Labrador: A geological analogue for lunar highland craters. (Abstract #7018). Nördlingen Ries Crater Workshop.

(2009)

Shankar B., Antonenko I., Osinski G. R., and Stooke P. J. (2009). A Multispectral Study of the Schrödinger Impact Basin on the Lunar Farside. Planetary Science Research Symposium.

Shankar B., Antonenko I., and Osinski G. R. (2009). Multispectral Study of the Schrödinger Impact Basin on the Lunar Farside. NLSI- Second Annual Lunar Science Conference.

Shankar B., Antonenko I., and Osinski G. R. (2009). *Multispectral Study of the Schrödinger Impact Basin on the Lunar Farside*. Eos Trans. AGU. **90**. 22. Jt. Assem. Suppl., Abstract P13A-05.

Petro N., Bleacher L., Bleacher J., Noble S., Cahill K.R.S., Fagan A., Mader M., and **Shankar B.** (2009). Towards a Sustainable Lunar Science Community: Developing the Next Generations of Lunar Scientists and Engineers. (Abstract # 2041). *2009 Annual Meeting of LEAG*.